NASA-CR-159039
19800016839

NASA CR 159039

Thermal-Structural Design Study of an Airframe-Integrated Scramjet Final Report

J.J. Killackey, E.A. Katinszky, S. Tepper
A.A. Vuigner, C.C. Wright, and G.G. Stockwell

AIRESEARCH MANUFACTURING COMPANY OF CALIFORNIA
A Division of The Garrett Corporation

CONTRACT NAS 1-13984
May 1980

NASA
National Aeronautics and
Space Administration

Langley Research Center
Hampton, Virginia 23665
AC 804 827-3966

NASA CR 159039

Thermal-Structural Design Study of an Airframe-Integrated Scramjet Final Report

J.J. Killackey, E.A. Katinszky, S. Tepper
A.A. Vuigner, C.C. Wright, and G.G. Stockwell

AIRESEARCH MANUFACTURING COMPANY OF CALIFORNIA
A Division of The Garrett Corporation

CONTRACT NAS 1-13984
May 1980

National Aeronautics and
Space Administration

Langley Research Center
Hampton, Virginia 23665
AC 804 827-3966

CONTENTS

CONTENTS (Continued)

LIST OF ILLUSTRATIONS

ILLUSTRATIONS (Continued)

LIST OF TABLES

INTRODUCTION

The Langley Research Center of NASA has been involved in a research program for the development of airframe-integrated Scramjet concepts. These concepts use the entire undersurface of the aircraft to process the engine airflow. The forebody of the aircraft serves as an extension of the engine inlet and the afterbody serves as an extension of the engine nozzle.

The NASA Hypersonic Research Engine (HRE) program (ref. 1) was a major contributor to the development of Scramjet technology. This program culminated in two major milestones: (1) successful development of the first flight-weight, hydrogen-cooled engine structure, including verification tests in the NASA-Langley 8-Foot High-Temperature Structures Tunnel; and (2) confirmation of dual-mode (subsonic/supersonic combustion) aero-thermodynamic performance at Mach 5 to 7 in the NASA-Lewis facility at Plum Brook. Baseline data for the current study were also taken from the NASA-sponsored hydrogen-cooled panel studies (refs. 2 and 3).

Subsequent research at NASA-Langley has led to a lightweight, fixed-geometry, modular, airframe-integrated Scramjet engine concept that promises high installed performance (net thrust) over a wide Mach number range. Performance predictions for this hydrogen-fueled, regeneratively cooled Scramjet indicate a cooling requirement that is less than the heat sink available in the hydrogen fuel up to at least a flight Mach number of 10. This provides a potential for actively cooling the airframe.

The current study is an extension of the preliminary thermal-structural design of an airframe-integrated Scramjet study conducted by NASA (ref. 4). The objective is to define a practical engine concept that has a sound basis in materials and manufacturing technology. Emphasis is placed on the engine thermal-structural design, although consideration is given to the fuel subsystem and the aircraft interface. The thermal-structural design evolved in the ref. 4 study and the HRE technology form the basis for this effort. The aerodynamic lines were defined by NASA-Langley and remained unchanged during the study. This report presents the results of the current study. A summary is given in ref. 5.

Engine design is based on a research-size aircraft to provide a focal point; however, technological development is aimed at more advanced applications. The importance of hypersonic technology, its potential applications, and the case for a hypersonic research vehicle are described by Hearth and Preyss (ref. 6). Convectively cooled engine and airframe structures for hypersonic flight are reviewed in ref. 7.

The Project Manager for NASA was Mr. A. R. Wieting, Thermal Structures Branch, Structures and Dynamics Division, NASA Langley Research Center. The AiResearch Program Manager was Mr. O. A. Buchmann. The principal contributors to the study were Messrs. J. J. Killackey and G. G. Stockwell (Program Engineer); E. A. Katinszky, G. D. Mueller, and S. Tepper (Structural Analysis); A. A. Vuigner (Thermal Analysis); C. C. Wright (Strut Flow Analysis); and M. Cooke (Mechanical Design).

Values for the physical quantities are given primarily in U.S. Customary units. Values are also given in SI units for much of the material presented. Calculations were made in U.S. Customary units. A conversion table from U.S. Customary to SI units is included in the Appendix.

Identification of commercial products in this report is to adequately describe the materials and does not constitute official endorsement, expressed or implied, of such products or manufacturers by the National Aeronautics and Space Administration.

SYMBOLS

E	Young's modulus, MPa (psi)
h	heat transfer coefficient, $W/cm^2-°C$ ($Btu/hr-ft^2-°F$)
k	thermal conductivity, W/cm-°C (Btu/hr-ft-°F)
M_∞	free-stream Mach number, dimensionless
q_∞	free-stream dynamic pressure, Pa (psf)
RA	reduction in area, dimensionless
R_x	local Reynolds number, dimensionless
V_∞	free-stream velocity, m/sec (ft/sec)
α	coefficient of thermal expansion, 1/°C (1/°F)
σ_y	yield stress, Pa (psi)
ϕ_c	cooling equivalence ratio (fuel used for regenerative engine cooling as fraction of fuel burned), dimensionless
ϕ_f	fuel equivalence ratio burned, dimensionless
ΔP	pressure drop, Pa (psi)
ΔT	temperature difference, K (°R)
T	temperature, K (°R)

P pressure, Pa (psi)

T_{wo} Temperature at outer (aerodynamic) surface of cooling jacket wall, K (°R)

T_{wi} Temperature at inner surface of cooling jacket wall, K (°R)

ΔT_w Temperature difference across cooling jacket wall, $T_{wo}-T_{wi}$, K (°R)

ENGINE DESCRIPTION

A typical installation of the Scramjet engines on a high-speed research airplane is shown in fig. 1. The rectangular modular engine is attached directly to the vehicle undersurface. The aircraft forebody serves as the air inlet compression ramp and the afterbody serves as an extension of the engine nozzle; the entire undersurface is integrated into the engine design. The modular engines provide maximum capture of the airflow between the body and bow shock with minimum external drag. Since the Scramjet does not operate at low speeds, some form of takeoff and acceleration system is required. In the research application, the vehicle is air launched at Mach 0.8, rocket boosted to test Mach number, and flown on the hydrogen-fueled Scramjets over the prescribed envelope.

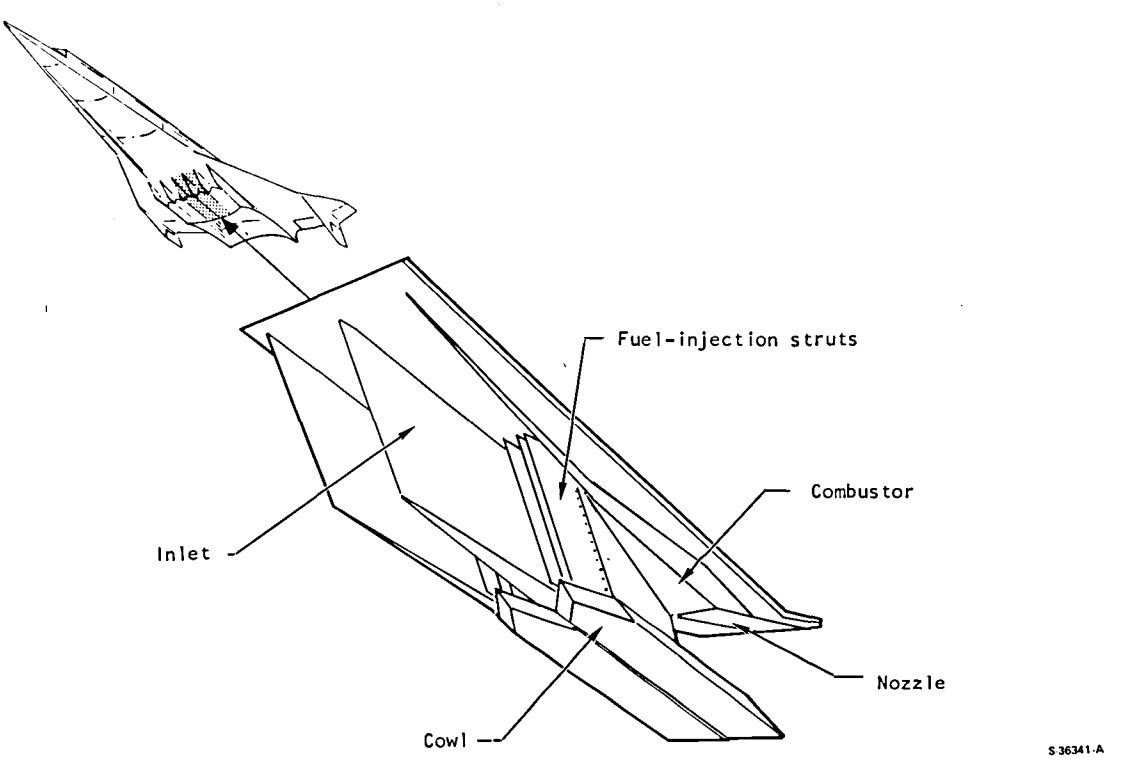

Figure 1.-Scramjet engine configuration and installation.

As a baseline, the Scramjets were sized for one concept of a hypersonic research vehicle that has a mass after rocket burn-out of 21,430 lb. The aircraft is 20.3 m (66.7 ft) long and requires six Scramjet engine modules that are located 12.2 m (39.9 ft) from the aircraft nose. Two inner Scramjet modules are shown in fig. 1; the side wall of one module is removed to show the internal engine surfaces. The Scramjet module is 45.7 cm (18.0 in.) high by 36.6 cm (14.4 in.) wide with an overall length of 314.3 cm (123.742 in.). External aerodynamic lines are defined in detail on Drawing 190062 (page 5).

The sidewall leading edges are swept back 48 deg and the cowl does not begin until engine station 49.031 (approximately 2.7 x inlet height); this provides an "open window" upstream of the cowl leading edge to spill flow downward during the inlet starting process at the low end of the Mach number range (ref. 4). This important design feature circumvents variable geometry.

Three fuel injection struts are used for multiplaner fuel injection, which enhances fuel mixing and thereby minimizes the combustor length and heat load to the internal surfaces. To provide accessibility and replaceability of parts, each Scramjet module comprises four structural components: topwall, cowl, sidewalls, and three fuel injection struts. The two side struts are identical, asymmetric, and have 3/2 of the chord of the symmetric center strut.

The two module structural design concepts shown in figs. 2 and 3 were considered. All engine internal and external surfaces exposed to gas flow are cooled regeneratively by circulating the cryogenically stored hydrogen fuel through a thermal protection system (TPS). The hydrogen fuel coolant is introduced at the leading and trailing edges (low heat load) and flows toward the engine throat (highest heat load), where it is collected in manifolds and directed to the fuel plenum. From there, the hydrogen is routed to fuel manifolds in each strut and injected into the airstream.

All leading edges are impingement cooled. Coolant is injected through multiple slots and impinges directly on the inside surface of the leading edge, turns, and then flows through the TPS surface. Impingement cooling using cryogenic hydrogen provides a maximum possible cooling effect in these areas of maximum heat flux. Pressure and thermal loads acting on the panels are accommodated by a honeycomb primary structure in the selected structural configuration. The panels are rigidly joined at the corners using a bolted connection and static seals to contain the gas flow. The struts are inserted through openings in the topwall and secured by a fixed mount in the topwall and a sliding support in the cowl. Bulkheads within the struts provide separate manifolds and contain the high-pressure hydrogen fuel and coolant.

The TPS is not considered as part of the primary load-carrying structure, although it must contain the high-pressure hydrogen coolant at elevated temperatures. In the combustor section, the heat flux is intense and the in-depth temperature gradient across the TPS is high. Under these conditions, the TPS goes into a plastic state and the controlling factor in structural design becomes cyclic life. The cooling flow passages are parallel channels in the panels and an offset pin-fin geometry in the struts. The passages are formed using photo-chemical machining techniques.

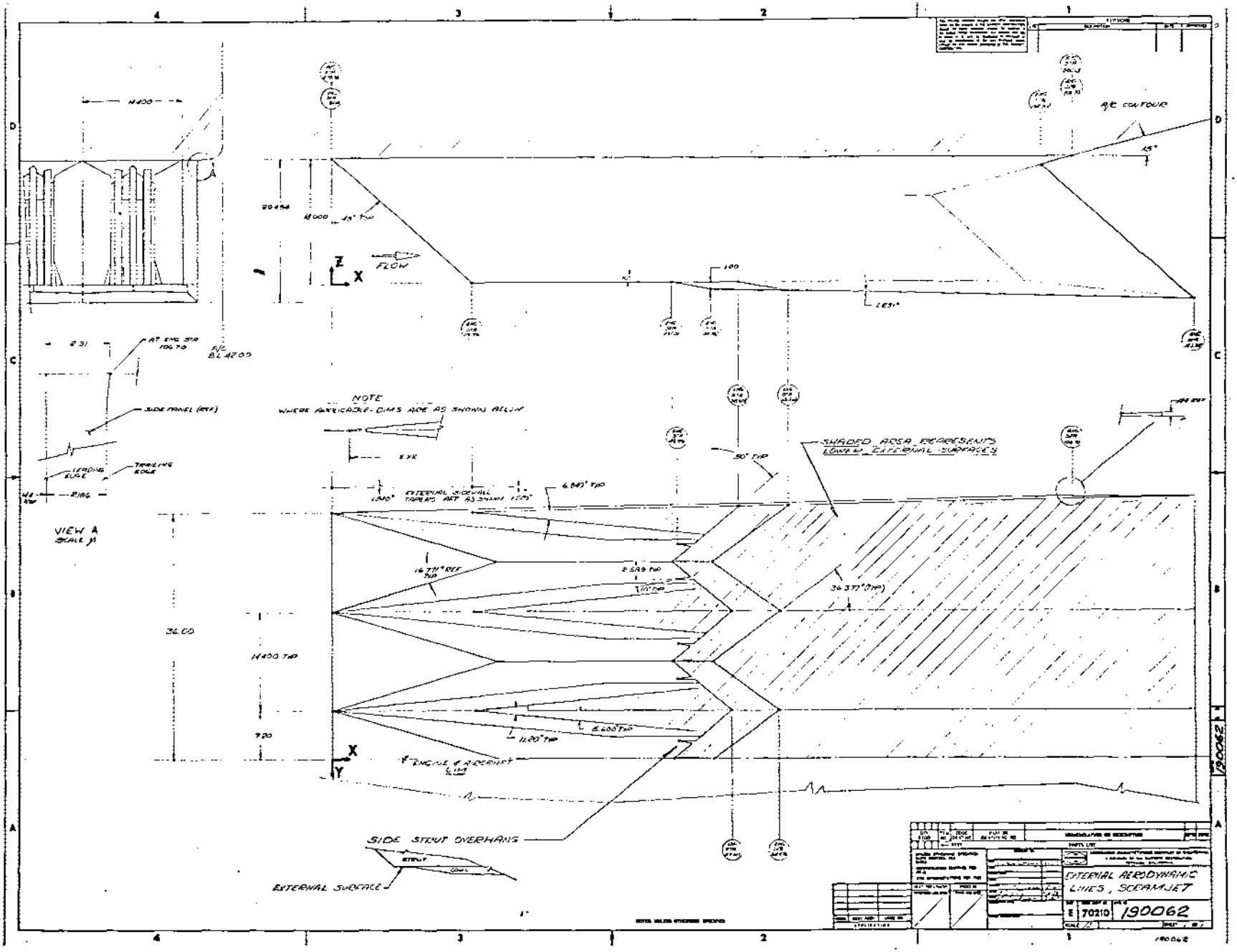
NOTE
WHERE APPLICABLE- DIMS ARE AS SHOWN BELOW
VIEW A
SCALE .1A
SIDE PANEL (REF)
LEADING EDGE
TRAILING EDGE
RIBS
FLOW
SHADED AREA REPRESENTS LOWER EXTERNAL SURFACES
EXTERNAL SIDEWALL TAPERS AT 3.3749° (.059)
SIDE STRUT OVERHANG
EXTERNAL SURFACE
STRUT
ENGINE & AIRCRAFT C/L
50° TYP
45°
90°
36.00
14.400 TYP
9.20
11.20° TYP
6.600 TYP
6.840° TYP
5.589 TYP
16.731° REF TYP
36.371° (TYP)
EXTERNAL AERODYNAMIC LINES, SCRAMJET
70210
190062

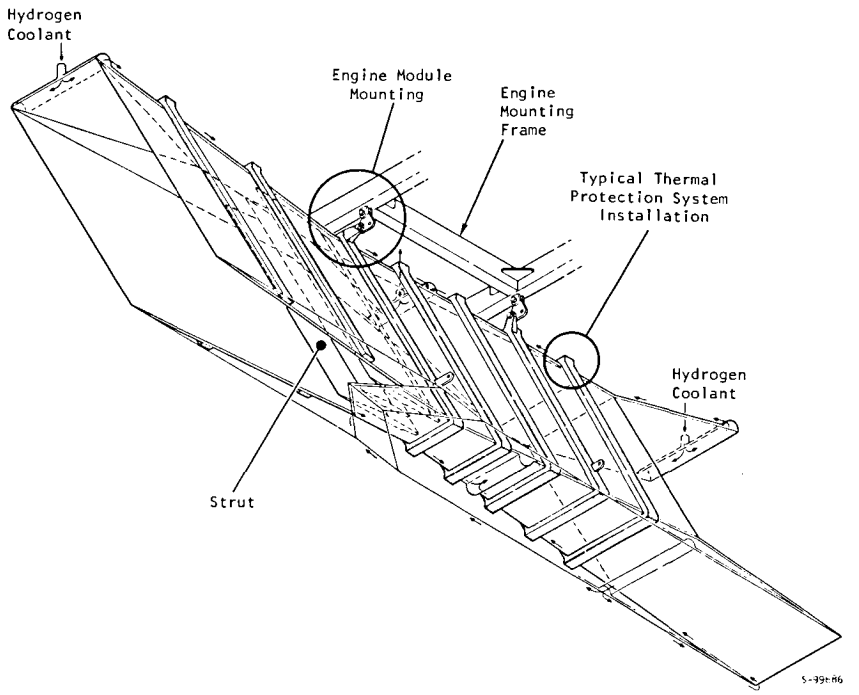

Figure 2.-Scramjet thermal-structural design.

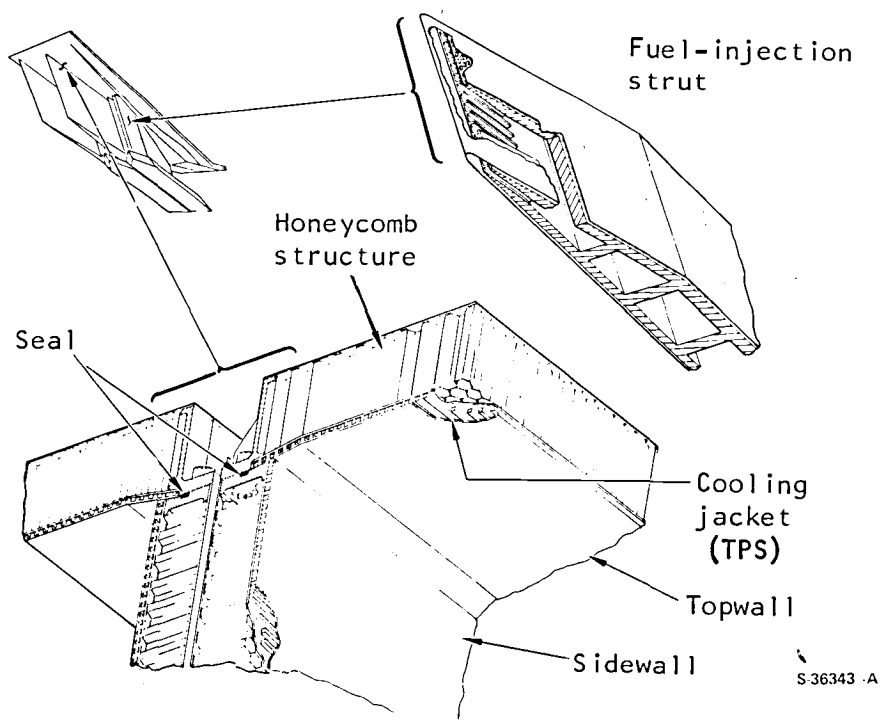

Figure 3.-Salient features of cooled scramjet structure.

Scramjet modules are assembled and joined to a separate support frame to transmit engine thrust, drag, and inertia to the aircraft. The support frame can also serve to mount coolant and fuel plenums and control valves. Differential thermal growths between the engine modules, support frame, and aircraft are accommodated by swing and sliding links. The engine compartment is sealed to prevent entry of hot gases. Materials of construction used in the design are: honeycomb panels (topwall, sidewalls, and cowl), Hastelloy X and Inconel 718; strut primary structure, Inconel 718; clips and beams, Inconel 718; manifolds and the leading and trailing edge support structure, Hastelloy X; TPS, Nickel-201 and Hastelloy X; and the mounts and mounting frame, Inconel 718.

DESIGN CONDITIONS

Normal engine operation is from Mach 4 to 10 with cruise at a dynamic pressure of 23.9 kPa (500 psf) and ascent at a dynamic pressure of 71.8 kPa (1500 psf). The engine also has the capability of undergoing a 2-g powered maneuver at any condition within this envelope. The altitude-Mach number envelope is shown in fig. 4. It is assumed that the engine can reach steady-state operation at any point within the envelope. Transient conditions such as startup or a throttle chop can dictate structural design, and are therefore considered in the study. All engine operating conditions (A through I) are taken from the contract statement of work (SOW).

Flight conditions resulting in maximum thermal loads and aero-pressure loading received special attention. Maximum thermal loading to the engine surfaces occurs during a 2-g maneuver at a flight Mach number of 10, a dynamic pressure of 71.8 kPa (1500 psf), and a combustion equivalence ratio of 1.5 (Condition H). Maximum aerodynamic pressure loading occurs during an engine unstart condition resulting in the event of thermal choking in the combustor. For a combustion equivalence ratio of 1.0, a 2-g maneuver, and a dynamic pressure of 71.8 kPa (1500 psf), this condition occurs at a flight Mach number of 5.1 (Condition G). This is a transient condition that produces a pressure pulse during the transition from supersonic to subsonic flow.

In addition to these conditions, several other conditions within the flight envelope were considered with regard to cooling requirements. Engine cooling performance throughout the envelope must be examined to substantiate the feasibility of using the excess hydrogen capacity for other aircraft components. Condition B requires maximum coolant utilization. Conditions A, D, E, and F are typical cruise conditions. The Mach 10, zero fuel equivalence ratio point, Condition I, represents a possible maneuver after a throttle chop. At Mach 4, Condition C, fuel is assumed to be injected from both the struts and from the sidewalls within the combustor section to gain additional thrust.

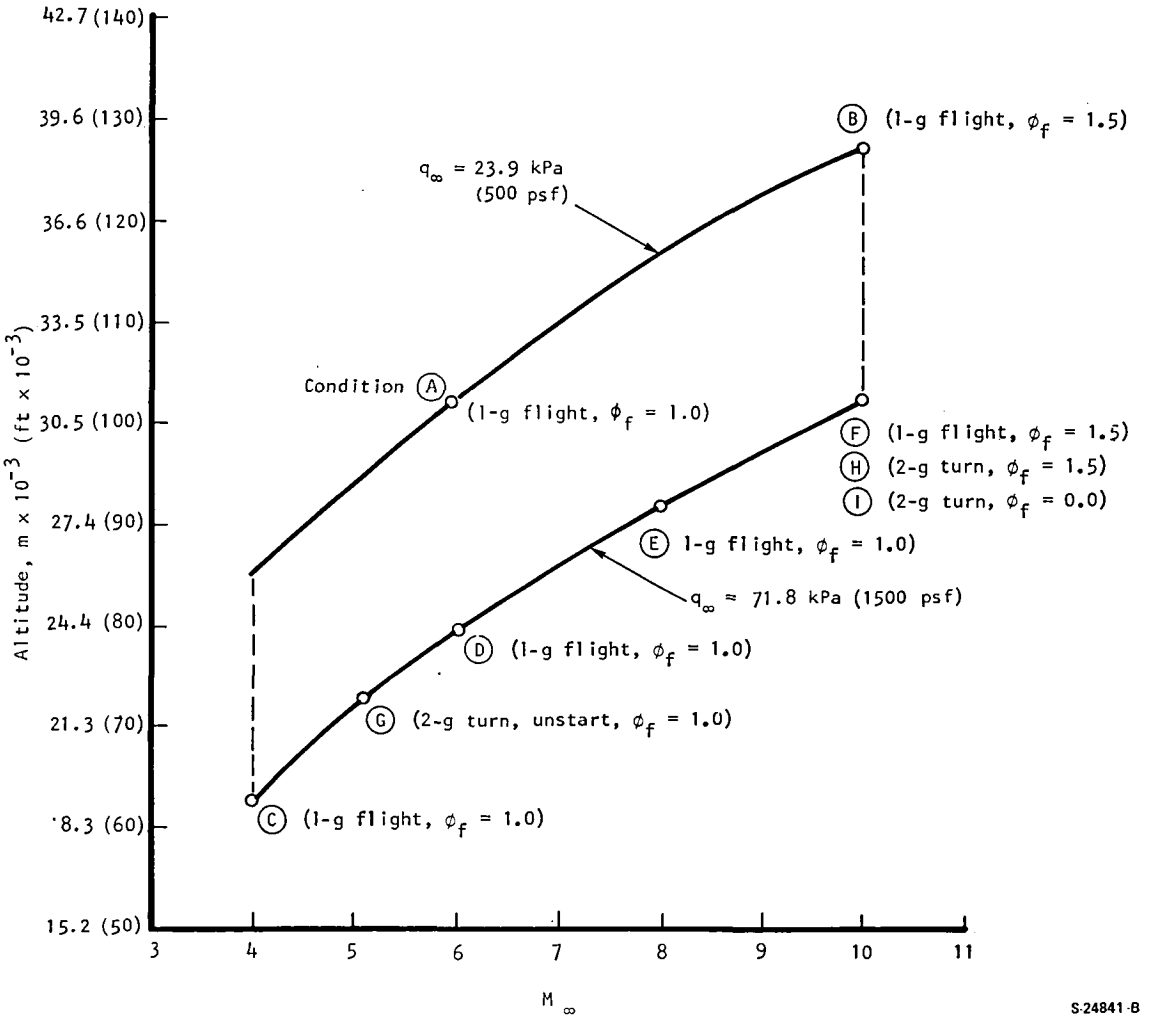

Figure 4.-Altitude-Mach number envelope.

Internal Flow Properties

Inviscid flow properties for the engine internal surfaces were provided by NASA-LaRC. Flow properties within the engine are constant along the 48-deg sweepline. Typical flow properties along the internal surface of an outboard sidewall are presented in fig. 5. The abscissa in fig. 5 is the distance measured along the X-axis from the sidewall leading edge for all vertical elevations from Z = 0.0 to 45.7 cm (18.00 in.).

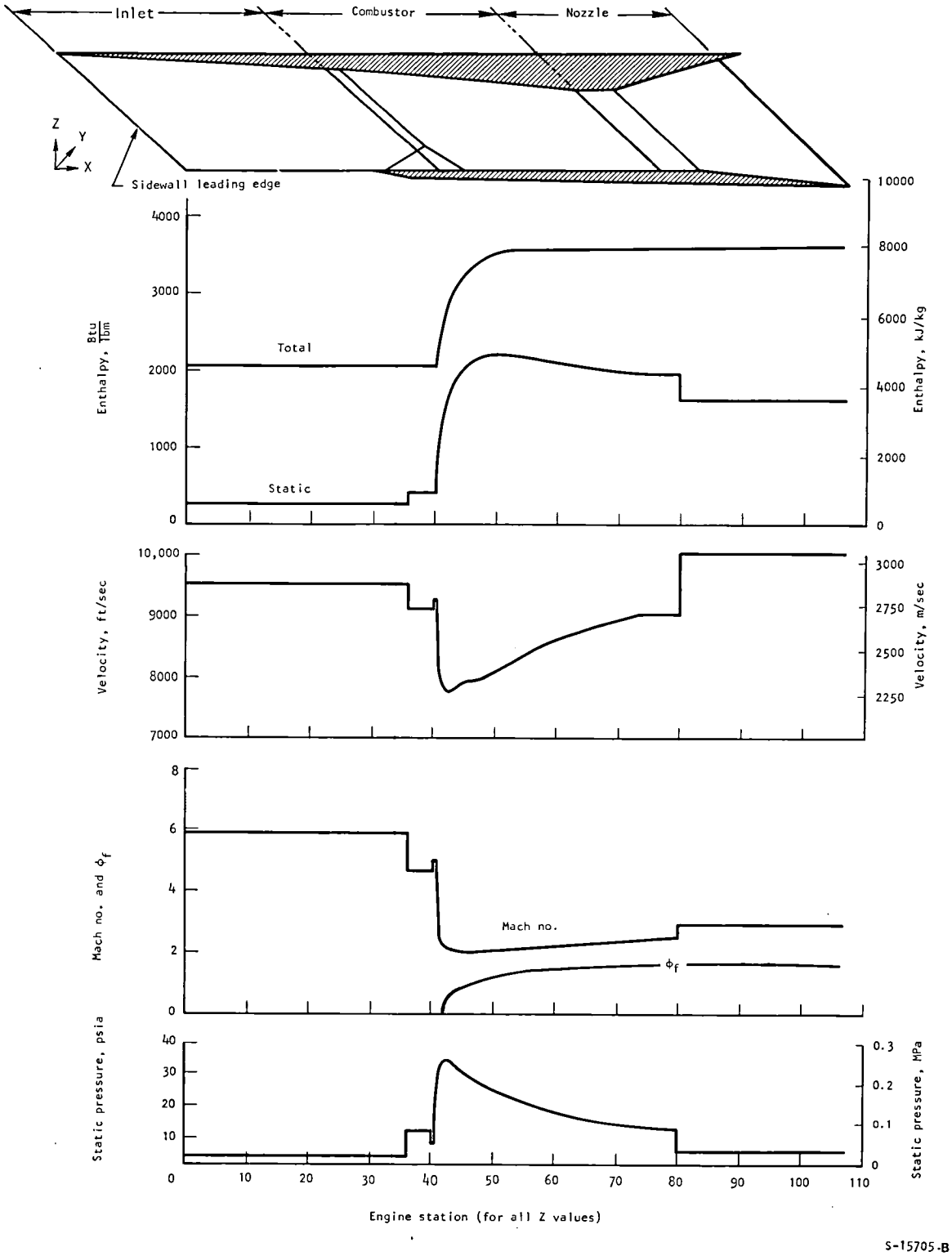

Figure 5.-Flow properties for internal surfaces of an outboard module (Condition H).

Pressure Loads

Maximum pressures through most of the engine are expected to occur during an engine unstart at Mach 5.1 (Condition G). Experimental data (ref. 8) indicate that the maximum unstart pressures are transient pressures, occurring as a shock wave moves upstream through the engine from the thermal choke line. Since the transient pressure pulse is not defined fully, the design pressure loading is taken conservatively as the envelope of the peak transient pressure. Pressure loads acting on the respective panels and struts are shown in fig. 6. The isobars are assumed vertical upstream of the thermal choke line.

For this analysis, it is assumed that the unstart pressure pulse is equivalent to a steady-state load. A pulse period close to the natural frequency of the panels on the struts could cause greatly increased loading. Dynamic loading is especially critical in the case of the struts, which are slender structural elements. More complete definition of the unstart dynamics is especially desirable for these reasons.

It is assumed that as a possibility, albeit remote, an unsymmetrical unstart condition can exist on the side strut (i.e., the flow is started (supersonic) on one side of the strut and unstarted (subsonic) on the other).

Inertia Loads

Inertia loads used in the analysis are defined in Table 1. These loads are typical for a research airplane that is air launched from a B-52, accelerated by rocket power, and lands without thrust. The effect of the inertia loads on the engine panels is not significant. These loads are of primary concern for the engine mounting design.

Structural Design Criteria

The basic design objective for the engine is to minimize engine mass and cooling requirements and maintain structural integrity during all flight conditions, including any engine unstarts and any periods of high heat flux to the engine with or without combustion. Design life goals are 100 hr of hot operation with 1000 operational cycles. In addition, the engine must withstand 10 engine unstarts during the 100-hr lifetime at the maximum aero-pressure loading condition. Thermal and mechanical distortions that occur during normal service are limited and can change the flow area by no more than 5 percent or an angle by no more than 0.4 deg.

In the combustor section and at the leading edges, the heat flux is intense and the in-depth temperature gradient across the TPS high. It is not possible to keep the TPS material within elastic limits and the material goes into a plastic state. The controlling structural design criterion is low-cycle fatigue. For the primary support structure, however, the design practice is to stay within the elastic limit, and the material yield strength becomes the governing design criterion. For design within the elastic limit, the material limit stress is not to exceed 2/3 of the ultimate strength, or 0.85 of the yield strength at 0.2 percent offset.

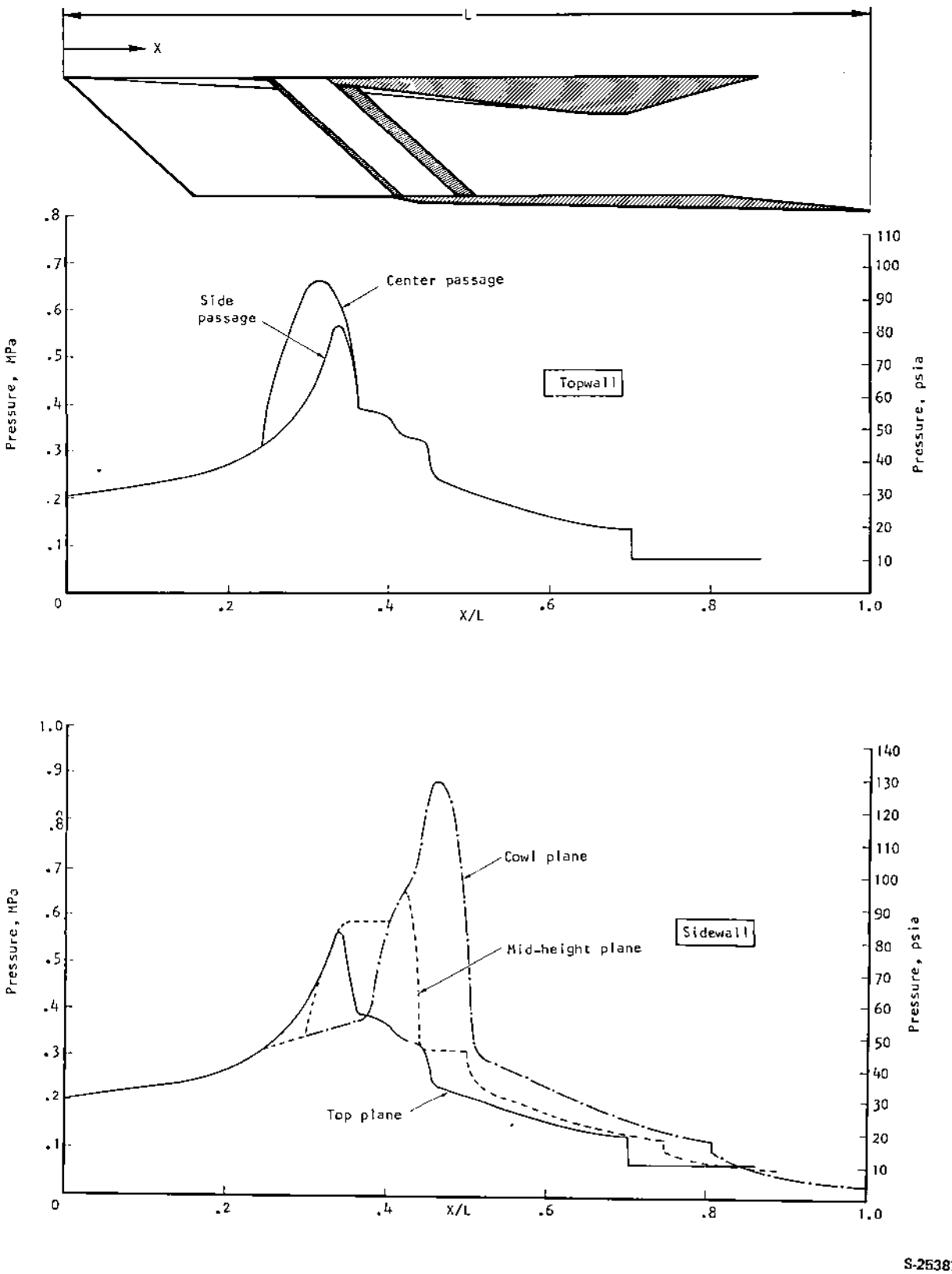

Figure 6.-Engine unstart pressure distributions.

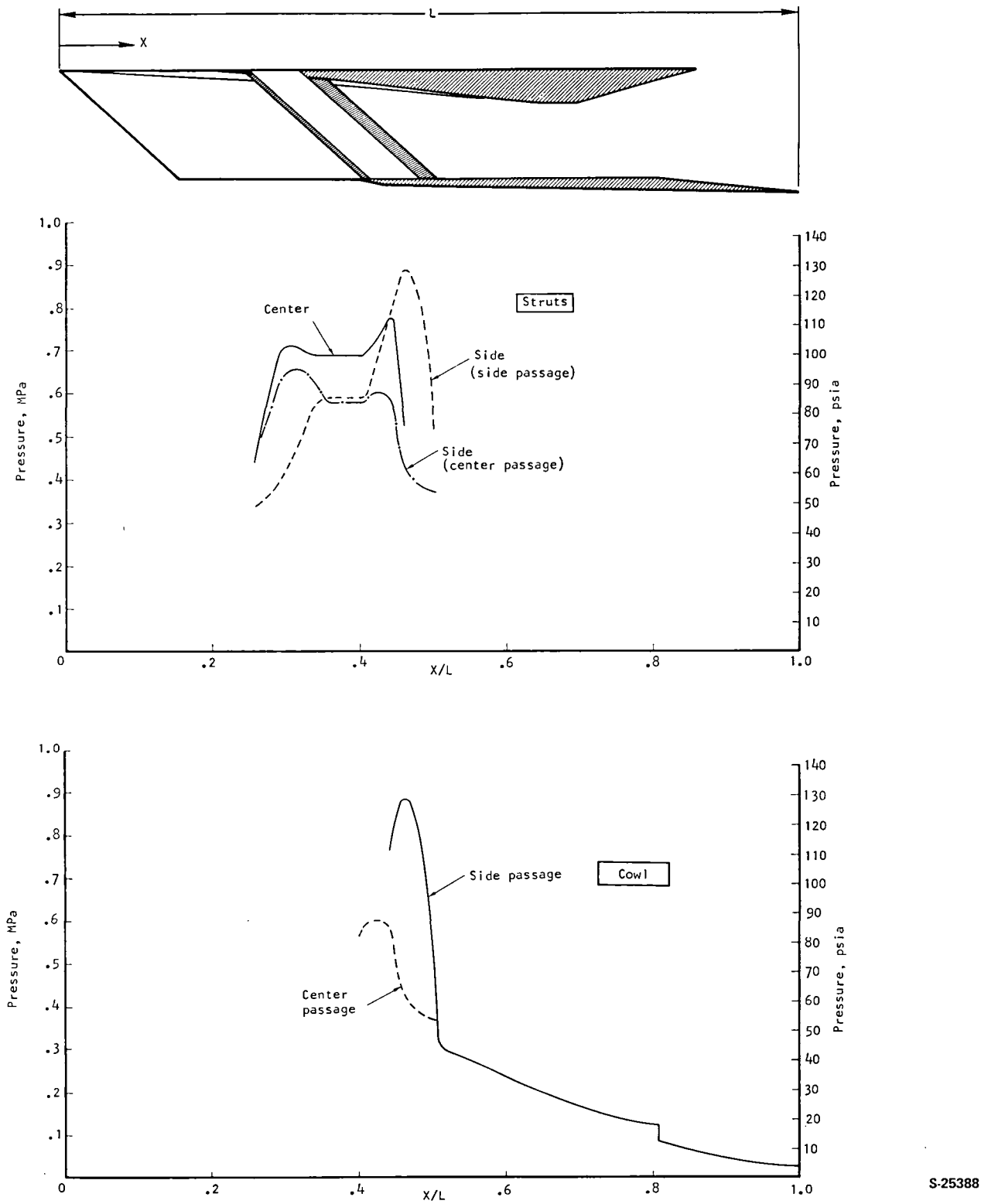

Figure 6.-Concluded.

TABLE 1.-INERTIA LOADING, G UNITS.

Condition	Maximum load, g		
	Vertical (Z)	Side (Y)	Fore-aft (X)
Thrust or no thrust			
1) Pull-up after B-52 drop	2.5	±0.5	+1.5 -0.5
2) Nose over after climb and burnout	-1.0	±0.5	+3.0 -0.5
3) Turn at Mach 10	2.0	±0.5	±0.5
Attached to B-52, no thrust (*)	+6.0 -2.0	±2.0	±2.0
Research plane landing, no thrust	+6.8	±1.0	±1.0

(*) Used only for aircraft engine interface design, cold conditions.

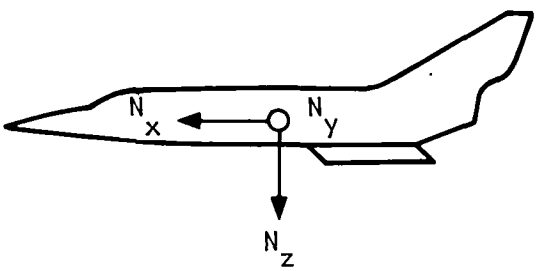

Baseline thermal-structural concepts and materials are derived from technology developed primarily on the NASA Hypersonic Research Engine (HRE) project (ref. 1) and hydrogen-cooled panel studies (refs. 2 and 3). Maximum operating temperature in these structures was limited to 870°C (1600°F) based on creep-rupture and low-cycle fatigue structural design criteria. This maximum temperature occurs in the outer fiber of the thermal protection system (TPS). Minimum operating temperature is equal to the hydrogen coolant supply temperature, 20 K (37°R). Reduced maximum operating temperatures are specified for the primary support structure to ensure meeting the elastic behavior design criteria.

The Scramjet structure and the associated operating condition based on the above criteria are summarized below.

Structure Element	Operating Conditions
Thermal protection system	20 to 1144 K (37° to 2060°R), exposed to hot products of combustion and high-pressure hydrogen coolant
Primary structure (honeycomb)	20 to 890 K (37° to 1600°R), exposed to hydrogen coolant (hot face)
Clips	56 to 890 K (100° to 1600°R), ambient air
Support beams	56 to 667 K (100° to 1200°R), ambient air

Because of the wide range of operating conditions, a single material will not necessarily be optimum for all areas.

Fuel/Coolant Conditions

The fuel/coolant is parahydrogen stored cryogenically as a liquid at 20 K (37°R) and 138 kPa (20 psia). For determination of coolant requirements and performance, the hydrogen temperature at the engine inlet is taken as 56 K (100°R) to allow for pump work and aerodynamic heating effects on the coolant prior to its introduction into the engine. For maximum utilization of the hydrogen heat sink capability, the design objective is to heat the hydrogen coolant to 890 K (1600°R) (primary structure temperature limit) within any cooling circuit.

Fuel flows were specified by NASA-LaRC. Minimum fuel manifold pressure was specified as 4.83 MPa (700 psia) to obtain the proper fuel flow rate and penetration into the airstream. The pressure drop across any cooling circuit was assumed to be 1.72 Mpa (250 psi), with an additional 0.34 MPa (50 psi) allowed across the fuel control valves and distribution system. The resulting engine coolant inlet manifold pressure is 6.9 MPa (1000 psia), which is compatible with the pressure containment capability of candidate structures and turbopump delivery pressures. This pressure level does not necessarily represent an upper limit for either.

DESIGN LOADING

Aerodynamic Heating

Aerodynamic heating of the internal engine surfaces (sidewall, top surface, cowl), strut sides, and external surfaces was determined for Condition H. This condition was selected because it is the maximum thermal load case. Calculations were performed by the adiabatic wall reference enthalpy method (ref. 9). Results are presented in figs. 7 and 8.

The peak combustor heat fluxes for the top surface, sidewall, and internal cowl of 2.27, 4.03, and 5.22 MW/m^2 (200, 355, and 460 $Btu/sec-ft^2$), respectively, reflect the location of the virtual origin of the boundary layer. For the top surface, the virtual origin of the boundary layer was taken as 1016 cm (400 in.) upstream of the engine inlet, based on engine installations ranging from 1219 to 965 cm (480 to 380 in.) aft of the aircraft nose. Because of this, it was assumed that the flow transitioned upstream of the engine inlet and that the flow on the engine top surface was turbulent. On the side surface, internal cowl surface, and side struts, a laminar-to-turbulent transition Reynolds number of 3×10^6 was used. The locations where transition occurs are indicated in figs. 7 and 8. On the center strut, the Reynolds number based on running length from leading edge was less than 3×10^6 at the perpendicular injectors, so a transition to turbulent flow was imposed on the boundary layer at the injector location.

The top surface and internal cowl surfaces are exposed to a complex pattern of shock wave bays in the engine inlet. Each bay has a unique and constant set of inlet flow properties. This produces a heat loading on these surfaces that is both width- and axial-dependent. The loading definition on other surfaces of the engine is governed by flow properties that vary in the engine axial direction only. For initial analysis, to facilitate the loading definition and the subsequent design, the various inlet streamlines produced by the complex shock bay pattern on the topwall panel were reduced to one streamline. This one streamline was a composite of those producing maximum heating along the engine axis. Alternate paths through the inlet would yield a different and possibly more precise design heat load, but the variation was not considered significant. The maximum heat load in the inlet portion of the top surface from this analysis is about 148 kW (140 Btu/sec) compared with a total module heat load of 7380 kW (7000 Btu/sec). Thus, the maximum variation in heat load due to path selection is less than 2 percent. The path specified results in a conservative design and is adequate for flow routing studies.

A separate detail analysis was performed on the topwall panel in which the variation in heat flux along parallel streamlines was considered. This analysis was conducted to determine the resulting temperature gradients and corresponding thermal stresses in the structure. The results of these thermal and stress analyses are reported in a subsequent section.

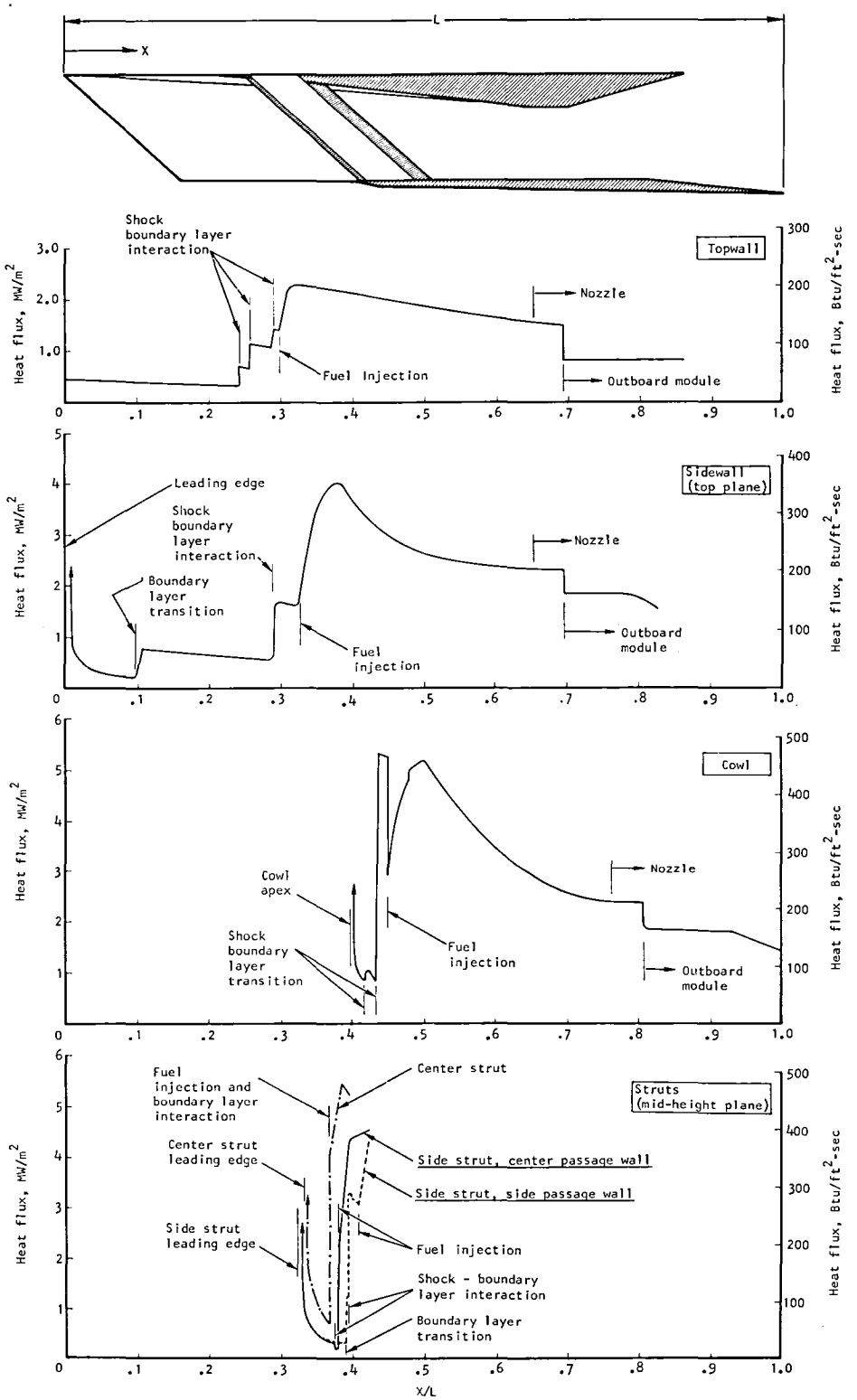

Figure 7.-Aerodynamic heating rates on engine internal surfaces, Condition H.

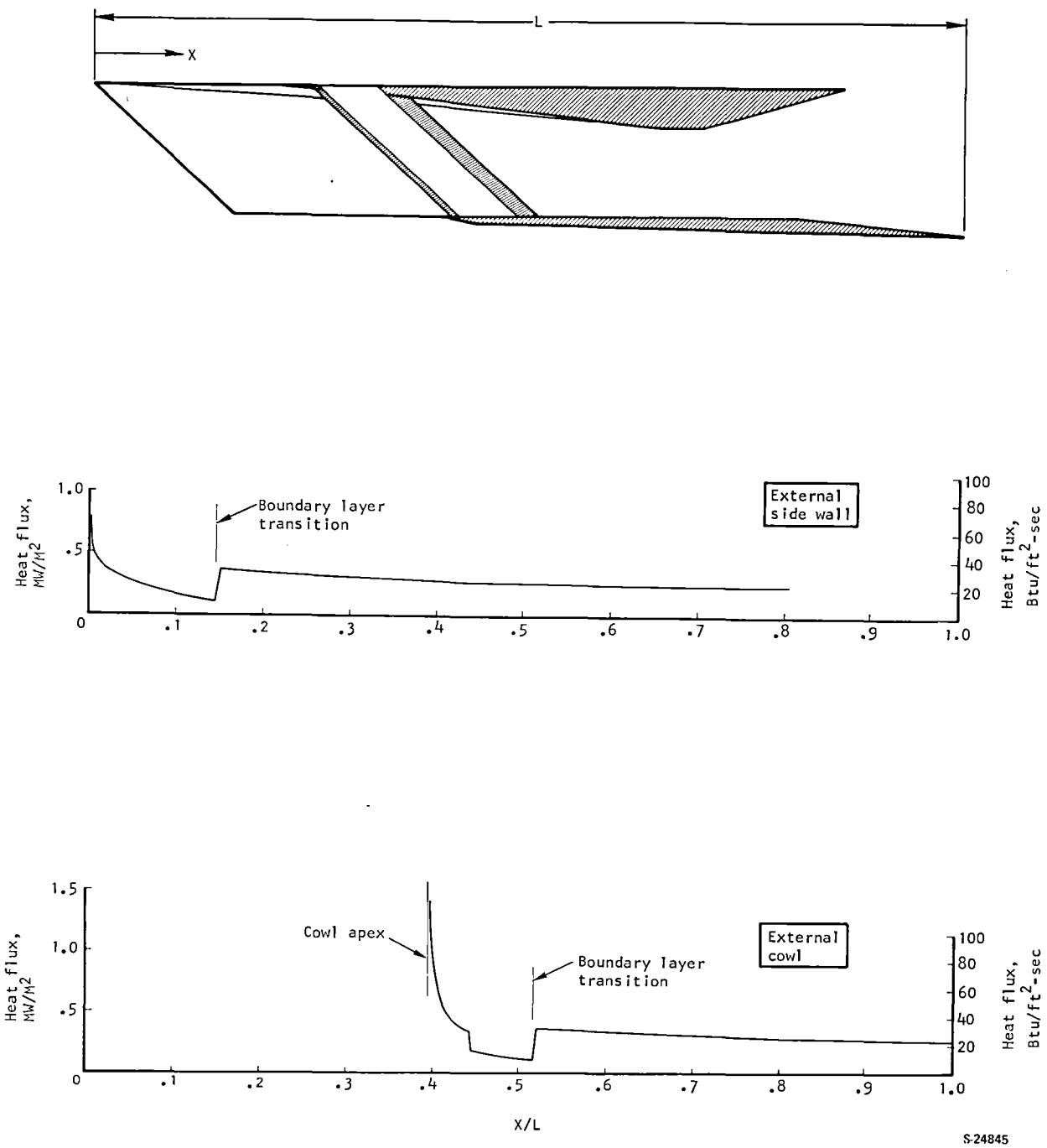

Figure 8.-External surface thermal loading, Condition H.

Effects of shock wave-boundary layer interaction were considered. They occurred in turbulent flow for topwall, sidewall, and strut (side passage wall) surfaces and induced transition to turbulent flow on the internal cowl and side strut (center passage wall) surface.

Aerodynamic heating on the side strut is not symmetrical. Hence, different distributions are shown in fig. 7 for each face of the side strut. Results of aerodynamic heating analyses on the external surfaces of the sidewall (outboard module) and external cowl surfaces (all modules) are presented in fig. 8.

Estimates of wall temperature distributions were made to determine panel aerodynamic loadings for Condition H in figs. 7 and 8. This was done to obtain estimates of overall loading levels and to determine aerodynamic heat transfer coefficients that are relatively insensitive to wall temperature, particularly with the adiabatic wall reference enthalpy method. Detailed wall temperature distributions for each panel can only be determined after a definition of coolant flow routing, TPS coolant passage geometry, and a thermal performance analysis using the aerodynamic heat transfer coefficients and hydrogen coolant coefficients. Results of these analyses are presented in a subsequent section.

Heat Load Summary

A summary of the heat loads for Condition H is presented in Table 2. These are the area integrated results of figs. 7 and 8 for internal and external surfaces. The total heat load for an inboard module is 6.853 MW (6500 Btu/sec), and for an outboard module is 7.618 MW (7319 Btu/sec).

Leading Edge Heat Flux

Aerodynamic heating rates at the sidewall, cowl, and strut leading edges are presented in Table 3 (Condition H). Heat fluxes were calculated using the normal stagnation point method of Fay-Riddell (ref. 10) modified for the 48-deg sweep of the sidewall and struts and the 50-deg sweep of the cowl lip. The effect of sweep angle was considered by using the normal component of total pressure in the calculation of leading edge velocity gradient. The wall temperature at the stagnation line was assumed to be 833 K (1500°R). Two prospective radii were considered; increasing the radius from 0.8 to 1.3 mm (0.030 to 0.050 in.) reduces the heat flux by about 23 percent.

The cowl apex is a special case because it is the intersection of two cylindrical leading edges. For design, the apex was assumed hemispherical and unswept, both of which produce higher heat fluxes than the cylindrical swept leading edges on the sidewall, struts, and cowl. In addition, there is also a point of sidewall shock wave intersection in the apex where the heat flux is intense.

Experimental evidence obtained during HRE testing has indicated that 0.8- to 1.3-mm (0.030- to 0.050-in.) radius leading edges can be adequately cooled

TABLE 2.-HEAT LOADS AT CONDITION H
(M_∞ = 10, q_∞ = 1500, 2-g TURN, ϕ_f = 1.5)

Location	Maximum flux	Average flux	Heat load
	MW/m^2 (Btu/sec-ft^2)		MW (Btu/sec)
Top surface	2.27 (200)	1.06 (93)	0.827 (784)
Sidewalls	4.03 (355)	1.79 (158)	2.918 (2768)
Internal cowl	7.32 (645)	2.50 (220)	1.286 (1220)
Center strut	5.45 (480)	2.62 (231)	0.479 (454)
Side strut, center	4.54 (400)	2.09 (184)	0.578 (548)
Side strut, side	4.31 (380)	1.50 (132)	0.413 (392)
External cowl	-	0.45 (40)	0.297 (282)
Bottom of sidewalls	-	0.68 (60)	0.055 (52)
Outboard sidewall	-	0.45 (40)	0.865 (819)*
Total heat load, inboard module			6.853 (6500)
Total heat load, outboard module			7.618 (7319)

*0.57 MW (540 Btu/sec) on external surface, 0.295 MW (279 Btu/sec) on extended internal surface

TABLE 3.-LEADING EDGE HEAT FLUXES AT CONDITION H

Leading edge	Heat flux, MW/m^2 (Btu/sec-ft^2)	
	0.8 mm (0.030-in.) radius	1.3 mm (0.050-in.) radius
Sidewall	13.7 (1206)	10.6 (935)
Side strut	19.5 (1718)	15.1 (1331)
Center strut	26.3 (2313)	20.3 (1792)
Cowl lip	18.5 (1634)	14.4 (1266)
Cowl apex	59.2 (5218)	45.9 (4042)

with hydrogen up to stagnation heat fluxes of about 23 MW/m^2 (2000 Btu/sec-ft^2). Higher and very localized heat fluxes produced by shock impingement on leading edges have also been accommodated when the shock impingement width on the leading edge is much smaller than the leading edge radius; however, cowl leading edge fluxes of 45 to 60 MW/m^2 (4000 to 5000 Btu/sec-ft^2) over a significant part of the radius is a definite departure from existing experimental data.

Corner Flow Heating

The effect of corner-flow fields on the aerodynamic heating rate was investigated to determine if this condition would control the thermal protection system design in the corners.

Ref. 11 was used as the primary basis of the investigation; however, results are primarily for laminar flow for unswept leading edges, with and without wedge angles. Turbulent flow was treated on a limited basis because of the limited test data available. The data are sufficient, however, to make judgments for this study.

One of the configurations from ref. 11 that was used in this study is shown in fig. 9. This configuration was selected because it has unwedged, 90-deg corners, approaches Mach numbers similar to the engine, and has a comparable number of data points for turbulent flow and laminar flow. This configuration is still different from the engine corners because (1) all engine corners have swept leading edges, (2) all engine corners have one surface that extends

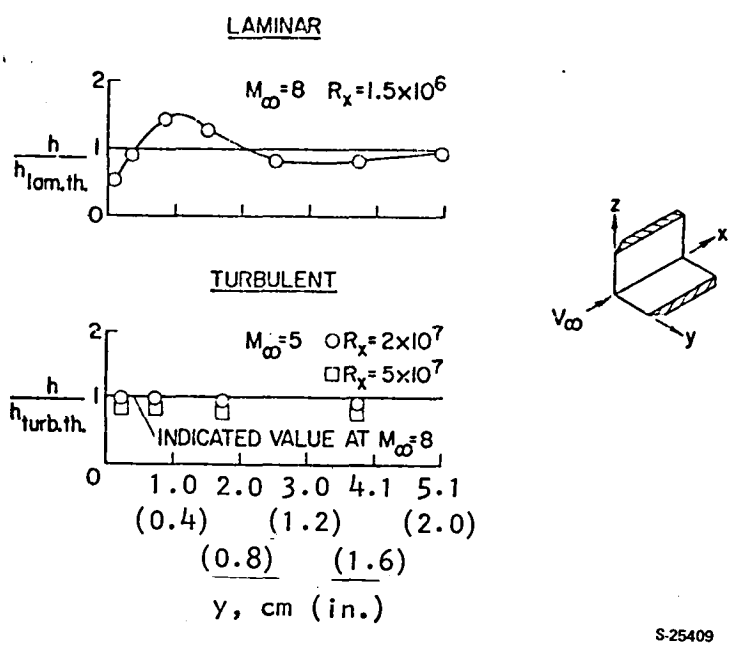

Figure 9.-Comparison of laminar and turbulent heating in a corner; sharp leading edge (ref. 11).

upstream from the origin of the corner so that this one surface already has an established boundary layer, and (3) all engine leading edges have leading edge radii of 0.8 to 1.3 mm (0.030 to 0.050 in.). These differences are thought to diminish the corner heating effect relative to results in ref. 11. The basic behavior of the aerodynamic heat transfer coefficient (h) for laminar and turbulent flow at approach Mach numbers of 5 and 8 is included in fig. 9 for the selected configuration. For laminar flow, the corner effect on h is noticeable and also Reynolds number (and flow length) dependent. The h in the corner is less than predicted by laminar flat-plate theory, but increases to a peak value of 1.4 to 1.5 times the flat-plate value 10 mm from the corner before diminishing to the flat plate value. For turbulent flow there is no corner effect on h (i.e., the h profile is flat with distance from the corner). This result does not appear to be affected by Reynolds number. In addition, the flat profile is approximately independent of approach Mach number, at least at the two values examined.

From these data, peak corner heating is not expected to be significantly higher than the laminar flat-plate values in the laminar flow region of the cowl inlet. In addition, laminar flow heating is only about 15 to 25 percent of the corresponding heating if turbulent flow existed. Therefore, corner heating should not affect the design because the TPS will be selected primarily on the basis of turbulent flow heating in the cowl/strut section of the inlet. In the turbulent flow region, no increase in heating is expected due to corners. Laminar corner heating can be significant if a large portion of the corner is heated by laminar flow, regardless of turbulence level, but this is not the present case.

Strut Pressure Loads

Pressure loads acting on the struts during the unstart condition (see fig. 6) were integrated and the results are shown in fig. 10 for the possible combinations. It was assumed that the unstarted pressure acts on the base of the trailing edge. Because the isobars are vertical on the unstarted side and swept on the started side, a torsional load is produced.

Using the resultant (net) lateral load, an average pressure load may be calculated by dividing the magnitude of the lateral (y directional) load resultant by the strut area projected on the x-z plane. The pressure intensity on this basis is 0.464 MPa (67.3 psi) for center passage unstart and 0.447 MPa (64.9 psi) for side passage unstart.

Panel Pressure Loads

The pressure distributions shown in fig. 6 were used directly in the various analyses. Load calculations were internal to these analyses and were not separately performed as for the struts.

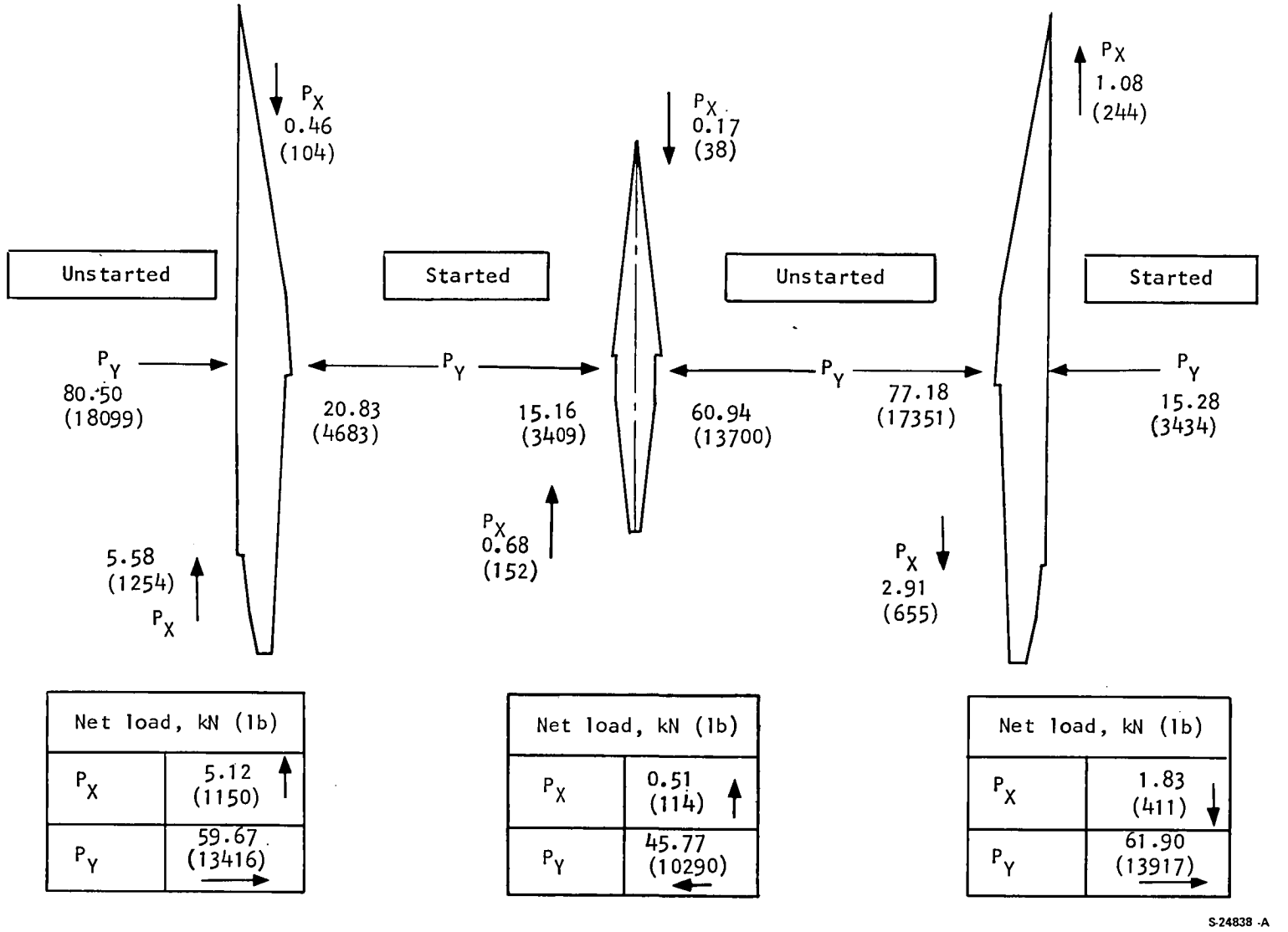

Figure 10.-Strut loads, transient unstart conditions.

DESIGN APPROACH

Cooling System

The thermal protection system was treated as a compact heat exchanger and analyzed using the methods presented in ref. 12. Heat transferred by radiation is considered negligible and the aerodynamic heat transferred to the structure is balanced by the heat removed by the coolant. All fluid properties were evaluated at the hydrogen bulk temperature as recommended (ref. 12) for offset-fin heat exchangers and at the wall-to-bulk film temperature for machined channels.

The topwall, sidewall and cowl, and the struts are each considered to be an independent cooling circuit; for maximum coolant utilization the coolant is allowed to reach the maximum allowable temperature of 890 K (1600°R). The basic flow scheme is to introduce cryogenic coolant at the leading and trailing edges where the panel heat load is low and withdraw it at the engine throat where the heat load is highest. Variations on this basic flow routing were examined to (1) match temperature gradients along the engine (minimum ΔT between panels); (2) minimize coolant pressure drop by providing optimum flow width and length; and (3) minimize local heat input by controlling surface temperature profiles. These studies result in specification of coolant flows and manifold location in each flow route.

Cooling requirements throughout the flight envelope were determined and compared with the available cooling capacity as dictated by the fuel flow. Heat load split between engine sections, inlet, combustor, nozzle, and struts was computed to provide a basis for coolant flow control design.

Material requirements were examined and selections made based on HRE experience and the current state of the art. These selections were used for all subsequent structural analyses.

The thermal protection system (TPS) was examined in detail. Experience with the rectangular, offset, plate-fin coolant passages on the HRE TPS indicated that, although adequate for research purposes, the thermal fatigue life of such structures is limited. The required Scramjet engine life of 100 hr and 1000 cycles is an order of magnitude greater than specified for the HRE.

The maximum thermal load case, Condition H, was used as the TPS design basis. The TPS response is fast (the time constant is a few seconds) and it will reach a steady-state condition even though Condition H is a transient operating point. Consequently, the TPS passage geometry and flow routing must be sized and located to meet the maximum thermal load conditions. If the TPS passage geometry were optimized for cruise conditions, then it may be impossible to achieve the required Condition H coolant flow because of excessive pressure drop in the coolant passages.

The TPS hot skin temperature is dependent on the heat flux, and hence, peak temperature will occur at Condition H. It is presumed that this condition will occur once during every mission.

Two flow passage geometries, machined channels and pin-fin, were selected as candidate surfaces because they have a potential for increased cyclic life. Heat transfer and pressure drop performance of the candidate heat exchanger flow geometries and structural materials were examined using the methods in ref. 12 and compared on the basis of in-depth temperature gradient and pressure drop. Thermal stress, and hence the cyclic life, are directly related to the ΔT across the TPS. Thus, the basic objective is to obtain the minimum ΔT within the coolant pressure drop limitations. Decreasing passage size and adding flow interruptions, as with the pin-fin geometry, reduce ΔT but increase ΔP for a fixed flow rate.

A parallel structural analysis of the TPS was performed to predict low-cycle fatigue life of the candidate TPS designs. Two different techniques are used: linear interaction using Miner's rule (ref. 13), and strainrange partitioning (ref. 14). The heat transfer and structural results were then reviewed and the best TPS geometry and materials selected.

Leading edges were given special consideration because of the high heat fluxes and geometry restrictions imposed. Hydrogen coolant is introduced at the leading and trailing edges of the individual panels, and the coolant inlet temperature is therefore at or close to the minimum supply temperature of 56 K (100°R). The design problem is similar to that for the TPS, where low-cycle fatigue was identified as limiting the cycle life. A design constraint is the leading edge radius, which should be minimized for aerodynamic reasons.

Fuel Injection Struts

The struts present a major design problem. They are slender structural elements with a span-to-depth ratio of 25 to 28. The torsional and bending stiffnesses are low. The struts must simultaneously perform the following functions:

(a) Support a large side load such as occurs during an unstart transient

(b) Contain high-pressure hydrogen at two temperature extremes

(c) Withstand high thermal stresses generated by asymmetric aerodynamic heating and internal convective heating from manifolds

The cross-sectional area available for flow of the hydrogen coolant and fuel is limited by the basic cross-sectional area and the need to provide structural members. Hence, flow maldistribution could occur and produce an unacceptable fuel injection pattern and local hot spots in the TPS.

Structural analyses, described in ref. 4, were continued by NASA. The primary tool was a three-dimensional finite element model analyzed using the SPAR (ref. 15) computer code. The side strut only was modeled, as the loading

was slightly more critical than the center-strut loading, and the results would be conservative for the center strut.

Two approaches were examined to determine the best means to reduce strut deflections and stresses. First, the boundary conditions were changed to reflect revised mounting constraints. A structural tie that joins the three struts together at their midpoint--a concept originally used in the ref. 4 analysis--was retained for this first approach. The second approach was to supply additional coolant to the strut TPS to reduce the temperature gradients along the strut, and thereby decrease the thermal stresses. It was believed that "overcooling" would result in a lower combined stress, and this would eliminate the mid-span tie, a decided complication in coolant flow routing and strut fabrication.

Initial results of the structural analysis were used to prepare design layouts for the strut cross-sections and flow routing schemes. From this basis the available flow areas for hydrogen fuel and coolant were established. Flow distributions were then determined using a computer program for one-dimensional compressible flow with friction in a manifold with continuous withdrawal of flow.

The interface between the side strut and the topwall was investigated to assess the performance of the seal at this interface and to provide the boundary conditions at the edges of the strut. The NASA-generated finite element model of the side strut was used in the computer analysis in conjunction with models of a section of the topwall and of the seal. Boundary conditions were used from previous analysis of the overall all-honeycomb structure.

Engine Primary Structure

Response of the overall engine structure to the maximum thermal and pressure loading conditions was determined using ANSYS, a finite element computer program (ref. 16). Although modeled relatively coarsely, the three-dimensional model had 4146 to 4794 degrees of freedom, depending on the type of structure analyzed. The model was made up primarily of triangular and quadrilateral plate elements with both membrane and bending stiffness. Equivalent stiffness of the honeycomb, including the hot and cold face sheets, beams and clips, coolant manifolds, and the leading and trailing edge structures, was represented in the computer program. The beams were permitted to slip along the clips to represent a differential thermal expansion provision.

Three basic structures were examined: (1) seven swept beams reinforcing 9.5-mm (3/8-in.) constant-thickness honeycomb sandwich panels, (2) seven vertical beams reinforcing 9.5-mm (3/8-in.) constant-thickness honeycomb sandwich panels, and (3) 6.4- to 50.8-mm (0.25- to 2.0-in.) variable-thickness honeycomb sandwich panels reinforced with two vertical beams. Maximum thermal and pressure loadings were applied to each of the models and the resulting deflections and stresses determined. Results were reviewed to select the structure that produces the minimum deflection for the least mass. Stress levels were checked to verify that the primary structure is within the elastic range.

Deformations were checked against the allowable aerodynamic line distortions. Panel-to-panel deflections were examined to establish the seal requirements.

A separate thermal and structural analysis was performed on the inlet portion of the topwall to assess the effects of the nonuniform heat flux in this area. Two-dimensional aerodynamic heating analyses were performed on the inlet and combustion sections of the topwall surface. A more realistic two-dimensional thermal loading was determined by analyzing six distinct streamlines that best represent the shock bay pattern in the engine inlet. Heat fluxes were computed along each flow path. A three-dimensional steady-state thermal performance analysis was conducted on the forward topwall TPS panel using these heat fluxes.

For the stress analysis, a model was constructed representing the stiffness and geometric features of the all-honeycomb topwall. A detail description of the model and the results of the analysis are contained in a subsequent section.

Transient Behavior

Maximum stresses in the primary structure are likely to occur during a transient condition, e.g., engine startup. To more clearly show the magnitude of this problem, transient studies were performed. Two primary structure configurations were analyzed: (1) the 9.5-mm (3/8-in.) constant-thickness honeycomb reinforced with seven swept beams, and (2) the variable-thickness honeycomb reinforced with two vertical beams (all-honeycomb design). These configurations were modeled in cross-section and the transient temperature profiles were determined for an assumed mission. From these profiles, the thermal stresses were determined and compared with material allowables.

Engine-Aircraft Interface

Deflection and load data from the engine finite element model were used to derive guidelines for engine mounting, including differential thermal expansion provisions and engine compartment sealing.

Fuel System

A complete fuel system schematic was developed including the turbopump and all control valves. No detail designs were formulated. Rather, existing equipment, especially valve designs used on the HRE program (ref. 1), was used as the basis to obtain an estimate of size and mass.

Layout Design

Drawings of engine panels and the struts were prepared to define the selected designs and to show manufacturing feasibility. An installation drawing was prepared to aid the aircraft designer. These drawings were used to establish a detail mass estimate for the Scramjet engine and as a basis for performance analysis.

DESIGN AND PERFORMANCE

Material Selection

The study is based on the premise that existing materials and known manufacturing materials will be used. Hastelloy X is the reference material because of an extensive data base and successful application in the Hypersonic Research Engine (HRE) program.

Since the initiation of the HRE program, several wrought superalloys with improved properties compared to Hastelloy X have been developed, e.g., Haynes 188 and Inconel 617. Refractory alloys were also considered. Molybdenum exhibits a more than threefold increase in creep strength/density ratio over Hastelloy X, and TZM shows a tenfold increase. In addition, both materials have much better thermal properties and a higher modulus. Another approach, as proven on HRE, is to use Nickel-200 (commercially pure nickel) and balance the improved thermal properties and ductility against a lower creep strength when compared with Hastelloy X.

Thermal protection system (TPS).--The design life of the HRE was 10 hr and 100 cycles, compared with 100 hr and 1000 cycles for the Scramjet. The necessary increases in creep and low-cycle-fatigue (LCF) life indicate that a Hastelloy X TPS could be marginal for this application and that changes in material or configuration may be required. A comparison of the material properties of the candidate alloys at two different maximum temperatures is shown in Table 4. Thin sheet properties are cited because they are more realistic for the TPS structure.

Two parameters are used to rank (in a preliminary fashion) the material resistance to LCF. The ductility parameter is

$$K_D = \sigma_y \, (RA)$$

where σ_y = yield stress

RA = reduction in area

This is a measure of the ability of the material to absorb plastic strain, which is related to fatigue life. The highest value of σ_y (RA) is best for sustaining a given thermal stress without cracking.

For comparison of the materials in a high-temperature environment, a thermal stress parameter can be developed:

$$K = \frac{E\alpha}{k}$$

where E = Young's modulus

α = Coefficient of thermal expansion

k = Thermal conductivity

TABLE 4.-MATERIAL PROPERTIES FOR TPS CANDIDATE ALLOYS
(SI UNITS)

Alloy	Nickel 200		Hastelloy X		Inconel 617		Haynes 188		TZM	
Temperature, K	1061	1144	1061	1144	1061	1144	1061	1144	1061	1144
Yield strength, σ_y, MPa	48	31	214	186	186	186	220	186	420	400
Reduction of area, RA	0.97	0.99	0.36	0.40	0.60	0.80	0.43	0.75	0.05	0.05
Young's modulus, E, MPa x 10^{-6}	0.14	0.12	0.14	0.13	0.14	0.12	0.17	0.16	0.21	0.20
Thermal expansion, α, cm/cm-°C x 10^6	16.2	16.4	16.2	16.4	15.3	15.7	16.4	16.9	5.6	5.6
Thermal conductivity, k, watts/cm-°C	0.64	0.66	0.25	0.26	0.25	0.27	0.25	0.25	1.09	1.07
100-hr stress to rupture, MPa	22.7	13.7	110	62	172	97	165	90	310	296
Thermal stress parameter, $E\alpha/k$	3.5	2.9	9.1	8.2	8.3	6.9	11.0	10.7	1.1	1.1
Ductility parameter, σ_y x RA	46.6	30.7	77.0	74.4	111.6	148.8	94.6	139.5	21.0	20.0

*Estimate of the most likely value for 0.38-mm-thick section without effects of brazing, coatings, or long-term exposure.

(U.S. CUSTOMARY UNITS)

Alloy	Nickel 200		Hastelloy X		Inconel 617		Haynes 188		TZM	
Temperature, °F	1450	1600	1450	1600	1450	1600	1450	1600	1450	1600
Yield strength, σ_y, ksi	7.0	4.5	31	27	27	27	32	27	61	58
Reduction of area, RA	0.97	0.99	0.36	0.40	0.60	0.80	0.43	0.76	0.05	0.05
Young's modulus, E, psi x 10^{-6}	20	17	20	19	20	17	24	23	31	29
Thermal expansion, α, in./in.-°F x 10^6	9.0	9.1	9.0	9.1	8.5	8.7	9.1	9.4	3.1	3.1
Thermal conductivity, k Btu/ft-hr-°F	37	38	14.2	15.2	14.7	15.4	14.2	14.5	63	62
100-hr stress to rupture, ksi	3.3	2.0	16	9	25	14	24	13	45	43
Thermal stress parameter, $E\alpha/k$	4.9	4.1	12.7	11.4	11.6	9.6	15.4	14.9	1.5	1.5
Ductility parameter, σ_y x RA	6800	4500	11 200	10 800	16 200	21 600	13 800	20 300	3100	2900

*Estimate of the most likely value for 0.015-in.-thick section without effects of brazing, coatings, or long-term exposure.

The lowest value of this parameter will yield the lowest thermal stress for a given temperature distribution. These parameters for the candidate alloys are also shown in Table 4.

Among the nickel- or cobalt-base wrought superalloys there is no clear-cut superiority, although the parameters do indicate an advantage for Inconel 617. The data base for Hastelloy X, especially for direct measurements of LCF life, is more extensive than for the other alloys.

Nickel-200 is an attractive alternate for the TPS because of its exceptionally high ductility. Its creep strength is low and, hence, the maximum operating temperature must be limited to 790°C (1450°F) or less. Directly applicable low-cycle fatigue data and high-temperature creep data are lacking.

The TZM refractory alloy is attractive because its thermal stress parameter is low; however, in the unprotected condition, refractory alloys have no oxidation resistance at the Scramjet operating conditions. Applicable coating technology has not advanced significantly beyond that available in the 1960-1965 period. Without further coating development, refractory alloys cannot be considered for the Scramjet.

Primary structure.--In this case, the maximum operating temperature is 617°C (1140°F). At this level, Inconel 718 is generally regarded as optimum because of superior yield strength compared with Hastelloy X or Inconel 617. There is more difficulty in fabricating the primary structure using Inconel 718 compared with Hastelloy X. Because yield strength is the governing design criterion for the primary structure, Inconel 617 has no advantage over Hastelloy X at the design temperatures. For this reason, Hastelloy X is preferred. Where higher strength is required, Inconel 718 is specified.

Final selections.-The materials selected for design are shown in Table 5. Data are lacking in the critical area of low-cycle fatigue, especially for the specialized TPS structures and materials under consideration. Thermal fatigue

TABLE 5.-MATERIALS SELECTED FOR DESIGN

Structural Element	Selected Material	Alternate Material
TPS	Hastelloy X	Nickel-200
Honeycomb	Hastelloy X	Inconel 718
Beams and clips	Inconel 718	Hastelloy X
Leading edge support structure	Hastelloy X	Inconel 718
Strut primary structure	Inconel 718	-
Mounts, mounting frame	Inconel 718	-

will no doubt be the limiting factor in engine life. NASA-LaRC has initiated a program to develop the required data (ref. 7). The plan is to obtain fatigue and creep data for the candidate materials, including a determination of environmental effects. Fabrication techniques are to be developed and prototype panels are to be tested to measure creep-rupture strength and cyclic life. Data from this program will be used to verify or modify the above material selections.

Coolant Flow Routing

Design conditions.--Coolant inlet and outlet temperatures are 56 and 890 K (100° and 1600°R), respectively. Coolant inlet pressure is 6.9 MPa (1000 psia) and the pressure drop in any one circuit is limited to 1.72 MPa (250 psi). The reference design TPS was used in this analysis, viz., a Hastelloy X plate-fin surface, 11 fins per cm (28 fins per in.), 1.3 mm (0.050 in.) high, 2.5 mm (0.100 in.) offset, and 0.15 mm (0.006 in. thick), with a 0.38-mm (0.015-in.)-thick hot face sheet.

Optimization was conducted at the maximum thermal loading case, Condition H. This condition involves a 2-g maneuver and is short term relative to a cruise condition where design optimization is usually performed. Heating rates vary between flight conditions, but the coolant temperature profiles and the primary structure temperature tend to be similar for all operating conditions with combustion. This is because the heat flux distribution is similar for each condition and the coolant inlet and outlet temperatures are maintained constant. The coolant flow is adjusted in response to the overall heat load. Since Condition H is used for the TPS design, it was retained for the flow routing optimization because of temperature profile similarity and because maximum coolant flow is required at Condition H and this controls manifold design.

Design goals.--The coolant pressure drop across the TPS should not exceed 0.83 MPa (120 psi) to allow 0.55 MPa (80 psi) for manifolds and ducts and 0.34 MPa (50 psi) for coolant control valves and distribution system. The local in-depth TPS temperature gradient should be less than 260°C (500°F) to meet cyclic life requirements. The 260°C (500°F) limit is an approximation and is used only for screening purposes. No specific limits are placed on the temperature difference between adjacent panels that are cooled by separate flow routes, although the ΔT should be small to minimize axial differential thermal growth of adjacent panels.

Manifold orientation.--The hot gas flow properties are constant along an engine sweep line, and hence all sidewall manifolds were oriented parallel to the engine 48-deg sweep line to achieve maximum coolant utilization. This arrangement also yields uniform temperature profiles along the sweep lines.

Component flow arrangement.--Possible routes through a typical component (top, sidewall, or cowl) are shown in fig. 11. The routes are designated as "P" or "C" to indicate a coolant path that is either parallel (P) or counter (C) to the airflow. Heat transfer and pressure drop performance was determined for each component using each of the flow route options. Most of the possible routes produced an excessive pressure drop, excessive temperature gradient, or

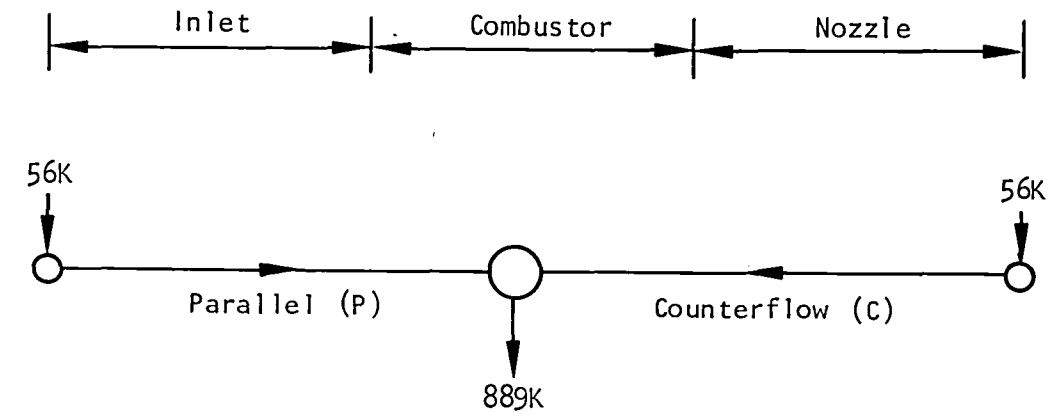

(a) P-C Configuration (Reference Design)

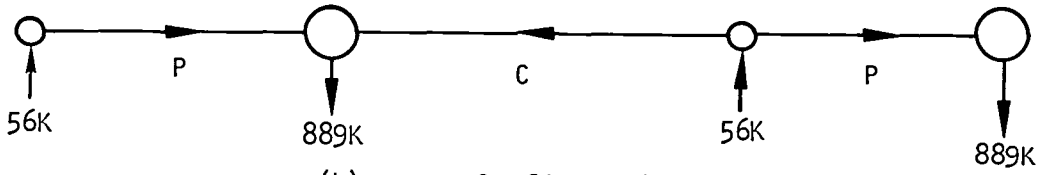

(b) P-C-P Configuration

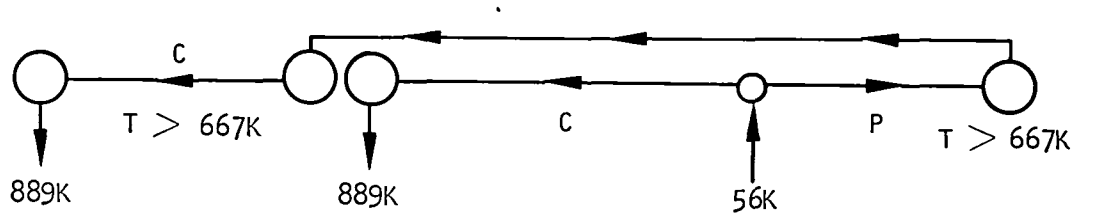

(c) P-C-C

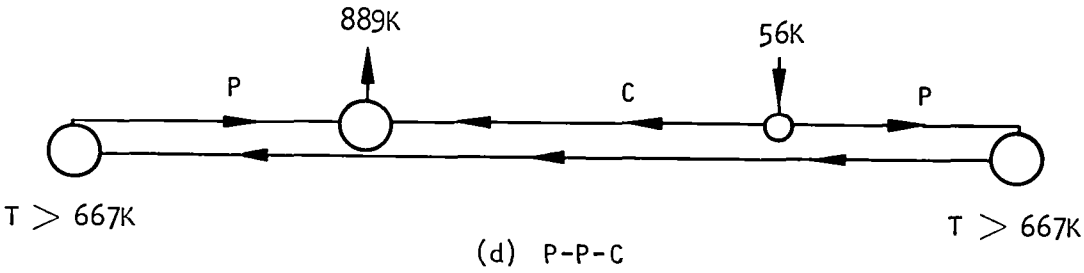

(d) P-P-C

S-15713-A

Figure 11.-Panel flow routing schemes.

a sudden step change in skin temperature of greater than 220 K (400°R). The reference design flow route (fig. 11a) met all design criteria. Moreover, this scheme requires a minimum number of manifolds and the flow is easy to meter because of an adequate pressure drop in each route. This reference design was selected for final optimization.

Outlet manifold position optimization.--Initial calculations were performed on the basis of achieving minimum coolant flow and a minimum TPS in-depth ΔT for each route. Based on these criteria, the optimum manifold locations were:

Component	Engine Station (sweepline intersection at cowl plane)
Topwall	80
Sidewall	65
Cowl	87

The primary structure temperature (hot face sheet of the honeycomb structure) profiles for the above manifold locations are shown in fig. 12(a). This arrangement produces an unacceptable temperature mismatch between intersecting panels, e.g., a 528°C (950°F) T between the sidewall and cowl (sweep line located at engine station 87). Large temperature gradients adversely affect the panel-to-panel seals and complicate the provisions for accommodating differential thermal growth. A viable method of controlling interpanel gradients must provide approximately equal coolant temperatures along any two intersecting panels.

Therefore, to alleviate the temperature mismatch, it was stipulated that the four panel outlet manifolds would be coplanar with the swept sidewall manifolds. A tradeoff analysis was conducted using coolant pressure drop and the TPS in-depth temperature gradient as parameters. The affect on overall engine coolant requirements was not significant.

The best attainable combination of TPS metal ΔT and pressure drop balance is achieved with the cowl segment of the exhaust manifold at Station 77.5. For this configuration, approximate internal surface temperature profiles are plotted in fig. 12(b). The structure temperature referred to in fig. 12 is the hot face temperature of the primary structure, which corresponds to the TPS cold-side surface. Excessive (250° to 350°C) interpanel gradients exist between sidewall and cowl at the leading edge of the cowl (Station 51), and between sidewall and top at the trailing edge of the sidewall (cowl Station 103). The basic problem is in the relative orientation of the panels (i.e., dissimilar lengths and leading and trailing edge locations); this arrangement results in large interpanel coolant temperature disparity along the axis of the engine.

A modified flow routing scheme (fig. 13) was devised to reduce the large interpanel temperature differences noted above. With this scheme, coolant for the entire aft end of the engine is fed through the trailing edges of the cowl and top surface. Redistribution shunt manifolds are located on the top surface and internal cowl surface in line with the trailing edge of the sidewall. At

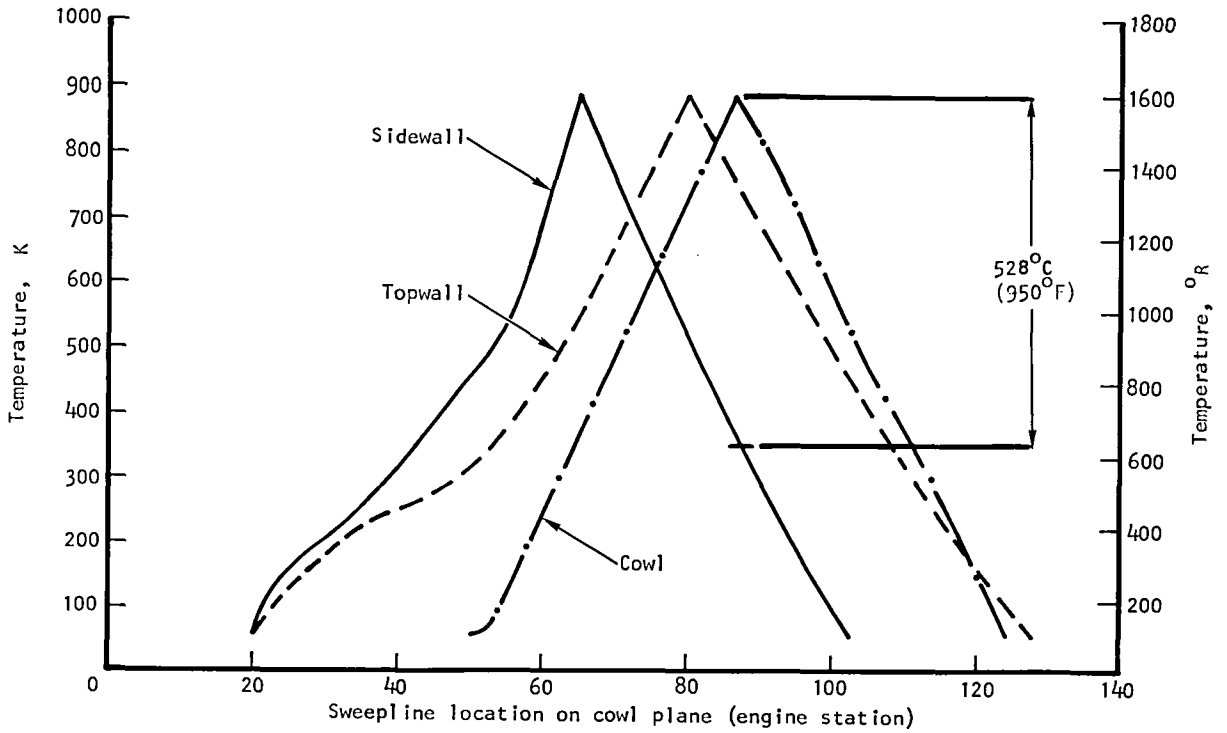

(a) Minimum coolant flow and TPS ΔT

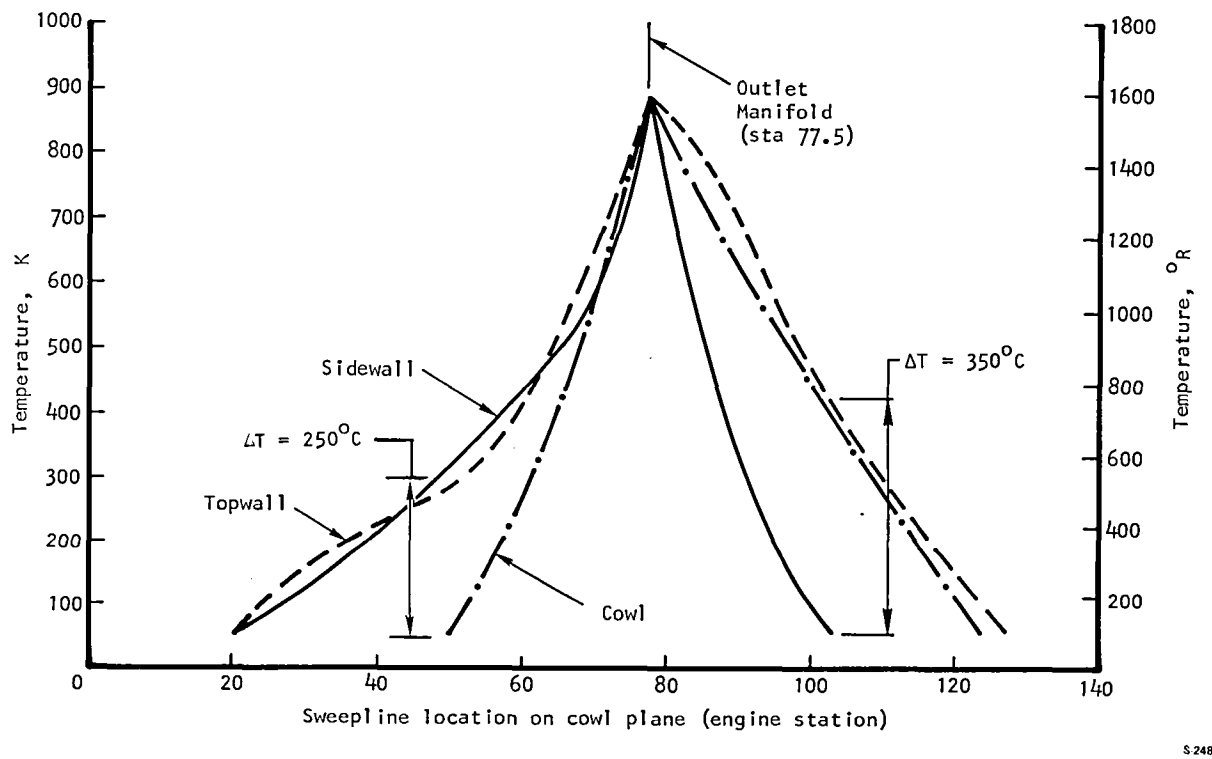

(b) Coplanar outlet manifolds

Figure 12.-Primary structure temperature profiles.

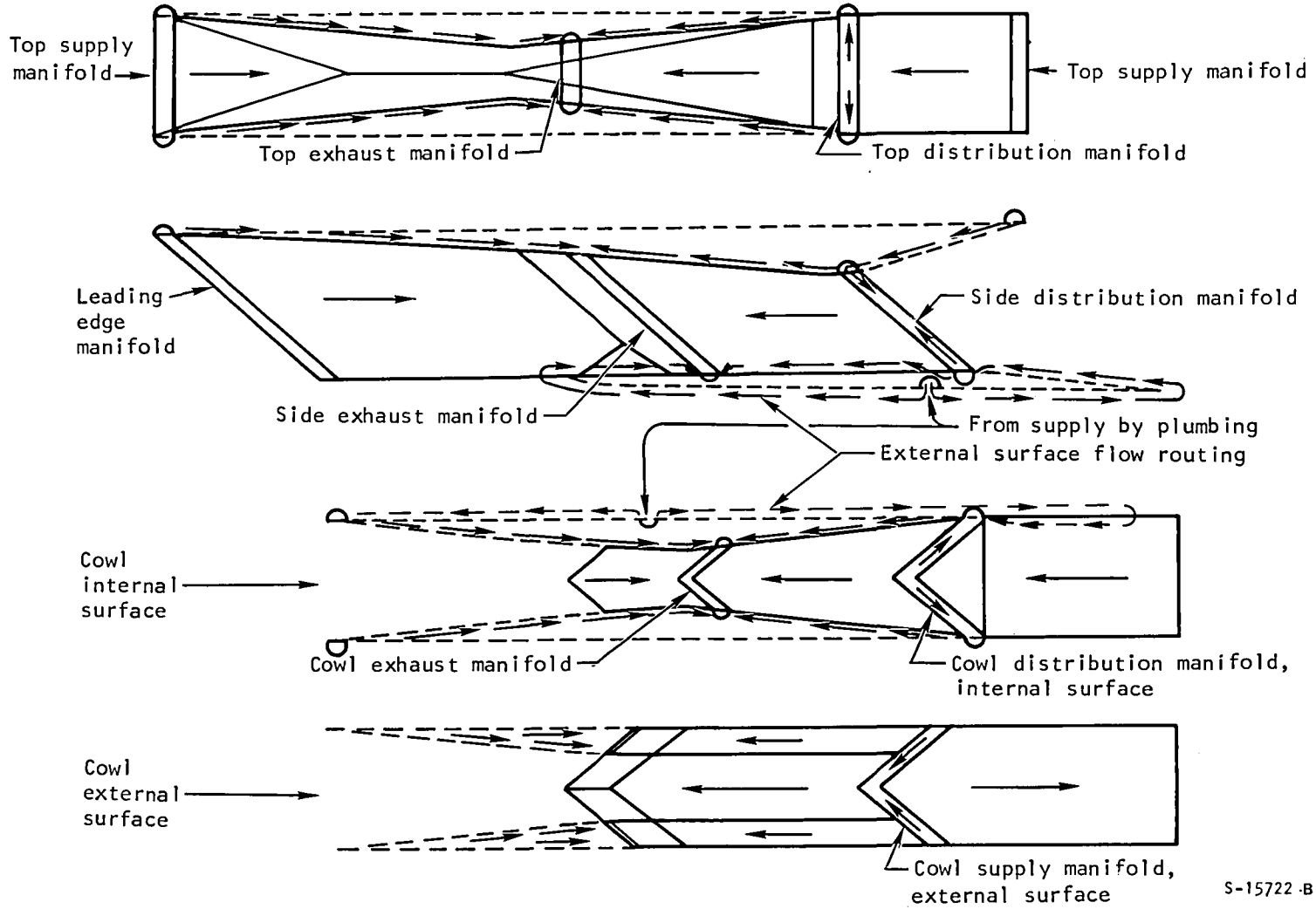

Figure 13.-Sidewall shunt coolant distribution concept.

this point a portion of the coolant flow is split from the aft top surface and aft internal cowl cooling circuits and is directed to an intermediate manifold. Flow is directed from this manifold to the aft portion of the sidewall circuits.

The pressure drop and TPS ΔT tradeoff analysis was repeated and the optimum outlet manifold position was determined to be located at Station 75 (at the cowl plane). The four outlet manifolds are on the same sweep line with the topwall outlet manifold at Station 59. The individual outlet manifolds are not necessarily interconnected.

The shunted flow route concept yields acceptable primary structure temperature profiles (honeycomb hot face sheet) as shown in fig. 14. The maximum interpanel temperature difference at any sweepline position is 120°C, which occurs between the sidewall and cowl at the cowl leading edge. This ΔT is considered acceptable at the low temperature indicated.

Coolant flows and conditions in each circuit are defined in fig. 15. Coolant pressure drop in each circuit was reasonable, but the TPS gradient exceeded the design goal in several instances. Thus, further studies were conducted to improve TPS performance, i.e., to reduce in-depth temperature gradient with acceptable coolant pressure drop. The shunt flow routing scheme and coolant flow noted above were retained.

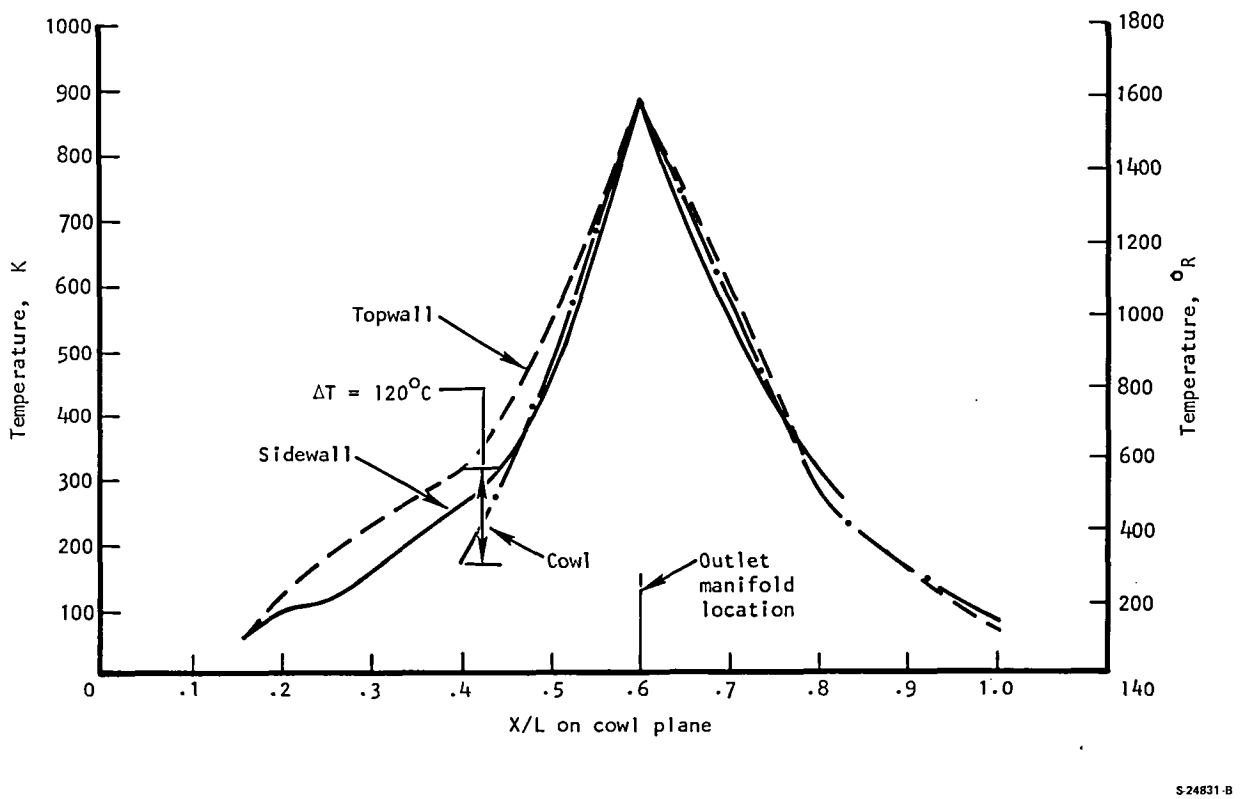

Figure 14.-Coplanar outlet manifolds and shunt flow routing.

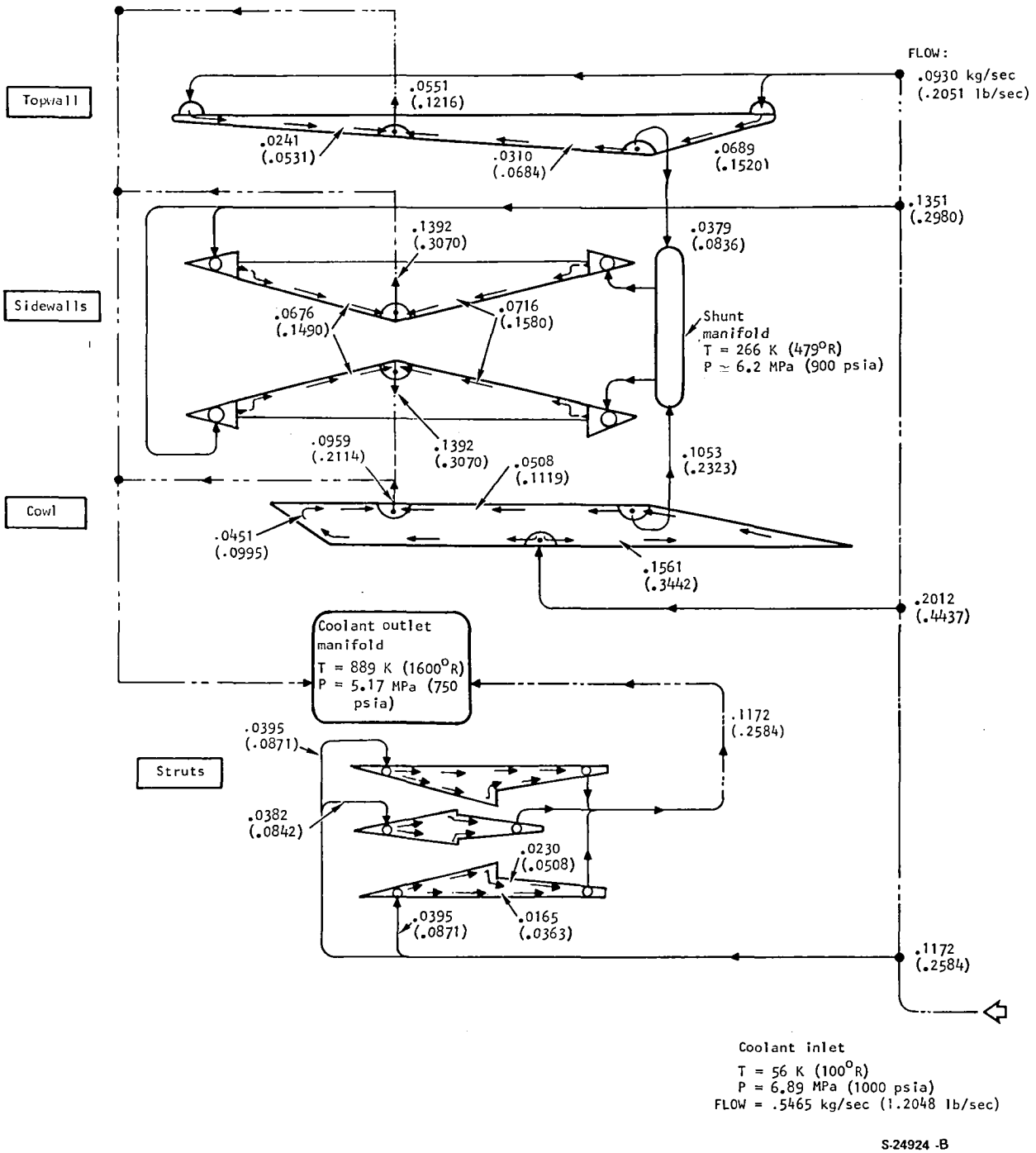

Figure 15.-Coolant flow conditions.

Strut flow routing.--Two strut flow routing schemes were examined: (1) coolant flow parallel to hot gas flow, and (2) coolant flow along the 48-deg sweep line. The second scheme did not offer any significant advantages and the resulting flow paths created significant temperature discontinuities. The selected flow path is with the hydrogen coolant parallel to hot gas flow, as shown in fig. 16 below. Coolant conditions for the strut flow are noted on fig. 15.

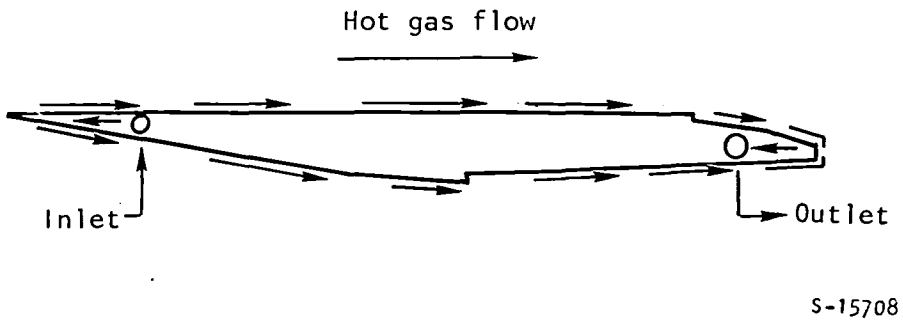

Figure 16.-Selected strut coolant flow path

Flight Envelope Cooling Requirements

To determine engine heat loads at conditions throughout the operating envelope (see fig. 4), the engine was divided into four regions: inlet, combustor, nozzle, and external surfaces (see fig. 5). Condition H heat loads were then scaled according to the particular heat transfer mechanism in each of these regions. The inlet has mostly laminar flow with constant total enthalpy (inlet air); the combustor has turbulent flow with increasing total enthalpy (inlet air to combustion products); the nozzle has turbulent flow with constant total enthalpy (combustion products); and the external surfaces have mostly turbulent flow with constant total enthalpy (inlet air). The calculations included the average effect of mass velocity, wall temperature, and hot gas fluid properties in each region.

Results are presented in Table 6 for an inboard module, an outboard module, and a six-module cluster (four inboard and two outboard modules). Minimum hydrogen coolant rates were established assuming that the coolant is heated from 56 K (100°R) to 890 K (1600°R) except for Condition A'. For this condition the coolant inlet temperature was increased until the entire coolant flow is heated to the 890 K (1600°R) maximum fluid outlet temperature and the cooling equivalence ratio, ϕ_c, was equal to 1.0. For this cruise condition, the coolant supply temperature may be increased to 420 K (756°R), which indicates that 44 percent of the coolant heat capacity is available for cooling other components. These coolant rates are considered minimum because of inherent inefficiencies in the cooling system.

TABLE 6.-ALTITUDE-MACH NUMBER ENVELOPE COOLANT REQUIREMENTS.

Flight condition (fig. 4)	Inboard module heat load, MW (Btu/sec)	Outboard module heat load, MW (Btu/sec)	Six module heat load, MW (Btu/sec)	Inboard module coolant flow, kg/sec (lbm/sec)	Outboard module coolant flow, kg/sec (lbm/sec)	Six module coolant flow, kg/sec (lbm/sec)	Inboard/ outboard module fuel flow, kg/sec (lbm/sec)	Six module fuel flow, kg/sec (lbm/sec)	Inboard module, cooling equiv. ratio, ϕ_c (ϕ_f = 1.0)	Outboard module, cooling equiv. ratio, ϕ_c (ϕ_f = 1.0)	Six module ϕ_c at ϕ_f = 1
A	1.48 (1407)	1.73 (1640)	9.39 (8908)	.118 (.261)	.138 (.304)	.748 (1.650)	.245 (.540)	1.470 (3.240)	.483	.563	.509
A'	1.48 (1407)	1.73 (1640)	9.39 (8908)	.245 (.540) T_{in} = 486 K (876°R)	.249 (.540) T_{in} = 420 K (756°R)	1.47 (3.240) T_{in} = 464 K (836°R)	.245 (.540)	1.470 (3.240)	1.000	1.000	1.000
B	3.58 (3399)	4.04 (3835)	22.42 (21266)	.285 (.629)	.322 (.710)	1.79 (3.936)	.365 (.804)	2.188 (4.824)	1.173	1.324	1.239
C	1.13 (1075)	1.44 (1366)	7.41 (7032)	.090 (.199)	.115 (.253)	.591 (1.302)	.584 (1.287)	3.503 (7.722)	.155	.197	.169
D	2.87 (2719)	3.31 (3135)	18.08 (17,146)	.229 (.504)	.264 (.581)	1.44 (3.175)	.607 (1.339)	3.644 (8.034)	.376	.434	.395
E	4.06 (3855)	4.60 (4361)	25.45 (24,142)	.324 (.714)	.367 (.808)	2.03 (4.471)	.581 (1.280)	3.484 (7.680)	.558	.631	.582
F	5.75 (5454)	6.41 (6076)	35.81 (33,968)	.458 (1.010)	.510 (1.125)	.285 (6.290)	.828 (1.826)	4.970 (10.956)	.829	.924	.861
G	2.70 (2562)	3.16 (2993)	17.12 (16,234)	.215 (.474)	.251 (.554)	1.36 (3.006)	.667 (1.471)	4.003 (8.826)	.332	.377	.341
H	6.85 (6500)	7.72 (7319)	42.85 (40,638)	.546 (1.205)	.615 (1.355)	3.41 (7.526)	1.007 (2.220)	6.042 (13.320)	.813	.915	.848
I	3.25 (3078)	3.88 (3680)	20.74 (19,672)	.259 (.570)	.309 (.681)	1.65 (3.643)	0.0	0.0	-	-	.410

The coolant equivalence ratios, ϕ_c, in Table 6 are based on fuel flows for stoichiometric combustion at all operating conditions. The coolant requirements were determined from conditions listed in fig. 4, with ϕ_f = 0, 1.0, and 1.5. The fuel equivalence ratio, ϕ_f, of 1.5 is not used since it applies only to the selected design point for a research airplane. It is required to provide adequate thrust in this application and is not appropriate to a commercial airplane. The values given in Table 6 for ϕ_c at ϕ_f = 1.0 assume that the heat load and coolant flow are unchanged in going from ϕ_f = 1.5 to ϕ_f = 1.0. The maximum and minimum ϕ_c, which occur at Conditions B and C, respectively, reflect their extreme positions on the altitude-Mach number envelope (fig. 4).

The fraction of the stoichiometric fuel flow required to cool the Scramjet engine at two dynamic pressures is shown in fig. 17 as a function of Mach number. The fuel provides an adequate heat sink for cooling the engine at Mach numbers up to approximately 9 at a dynamic pressure of 24 kPa (500 psf), and to even higher Mach numbers at a dynamic pressure of 72 kPa (1500 psf). The cooling requirements are less severe at the higher dynamic pressure because the heat load increases at the 0.8 power of the dynamic pressure, while the fuel requirement increases linearly. At lower Mach numbers there is surplus hydrogen fuel heat sink for cooling other components and/or additional engine cooling.

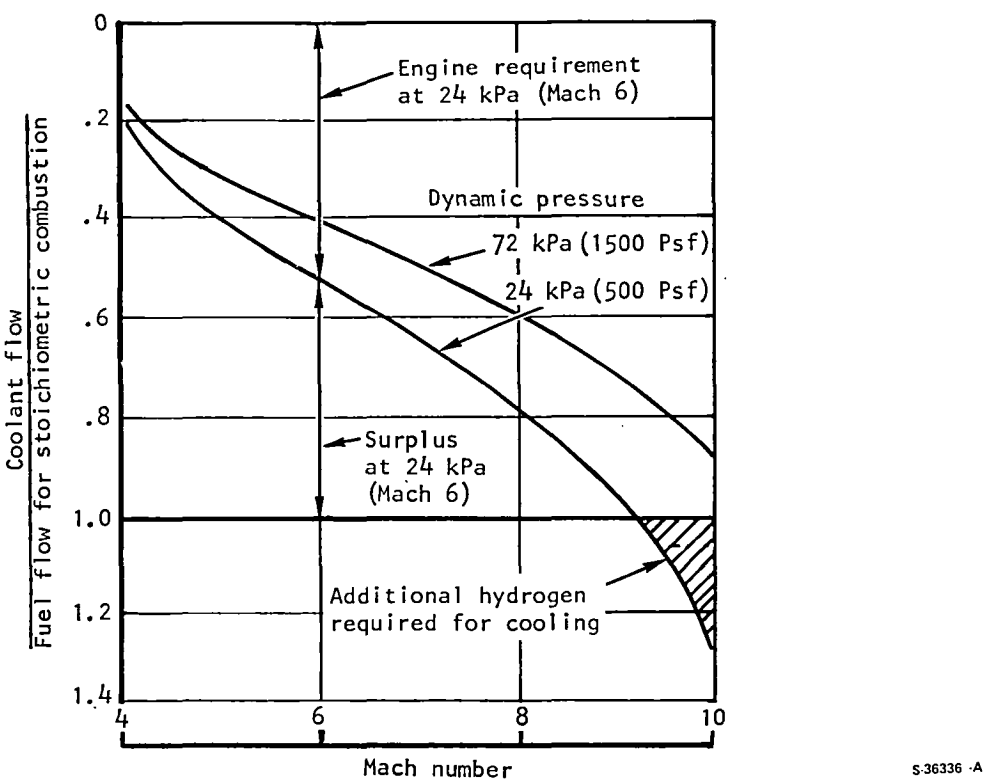

Figure 17.-Engine cooling requirements.

A breakdown of heat load by engine section is presented in fig. 18a. The inlet section is composed of all internal surfaces up to the fuel injectors; the combustor section extends to the internal sweepline from station 80.755 on the top surface to 94.649 on the cowl, and the nozzle section extends to the end of the engine (see fig. 5). Included is the small fraction of external heat loads. The major portion of the heating occurs in the combustor section. There is no fixed relationship in the heating rates between sections.

Another breakdown of engine heating is presented in fig. 18b, where the heating on the forward engine section is presented as a percentage of total engine load. The forward section includes the inlet section plus the forward external surfaces. The aft section (the complement of the forward section on a percentage basis) includes the combustor, nozzle, and aft external surfaces. This heating breakdown corresponds to the loading on forward and aft coolant flow routes on the engine. Again, there is no fixed relationship in the heating rates between sections.

Thus, for efficient utilization of coolant throughout the operating envelope, active controls must be used to vary the coolant flow split between the forward and aft portions of the engine. Flow control by means of fixed orifices would not suffice. A preliminary design of a scramjet fuel system with active coolant flow controls is presented in a subsequent section entitled Hydrogen Flow Control.

Thermal Protection System (TPS)

Heat exchanger design.--Three types of TPS configurations were considered: (1) rectangular offset plate-fin, (2) rectangular plain machined channel, and (3) equally spaced (equilateral triangle) circular pin-fin. Fig. 19 presents a sketch of these surfaces and the dimensional ranges.

The 11-fin-per-cm rectangular offset fin is the reference design and is the basis of comparison. The 14-fin-per-cm fin is one-half the above passage height and is considered for high heat flux areas to minimize in-depth temperature differences (ΔT's). For the machined fins, the 2.0-mm (0.080-in.) fin spacing and 0.51-mm (0.020-in.) fin thickness are reasonable manufacturing limits. The pin-fin was considered because it can provide the interrupted coolant passage characteristics of an offset plate-fin. Spacing-to-pin diameter ratios (S_p/D_p) of 2 and 2.7 were selected to provide adequate coolant pressure containment. In all configurations, a 0.38-mm (0.015-in.) face sheet was used.

Coolant flow rates and passage lengths in each circuit were defined by the flow routing studies and are fixed. The coolant pressure drop in each circuit is limited to approximately 0.83 MPa (120 psi) (0.55 MPa for manifolds and ducting); each circuit should expend as much as possible of this allotment. The struts have shorter flow lengths than the panels, and hence the unit pressure drop can be higher.

Heat transfer performance curves were developed for each surface; typical examples are shown in fig. 20. It is possible to trade off reductions in the

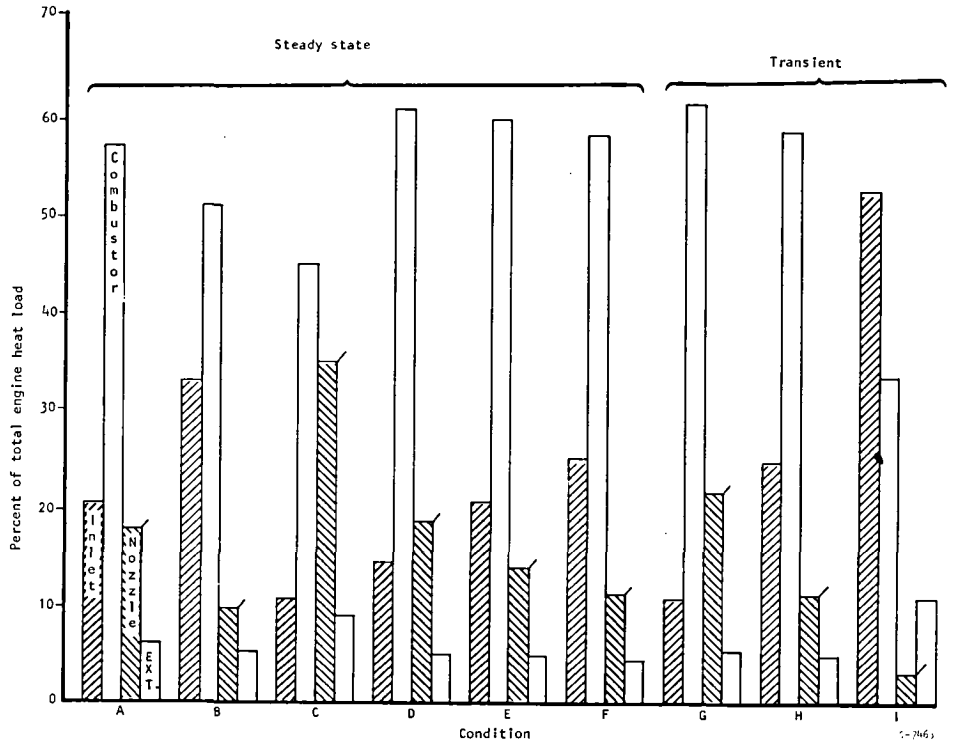

a. Heat load split between engine sections.

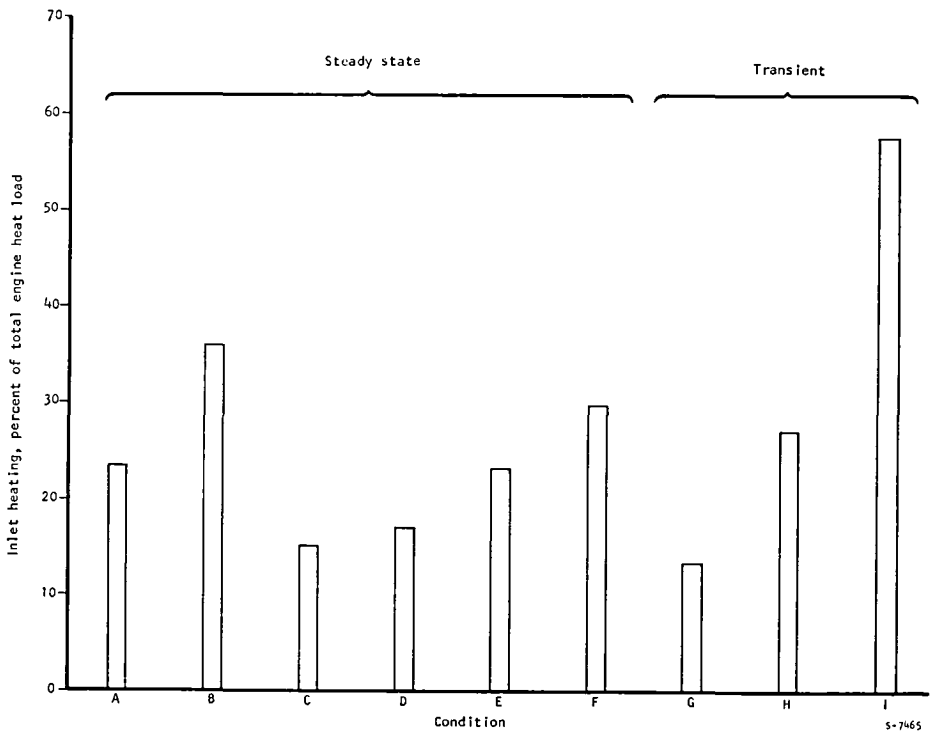

b. Inlet heating fraction.

Figure 18.-Engine heat loads.

Rectangular offset plate fin

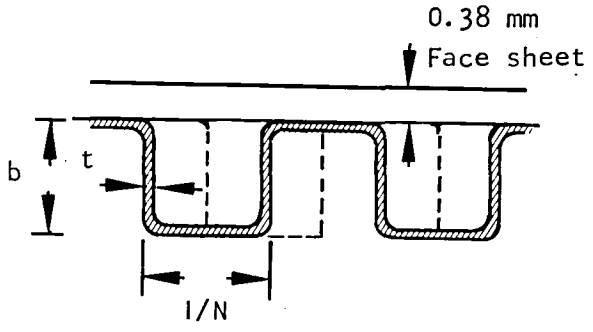

N = fins per cm of flow width

Fins considered:

(1) N = 11, b = 1.3 mm, t = 0.15 mm

(2) N = 14, b = 0.64 mm, t = 0.05 mm

Pin fin

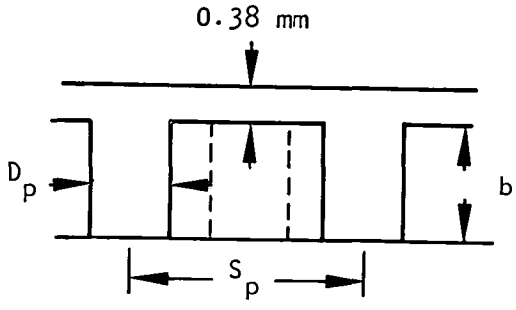

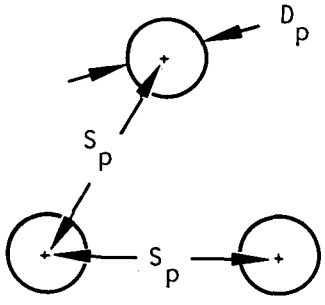

Dimensions considered:

S_p = 2.0 mm

D_p = 0.76 and 1.02 mm

b = 0.64, 1.27, 1.91 mm

Machined channel

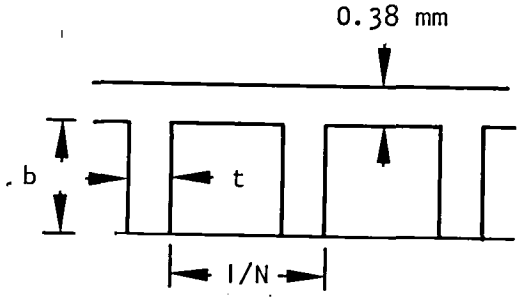

Dimensions considered:

1/N = 2.0 mm

t = 0.5 mm

b = 0.64 and 1.27 mm

S-15719-A

Figure 19.-TPS heat exchanger configurations.

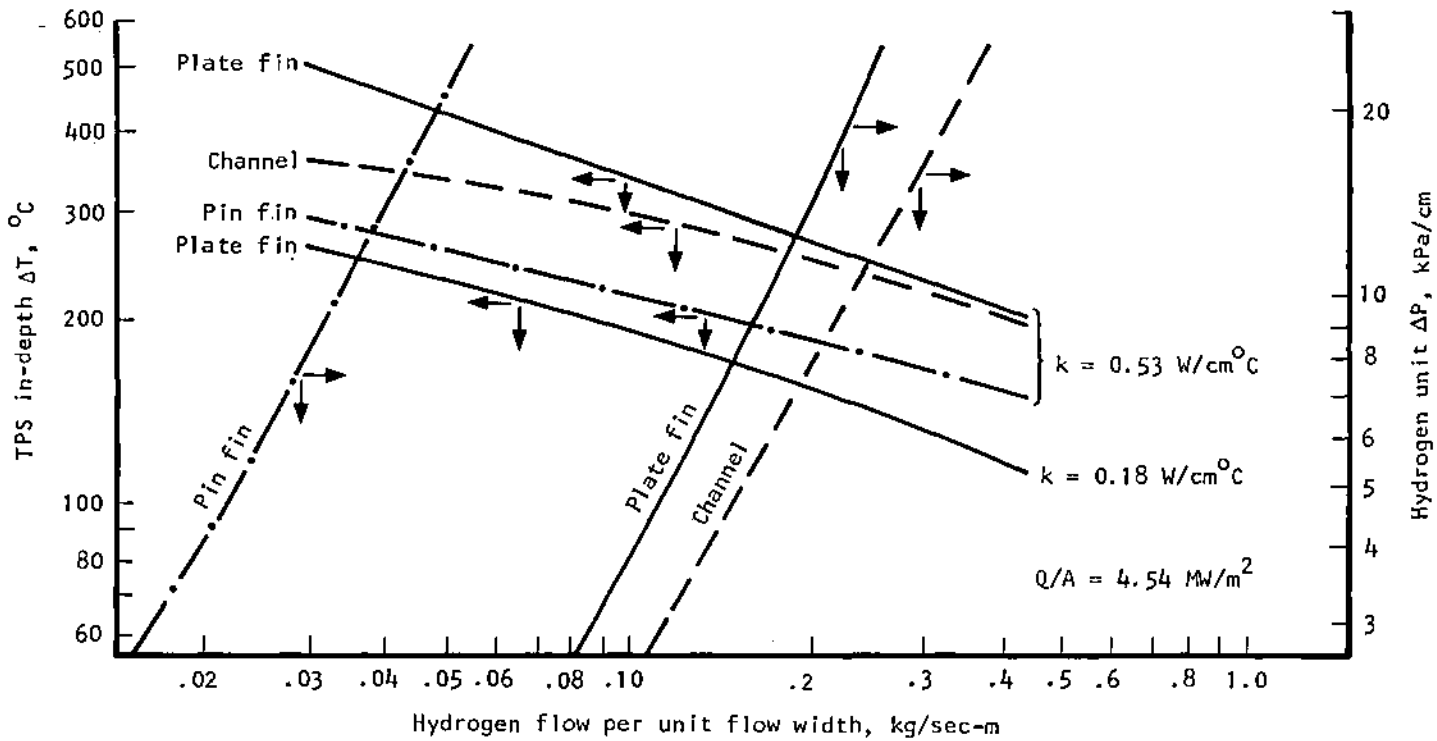

Flow passage geometries

Plate fin: 11 fins/cm

Channel: 0.64 mm depth

Pin fin: 0.64 mm depth, 1.0 mm pin diameter

Hydrogen flow conditions

P = 6.2 MPa

T = 556 K

S-24843

Figure 20.-TPS heat exchanger performance.

TPS in-depth temperature gradient with increases in coolant pressure drop or in TPS material (thermal conductivity).

The performance in each flow route was determined for each candidate surface at average hydrogen flow conditions. Coolant pressure drop was estimated for the entire flow route; the TPS ΔT was determined only at the peak heat flux condition. Results for the sidewall are shown in Table 7. Here, the 0.64-mm (0.025-in.)-deep channel provides the lowest ΔT within the pressure drop guidelines.

Thermal conductivity has a pronounced effect on the TPS thermal gradient. The following results are for the sidewall forward flow route:

	TPS Material	
	Hastelloy X, k = 0.18 W/cm-°C (10 Btu/hr-ft-°F)	Nickel-200, k = 0.53 W/cm-°C (30 Btu/hr-°F)
TPS hot skin temperature, K (°R)	784 (1412)	685 (1233)
Primary structure temperature, K (°R) (honeycomb hot face sheet)	550 (990)	550 (990)
TPS temperature gradient, maximum ΔT, K (°R)	234 (422)	135 (243)

For external surface cooling, passive as well as active schemes were investigated with the following results at steady state:

Method	Metal substrate temperature, K (°R)	Net heat input, MW/m (Btu/sec-ft^2)
Reusable surface insulation (RSI) 0.25 in. thick, k = 0.18 W/cm-°C (1.0 Btu/hr-ft-°F)	1300 (2340)	0.054 (4.8)
Rockide Z insulation, 0.025 in. thick, k = 0.018 W/cm-°C (0.1 Btu/hr-ft-°F)	1420 (2550)	0.093 (8.3)
Bare metal, emissivity = 0.8	1440 (2590)	0.10 (8.9)
Active cooling with hydrogen, inlet temperature = 56 K (100°R)	200 (360)	0.45 (40)

The internal structure was assumed to be at 278 K (500°R) in all cases. RSI thickness is limited by the cowl depth.

TABLE 7.-SIDEWALL TPS TEMPERATURE GRADIENT AND PRESSURE DROP

SI UNITS

Material: Hastelloy X, k = 0.18 watts/cm-°C
Hydrogen Conditions: T = 556 K, P = 6.20 MPa

Surface Description		Forward flow route(1)		Aft flow route(2)	
		ΔT, °C	ΔP, MPa	ΔT, °C	ΔP, MPa
Plate fin	11 fins/cm	256	1.14	189	0.94
	14.2 fins/cm	206	5.10	152	4.03
Channel	1.27 mm deep	357	0.12	266	0.09
	0.64 mm deep	234	0.70	178	0.52
Pin-fin	1.02 mm dia by 0.64 mm deep	172	24.06	131	19.03
	1.02 mm dia by 1.27 mm deep	220	7.10	162	5.64
	1.02 mm dia by 1.91 mm deep	254	3.15	188	2.44
	0.76 mm dia by 1.27 mm deep	232	3.34	172	2.54

(1) Flow = 0.0631 kg/sec, average flow width = 0.419 m, flow length = 1.40 m, heat flux = 4.02 MW/m^2.

(2) Flow = 0.0692 kg/sec, average flow width = 0.349 m, flow length = 0.63 m, heat flux = 3.27 MW/m^2.

U.S. CUSTOMARY UNITS

Material: Hastelloy X, k = 10 Btu/hr-ft-°F
Hydrogen Conditions: T = 1000°R, P = 900 psia

Surface Description		Forward flow route(1)		Aft flow route(2)	
		ΔT, °F	ΔP, psi	ΔT, °F	ΔP, psi
Plate fin	28 fins/in.	460	165	340	136
	36 fins/in.	371	740	274	585
Channel	.050 in. deep	643	18	478	13
	.025 in. deep	422	101	320	76
Pin fin	.040 in. dia by .025 in. deep	310	3490	235	2760
	.040 in. dia by .050 in. deep	396	1030	292	818
	.040 in. dia by .075 in. deep	458	457	338	354
	.030 in. dia by .050 in. deep	418	484	310	368

(1) Flow = .1392 lb/sec, average flow width = 1.375 ft, flow length = 55 in., heat flux = 354 Btu/sec-ft^2

(2) Flow = .1527 lb/sec, average flow width = 1.144 ft, flow length = 25 in., heat flux = 288 Btu/sec-ft^2

The passive schemes are all feasible in that the equilibrium temperature of the metal substrate is below the melting point of a Hastelloy X structure. The net heat input is low, but means to absorb this input are still required. The primary drawback to passive cooling is that the hot substrate must be attached to the cooler engine structure, with resulting problems in heat leak and thermal stress. The selected approach is to use active cooling and accept the greater heat input.

Structural design.--In the TPS, the primary structure is relatively cold and limits the thermal expansion of the hot surface, which is less stiff. In fig. 21, curve OA represents the elastic-plastic loading produced by the temperature gradient across the TPS. Without hold time, the ΔT gradient decreases to zero and the line AC represents the unloading; however, even a short hold time--especially if the stress at A is high--will produce stress relaxation (point B in fig. 21). The amount of relaxation will depend on the stress, temperature, and creep properties of the material under consideration. The amount of damage incurred in one cycle increases as point B_1 moves to B_2 (more creep). Repetitive cycles around the hysteresis loop (fig. 21) result in accumulated damage and eventually a fatigue crack develops. The failure mechanism is low-cycle fatigue (LCF).

Thermal stresses are the predominant load in the TPS structure. Bending stresses induced by the hot gas flow are secondary. Thus, the life of the TPS is governed by LCF considerations. The basic analytical approach is to consider creep relaxation effects with an elastic plastic mode of behavior.

Design configurations: The two basic designs selected for analysis of relative merits are: (1) a formed plate fin, and (2) a machined fin. Dimensions of the TPS and supporting structure are shown in fig. 22. Dimensions used here are different from those finally selected (see fig. 19). The resulting cycle life predictions, however, are valid for comparison purposes.

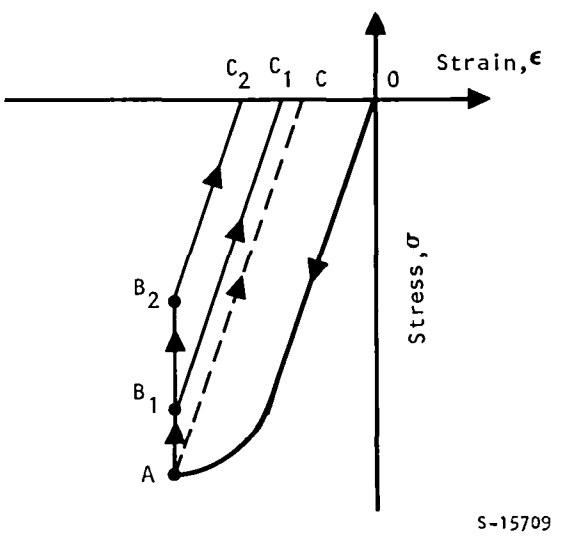

Figure 21.-Elastic-plastic cycle.

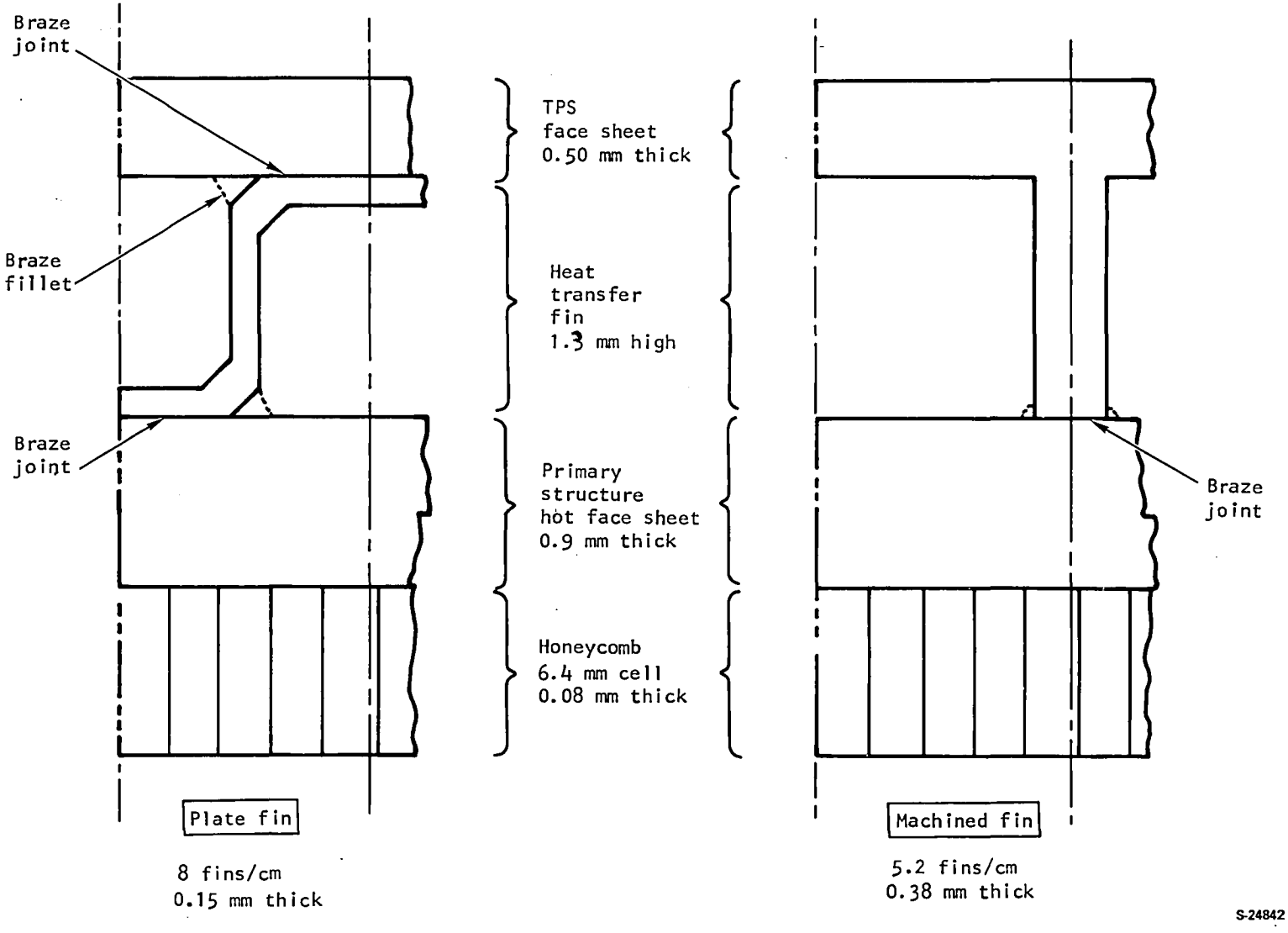

Figure 22.-TPS structural design fin configurations.

The machined fin is considered an attractive alternate because of (1) reduced stress concentration, and (2) elimination of a braze joint next to the hot face sheet. Brazing is known to adversely affect fatigue life.

Thermal stress analysis: Finite element models of the candidate structure were constructed and the boundary conditions defined. The plate-fin model is shown in fig. 23. Hastelloy X material was first evaluated. A TPS hot face temperature of 788°C (1450°F) was specified because it is an average value of the temperature gradient across the face sheet at the maximum imposed heat flux condition. Coolant pressure was assumed to be 5.52 MPa (800 psia) and the hot gas pressure equal to 0.69 MPa (100 psia).

Maximum elastic stresses and displacements were determined for a range of in-depth temperature gradients. A typical stress result for the plate-fin design is shown in fig. 24. For the high gradient cases, the resultant stresses are sufficient to cause plastic deformation plus creep. The elastic analysis indicated that the plastic region (that area where the stress exceeds the material yield strength) would be extensive, and hence, a full elastic-plastic analysis including creep relaxation was performed using finite element models. Temperature differences of 193°, 354°, and 499°C (379°, 670°, and 930°F) were imposed across the TPS face sheet and fins. Resulting strains were determined as a function of hold time at temperature from 4 sec to 700 hr. Strain is the most important parameter because it defines the number of fatigue cycles the structure can withstand without cracking.

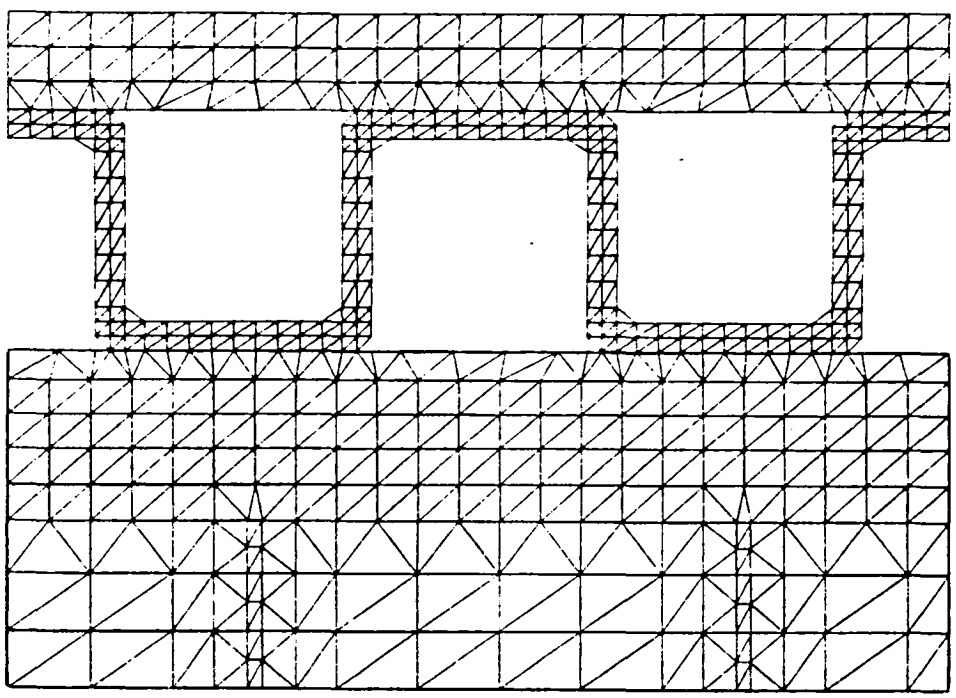

S-24839

Figure 23.-Finite element model.

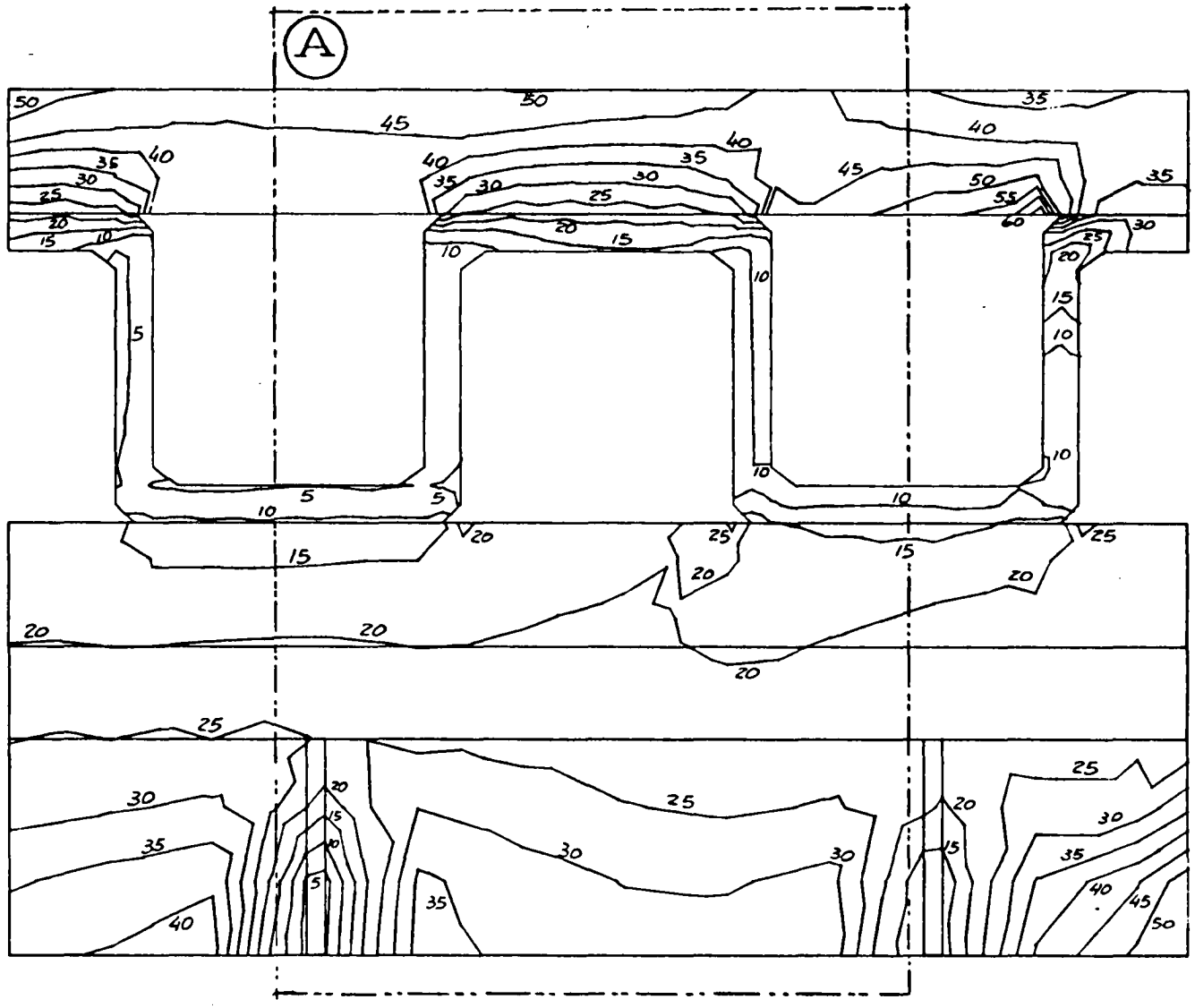

Figure 24.-Effective stresses (ksi) in plate-fin structure.

Results: Plastic plus creep strains for the plate-fin and machined-fin structures are shown in fig. 25. The particular area under examination is the TPS hot face sheet where the strains are maximum. The maximum primary structure temperature, 616°C (1140°F), was used as the baseline. The plastic flow region is well developed within the first minute. The stress relaxation is greater for the larger temperature differences, but less than the direct proportion between gradients.

The rate of strain development as ΔT is increased differs between the two structures, primarily because of the difference in the ratio of fin-to-face sheet stiffness. With the formed fin structure, the fin is flexible relative to the face sheet, and thus the face sheet absorbs most of the axial load. In the machined-fin structure, more of the thermally induced load is taken by the fin. In the area of interest, i.e., ΔT = 222° to 278°C (400° to 500°F), more plastic strain is developed in the machined-fin structure; however, this does not necessarily relate to a lower cycle fatigue life. A larger radius at the root of the machined fin would reduce the plastic strain.

Low-cycle fatigue (LCF) analysis: Two techniques were used to relate creep damage to LCF: linear interaction, a technique described in refs. 17 and 18, and strainrange partitioning, the most recent evolution, described in refs. 19, 20, and 14.

Strainrange partitioning involves the concept that two modes of deformation may exist separately or concurrently, and that their interaction influences the fatigue behavior of the material to a significant degree. In this method, the two strain modes of plastic flow and creep are distinguished in relation to their time dependency. Plastic flow is regarded as the inelastic strain component that occurs immediately upon application of stress, while creep is regarded as the time-dependent component. This distinction allows the separation of the inelastic strain components by relatively simple experimental procedures.

Safety factors for linear interaction were as follows:

Creep damage fraction	4 (on time)
LCF damage fraction	10 (on life)

With strainrange partitioning, a 2.5 to 4.0 safety factor was assigned, depending on the relative amounts of plasticity or creep in the hysteresis loop. A higher safety factor is used where creep dominates.

Cycle life predictions for Hastelloy X material are presented in figs. 26 and 27. Strainrange partitioning gives a more conservative cycle life prediction in the range of interest, i.e., temperature gradients less than 360°C (650°F). At high temperature gradients, i.e., high strain levels, the life fractions method is probably more reliable. The recommended design curve was drawn to reflect the most conservative approach.

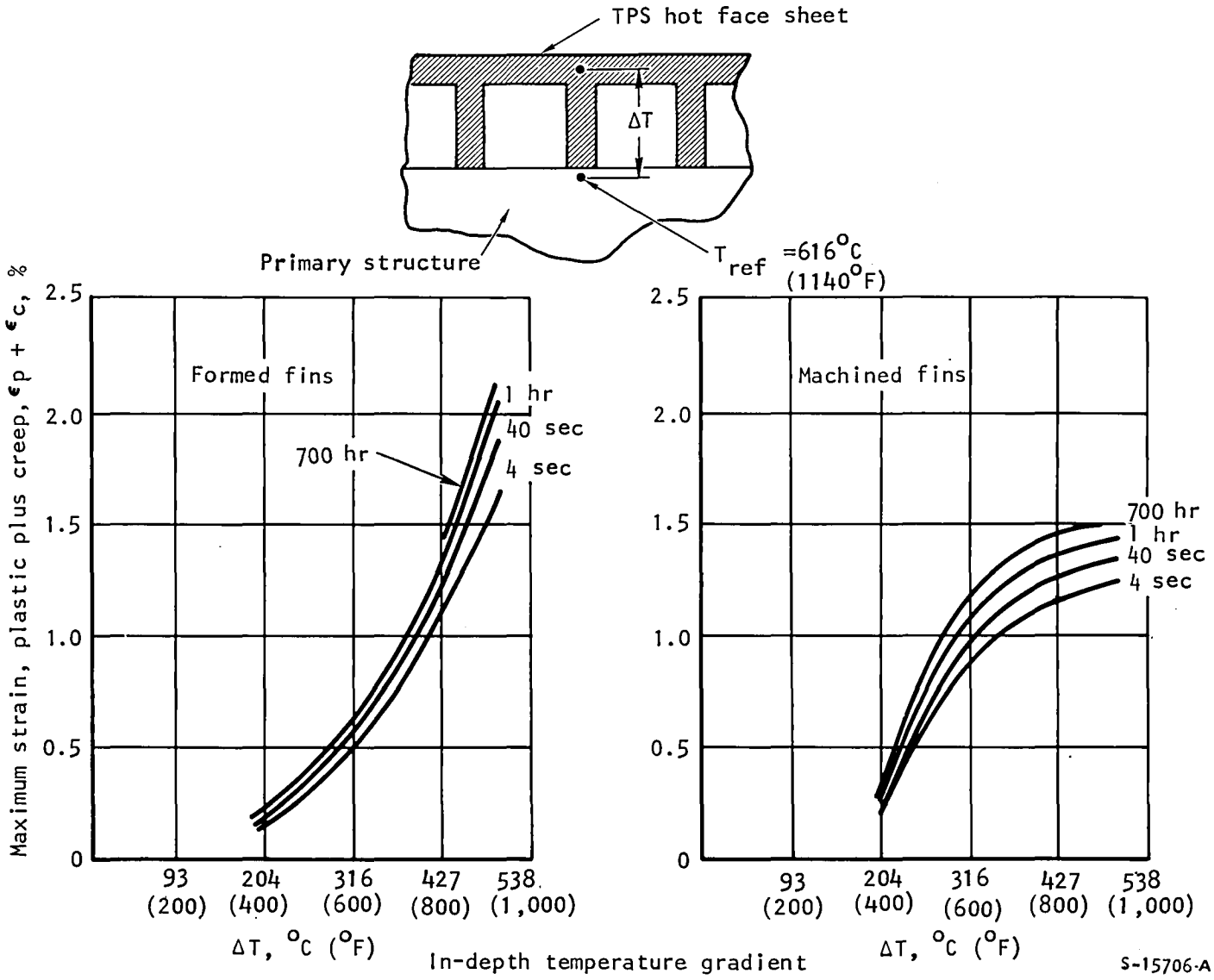

Figure 25.-TPS response to thermal gradient.

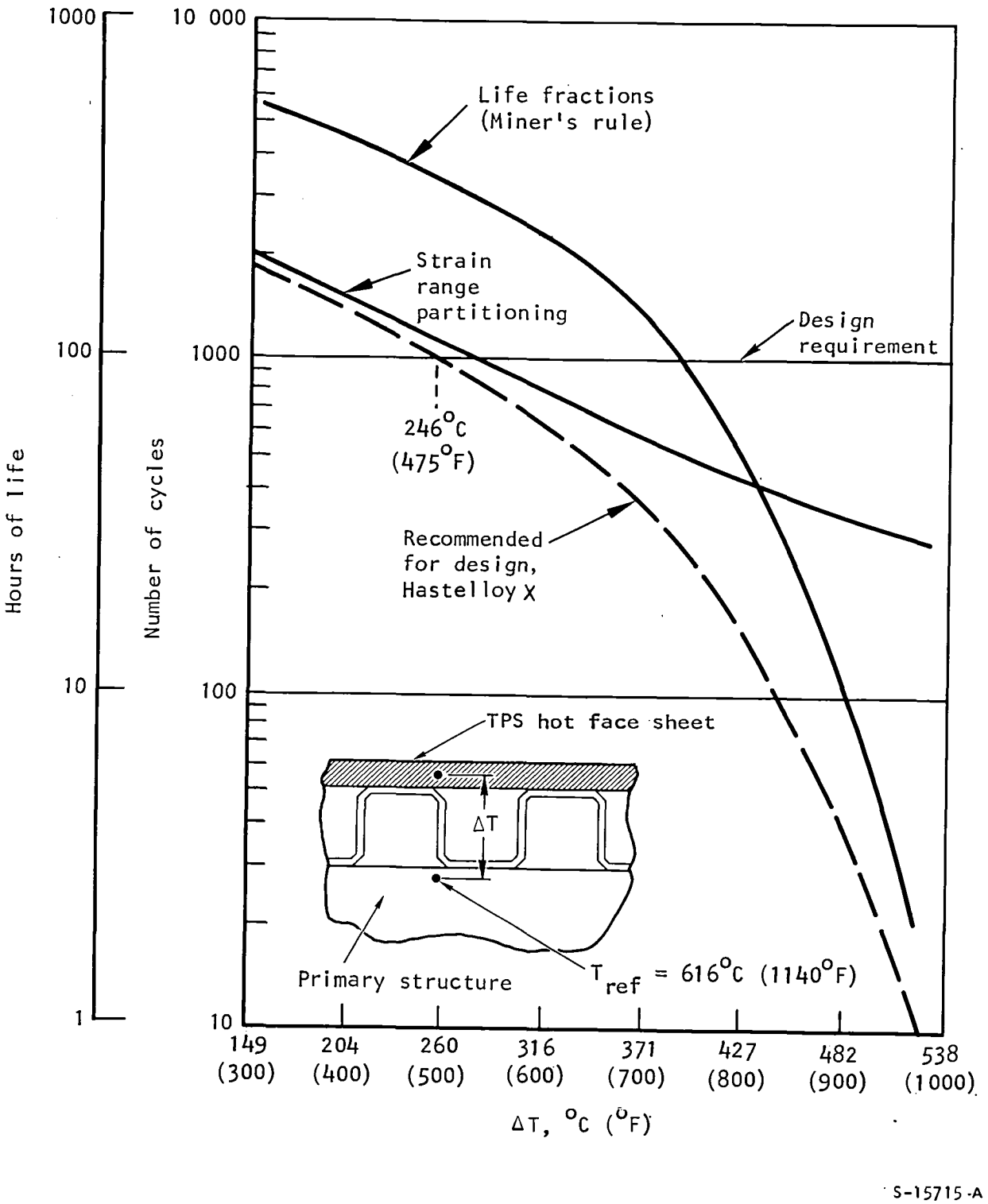

Figure 26.-Cycle life for formed-fin TPS.

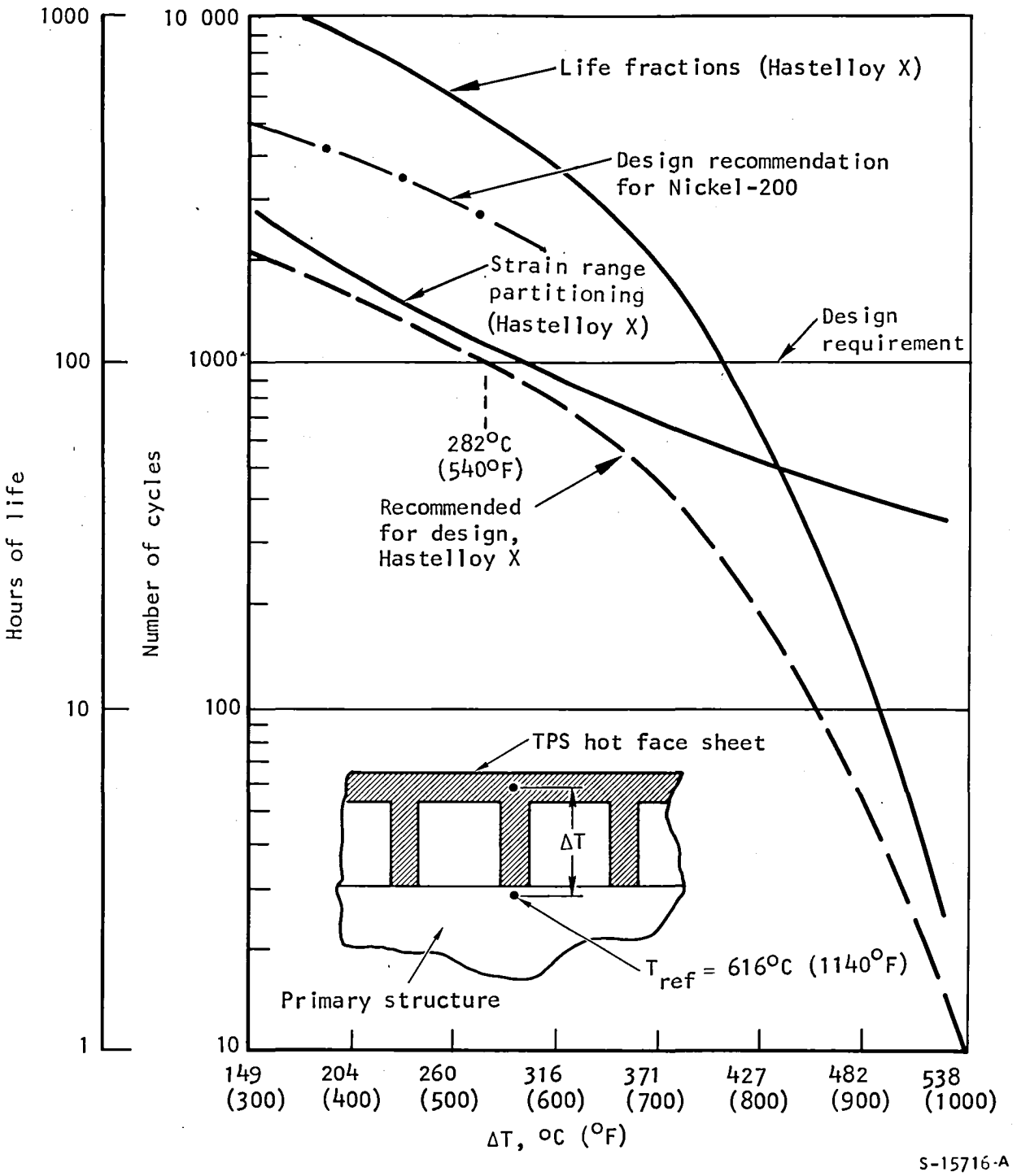

Figure 27.-Cycle life for machined-fin TPS.

In terms of cycle life, the machined fin is superior to the formed-fin structure, even though the amount of plastic strain is greater for the machined fin at temperature differences less than 444°C (800°F) (see fig. 25). The formed-fin structure cycle life is degraded because of two factors. First, the ultimate tensile strength and ductility, important factors in the cycle life equation, are degraded by about 15 percent to account for brazing adjacent to the critical section (TPS hot face sheet). Second, there is a greater proportion of creep damage in the overall cycle with the formed fin. The relationship between creep and fatigue damage fractions is especially significant in the strainrange partitioning analysis.

Fatigue life for a Nickel-200 machined-fin structure was estimated by assuming that the strain versus ΔT behavior was similar to that predicted for Hastelloy X. The strain was adjusted, however, to reflect the difference in Young's modulus. The estimated life is shown in fig. 27 for the temperature range where the estimate is most valid.

Performance summary.--Final selections and estimated performance for the TPS are presented in Table 8 and fig. 28. The following criteria were used: (1) overall coolant pressure drop including any shunt circuits must be less than 1.38 MPa (200 psi); (2) Hastelloy X material except where in-depth ΔT exceeds 222°C (400°F); (3) Nickel-200 material in high heat flux areas where Hastelloy X is not suitable; and (4) maximum TPS face sheet temperature less than 1144 K (2060°R) for Hastelloy X and 1060 K (1910°R) for Nickel-200.

The cyclic life given for the channel structures is in accordance with the recommended design curves in fig. 27. For the Nickel-200 pin-fin structure, as used in the strut, the cycle life was computed as follows: (1) a two-dimensional finite element model of the contoured cross-section was constructed and the strain concentration factor determined; (2) the creep strain was computed assuming that the stress would be fully relaxed during the cycle; and (3) the cycle life was determined using the strainrange partitioning technique.

For external surface cooling, TPS passage geometry is not critical. Formed or machined fins, spaced circular tubes, or D-tubes are all feasible. A machined channel is recommended because of greater structural rigidity, low temperature gradients, and compatibility with the other TPS geometries.

Leading Edges

Two basic cooling options shown in fig. 29 were considered: impingement, direct and indirect; and parallel-flow concepts. Impingement can be directed parallel to the hot gas flow or normal to the sweep line. With indirect impingement, the flow turns nearly 180 deg (less the wedge angle), thus producing a near-impingement cooling effect.

In parallel-flow cooling, the coolant flows in a channel just behind and parallel to the leading edge, as shown in fig. 29. The inherent disadvantage of this basic concept is that the coolant heat transfer coefficient is lower than with impingement, pressure drop is higher, and the flow routing is not compatible with the longitudinal flow routing of the engine panels.

TABLE 8.-TPS PERFORMANCE

Flow circuit	Configuration	Material	Cooling jacket in-depth temperature difference, K (°R)	Maximum skin temperature, K (°R)	Total ΔP, MPa (psi)	Cycle life
Cowl, forward	Channel, 0.64 mm deep	Nickel	169 (305)	423 (761)	0.76 (110)	5000 +
Cowl, aft*	Channel, 0.64 mm deep	Hastelloy X	202 (363)	1102 (1983)	1.07 (155)	1450
Side, forward	Channel, 0.64 mm deep	Nickel	135 (243)	685 (1233)	0.70 (101)	10,000 +
Side, aft	Channel, 0.64 mm deep	Hastelloy X	178 (320)	1078 (1940)	1.24 (180)	1820
Top, forward	Channel, 0.64 mm deep	Hastelloy X	146 (263)	608 (1094)	0.35 (51)	5000 +
Top, aft	Channel, 0.64 mm deep	Hastelloy X	119 (215)	1019 (1835)	0.65 (94)	5000 +
Strut, center	Pin-fin, 1.0 mm dia by 0.64 mm deep	Nickel	167 (300)	1011 (1820)	0.33 (48)	2500 +
Strut, side	Pin-fin, 1.0 mm dia by 0.64 mm deep	Nickel	138 (249)	1038 (1869)	0.79 (114)	4000 +

*External cowl and nozzle portions of the topwall and internal cowl utilize a 1.27-mm-deep channel surface.

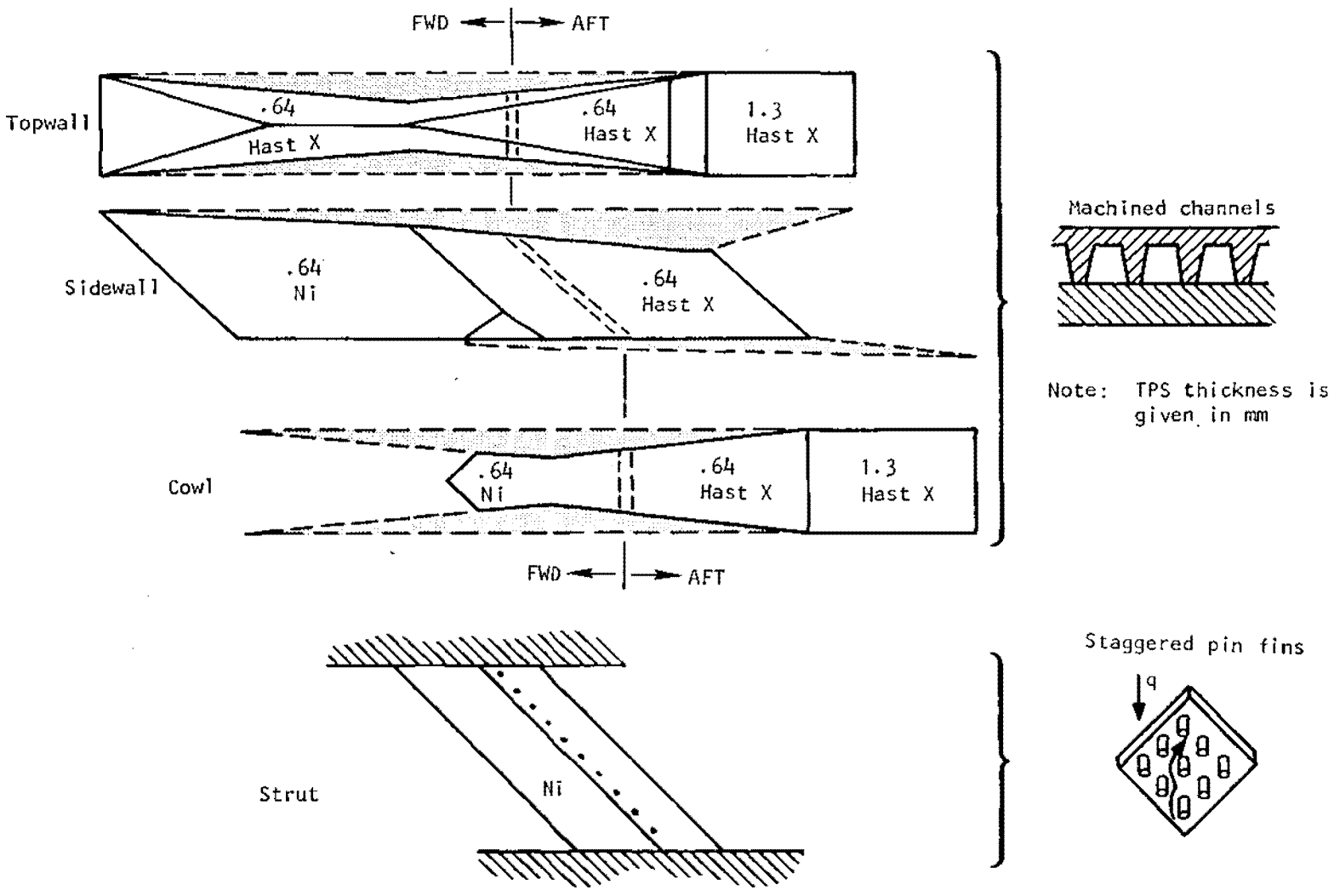

Figure 28.-TPS configuration.

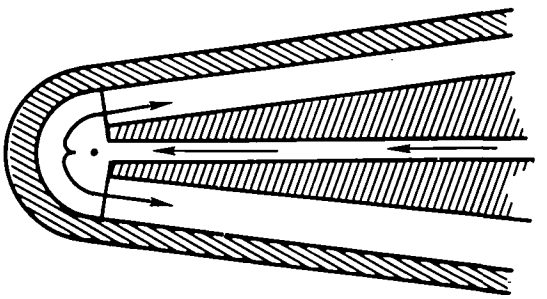

a. Direct impingement

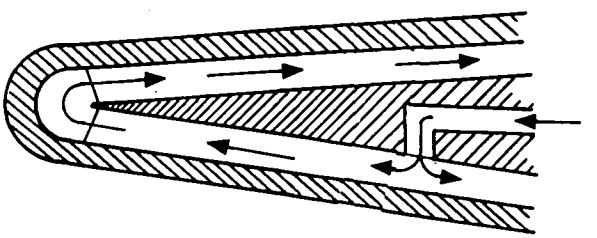

b. Indirect impingement

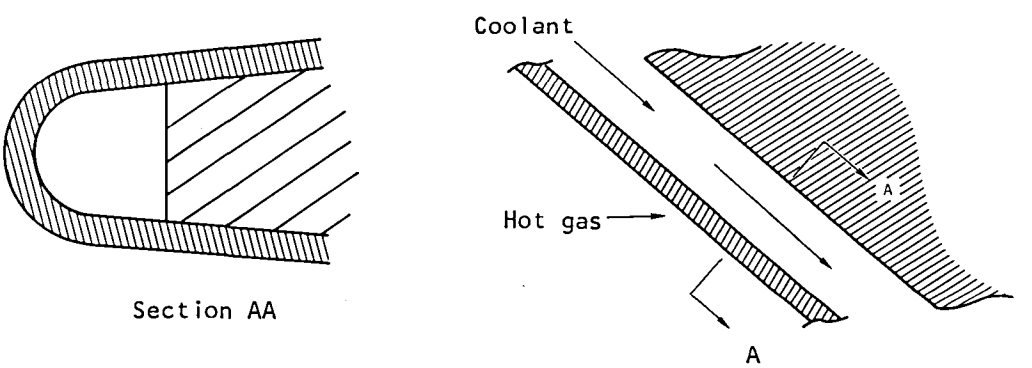

c. Parallel flow

S-15981-A

Figure 29.-Leading edge cooling options.

Flow route options.--Inlet coolant flow can be split with only a portion of the flow directed to the leading edge. The leading edge flow is subsequently joined with the main flow stream. This scheme is sometimes necessary because of pressure drop considerations. It was verified that the total coolant flow for a particular route could be flowed through the leading edge with reasonable pressure drop. This route is preferred to obtain maximum possible cooling.

Flow routing and control considerations favor a common leading edge assembly for adjacent sidewall panels. This concept is best for leading edge life and was used for this analysis.

For the sidewalls and struts, direct impingement cooling is inherently better because the coolant flow is about twice that available with indirect impingement cooling. For the cowl, ducting simplicity in the basic flow route, wherein the flow is first through the external surface, favors indirect impingement.

The cowl apex is a unique cooling point because it is the intersection of two swept leading edges. As noted in Design Conditions, the local heat flux can be especially high at the apex. Direct or indirect impingement cooling of the cowl with the flow parallel to the hot gas flow is feasible. The apex cooling rate can be augmented by using a separate tube to flow coolant directly at the apex.

Geometric constraints.--To accommodate direct impingement concepts, a minimum leading edge radius of 1.3 to 1.5 mm (0.050 to 0.060 in.) is required. This limitation is illustrated below using the sidewall common leading edge as an example (cross-section parallel to gas flow).

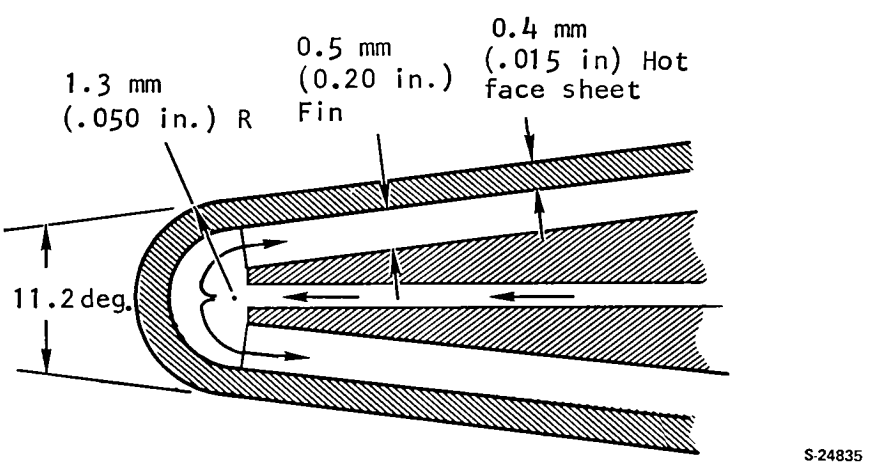

Figure 30.-Leading edge radius for direct impingement concept.

A sharper leading edge radius is possible with indirect impingement as illustrated below for the sidewall common leading edge (cross-section parallel to hot gas flow). Because of the small wedge angle, a large unsupported area results and this configuration is not structurally tenable. Hence, a 1.3-mm (0.050-in.) leading edge radius was used for evaluation of all cooling concepts. The larger radius also reduces the heat flux, although there is an increase in drag.

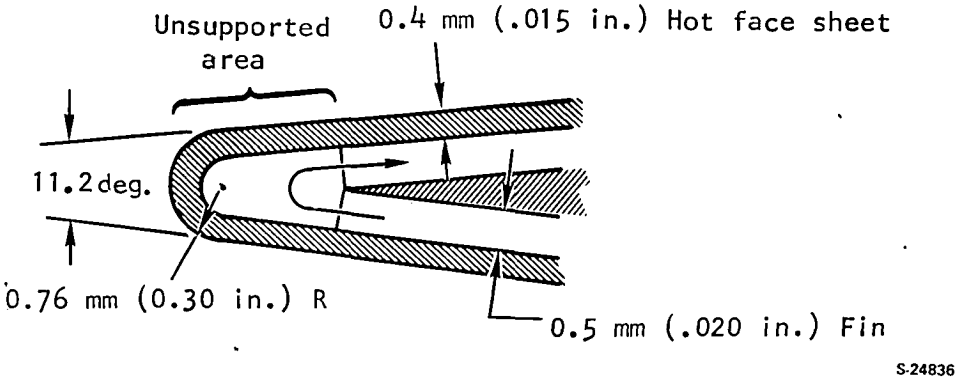

Figure 31.-Leading edge radius for indirect impingement concept.

Heat transfer performance.--Typical temperature gradients around the sidewall and side strut leading edges are shown in fig. 32. Metal temperatures are for 0.38-mm (0.015-in.)-thick Hastelloy X material. Performance with direct or indirect impingement cooling is similar except for the first 2.5 mm (0.1 in.) of length. Results are summarized in Table 9.

The temperature difference across the leading edge is not directly proportional to the heat flux. This results because: (1) two-dimensional heat transfer conduction paths are dependent on the hydrogen flow path, and (2) the resulting difference in temperature level around the structure affects the material thermal conductivity, and hence the temperature gradient.

Direct impingement normal to the sweep line gives the lowest temperatures except for the cowl and cowl apex, where indirect impingement is best. The sidewall, cowl, and side strut leading edge temperatures appear to be acceptable, although temperature differences are high. Performance at the cowl apex is unacceptable with Hastelloy X. Nickel-200 was therefore considered for use here and to increase the cycle life of other leading edges.

The parallel flow concept was checked for the sidewall leading edge with a 1.3-mm (0.050-in.)-radius leading edge. With a flow of 0.90 g/sec (0.002 lb/sec) (total flow for the sidewall route is 36.3 g/sec (0.080 lb/sec)), the outer surface reached 1389 K (2500°R) and the flow choked before the outlet was reached. It was concluded that parallel flow concepts are unacceptable for this application.

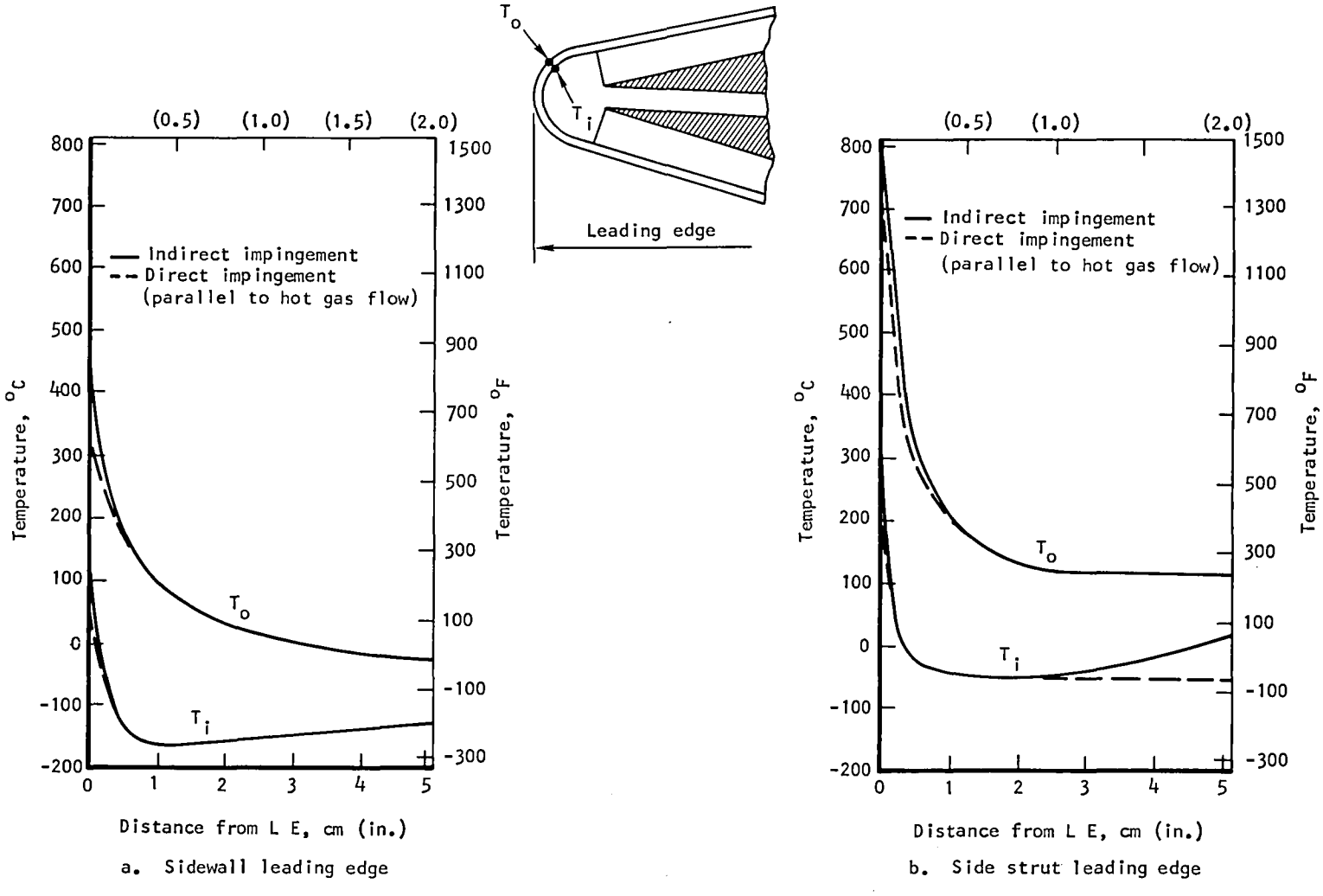

Figure 32.-Typical temperature gradients around sidewall and side strut leading edges.

TABLE 9.-LEADING EDGE THERMAL PERFORMANCE, HASTELLOY X MATERIAL

Leading edge	Heat flux, MW/m^2 (Btu/s-ft^2)	Indirect impingement			Direct impingement					
					Parallel to hot gas flow			Normal to sweep line		
		T_{wo}, K (°R)	T_{wi}, K (°R)	ΔT_w, K (°R)	T_{wo}, K (°R)	T_{wi}, K (°R)	ΔT_w, K (°R)	T_{wo}, K (°R)	T_{wi}, K (°R)	ΔT_w K (°R)
Sidewall	10.61 (935)	758 (1365)	464 (835)	294 (530)	587 (1057)	313 (564)	274 (493)	560 (1008)	286 (515)	274 (493)
Cowl	14.36 (1266)	582 (1048)	211 (380)	371 (668)	681 (1226)	310 (558)	371 (668)	- -	- -	- -
Cowl apex	45.84 (4042)	1364 (2456)	440 (792)	924 (1664)	- -	- -	- -	1494 (2690)	639 (1150)	855 (1540)
Center strut	20.25 (1792)	1261 (2270)	835 (1503)	426 (767)	1125 (2025)	599 (1079)	526 (946)	1052 (1893)	527 (948)	525 (945)
Side strut	15.04 (1331)	1037 (1867)	657 (1165)	390 (702)	901 (1621)	511 (919)	390 (702)	840 (1512)	394 (710)	446 (802)

Note: Temperatures are for conditions at the stagnation line. Heat fluxes are shown for T_{wo} = 833 K (1500°R)

Cycle life analysis.--The estimated leading edge cycle life is shown in Table 10. The analysis used the strainrange partitioning technique with a safety factor of 4. Typical material properties and a strain concentration factor of 2.0 were specified. For Hastelloy X material, the temperature data presented in Table 9 were used directly. For Nickel-200 material, the data in Table 9 were ratioed by the thermal conductivities to estimate the operating temperatures.

TABLE 10.-LEADING EDGE CYCLE LIFE

Location	Impingement cooling mode	Cycle life with candidate materials	
		Hastelloy X	Nickel-200
Sidewall	Direct	2800	10,000
	Indirect	500	-
Cowl	Indirect	1000	16,000
Cowl apex	Indirect	40	1400
Side strut	Direct	400	2600
	Indirect	300	-
Center strut	Direct	-	-
	Indirect	150	1700

These results lead to the following conclusions:

(a) Cycle life requirements can be met by using Nickel-200 material for all leading edges, including the cowl apex.

(b) Direct impingement cooling should be used for the sidewalls and struts because it produces superior cycle life.

Although Nickel-200 is the recommended material, its creep strength is low. The selection of Nickel-200 is based on the use of general LCF correlations (refs. 14, 19, and 20). To confirm this selection, both detailed mathematical modeling and experimental evaluation of the long-term behavior of the leading edge structure with combined creep and fatigue loading are required. Consideration must also be given to the degradation of material properties in the braze-affected zone. Relevant basic experimental data on Nickel-200 is being obtained under NASA Contract NAS1-14180.

Cycle life at the cowl apex is marginal. A supplementary cooling circuit can be utilized to impinge a jet of cold hydrogen directly on the apex. Another option is to blunt the apex in the cowl plane, as shown in fig. 33.

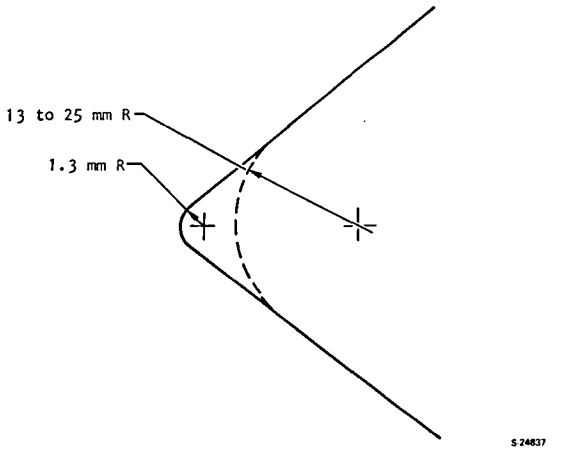

Figure 33.-Cowl apex in the cowl plane.

Blunting eliminates the 1.3-mm (0.050-in.) hemispherical radius, thereby reducing the stagnation heating from three-dimensional to two-dimensional with a corresponding 25 percent reduction in heat input. By blunting the radius to 13 to 25 mm (0.5 to 1.0 in.) and without any supplementary cooling, the cowl apex cycle life can be increased to greater than 5000 cycles.

Because of the uncertainty of the inlet shock structure and the heat flux intensity, the recommended approach is to blunt the apex and to use supplementary cooling.

Fuel Injection Struts

Hydrogen manifolding design options.--The fuel and coolant can be routed through the struts either by separate lines within the strut structure or by using the strut structure itself to contain the hydrogen. The two concepts are shown in fig. 34.

The integral manifold approach was evaluated in ref. 4 and was found to be effective. The key feature in the design was the use of a thermal buffer (a layer of stagnant hydrogen) that reduces the internal convection heating from the hot hydrogen in the manifolds. The resulting thermal stresses were reasonable.

An alternate approach with tubular manifolds was also considered for this study. It was believed that by using separate lines to contain the fuel and coolant, the overall plumbing arrangement would be simplified and the thermal stresses minimized.

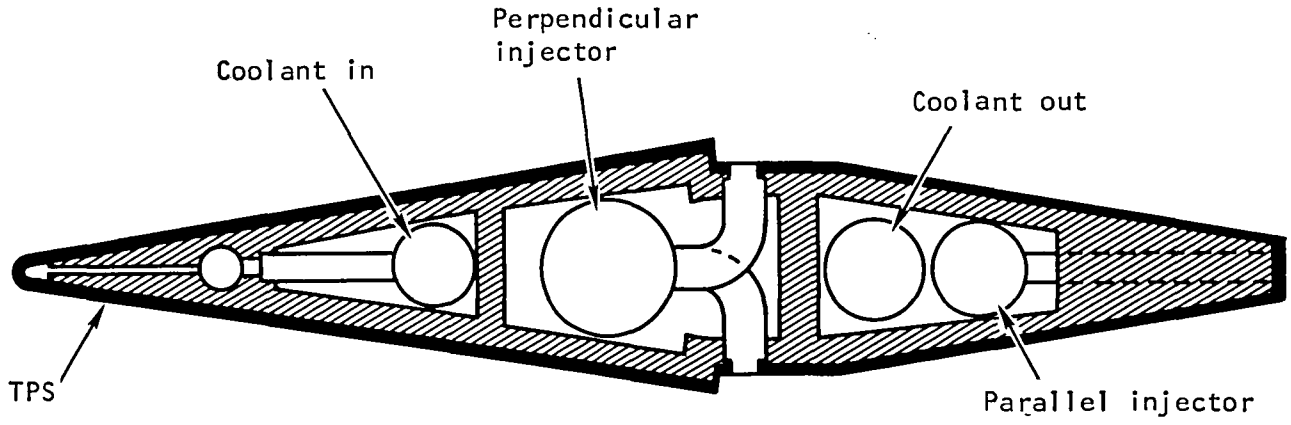

a. Tubular Manifold

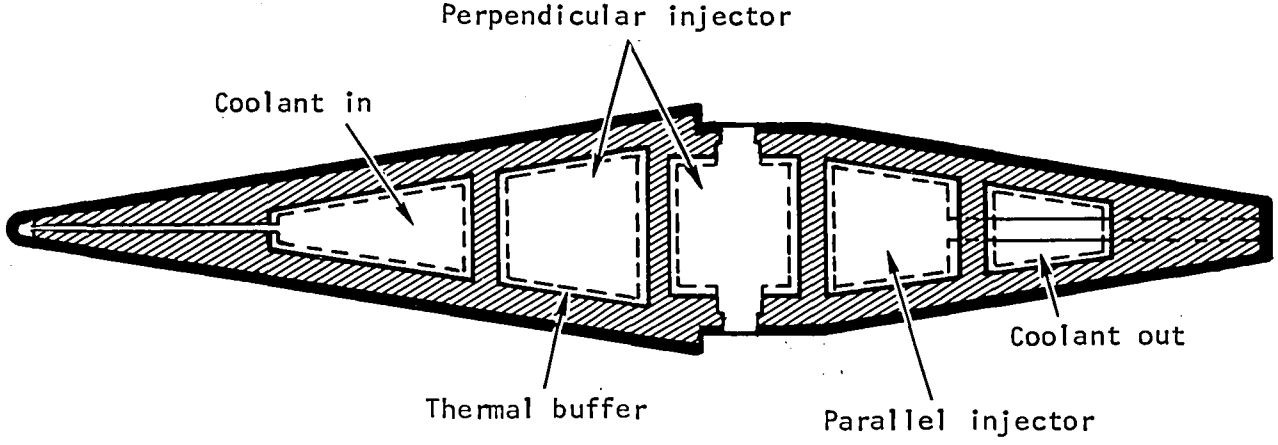

b. Integral Manifold

S-7511-B

Figure 34.-Center strut fuel/coolant passages concepts.

Manifold design conditions--Maximum flow conditions are shown in fig. 15. The inlet and outlet temperatures shown for Condition H in fig. 15 are assumed to be identical for all flight conditions.

For the perpendicular injectors, maximum fuel flow occurs at the Mach 10 maximum thermal loading condition and is 1.01 kg/sec (2.22 lb/sec). This flow is equally divided between the three struts. This is a transient operating condition with a fuel equivalence ratio of 1.5. Fuel flows at steady-state cruise condition are less. Moreover, it is at cruise condition that ideal flow distribution is most essential. The maximum flow condition was selected for preliminary design, however, to ensure that reasonable flow distribution could be achieved at all operating conditions.

The estimated internal module aerodynamic heat load at Condition H is about 6.85 MW (6500 Btu/sec). Assuming no airframe cooling requirements for the 1.01 kg/sec hydrogen flow, the mixed mean temperature of the coolant outlet hydrogen (889 K, 1600°R) and the hydrogen directly from the tank is 507 K (913°R). This was increased to 611 K (1100°R) to account for a 20-percent uncertainty in the aerodynamic heating. The minimum fuel manifold pressure is 4.82 MPa (700 psia).

For the parallel (supersonic) fuel injectors, the maximum flow occurs at the Mach 5.1 Condition G and is 0.445 kg/sec (0.981 lb/sec). Fuel flow per strut is 0.148 kg/sec (0.327 lb/sec). Hydrogen fuel inlet conditions of 4.82 MPa (700 psia) and 611 K (1100°R) were selected.

Tubular manifold design--Initial estimates of the required flow area of the tubular manifolds compared with the available strut cross-section indicated some severe conflicts. To reduce the flow velocity head at the fuel manifold inlets to a value consistent with acceptable flow distribution, it was necessary to flow hydrogen from both ends of the strut. A summary of manifold sizes and performance is presented in Table 11.

Manifold routing within the limited space available in the cowl was found to be a complex, difficult design problem. It was concluded that the tubular approach did not offer any design advantages. Therefore, the integral manifold design was selected and this design was utilized in subsequent analyses.

Integral manifold design.--A detailed preliminary design analysis of the hydrogen flow distribution and pressure drop in the fuel injector manifolds, TPS coolant manifolds, and the TPS in the center and side struts was conducted. In addition, the fuel injector nozzles were sized, and heat transfer coefficients in all flow passages were computed. The analysis was based on the integral manifold design concept, with both inlet and outlet plumbing ports located at the top of the struts.

Configuration of strut flow passages and injection nozzles: Strut assembly Drawing 192223 (see Engine Layout Design section) depicts the arrangement of the fuel injector manifolds, TPS coolant manifolds, and fuel injection nozzles,

TABLE 11.-TUBULAR MANIFOLD PERFORMANCE

	Coolant inlet	Perpendicular injectors	Parallel injectors	Coolant outlet
Tube pattern at topwall surface			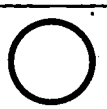	
Tube pattern at cowl surface		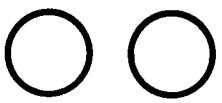	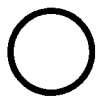	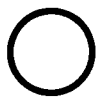
Tube sizes	1 at 8 mm OD by 0.25 mm wall (1 at 5/16 OD by 0.010 in. wall)	4 at 13 mm OD by 0.5 mm wall (4 at 1/2 OD by 0.020 in. wall)	2 at 13 mm OD by 0.5 mm wall (2 at 1/2 OD by 0.020 in. wall)	2 at 13 mm OD by 0.5 mm wall (2 at 1/2 OD by 0.020 in. wall)
Flow area, sq cm (sq in.)	0.434 (0.0672)	4.29 (0.6648)	2.14 (0.3324)	2.14 (0.3324)
H_2 flow rate per strut, kg/sec (lb/sec)	0.0454 (0.100)	0.336 (0.740)	0.148 (0.327)	0.0454 (0.100)
H_2 total pressure, MPa (psia)	6.89 (1000)	4.83 (700)	4.83 (700)	5.17 (750)
H_2 total temperature, K (°R)	56 (100)	611 (1100)	611 (1100)	889 (1600)
Mach number	0.061	0.220	0.196	0.067
Velocity head, kPa (psi)	17.9 (2.6)	158 (22.9)	126 (18.3)	15.9 (2.3)

A-3648

Σ Flow area through strut top = 4.88 sq cm (0.757 sq in.)

together with cross-sectional details of the strut manifolds, leading edges, and trailing edges. The drawing shows two strut manifold configurations. Both of them are feasible, but only the preferred configuration (strut configuration No. 2) was analyzed in detail. Configuration No. 2 was selected because the feed tubes to the parallel injection nozzles in both struts and the aft perpendicular injection nozzles in the side struts are not only shorter, but pass through only one rib.

Additional cross-sectional details of the strut manifolds are shown in figs. 35 and 36. Fig. 35 shows the side strut and an expanded view of the TPS wall structure; fig. 36 shows the center strut. A sketch of the TPS coolant flow path in the pin-fin TPS passages is presented in fig. 37. Flow dividers are used to minimize flow skewing in the pin-fin surface as a result of manifold pressure gradients.

Design conditions: The design condition total flow for the perpendicular fuel injection manifolds and nozzles is 2.220 lb/sec, which corresponds to Condition H (2-g maneuver at Mach 10 and combustion equivalence ratio of 1.5). The design condition total flow for the parallel fuel injection manifolds and nozzles is 0.981 lb/sec, which corresponds to Condition G (2-g maneuver at Mach 5.1 and a combustion equivalence ratio of 1.0).

A summary of the design point conditions upon which the flow distribution analysis of the fuel injection manifolds and nozzles was based is presented in Table 12.

The thermal protection system (TPS) design conditions are summarized in Table 13. The flow distribution in the TPS manifolds was based on a flow of 0.10 lb/sec to each strut at inlet conditions of 6.894 MPa (1000 psia) and 55.6 K (100°R). The strut heat flux distribution, which was needed to determine the temperature distribution in the TPS, was obtained from fig. 38.

Method of Analysis: The analysis was performed with an AiResearch computer program that was developed using the experimental and analytical work of a number of investigators as a basis (see refs. 21 through 27). The program analyzes compressible or incompressible flow with friction for both one-dimensional and two-dimensional mathematical modes.

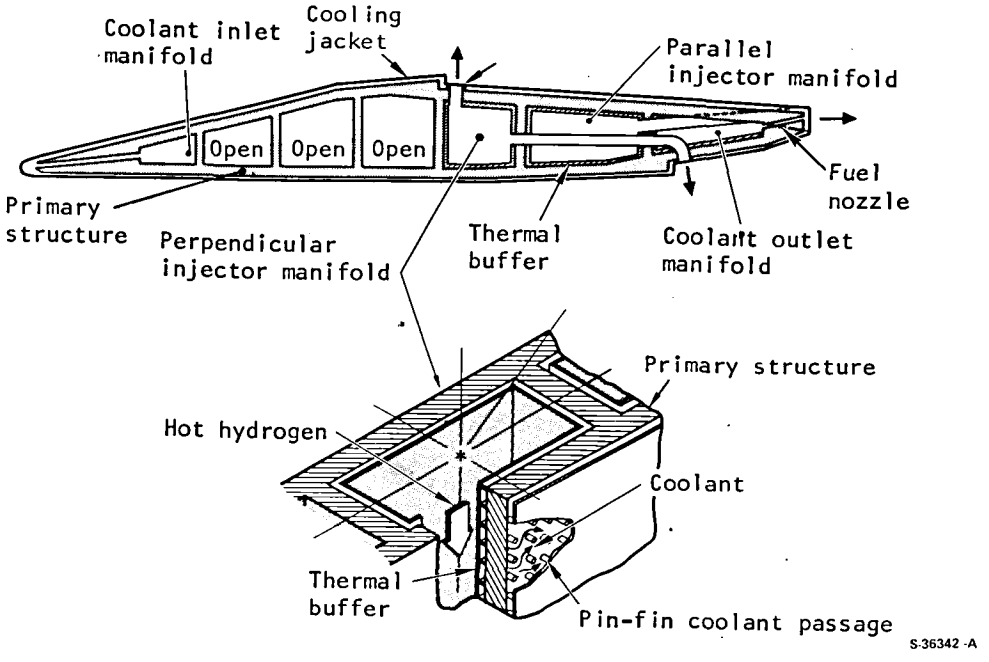

Figure 35.-Cross-sectional sketch of side strut and TPS wall structure.

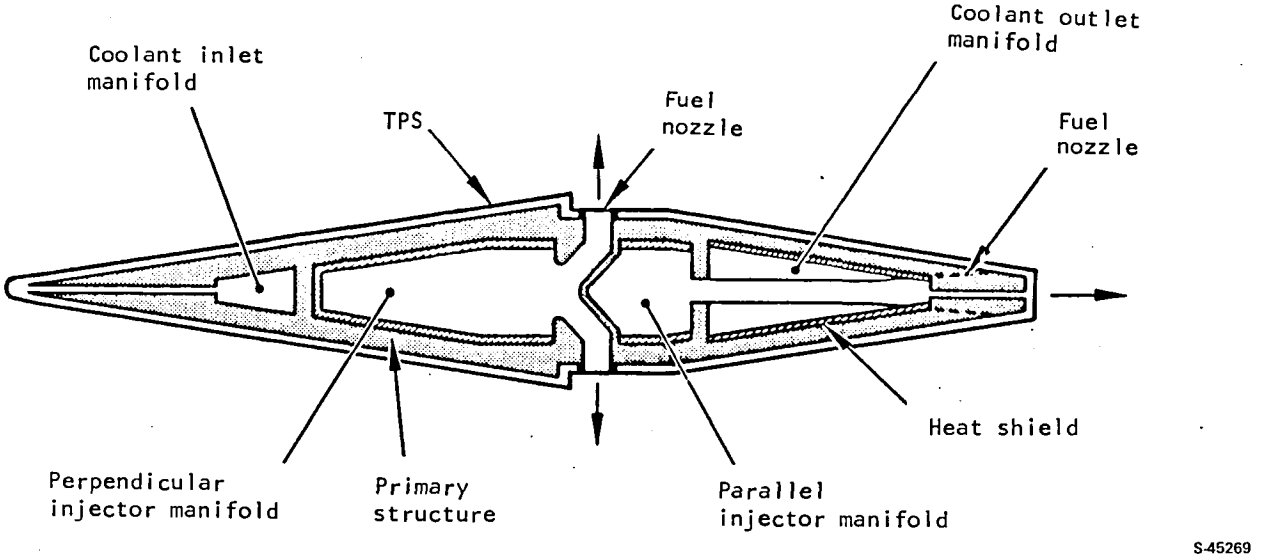

Figure 36.-Cross-sectional sketch of center strut.

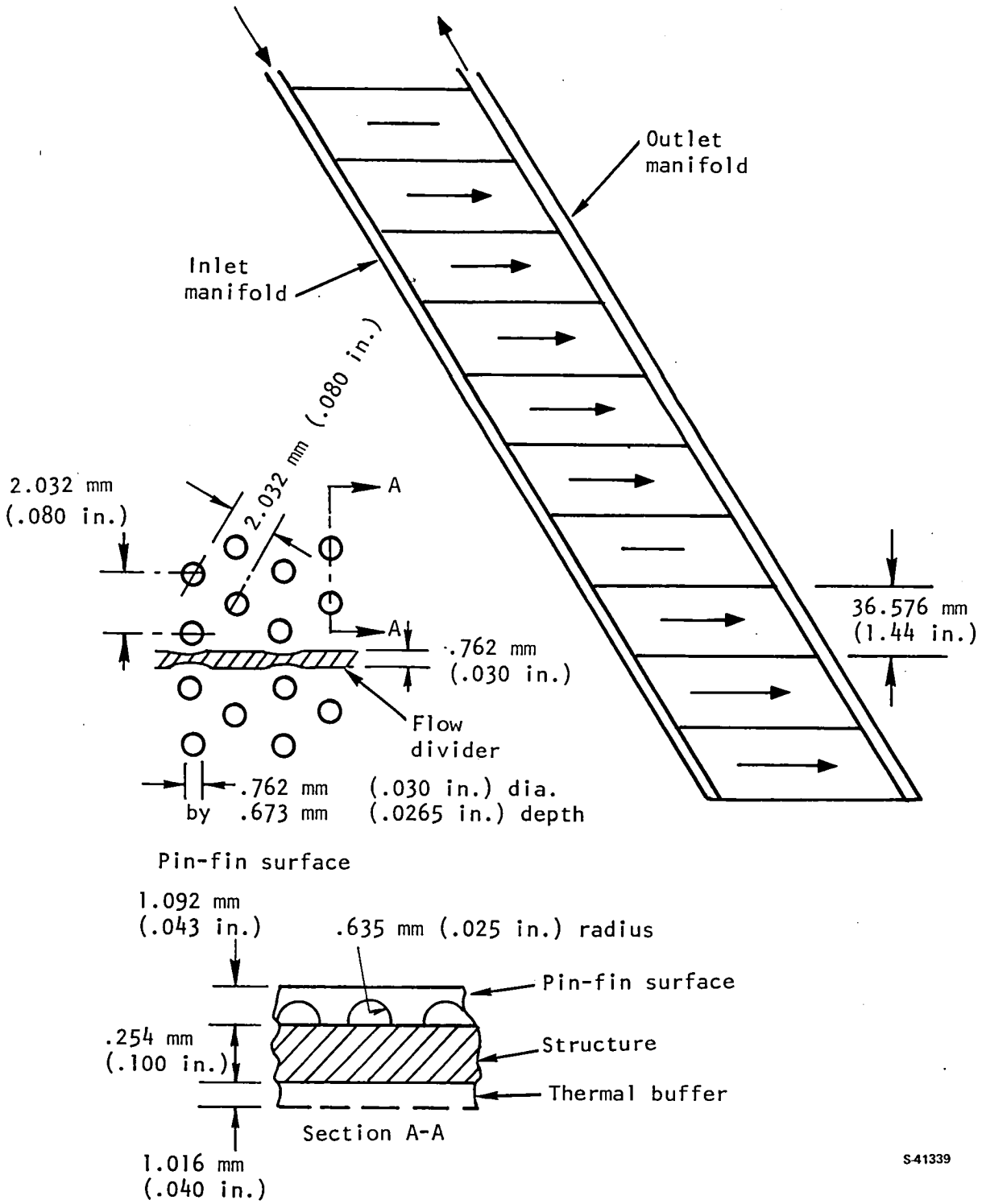

Figure 37.-TPS coolant flow path.

TABLE 12.-STRUT FUEL INJECTION MANIFOLD AND NOZZLE DESIGN CONDITIONS

Strut		Center Strut		Side Struts	
Injection manifold		Perpendicular	Parallel	Perpendicular	Parallel
Manifold inlet conditions	Pressure, MPa (psia)	4.826 (700)	4.826 (700)	4.826 (700)	4.826 (700)
	Temperature, K (°R)	611 (1100)	611 (1100)	611 (1100)	611 (1100)
	Flow rate, g/sec (lb/sec)	335.658 (0.740)	148.325 (0.327)	335.658 (0.740)	148.325 (0.327)
Number of nozzles		20 (10 each side)	10 (at trailing edge)	20 (10 each side)	9 (at trailing edge)
Flow rate per nozzle, g/sec (lb/sec)		16.783 (0.0370)	14.833 (0.0327)	16,783 0.0370)	16.479 (0.03633)

Notes: (1) Perpendicular injection nozzles are sonic; (2) parallel injection nozzles are supersonic with exit to throat area ratio of 3; (3) see drawing 192223 presented in the Engine Layout Design section for location of nozzles

TABLE 13.-STRUT COOLANT MANIFOLD AND TPS DESIGN CONDITIONS

Strut		Center strut	Side strut
Manifold inlet conditions	Inlet Pressure, MPa (psia)	6.895 (1000)	6.895 (1000)
	Temperature, K (°R)	55.6 (100)	55.6 (100)
	Inlet flow rate, g/sec (lb/sec)	45.36 (.10)	45.36 (.10
Outlet manifold conditions	Temperature, K (°R)	889 (1600)	889 (1600)
	Outlet flow rate, g/sec (lb/sec)	45.36 (.10)	45.36 (.10)
Flow to TPS, g/sec (lb/sec)	Center passage side	22.68 (.05)	26.51 (.05844)
	Side wall passage side	22.68 (.05)	18.85 (.04156)

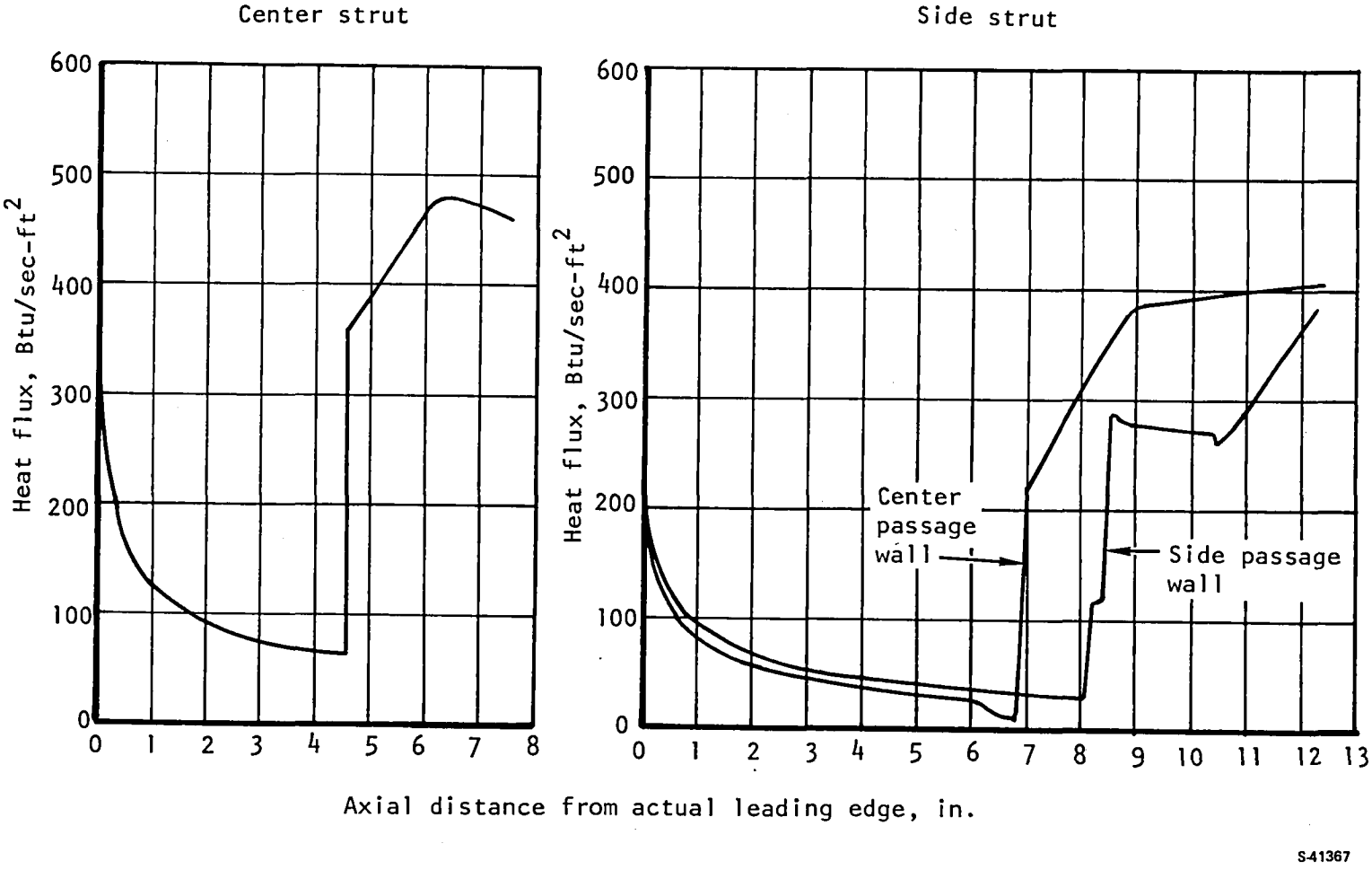

Figure 38.-Strut heat flux distribution.

The flow model consists of an inlet header (or manifold) and an outlet header with a core connecting the two headers, as depicted in fig. 39. The analysis is based on a finite element (100 elements) solution to the equations of motion. Each header is considered as a separate entity with a specified flow distribution as an input. Inlet header turning (or branching) losses are accounted for in the core, whereas outlet header turning losses are accounted for in the outlet header. The output is a static pressure distribution based on the assumed flow distribution input. An iterative procedure based on the core pressure loss characteristics is utilized to determine the actual flow distribution.

The strut perpendicular and parallel injector manifolds are a special case. Each core is a series of choked nozzles that respond to the total pressure in the inlet manifold. There is no outlet manifold; the discharge is to the air stream.

In the case of the TPS coolant flow through the coolant passages of the struts, the core is the coolant passage under the skin. A U-flow heat exchanger/manifold problem exists with flow from the inlet header into the outer header. The flow through the core is a function of the static pressure difference between the inlet and outlet headers.

The procedure used for computing the manifold pressure distribution for one-dimensional incompressible flow and discrete withdrawal of fuel is as follows. Assume uniform withdrawal (equal flow out of each nozzle). This is reasonable because all of the nozzles are choked, and the total pressure is quite high (about 750 psia). Referring to fig. 40, which is a summary of the equations for determining manifold pressure distribution for discrete withdrawal, the static pressure rise across the nozzle port is

$$\left(P_2 - P_1\right) = \frac{\dot{W}_n}{g_c \rho A^2}\left(\dot{W}_1 - \frac{\dot{W}_n}{2}\right)$$

where

P = manifold pressure

A = manifold flow area

ρ = fluid density in the manifold

$\dot{W}$ = fluid weight flow rate in the manifold

$\dot{W}_n$ = weight flow rate out the nozzle ($\dot{W}_1 - \dot{W}_2$)

g_c = proportionality factor in Newton's second law

Subscripts 1 and 2 refer to positions in the manifold just upstream and downstream of the nozzle port.

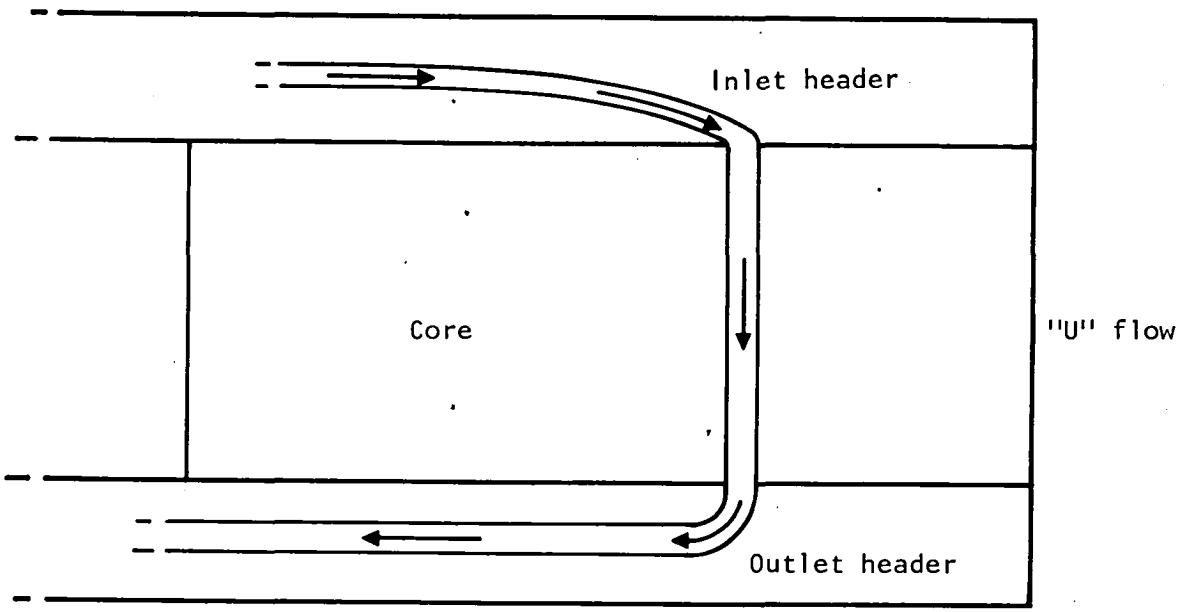

Figure 39.- Header flow model.

S-17496

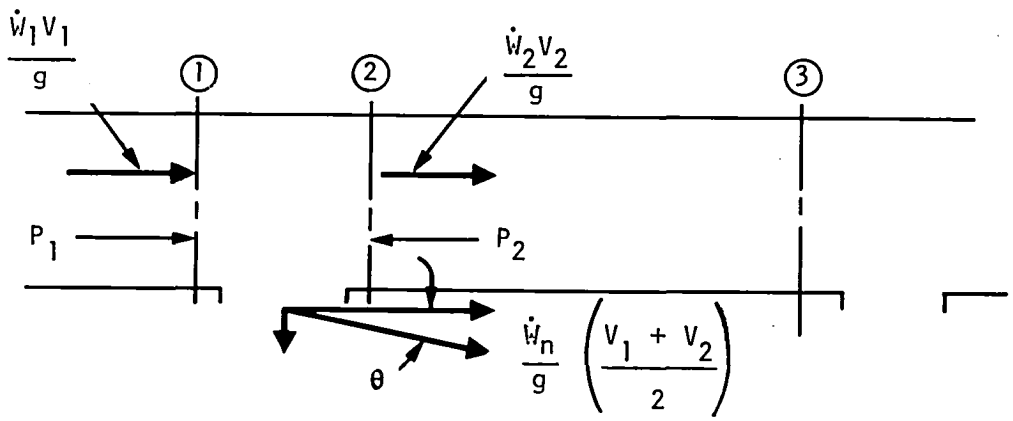

Static pressure rise: $(P_2 - P_1) = \frac{\dot{W}_n}{g\rho A^2}\left(\dot{W}_1 - \frac{\dot{W}_n}{2}\right)$

Friction pressure drop: $P_2 - P_3 = \left(\frac{\dot{W}_2}{A}\right)^2 \frac{fL}{2g\rho r}$

Total pressure = static pressure + velocity head, $\frac{(W/A)^2}{2g\rho}$

Turning losses taken in nozzle or outlet duct

S-45982

Figure 40.-Manifold pressure distribution equation for discrete fluid withdrawal.

The frictional pressure drop in the manifold between adjacent nozzle ports is

$$P_2 - P_3 = \left(\frac{\dot{W}_2}{A}\right)^2 \frac{f\ L}{2\ g_c \rho r}$$

where

f = Fanning friction factor for smooth rectangular duct

L = manifold length between ports

r = manifold hydraulic radius (A/p) where p is the wetted perimeter

The manifold total pressure (which is used to size the nozzles) is the static pressure plus the velocity head, $(W/A)^2/2g_c\rho$.

Starting at the inlet of the manifold, and taking $\dot{W}_n = W_{total}/$no. nozzles (same flow to each nozzle), the pressure distribution was determined in a stepwise, port by port manner from the above equations, together with f versus Reynolds number for the hydrogen flow in the manifold.

The computer program analysis for continuous withdrawl does essentially the same analysis except that 100 finite elements were used. Also, the manifold flow friction shear forces were included in the momentum equation.

All fuel injection nozzles were sized at their local inlet total pressures according to the sonic nozzle equation.

$$\frac{W}{A^*} = CP_n\sqrt{\frac{\gamma g_c}{RT_o}\left(\frac{2}{\gamma + 1}\right)^{\frac{\gamma+1}{\gamma-1}}}$$

where

W = flow rate per nozzle

A^* = nozzle choked (M = 1) area = $\frac{\pi}{4} D_n^2$

D_n = nozzle diameter

P_n = nozzle total pressure

γ = ratio of specific heats

R = gas content

T_o = total temperature

g_c = proportionality factor in Newton's second law

c = constant

The nozzle total pressure was computed from

$$P_n = P_m - \Delta P_e - \Delta P_b - \Delta P_f$$

where,

P_m = manifold total pressure

ΔP_e = nozzle entrance turning loss = 1.5 times the velocity head in the manifold

ΔP_b = bend losses inside the nozzle or feed tube = bend loss coefficient times the velocity head in the nozzle or tube (in the center strut perpendicular injector nozzles, the mitre bend loss coefficient was taken as 0.35, and in the side strut aft perpendicular injector feed tube, the loss coefficient was unity.)

ΔP_f = friction pressure loss in the feed tubes, where applicable. Adiabatic, constant area (Fanno line process) flow was assumed.

The nozzle discharge coefficient was taken as 1.0 for the sonic nozzle where all losses are accounted for in the calculation of the nozzle total pressure. In the case of the supersonic nozzles the additional friction in the converging section was accounted for by using a discharge coefficient of 0.95.

In the fuel injection and TPS coolant manifolds, the heat transfer coefficients were computed from:

$$h = \frac{C\ j\ c_p}{Pr^{2/3}}$$

where C = constant

h = heat transfer coefficient

G = mass velocity, $\dot{W}/A$

c_p = fluid specific heat at constant pressure

P_r = fluid Prandtl number

j = Colburn heat transfer modulus

For the Reynolds number involved (all were in the turbulent flow regime), the Colburn modulus for flow in the manifold is approximately

$$j = \frac{.0205}{Re^{0.20}}$$

where

$$Re = \text{Reynolds number } \frac{4rG}{\mu}$$

r = manifold hydraulic radius

μ = fluid viscosity

All fluid properties were obtained from ref. 28.

Summary of Results: A summary of the nozzle sizes for the perpendicular and parallel injector nozzles for the center and side struts is given in figs. 41 through 44. The results include flow rates, manifold total pressure, manifold velocity head, nozzle sizes, arithmetic average of nozzle sizes, and flow maldistribution (with all nozzles having the same average diameter). The flow maldistribution for equal size nozzles is 0.6 percent for the side strut parallel injector nozzles and 5 to 7 percent for all other nozzles.

A plot of the static pressure distribution in the center strut TPS coolant inlet and outlet manifolds is shown in fig. 45. In this case the fluid withdrawal from the inlet manifold is very nearly continuous because of the numerous small diameter channels connecting the manifold to the leading edge. Fluid feed to the outlet manifold is similar, except that the multiple small diameter outlet channels are interrupted by the fuel injector nozzles. The flow through the TPS pin surface is not quite uniform (about 5.7 percent maldistribution) because the pressure drop in the outlet manifold is greater than the corresponding pressure rise in the inlet manifold. The presence of the parallel injector nozzle feed tubes in the coolant outlet manifold can greatly increase the pressure drop and flow maldistribution unless the blocked flow area is reduced by using elliptical or flattened tubes. The TPS outlet pressure distribution curve in fig. 45 is based on the use of an equivalent friction factor equal to the flow friction of a smooth duct plus .015. This was obtained by using an elliptical tube having a minor diameter of about .115 in. (61 percent of the diameter of a round tube).

The pressure and flow variations in the TPS coolant system of the side strut are given in fig. 46. Again, as in the case of the center strut TPS system, the flow in the outlet manifold is partially blocked by the parallel injector feed tube; in addition, the perpendicular injector feed tube also blocks part of the passage. The net effect of such blockage was calculated to be an 11 percent flow variation between the TPS passage closest to the manifold open end, and those closest to the closed end of the manifold. Unlike the center strut approach, use of elliptical tubes does not appear to be required here. However, the outlet manifold flow area could easily be increased by relocation of a bulkhead, thus promoting better flow uniformity.

Graphs of the TPS coolant temperature distributions in the center and side struts versus axial distance from the virtual origin (wedge apex) point are presented in figs. 47 and 48. These temperature distributions were based on the wall heat flux distributions in fig. 38, enthalpy data from ref. 28, and

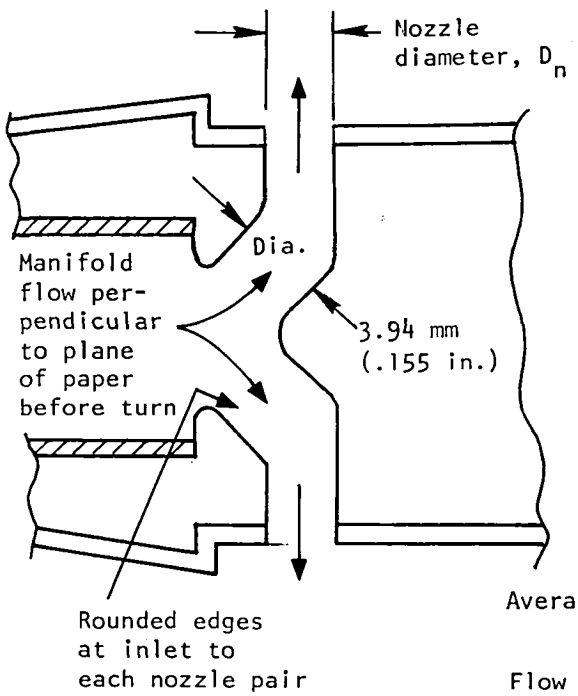

Inlet flow to manifold = .3357 kg/sec (.74 lb/sec)

10 nozzles on each side of strut spaced 6.223 cm (2.45 in.) apart

Flow per nozzle = 6.78 g/sec (.037 lb/sec) at 611 K (1100°R)

Average nozzle diameter = 3.353 mm (.132 in.)

Flow maldistribution if all nozzles have same diameter as average = ±7 percent

Nozzle pair location X/L	Manifold total pressure, P_m		Manifold velocity head, q_m		Sonic nozzle diameter, D_n, for equal flow	
	MPa	psia	MPa	psi	mm	in.
.05	5.266	763.7	.396	57.5	3.472	.1367
.15	5.238	759.7	.308	44.7	3.419	.1346
.25	5.225	757.8	.238	34.5	3.373	.1328
.35	5.215	756.3	.177	25.6	3.338	.1314
.45	5.208	755.3	.127	18.4	3.307	.1302
.55	5.203	754.7	.086	12.5	3.284	.1293
.65	5.199	754.1	.052	7.5	3.264	.1285
.75	5.199	754.0	.026	3.8	3.274	.1289
.85	5.197	753.7	.010	1.5	3.241	.1276
.95	5.195	753.5	.001	.2	3.236	.1274

S-41340

Figure 41.-Summary of center strut perpendicular injector nozzle sizes.

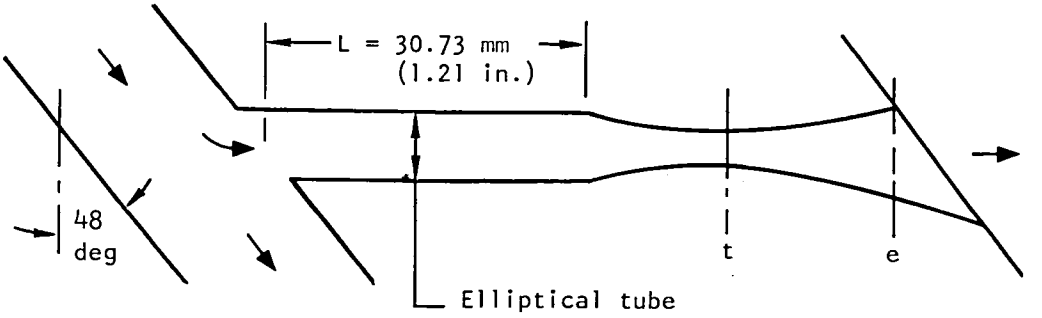

Elliptical tube
minor diameter = 2.921 mm (.115 in.)
major diameter = 7.620 mm (.300 in.)
wall thickness ≈ .254 mm (.010 in.)

10 nozzles spaced 6.223 cm (2.54 in.) apart
Flow per nozzle = 14.83 g/sec (.0327 lb/sec)
at 611 K (1199°R)

Average throat area, A_t = 7.448 mm^2 (.011545 $in.^2$)
Flow maldistribution if all nozzles
have the same area as the average = ±5 percent

Nozzle location	Manifold total pressure, P_m		Manifold velocity head, q_m		Supersonic nozzle areas for equal flow			
					Throat, A_t		Exit, A_e	
X/L	MPa	psia	MPa	psi	mm^2	$in.^2$	mm^2	$in.^2$
.05	5.195	753.5	.341	49.5	7.787	.01207	23.368	.03622
.15	5.177	750.8	.272	39.4	7.658	.01187	22.981	.03562
.25	5.163	748.9	.210	30.5	7.510	.01164	22.529	.03492
.35	5.152	747.3	.157	22.7	7.374	.01143	22.129	.03430
.45	5.144	746.1	.112	16.2	7.310	.01133	22.574	.03499
.55	5.138	745.2	.074	10.8	7.245	.01123	21.735	.03369
.65	5.135	744.7	.046	6.6	7.200	.01116	21.600	.03348
.75	5.131	744.2	.023	3.4	7.155	.01109	21.471	.03328
.85	5.130	744.0	.009	1.3	7.135	.01106	21.406	.03318
.95	5.129	743.9	.001	.2	7.110	.01102	21.329	.03306

S-41343

Figure 42.-Summary of center strut parallel injector nozzle sizes.

Tube number	①	②
Average nozzle diameter, mm (in.)	3.175 (.125)	3.302 (.130)
Flow maldistribution using average diameter	± 6 percent	±6 percent

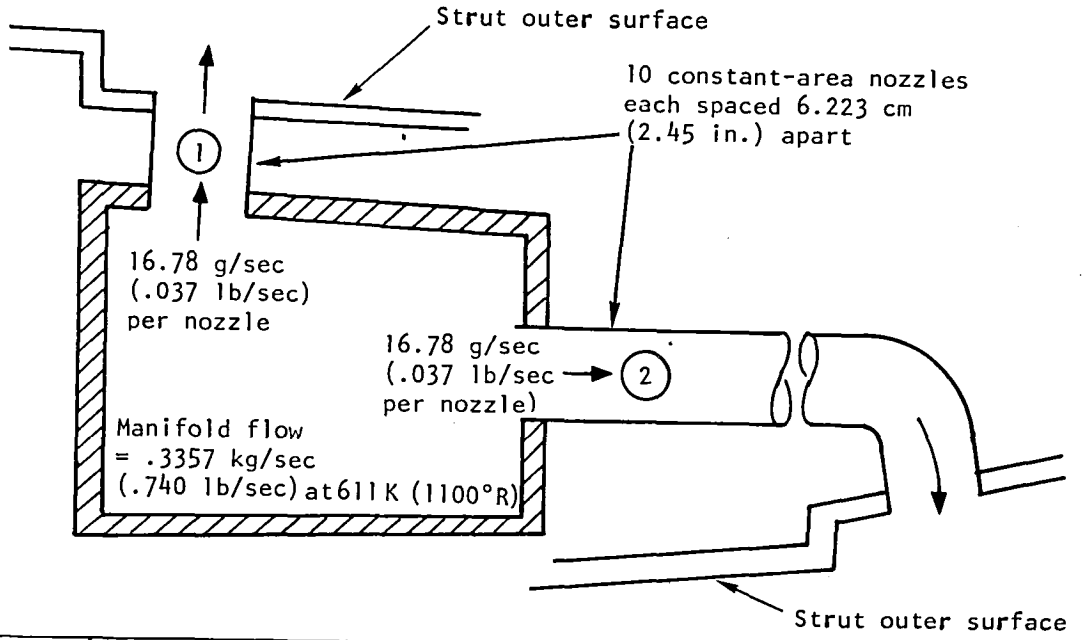

Nozzle location	Manifold total pressure, P_m		Manifold velocity head, q_m		Sonic nozzle diameter, D_n, for equal flow			
					① Center passage wall		② Side passage wall	
X/L	MPa	psia	MPa	psi	mm	in.	mm	in.
.10	5.203	754.6	.389	56.4	3.277	.1290	3.414	.1344
.20	5.195	753.4	.311	45.1	3.241	.1276	3.373	.1328
.30	5.190	752.7	.243	35.2	3.208	.1263	3.340	.1315
.40	5.188	752.5	.183	26.6	3.178	.1251	3.310	.1303
.50	5.189	752.6	.134	19.4	3.155	.1242	3.284	.1293
.60	5.192	753.0	.092	13.3	3.134	.1234	3.264	.1285
.70	5.195	753.4	.059	8.5	3.117	.1227	3.246	.1278
.80	5.199	754.1	.032	4.7	3.104	.1222	3.233	.1273
.90	5.204	754.8	.014	2.1	3.094	.1218	3.223	.1269
1.0	5.208	755.4	.003	.5	3.089	.1216	3.216	.1266

S-41338

Figure 43.- Summary of side strut perpendicular injector nozzle sizes.

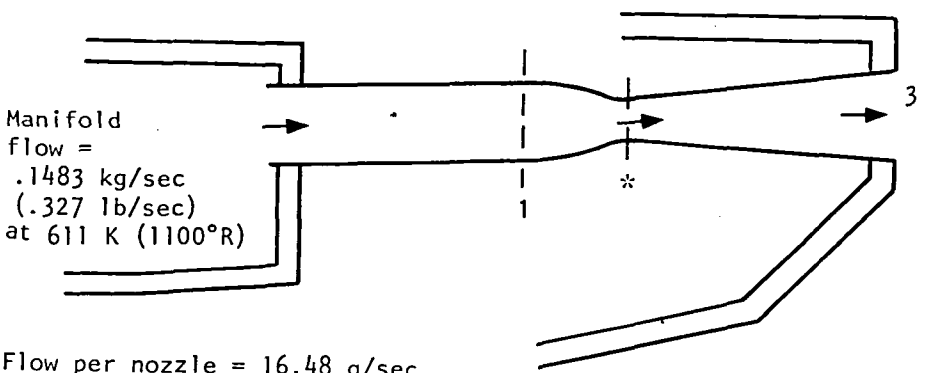

Flow per nozzle = 16.48 g/sec
(.0363 lb/sec)

9 nozzles spaced
6.223 cm (2.45 in.) apart

Maximum flow maldistribution = .6 percent
Tube ID, D_1 = 4.496 mm (.177 in.)
Throat ID, D_* = 3.277 mm (.129 in.) (Same for all nozzles)
Exit ID, D_3 = 5.664 mm (.223 in.)

Nozzle location	Manifold total pressure, P_m		Manifold velocity head, q_m		Nozzle flow, w	
X/L	MPa	psia	MPa	psi	g/sec	lb/sec
.11	4.855	704.1	.045	6.48	16.420	.0362
.22	4.846	702.9	.035	5.12	16.420	.0362
.33	4.839	701.9	.027	3.92	16.466	.0363
.44	4.833	701.0	.020	2.88	16.466	.0363
.56	4.828	700.3	.014	2.00	16.466	.0363
.67	4.824	699.7	.009	1.28	16.511	.0364
.78	4.822	699.3	.005	.72	16.511	.0364
.89	4.820	699.1	.002	.32	16.511	.0364
1.0	4.819	699.0	.001	.08	16.511	.0364

S-41336

Figure 44.- Summary of side strut parallel injector nozzle sizes.

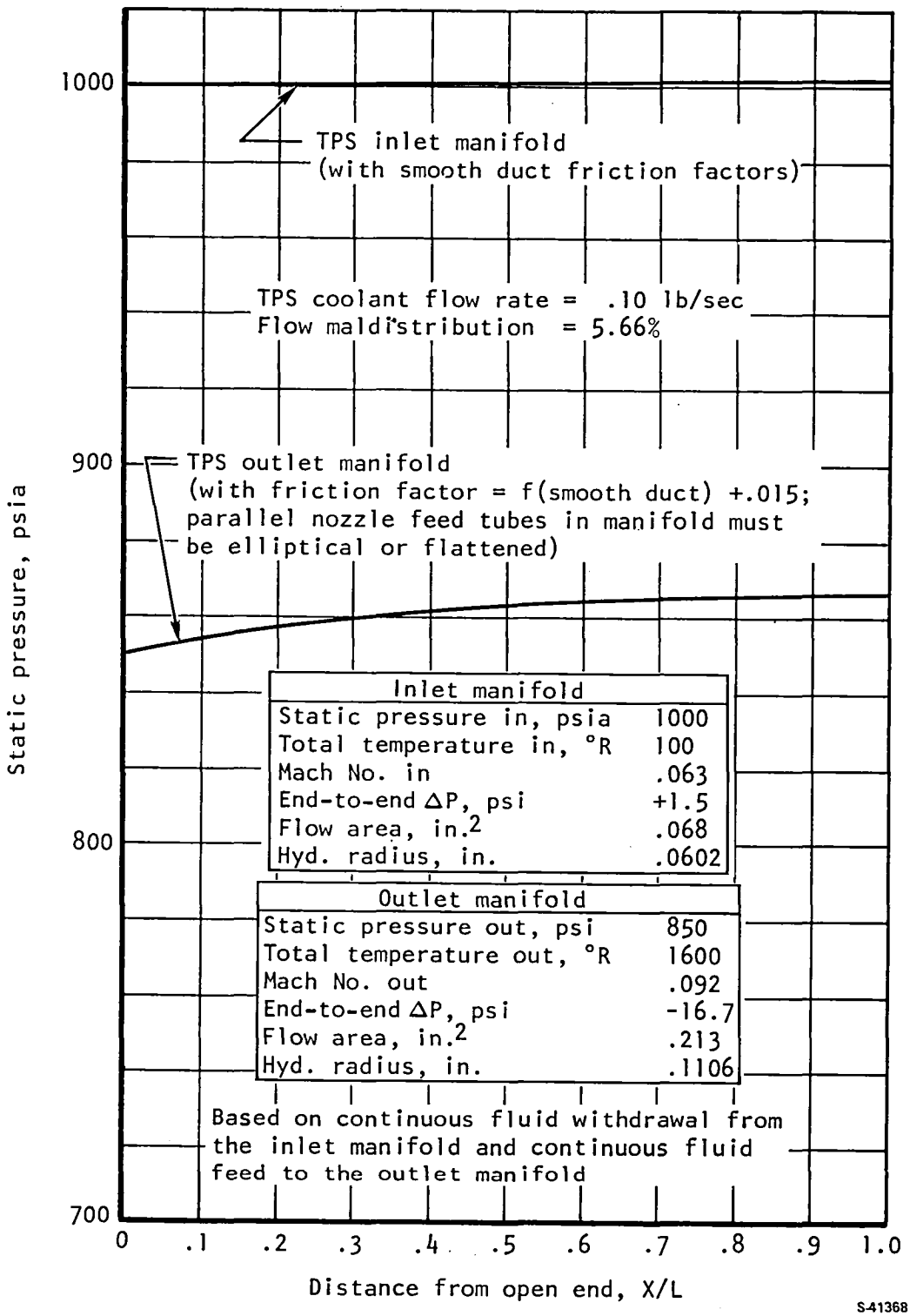

Figure 45.-Static pressure distribution in center strut TPS coolant manifolds.

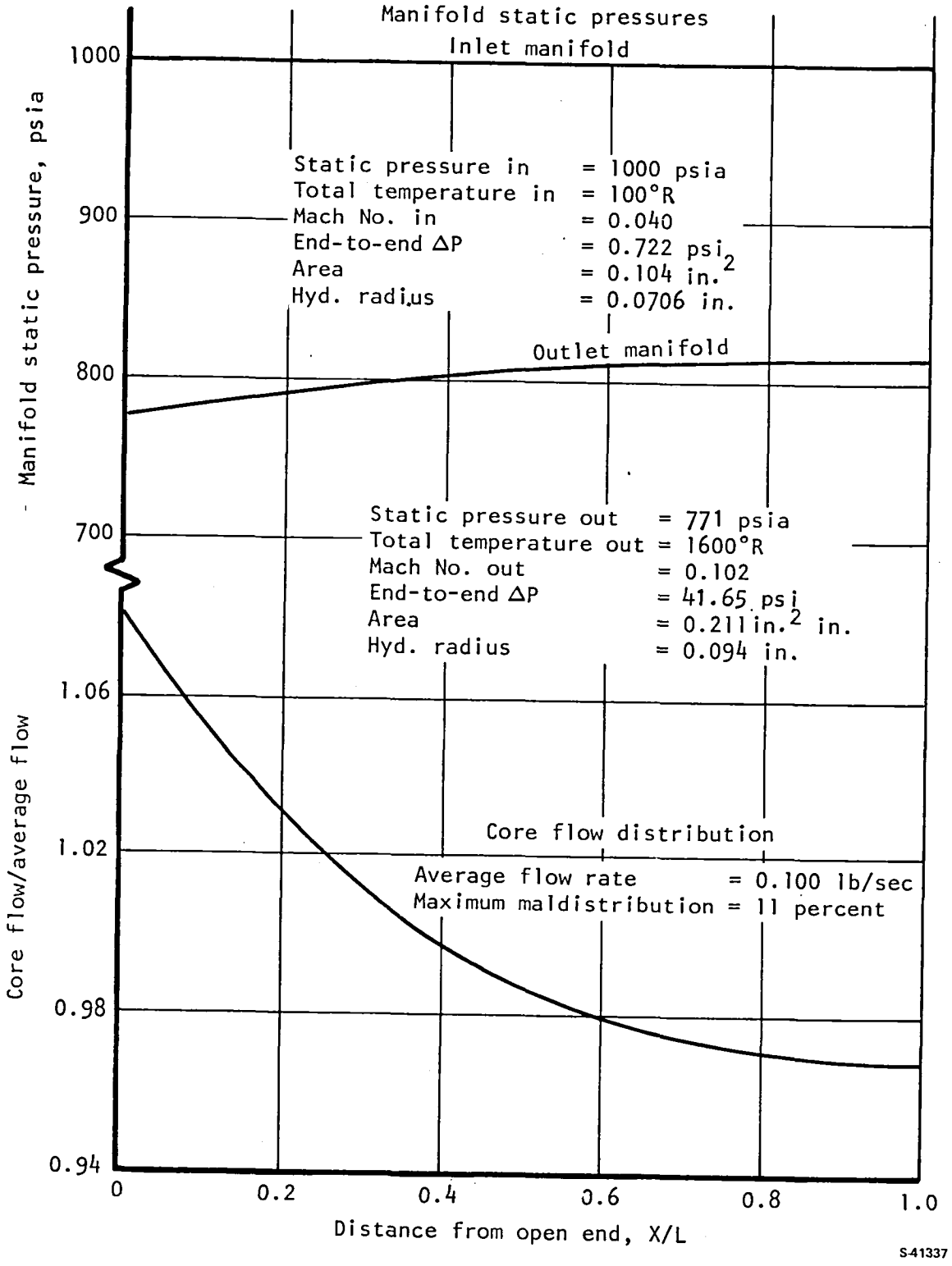

Figure 46.- Static pressure and flow distribution in the side strut TPS coolant manifolds.

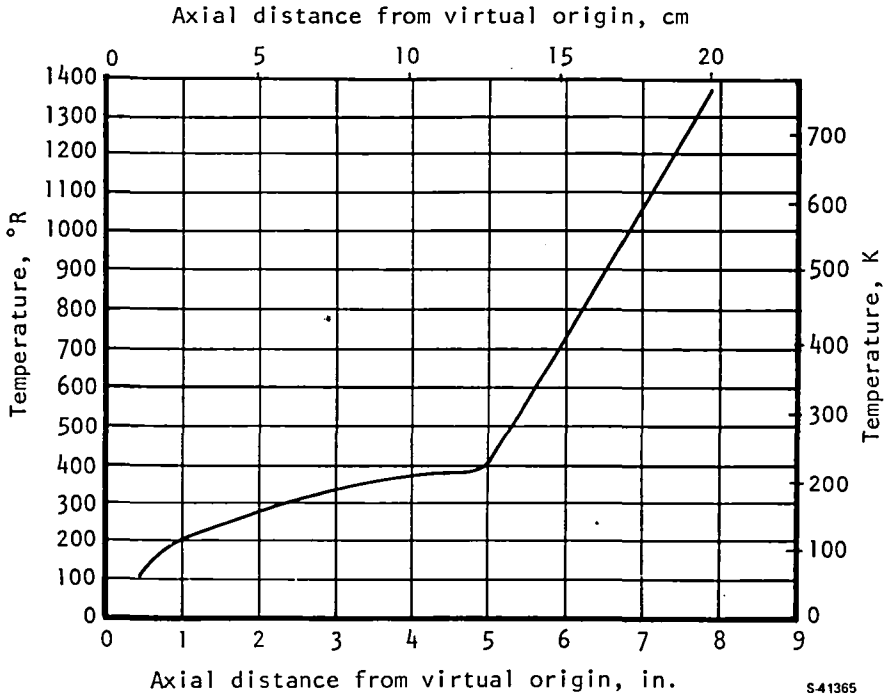

Figure 47.-TPS coolant temperature distribution in the center strut.

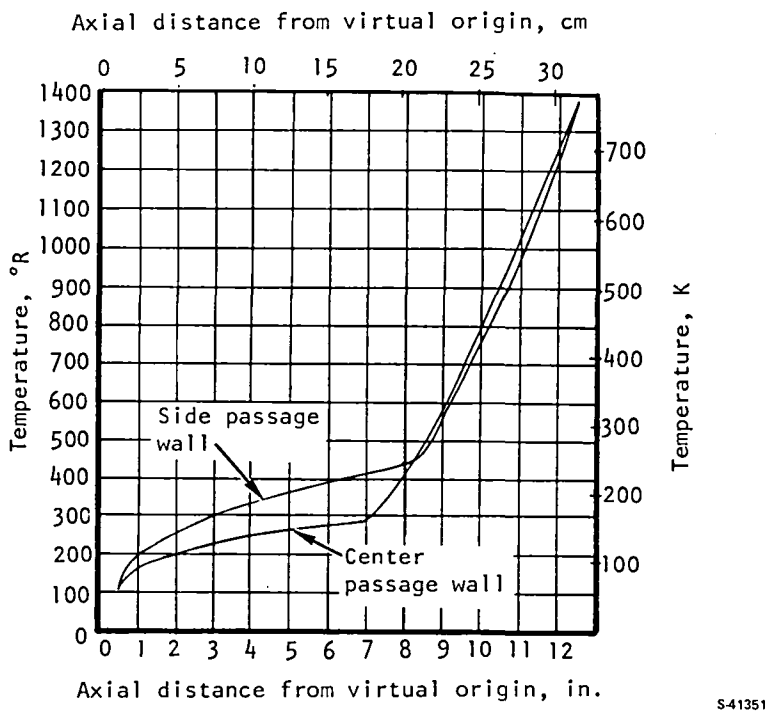

Figure 48.-TPS coolant temperature distribution in the side struts.

coolant flow rates of 45.36 g/sec (0.100 lb/sec) in each strut. This flow was equally divided in the center strut, but unequally divided in the side struts (58.4 percent in the center passage wall and 41.6 percent in the side passage wall). In both struts the TPS coolant outlet temperature is 1380°R, which is 220°R below the design limit of 1600°R. This result allows for approximately 18 percent margin in heat flux uncertainties.

Graphs of the heat transfer coefficients in the center and side strut TPS coolant surfaces versus axial distance from the virtual origin point are presented in figs. 49 and 50. The heat transfer coefficients in the TPS coolant pin-fin surfaces were determined from basic flow friction/heat transfer data for the pin-fin flow passage geometry, the fluid mass velocities, and the local fluid transport properties. The properties were evaluated at the temperature versus flow length profiles shown in figs. 47 and 48. No corrections for fluid property variation normal to the flow are needed because of the highly interrupted nature of the flow.

Graphs of the heat transfer coefficients in the center and side strut TPS inlet and outlet coolant manifolds versus distance from the open end are presented in figs. 51 and 52. The fluid properties were evaluated at the following temperatures and pressures: center and side strut inlet manifolds at 55.6 K (100°R) and 6.895 MPa (1000 psia), center strut outlet manifold at 766.7 K (1380°R) and 5.861 MPa (850 psia), side strut outlet manifold at 769.4 K (1385°R) and 5.516 MPa (800 psia).

The heat transfer is based on flow through smooth rectangular flow passages uncorrected for fluid property variations normal to the flow. Computation of the temperature profiles of the wall or thermal buffer surface in the TPS manifolds should be based on a reduced coefficient, $h(T_m/T_w)^{0.5}$, where T_w is the absolute wall or surface temperature and T_m is the absolute mean fluid temperature. Also, in order to account for the higher local mass velocities at the locations where the parallel injector tubes pass through the TPS coolant outlet manifolds, the local heat transfer coefficient has been increased by 50 percent. This is indicated by the blips in figs. 51 and 52.

Graphs of the heat transfer coefficients in the center and side strut perpendicular and parallel injector manifolds are presented in figs 53 and 54. The fluid properties were evaluated at 611 K (1100°R) and 4.826 MPa (700 psia). As in the TPS inlet and outlet manifolds, the heat transfer is based on flow through smooth rectangular flow passages, where the same type of $(T_m/T_w)^{0.5}$ correction should be made. Also, the stepwise decrease of the heat transfer coefficient versus flow length results from the discrete withdrawal from the manifolds through the injector nozzles.

Based on the above results, adequate coolant and fuel distribution within the strut manifolds can be achieved.

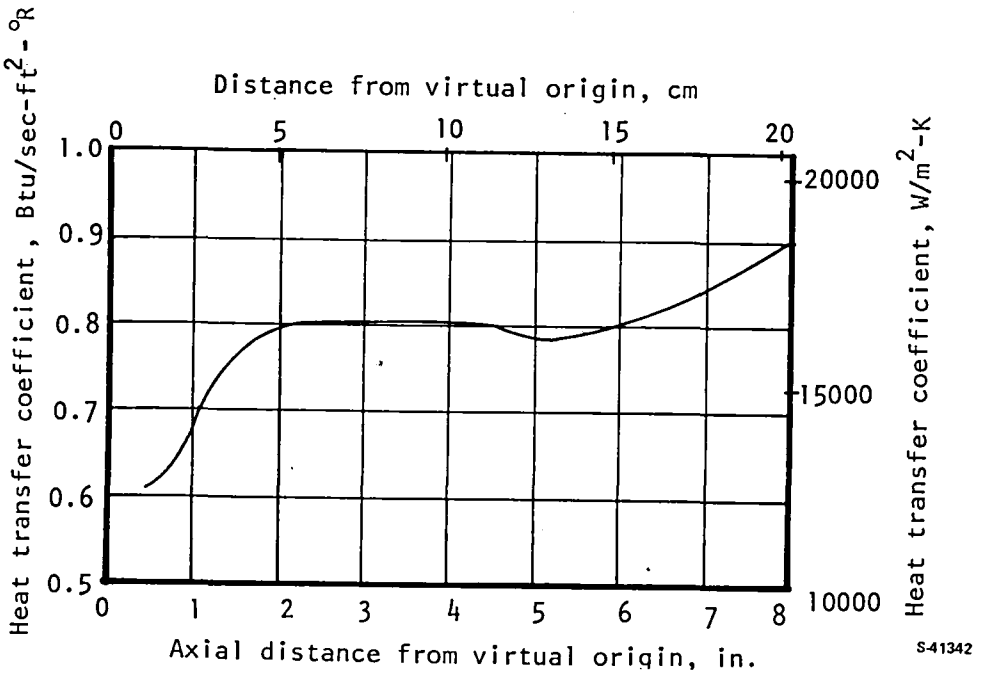

Figure 49.-Heat transfer coefficients in center strut TPS coolant surfaces.

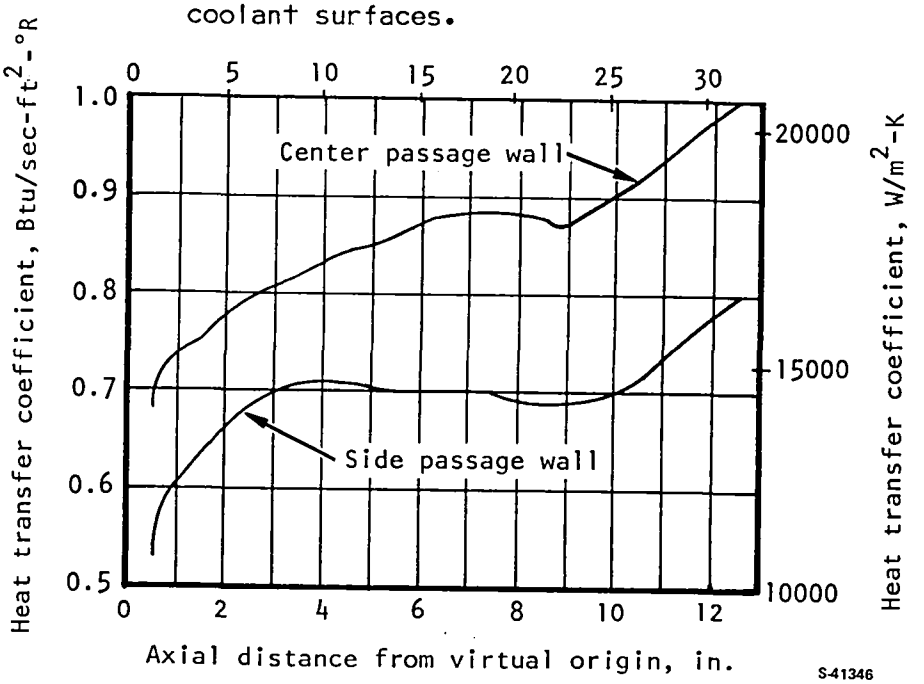

Figure 50.-Heat transfer coefficients in the side strut TPS coolant surfaces.

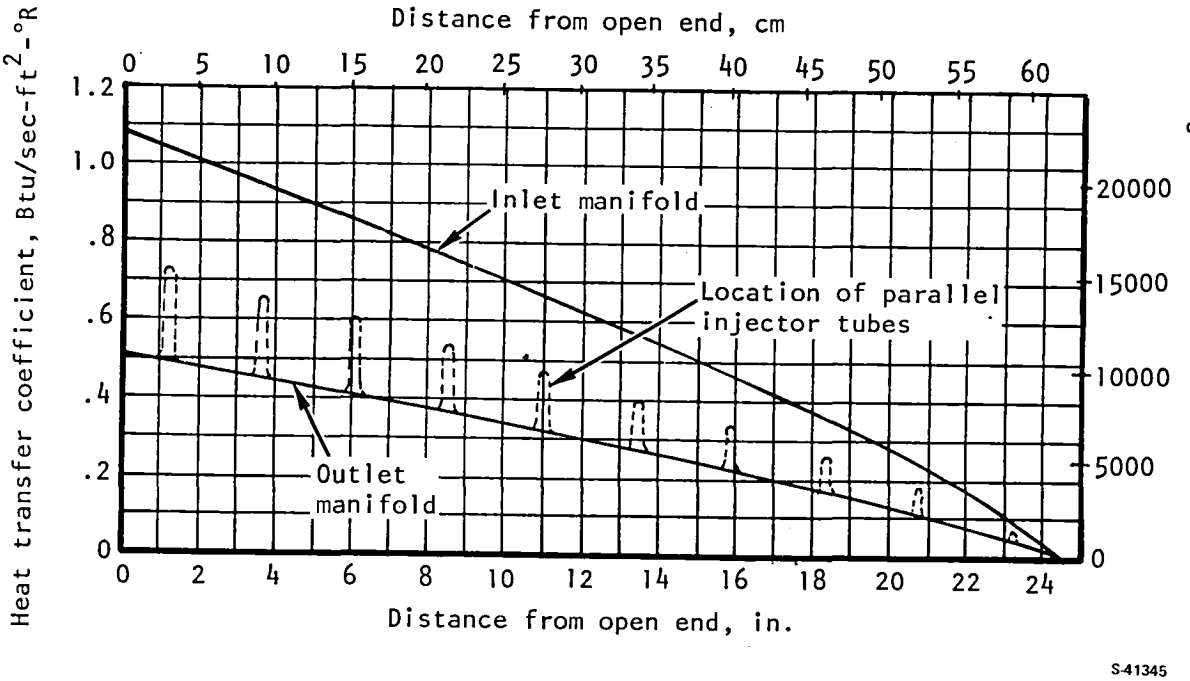

Figure 51.-Heat transfer coefficients in the center strut TPS inlet and outlet coolant manifolds.

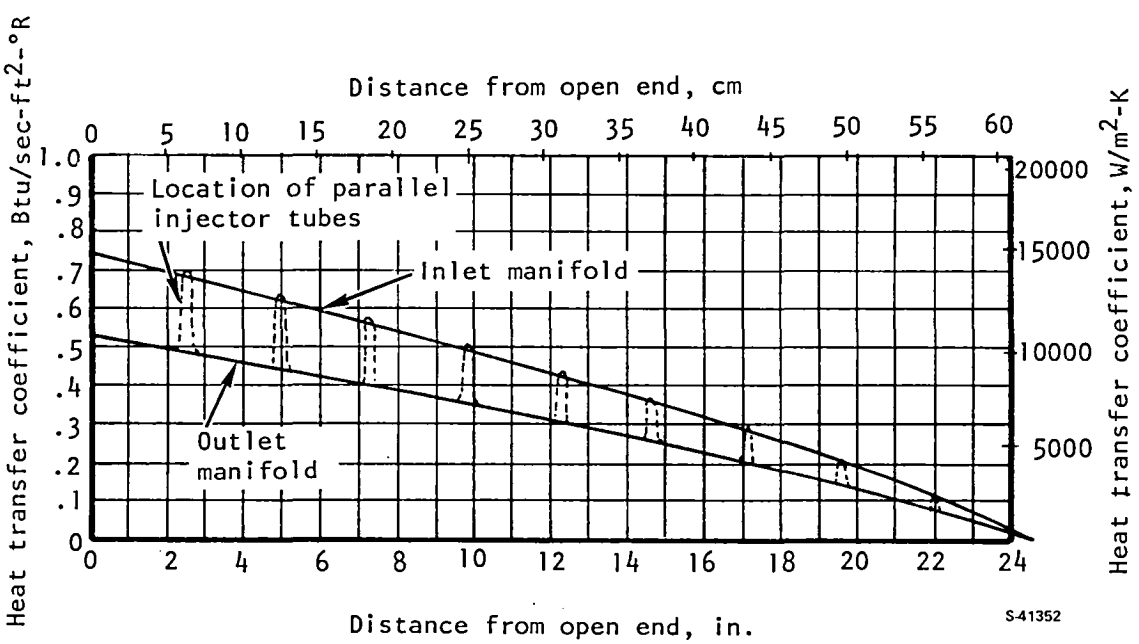

Figure 52.-Heat transfer coefficients in the side strut TPS inlet and outlet coolant manifolds.

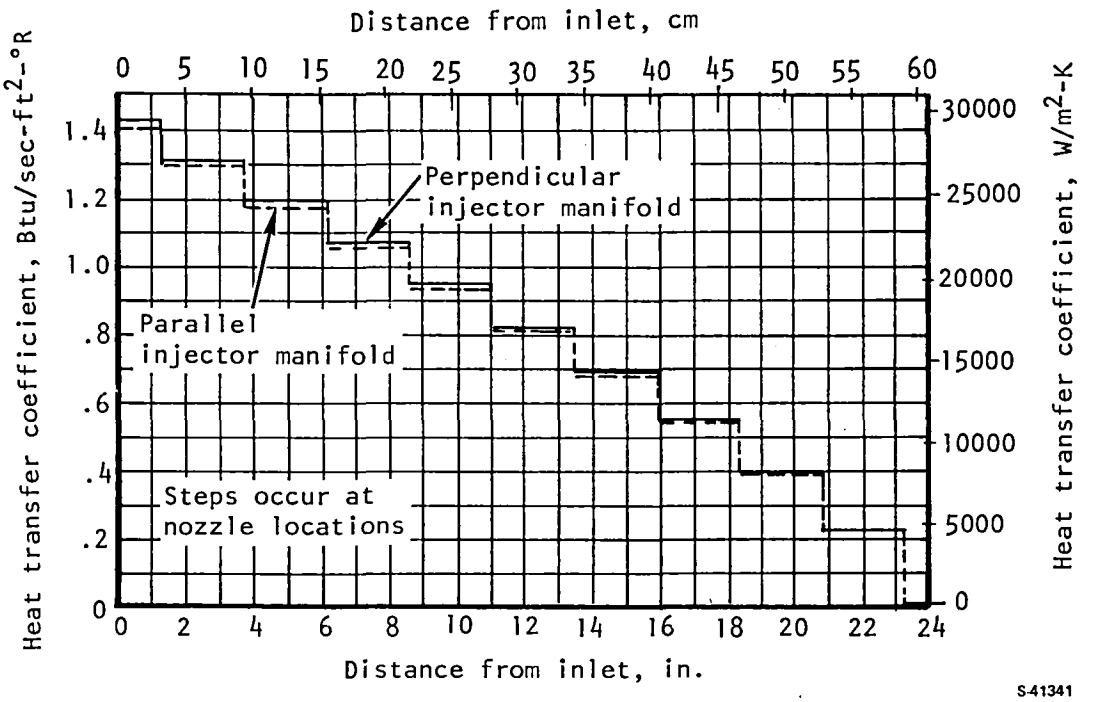

Figure 53.-Heat transfer coefficients in the center strut perpendicular and parallel injector manifolds.

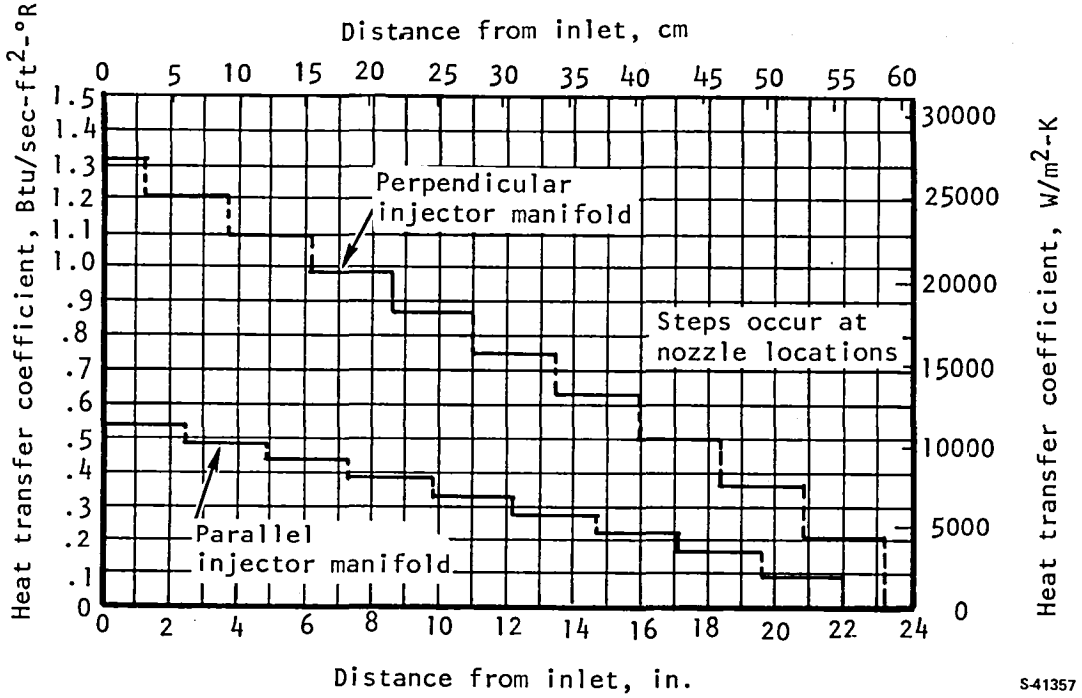

Figure 54.-Heat transfer coefficients in the side strut perpendicular and parallel injector manifolds.

Midspan tie.--Structural analyses conducted by NASA-LaRC (ref. 4) indicated an excessive stress level within the side strut when subjected to an unsymmetrical unstart condition. A possible solution is to tie the struts together at their mid-point, thereby decreasing the bending stresses due to the external side load by a factor of 2.

This concept was investigated in greater detail. For evaluation, a symmetrical diamond airfoil, 1.52 cm thick by 7.62 cm chord, was specified (fig. 55). The tie is placed with an angle of attack of 10 deg, which corresponds with the flow direction through the struts at Condition D.

A finite element model of the three-strut assembly was constructed as shown in fig. 56. The ends of the strut were assumed at first to be simply supported at the bottom and guided at the top, restraining rotation in all three axes but allowing axial movement. Space limitations at the cowl limit the amount of fixity that can be achieved. This is considered to be a coarse model and was used as a first approximation.

A uniform net pressure load of 0.69 MPa (100 psi) was applied to the side strut, simulating the unstart condition. This load is approximate and was used only to gain insight on strut behavior. The strut will deflect 8 mm (0.32 in.) or 13 mm (0.5 in.), depending on end fixity conditions if no midspan tie is used. Since the normal distance between struts is about 25 mm (1.0 in.), the deflection is significant. The deflection with a midspan tie was reduced to 4 to 6 mm (0.15 to 0.22 in.).

The capability of the midspan tie to stiffen the struts against lateral pressures such as the unsymmetric unstart is clearly demonstrated, even with a tie connecting only the struts, without attachment to the engine side walls.

Unstart condition dynamic response: Transient data obtained from a 3.8-cm-high model of the Scramjet (ref. 8) indicate that the unstart shock propagation velocity is on the order of 30.5 m/sec (100 ft/sec). For the 31.8-cm 12.5-in.)-long chord side strut, the period of the unstart disturbance is about 100 Hz. The period is in the range of the strut natural frequency, indicating a potential for load amplification. To explore this possibility, the finite element model (fig. 56) was subjected to natural frequency vibration analysis with the following results:

Strut midspan tie	Natural frequency, Hz	Strut
No	274 (first mode)	Side
No	323 (first mode)	Center
Yes	380 (first mode)	Side
Yes	567 (second mode)	Side
Yes	792 (third mode)	Side

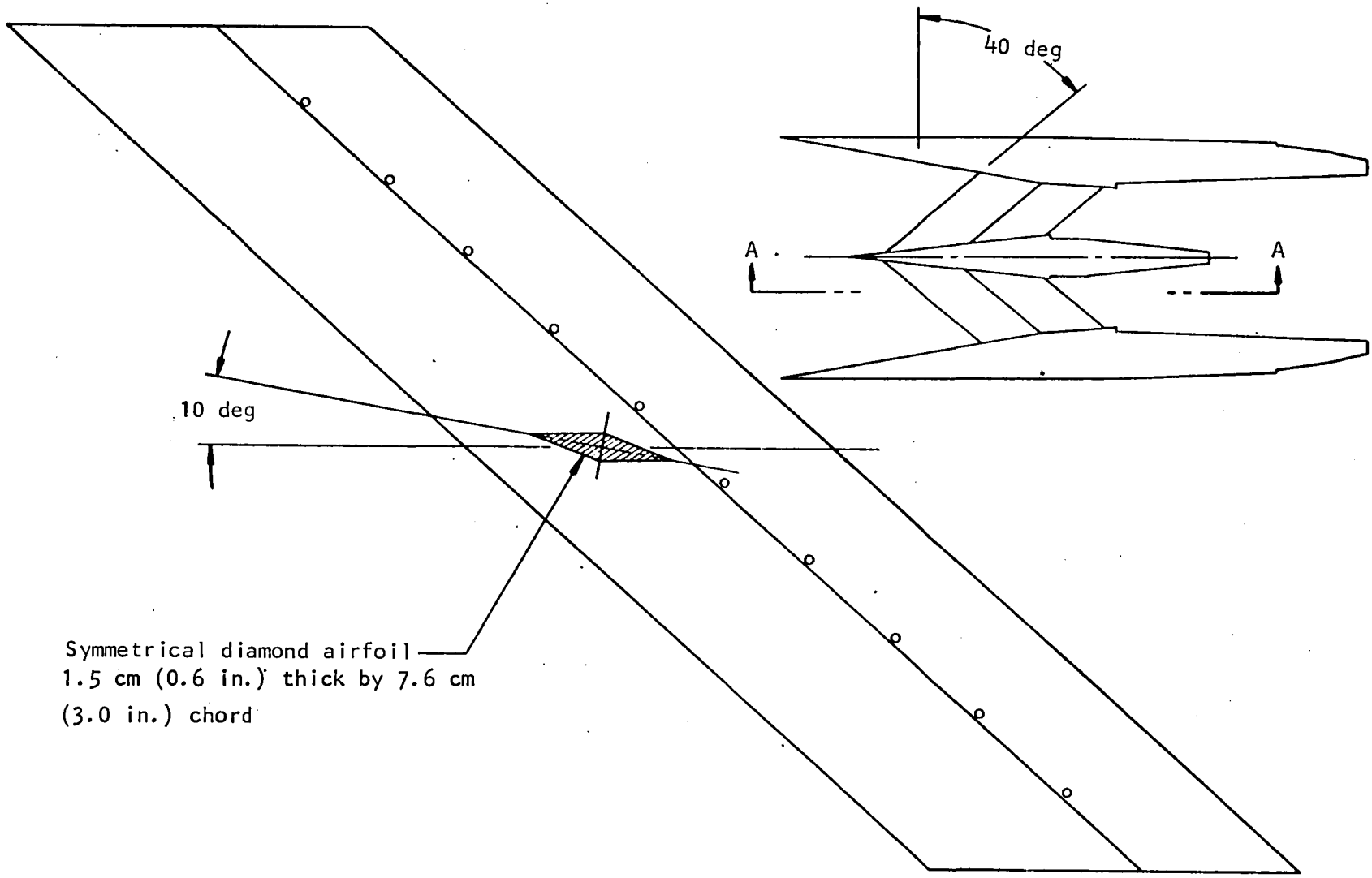

Figure 55.-Midspan tie design.

S-15738

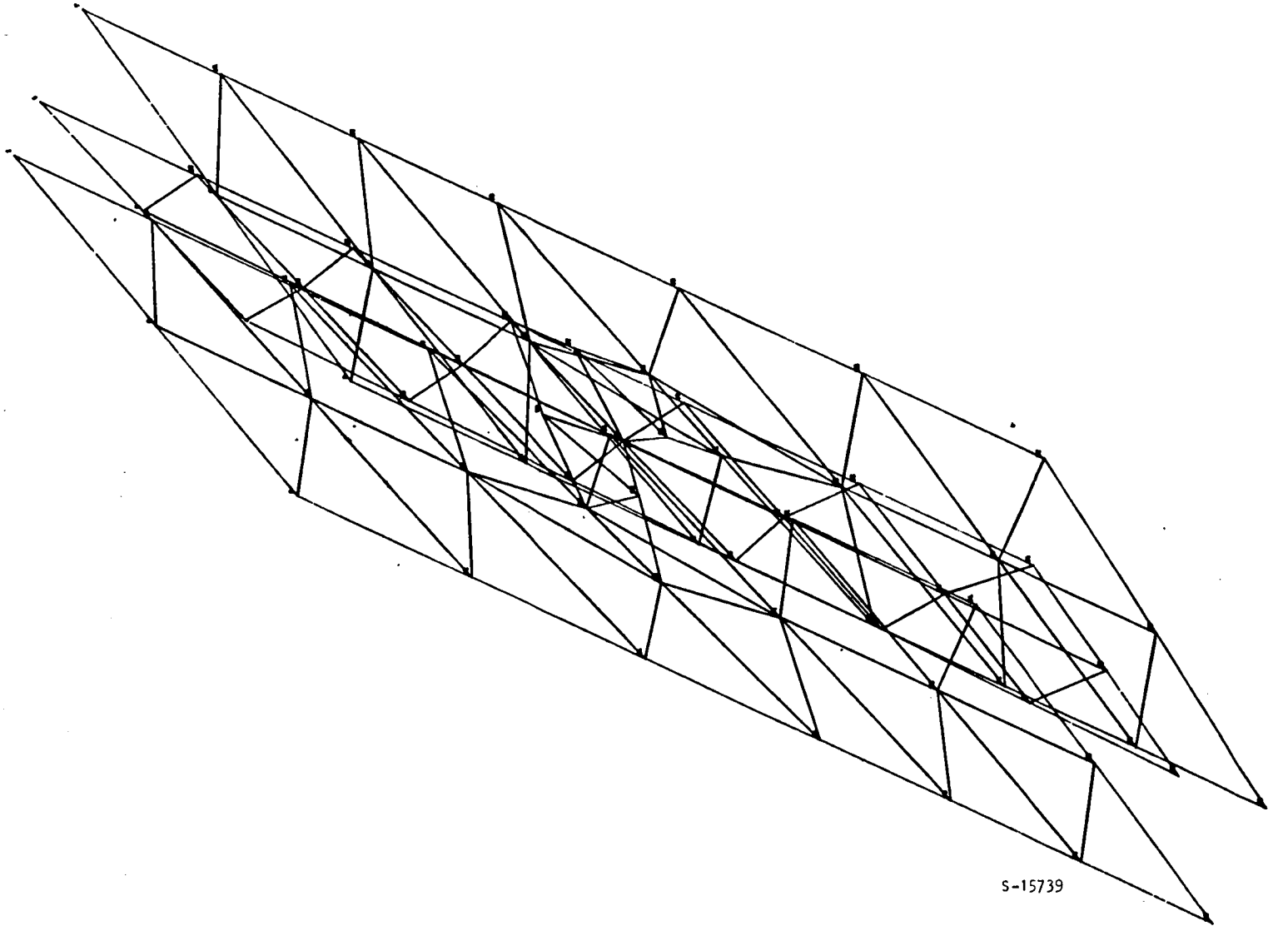

Figure 56.-Finite element model of three-strut assembly.

The midspan tie can increase the natural frequency of the struts by 38 percent (side strut) to over 150 percent (central strut). By moving the tie along the strut height, the strut structural vibration response can be conveniently tuned (or detuned).

For a side strut without a tie, the ratio of pulse period to strut period is 0.37, which yields a loading factor of 1.3 (half sine wave shock profile). By adding a midspan tie, the loading factor is decreased to 0.9. These calculations must be considered to be approximate, but they do show the load reduction provided by a midspan tie.

Conclusions: a midspan tie can provide several benefits and is structurally and aerodynamically feasible; however, the resultant complications in coolant flow routing and strut fabrication are substantial. It is also recognized that the data used in establishing the loading condition are uncertain. Means for reducing the thermal loading were therefore considered as an alternate approach to reduce the combined loading without resorting to a midspan tie.

Side strut structural analysis.--A large 3-dimensional finite element model of the side strut was constructed by NASA using the SPAR computer code (ref. 14). Only the side strut was modeled, as its loading was slightly more critical than the center strut loading and the results would be conservatively representative for the center strut. The model was primarily comprised of triangular and quadrilateral plate elements with both membrane and bending stiffness, and had 1708 unrestrained degrees of freedom.

Initial results, described in ref. 4, are based on the following strut mounting scheme: at the top, a three-point suspension is used in which the leading edge is fixed and the other two points have two degrees of freedom each. The strut is permitted to move chordwise from the leading edge and laterally from one side. At the cowl, the strut is fitted to a slot that permits longitudinal expansion but provides support for side loads. Local stresses developed with this scheme were found to be excessive.

Performance with revised mounting scheme: Boundary conditions were adjusted to permit thermal growth and rotation along the strut main plane; a set of springs was used to represent the midspan tie. These conditions are shown schematically in fig. 57.

The finite element model was constructed on the basis of the following: (1) two main longitudinal webs, 2.79 mm (0.11-in.) thick; (2) uniform thickness sidewalls, 2.03 mm (0.080-in.) thick; and (3) 6.60 mm (0.26 in.) by 28.45 mm (1.12 in.) leading and trailing edge sections.

Pressure loads defined for an unsymmetrical unstart (at Condition G) were applied along with the Condition H thermal loading. It is presumed that the coolant flow is modulated to maintain the coolant outlet temperature at 889 K (1600°R). Hence, the coolant temperature distribution, the primary structure temperature distribution, and the resulting thermal stresses are similar for all operating conditions even though the overall heat input varies.

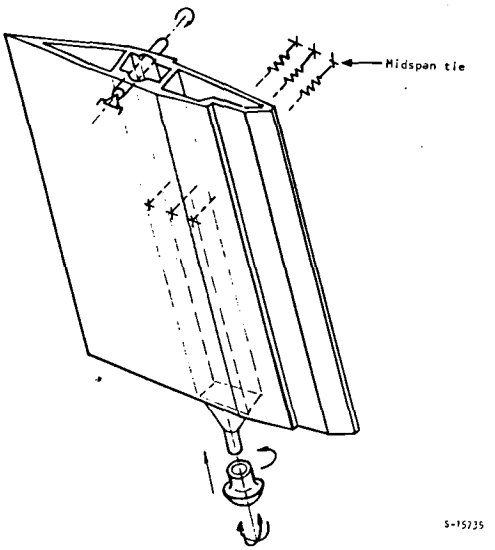

Figure 57.-Boundary conditions adjusted for thermal growth and rotation

Results of the computer runs for the pressure loads alone and for the pressure loads combined with the temperature distributions were reviewed and the following conclusions were reached:

(1) High stresses are mainly due to the pressure loads and are basically local stresses.

(2) Most of the high stresses are on the outside wall (side facing the sidewall), with some high stresses on the inside wall.

(3) Use of a midspan tie is essential for the specified loading conditions.

Fig. 58 shows the high stress areas for the pressure only and for the pressure plus temperature cases. Although effective (von Mises) stresses are not excessively high, a level of 70 to 80 ksi should be considered as the recommended upper limit for Inconel 718 material at the operating temperatures. The stress levels in the high stress areas exceed this recommended upper limit and could increase significantly when dynamic effects such as impulse loading and combustion-induced vibrations are considered.

Figs. 59 and 60 depict deformation maps for several representative locations (leading and trailing edge, top, bottom, and mid-distance) along the strut due to pressure loading. These results indicate that:

(1) The trailing edge displaces significantly more than the leading edge.

(2) The overall strut rotates along the axis defined by the two end constraints.

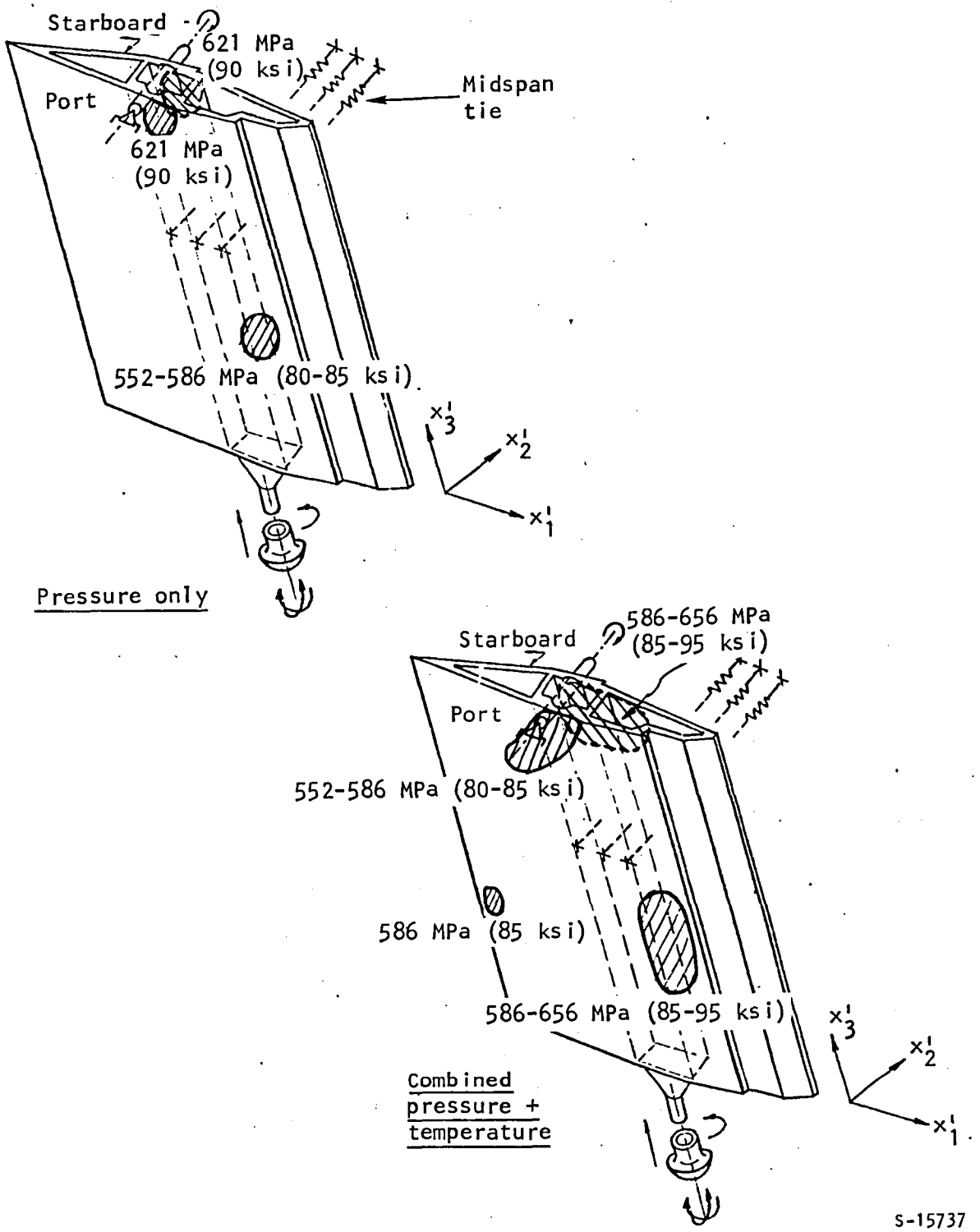

Figure 58.-Effective (von Mises) stresses--highly stressed areas with midspan tie.

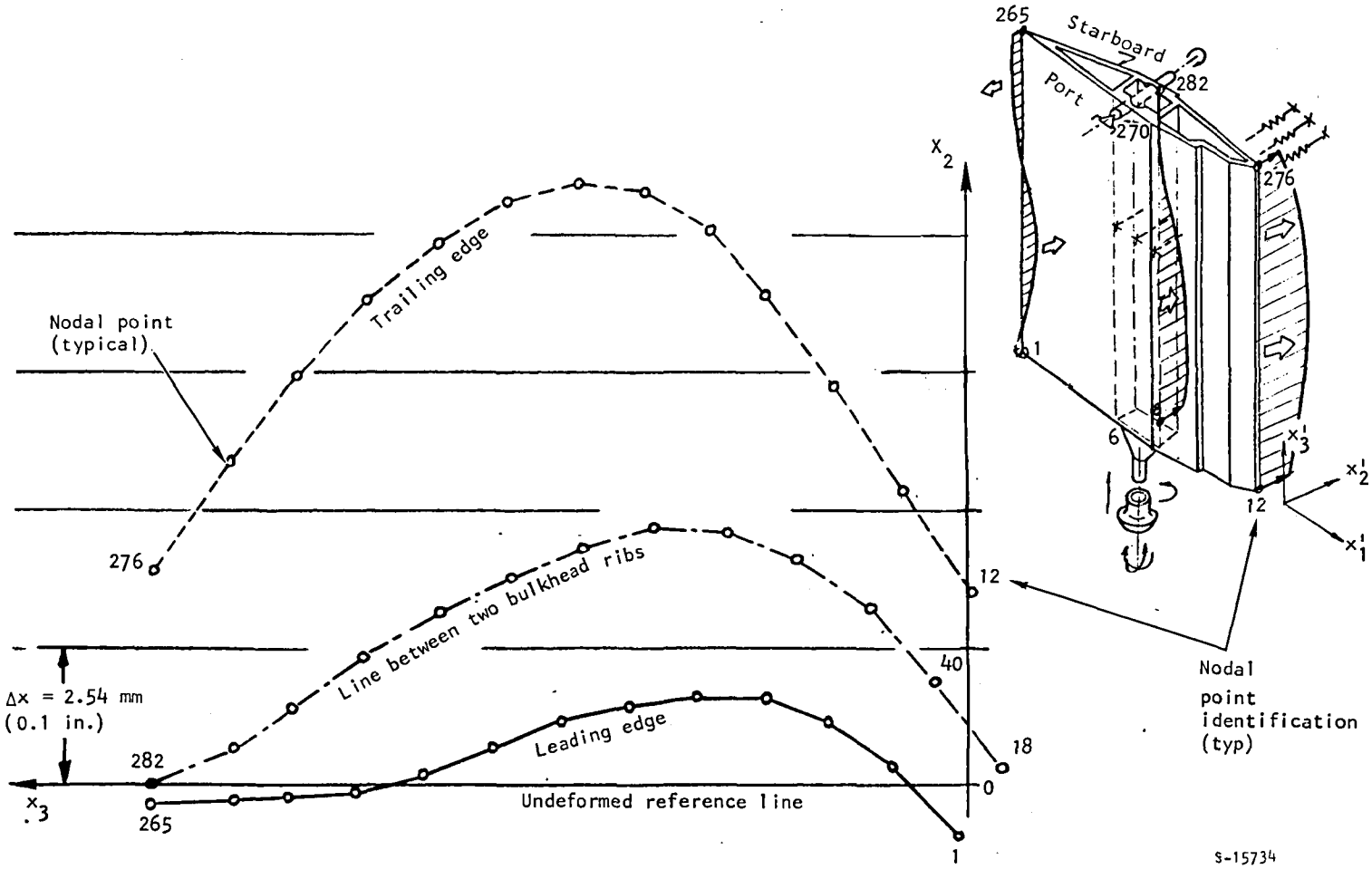

Figure 59.-Absolute deformation with midspan tie, perpendicular to flow, due to pressure only.

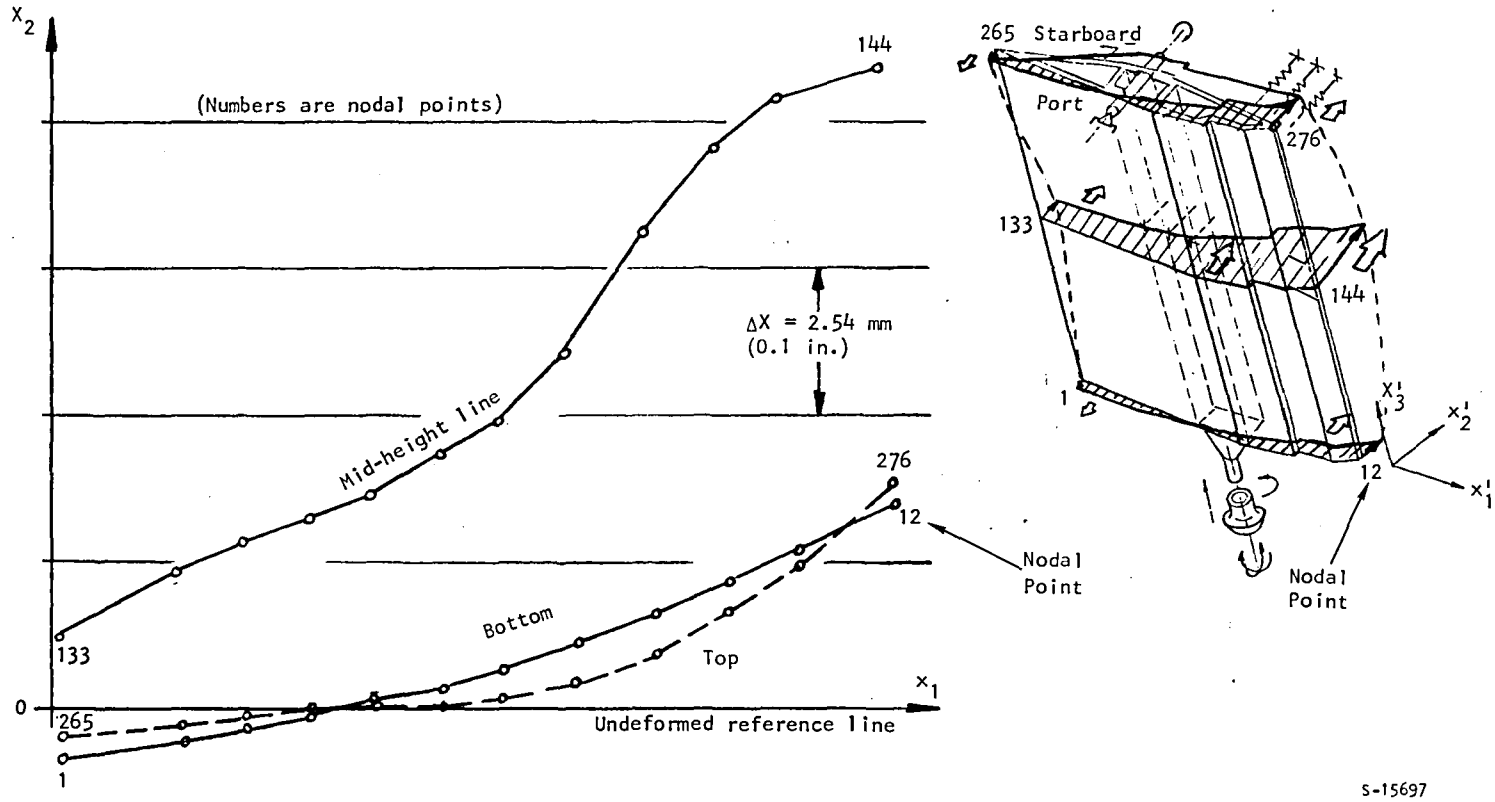

Figure 60.-Absolute deformation with midspan tie, parallel to flow, due to pressure only.

(3) Although the midspan tie somewhat restrains bowing, there are large local deformations along the strut trailing edge due to bending in a spanwise direction about the midspan tie.

(4) Strut deformation is not excessive in that it is a transient condition and the strut will not contact the adjacent strut or sidewall.

Bending of the strut in the $x_1 - x_2$ plane (transverse bending) can be observed by subtracting the strut rotation from the absolute deformation as shown in fig. 60. A straight line connecting the leading and trailing edge nodes represents pure rotation; any deviation from this straight line indicates strut bending in the flow direction.

Various modifications were considered to limit strut deflection and achieve a corresponding reduction in the primary structure stress level. As a general guideline, it was stipulated that if additional constraints are to be used, they should control pressure-produced displacements without interfering with the temperature displacements.

Fig. 61 illustrates a modified configuration. Two pins are placed on the end plates near the trailing edge. These pins will engage slots or holes on the supporting structure, which will limit the overall strut rotation without adding restraints to the thermal deformation. Four additional longitudinal ribs, 3 to 3.6 mm (0.12 to 0.14 in.) thick, are specified to control spanwise bowing. Transverse bending would be controlled by adding three transverse ribs, 3 to 3.8 mm (0.12 to 0.15 in.) thick. This configuration will reduce the absolute deformations below 3 to 3.3 mm (0.12 to 0.13 in.) and reduce the maximum effective stresses by 103 to 207 MPa (15 to 30 ksi). The primary structure stress level is then well within the capabilities of Inconel 718 material, including an allowance for dynamic loading.

Performance with increased cooling: The coolant outlet temperature was reduced to 417 K (750°R) from 889 K (1600°R), which results in increasing the TPS coolant flow by a factor of 2. The increased flow at Condition G is then about equal to the maximum coolant flow at Condition H with a 889 K (1600°R) coolant outlet temperature. The overall engine coolant ø at Condition G is increased by about 20 percent. This is considered a reasonable trade if the strut midspan tie can be eliminated.

The primary structure was modified to the configuration shown in fig. 62. The primary structure included three spanwise bulkheads, 2.5 mm (0.100 in.) thick, to resist bending. These bulkheads also separate the coolant and fuel manifolds. Seven thin bulkheads, 0.3 mm (0.012 in.) thick, take tensile loads only and are used to react the internal hydrogen pressure. The thin bulkheads can be perforated to facilitate communication between compartments. The midspan tie was eliminated from the model.

These changes are certainly feasible. The increased flow rate is about equal to that at Condition H, the maximum thermal loading operation, so the available coolant flow area can accept the increased flow at Condition G.

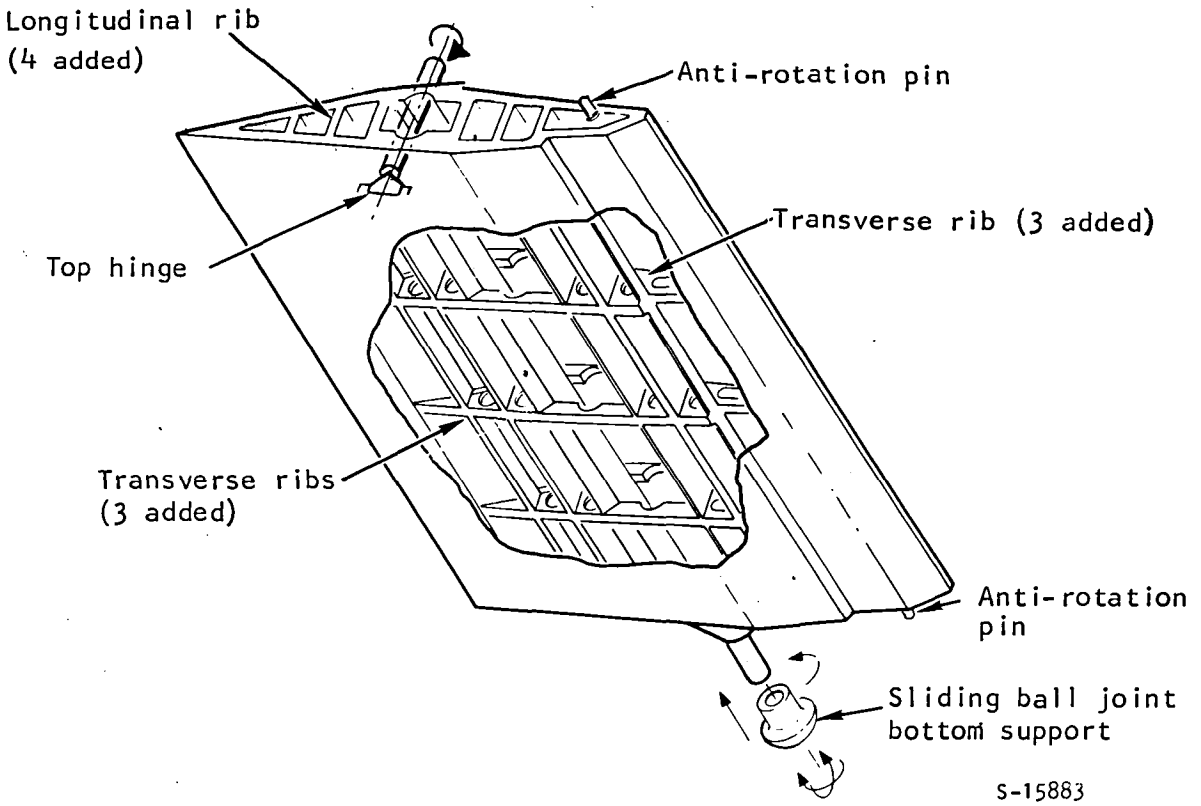

Figure 61.-Modified strut structural design with midspan tie.

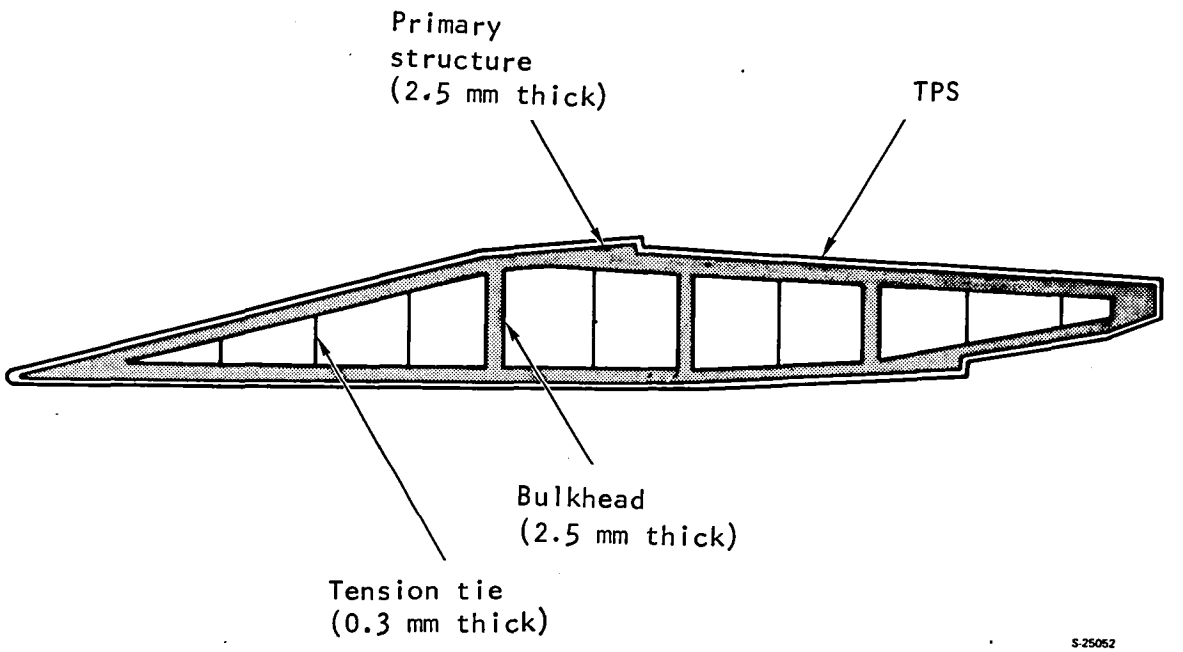

Figure 62.-Side strut structure for increased-cooling analysis.

With the resulting reduced temperature level, two benefits result: (1) the thermal stresses are reduced, and (2) the Inconel 718 allowable stress is increased. Elimination of the midspan tie is highly desirable because of the structural and cooling complexities introduced by this modification. Elimination of the chordwise ribs alleviates the pressure drop and flow distribution problems in the internal manifolds.

The side strut was stress-analyzed by NASA using the SPAR computer program and the output was forwarded to AiResearch for review. The case that was analyzed is titled "Case 2, Mach 5.1 Unstart Temperatures and Unstart Pressures". As before, a steady-state unsymmetrical unstart at Condition G operation was the basis for analysis.

Some modifications of the original model were made by NASA. There are now seven internal ties. The model, as shown in fig. 63, is constrained as follows:

Node	Location	Constrained Degree of Freeedom
287	Cowl	(δ_1:δ_2 -about local axis with Z parallel to sweep line)
270	Port topwall	(δ_1:δ_2:δ_3:θ_1:θ_3)
282	Starboard topwall	(δ_1:δ_3:θ_1:θ_3)

Notes: δ = Displacement

θ = Rotation
1, 2, 3 refer to directions X,Y, and Z, respectively

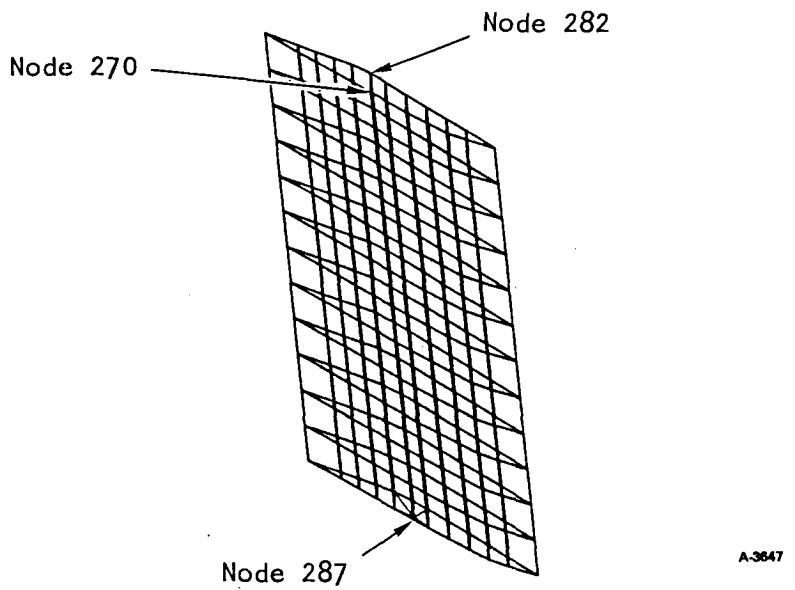

Figure 63.-Side strut model with key nodes.

A review and analysis of the NASA computer results using the NASA modified structure was conducted. Maximum and minimum principal stress maps are shown in figs. 64 through 67 for the starboard and port walls. The starboard wall displacements are shown in fig. 68 on an isometric deformation map. A schematic of the starboard wall of the model is shown in fig. 69.

The current model output indicates stresses that are higher than those reported previously. However, the metal temperatures are lower than previously reported because the strut is being overcooled. For the temperature reported on the strut, the allowable stress is 130 ksi (10 unstarts). The stresses in the model exceed the allowable stress only at the topwall support. This allows the midspan tie to be eliminated.

The strut is being bent laterally and is being twisted. This can be seen in the deformation and stress patterns. The stress patterns are similar for both the starboard and port walls. A large central area is above 100 ksi. The deformations are large, but no contact will occur with the adjacent strut or the sidewall panel. The trailing edge has a larger displacement than the leading edge--0.628 in. and 0.386 in., respectively.

The effects of the loading can be best visualized by observing the reactions at the constraints (fig. 70). The strut is reacting similarly to a fixed simple beam.

It is doubtful that the deformations at the topwall that are shown in fig. 68 could be as large as have been calculated. The reason for this is that the seal and surrounding support structure in the topwall will provide additional support to the strut at the area of contact. This will significantly reduce the torsional couple at the topwall seen in the loading pattern of fig. 70. This will, in turn, result in lower stresses physically existing in this area. The analysis to assess the performance of the seal at the intersection of the side strut and the top panel is described in detail in the next section.

Further, in the analysis the support conditions at the top of the strut have not taken into consideration the stiffness of the topwall structure. Consideration of the stiffness will help distribute the loads and thereby reduce the stress.

If necessary, the stresses at the topwall (nodes 270 and 282) can be reduced by sharing the topwall reactions by two mounts. This will cut the reaction per mount (and therefore the stress) at the topwall approximately in half. In addition, the torsional couple at the topwall can be reacted better as two lateral (direction 2) forces acting over a large span (fore and aft mount distance).

Strut/panel interface analysis.--This consisted of a structural analysis of a side strut and the region surrounding it when subjected to the maximum symmetrical unstart load condition. An analysis was conducted to assess the performance of the seal at the intersection of the side strut and the top panel, and to provide the boundary conditions at the edges of the side strut. A portion of the engine, including a side strut and a portion of the topwall incorporating the strut support and seal assembly, was isolated for the analysis. Consistent

Mach 5.1 unstart temperatures and unstart pressures,
Case 2

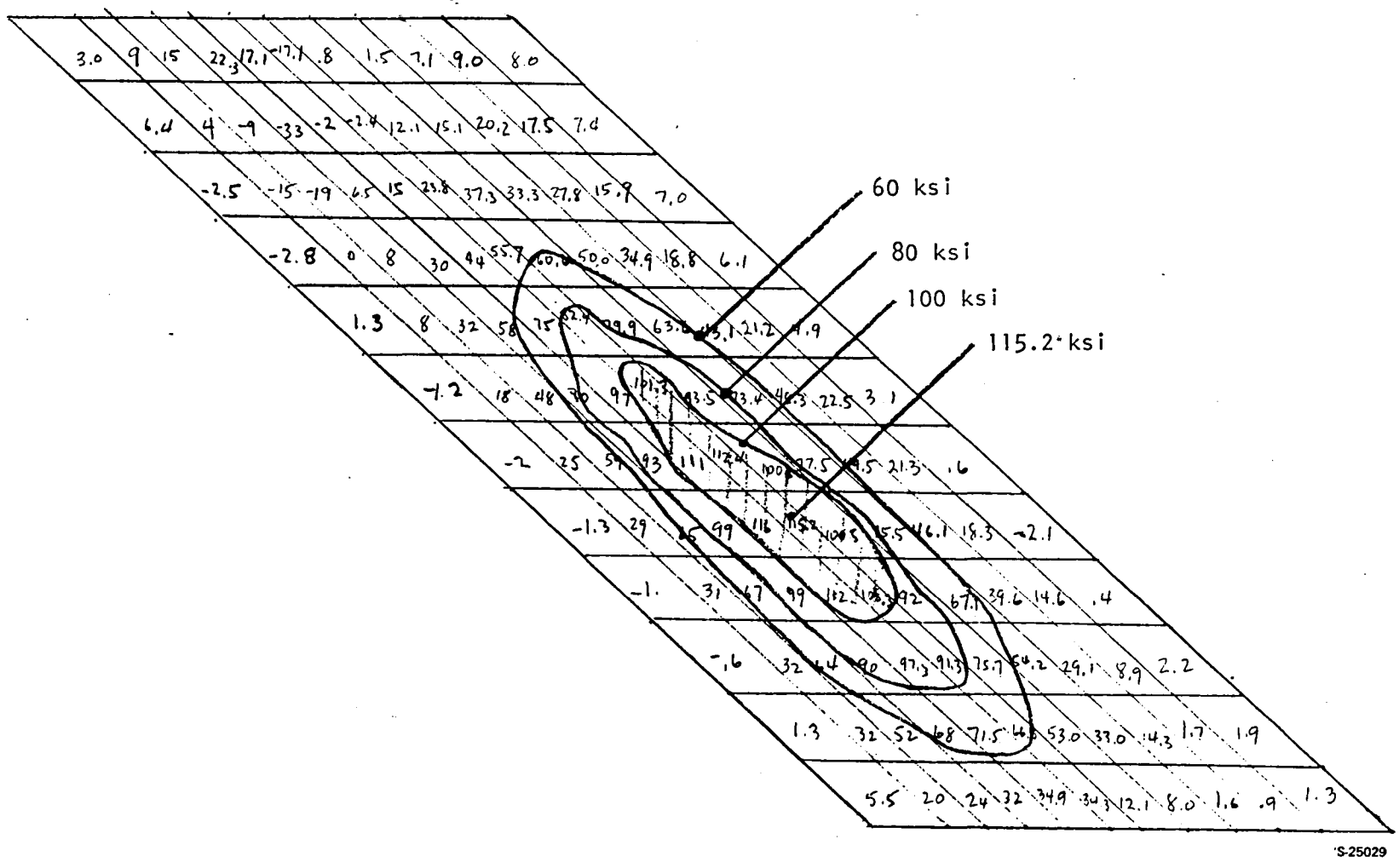

Figure 64.-Starboard wall centroid maximum principal stress, surface C.

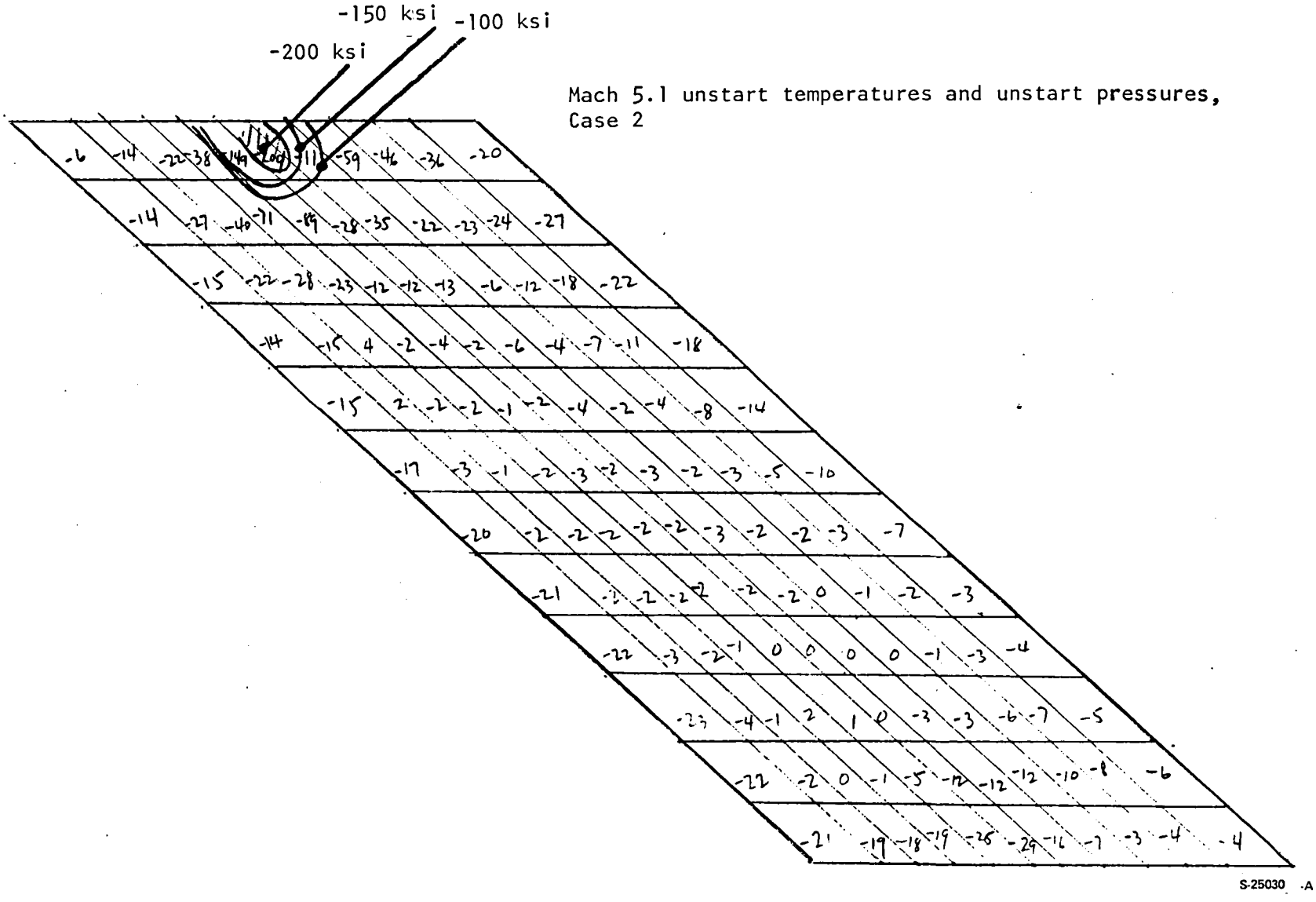

Figure 65.-Starboard wall centroid minimum principal stress, surface C.

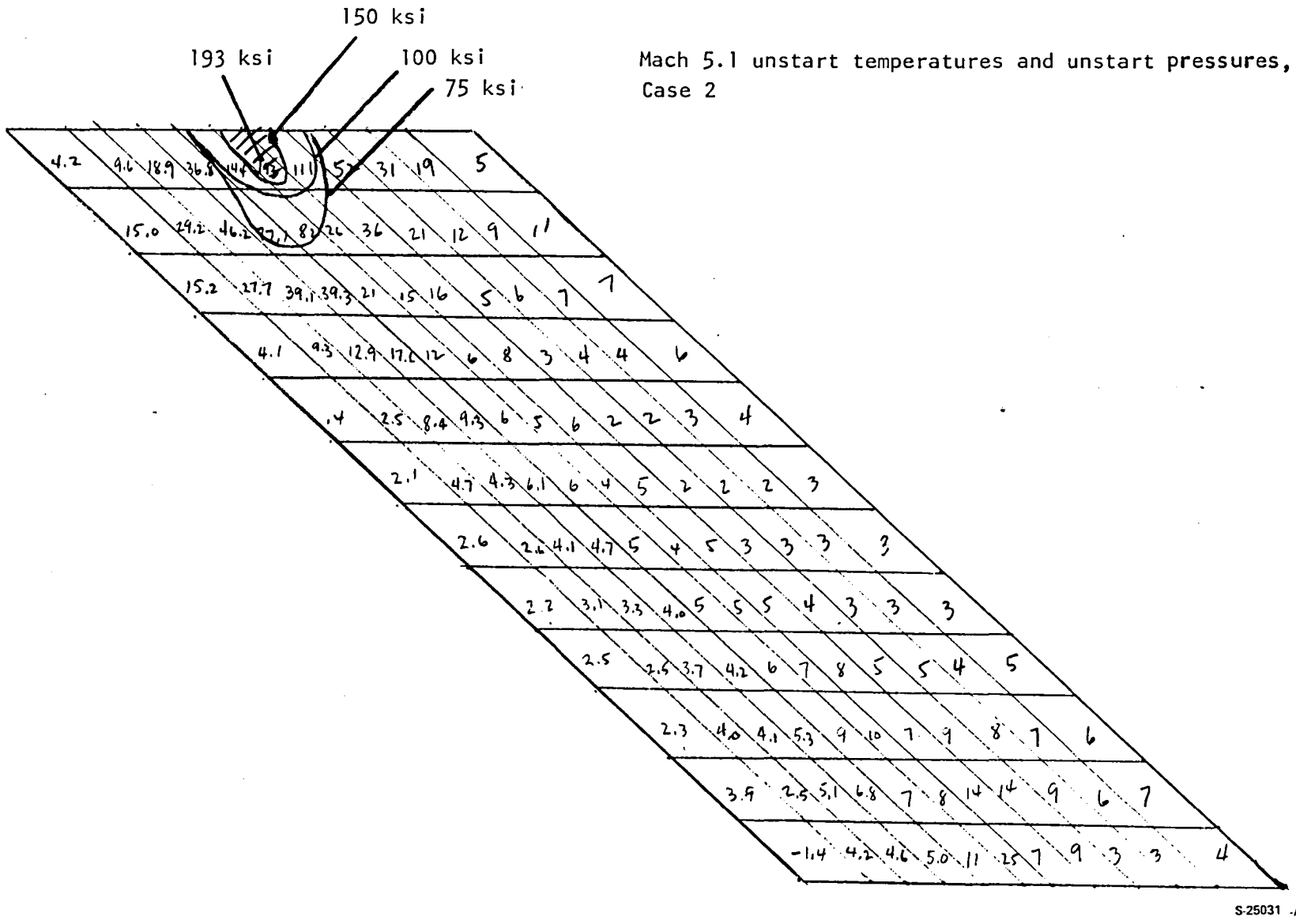

Figure 66.-Port wall centroid maximum principal stress, surface C.

Mach 5.1 unstart temperatures and unstart pressures, Case 2

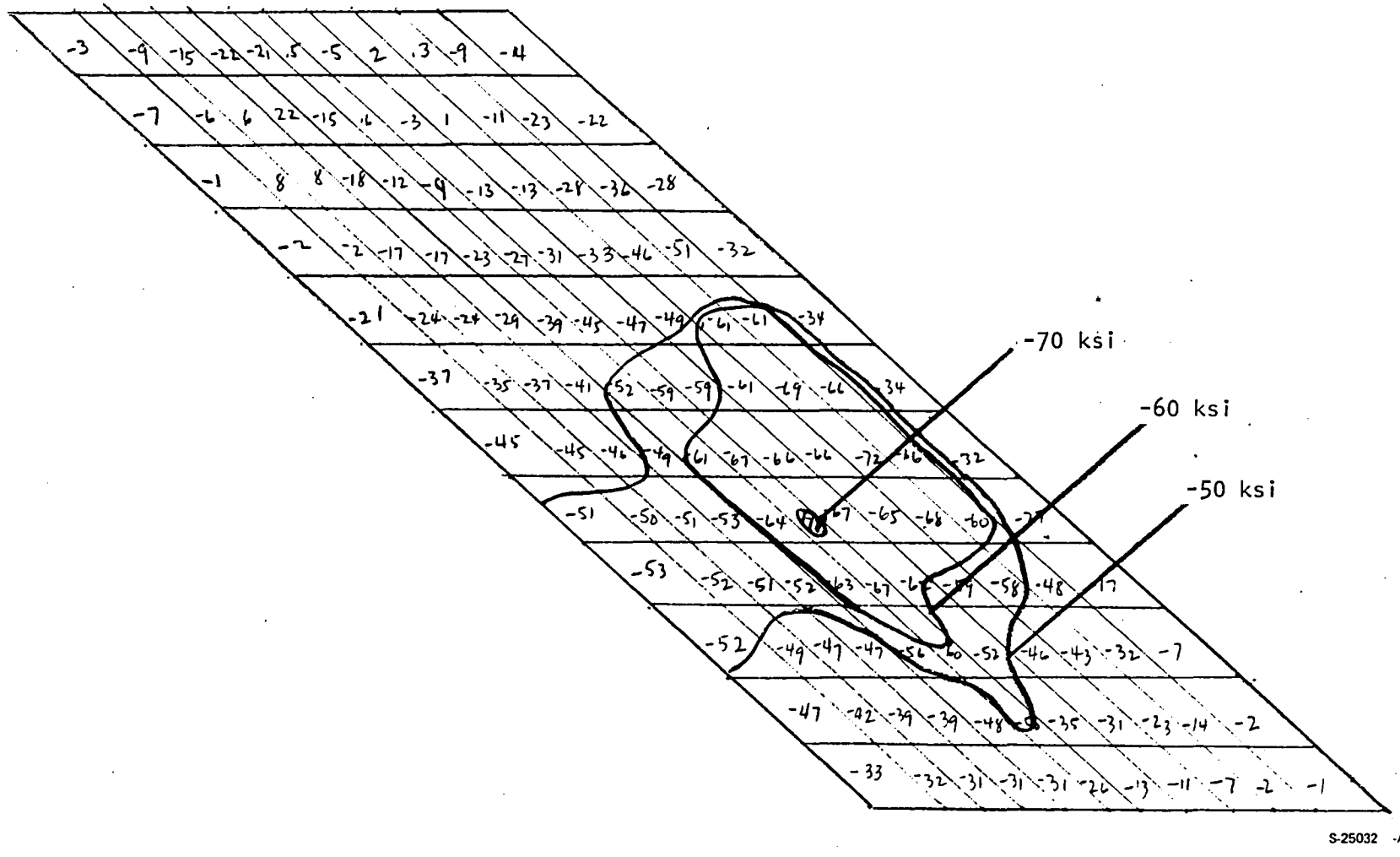

Figure 67.-Port wall centroid minimum principal stress, surface C.

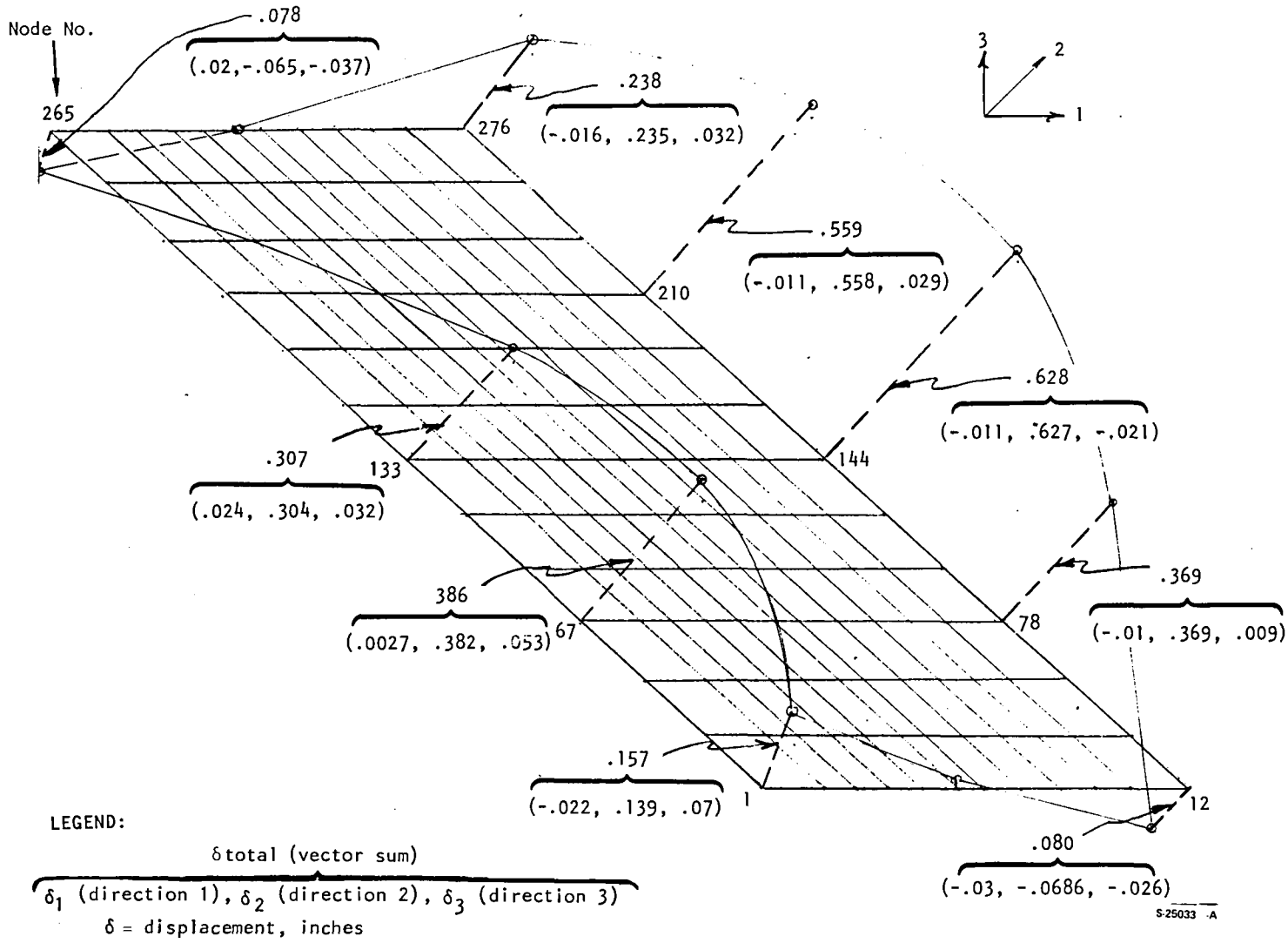

Figure 68.-Starboard wall displacements.

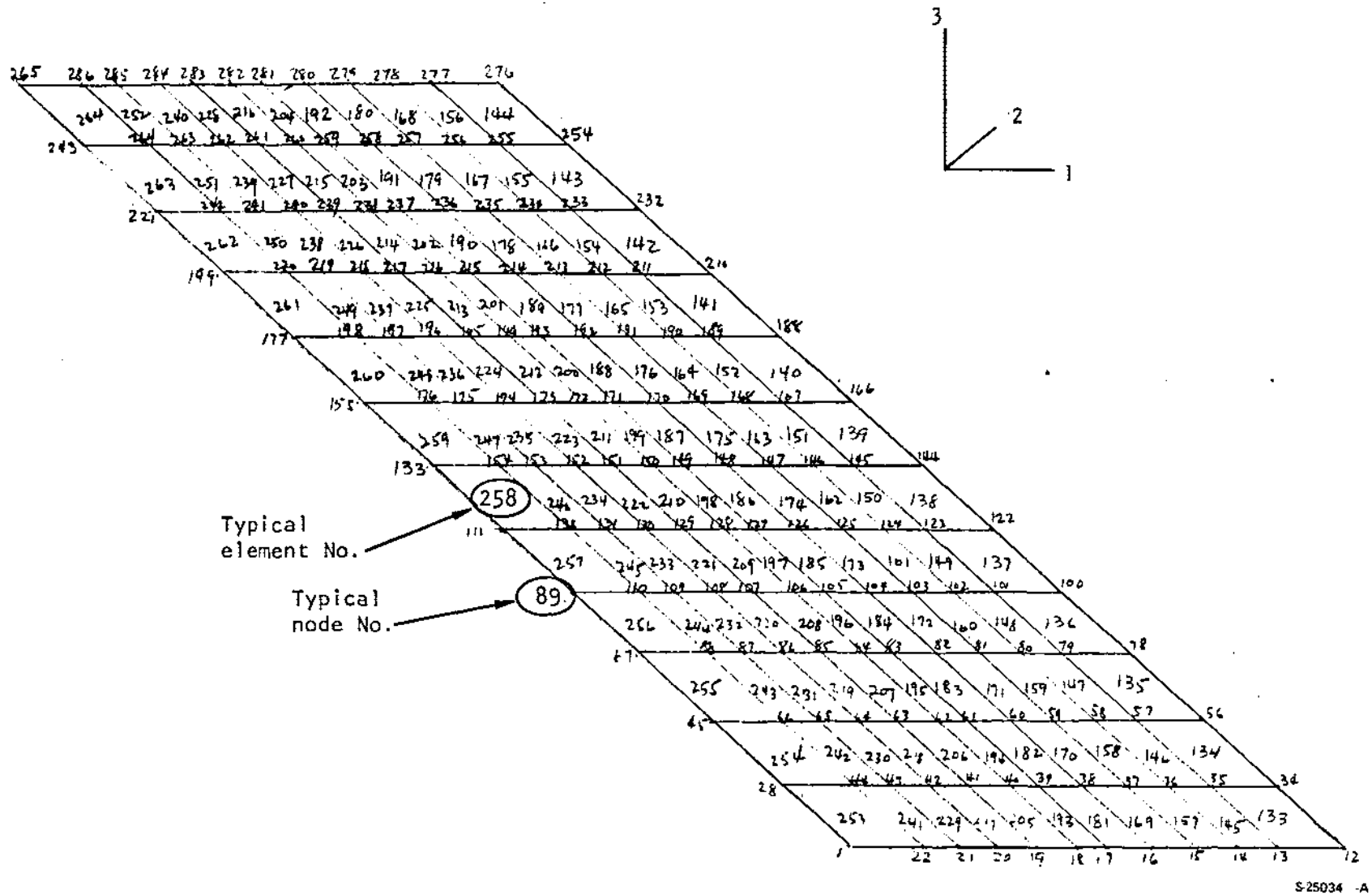

Figure 69.-Starboard wall schematic

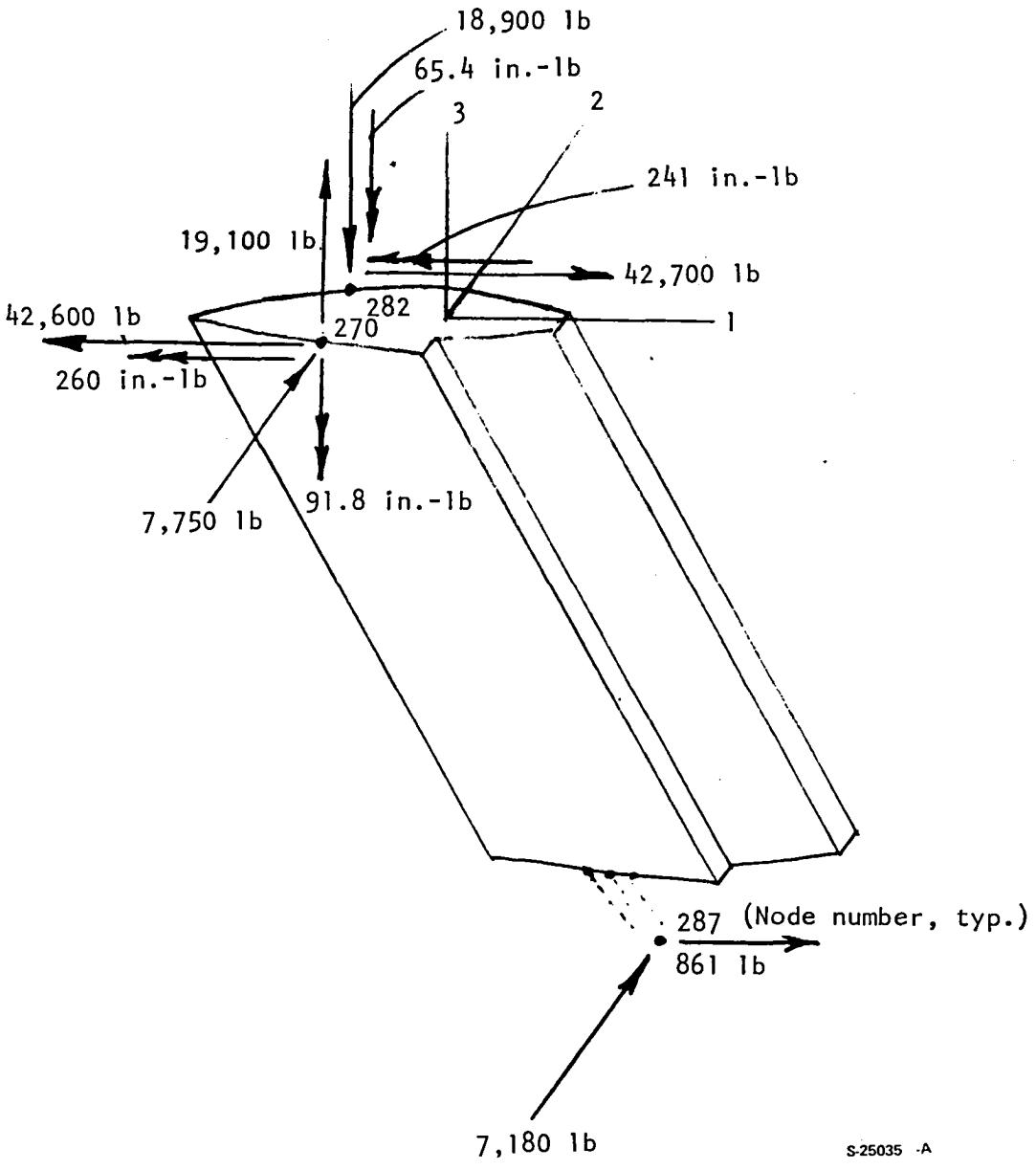

Figure 70.-Reactions at constrained degrees of freedom, SPAR output

with the assumption of a symmetrical unstart loading, only one-half of the structure needed to be considered for the analysis.

To limit the size of the problem, the structure was divided into three convenient substructures, or superelements, as follows:

- A substructure of the side strut
- A substructure of the topwall
- A substructure of the seal between the side strut and the topwall

The theory behind creating a substructure or a superelement is analogous to the process of mass-lumping reduction commonly used in the dynamic analysis. The stiffnesses (and masses) for a specified degree of freedom at selected nodes are retained as the characteristics of a superelement, whereas the remaining degrees of freedom are eliminated. The retained degrees of freedom are called active degrees of freedom. Such a superelement can then be used in any of the subsequent analysis simply as another type of element. The details of each of these substructures are described in the followng paragraphs.

For a given loading condition, a specified set of displacements has to be imposed as boundary conditions along the edges of the isolated portion of the topwall and the side strut interface with the cowl. The results of the all-honeycomb 3-D analysis of the overall structure was used in defining the boundary conditions. These boundary conditions already include the effects of the side walls, cowl, and center strut.

Substructure No. 1, Side Strut: A finite element model of the side strut (with the AiResearch-derived structural configuration) was previously prepared by NASA for analysis with the SPAR computer program and was made available to AiResearch. The walls, ribs, and webs of the side strut were modeled using thin shell finite elements. A card deck of the SPAR finite element model of the side strut was received from NASA. The deck contained information regarding the geometry and the loading condition for which the strut was analyzed.

The geometry of the SPAR model of the side strut was converted by AiResearch for use with the ANSYS computer program; however, the order of the elements as converted from the SPAR model had an exceptionally high element wavefront of 1650, which is too large to be analyzed using the ANSYS program. A wavefront optimization program developed by AiResearch was utilized to rearrange the order of the elements, which reduced the element wavefront to 210. Computer plots of the reordered model are shown in fig. 71

In the SPAR model, 18 in. of the side strut above the cowl had been considered for analysis. For the present analysis, the model has been modified in order to locate the strut modes at the seal level to correspond with the adjacent nodes in the topwall. The modified strut model has a total of 476 elements and 331 nodes with 1983 active degrees of freedom.

The location and orientation of the coordinate axes used in defining the ANSYS strut model are identical to the ones used for the SPAR strut model.

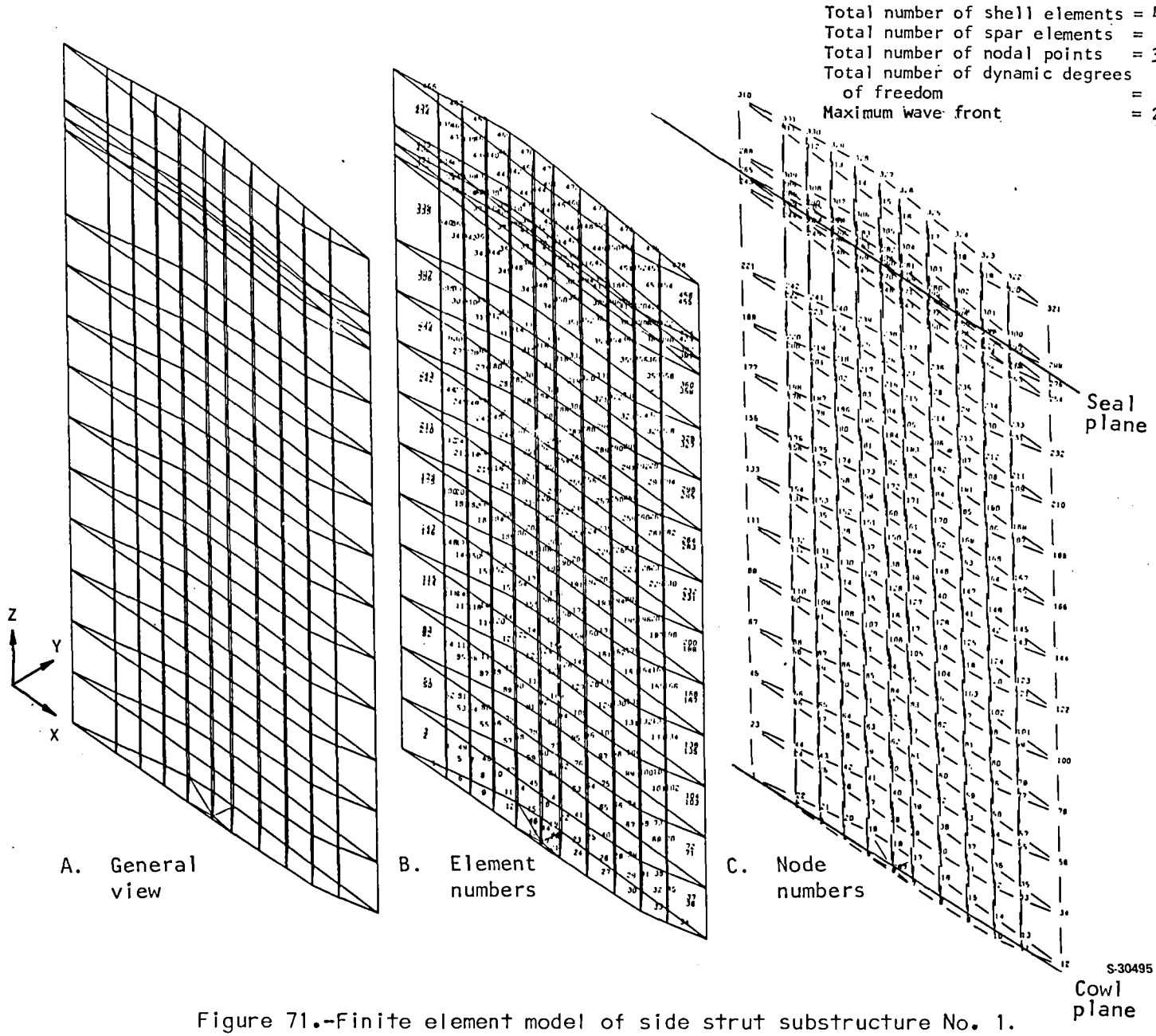

Figure 71.-Finite element model of side strut substructure No. 1.

The material used in the side strut for primary structure is Inconel 718. The material properties were assumed to be isotropic and are identical to the ones used for the SPAR strut model. The temperature dependence of the material properties was accounted for by varying their values in accordance with the actual temperature distribution of the relevant areas, and were as follows:

Young's modulus	$E = 24.5 \times 10^6$ at T = 960°F to 29.6×10^6 psi at T = 78°F
Poisson's ratio	$\mu = 0.29$
Coefficient of thermal expansion	$\alpha = 7.1 \times 10^{-6}$ at T = 78°F to 8.3×10^{-6} in./in./°F at T = 960°F
Density	$\rho = .296$ lb/cu in.
Stress-free temperature	T = 78°F

In a substructure analysis, two types of boundary conditions need to be considered as follows:

- Constraints at specified nodes to reproduce the physical support conditions and imposed deflections, if any.
- Active degrees of freedom at selected nodes to retain the characteristics of the substructure for use in the later analysis. Note that the imposition of the constraints can be delayed to a later run by retaining the corresponding degrees of freedom as the active degrees of freedom.

For the substructure of the side strut, the following boundary conditions were specified:

(a) Nodes 265 through 286: These nodes are located on the strut surface at the seal level above the intersection of the side strut and the topwall. The translation degrees of freedom in the X, Y, and Z directions were retained as active degrees of freedom for use in the analysis of substructure No. 3 (see fig. 72).

(b) Node 287: This node represents the location of the sliding ball joint at the bottom of the side strut and the cowl. Specified displacements from the previous 3-D analysis model have to be imposed here as support constraints. However, instead of imposing the specified displacements at this stage, the translation degrees of freedom in X, Y, and Z directions were retained as active degrees of freedom at the node. The corresponding specified displacements were imposed during the analysis of substructure No. 3.

(c) Nodes 293 and 305: These nodes represent the locations of the top hinge on the side strut. The translation degrees of freedom in X,

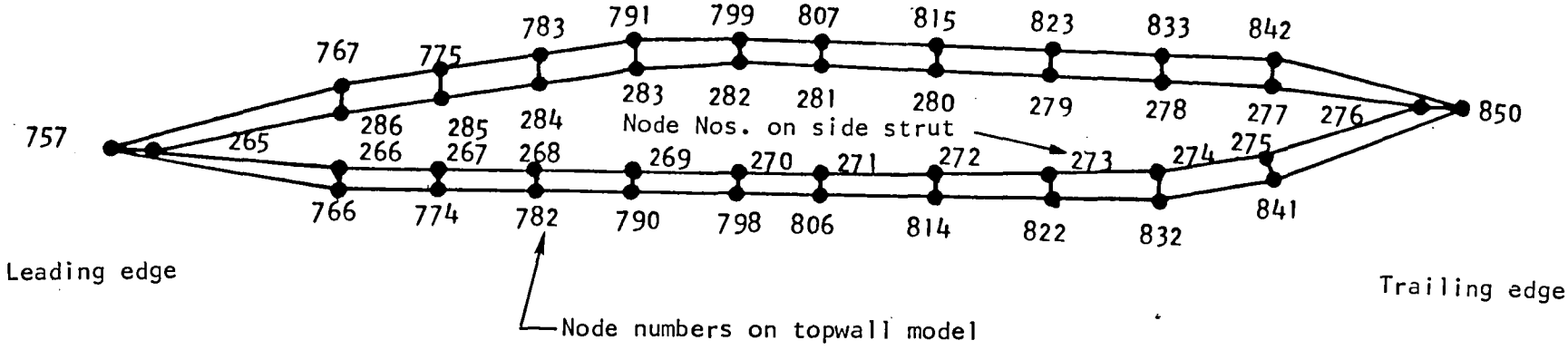

Total number of super elements (substructures)	= 2
Total number of 3-D interface elements	= 22
Total number of nodal points	= 49
Maximum wave front	= 138

Notes

1. Schematic diagram shows relative position of nodes in the topwall and side strut substructures at seal level. Each set of two nodes is connected by a 3-D interface element representing the seal action.

2. Nodes 287, 293 and 305 of the side strut model and nodes 998 and 999 of the topwall model are not shown on this schematic diagram.

S-30491

Figure 72.-Finite element model of seal between the side strut and the topwall, substructure No.3.

Y, and Z directions were retained as active degees of freedom. These degrees of freedom are required during the analysis of substructure No. 3 for coupling with the appropriate degrees of freedom of the corresponding nodes on the topwall to reproduce the hinge.

Thus, the finite element model of the side strut with 1983 active degrees of freedom was reduced to a substructure with only 75 active degrees of freedom.

The inertia load input to the ANSYS computer program consists of specifying a g factor. For the substructure of the side strut, a 2-g downward load factor was used. The format of the temperature and pressure loading data of the SPAR strut model had to be converted for use with the ANSYS strut model. In the SPAR strut model, the pressure loading was specified at the element nodes. For the ANSYS strut model, a constant pressure over the element obtained by averaging the nodal values has been specified.

Substructure No. 2, Topwall: A portion of the topwall incorporating the strut support and seal assembly (engine stations 27.7 to 41.5) was modelled using three-dimensional solid and membrane isoparametric finite elements. The effects of the grooves, holes, and local geometric variations have not been included in the model. The finite element model shown in fig. 73 has a total of 490 elements and 684 nodes with 2052 active degrees of freedom. The cross-sections through the solid elements shown in figs. 74 and 75 illustrate the layout of the finite element idealization in various planes.

The portion of the topwall under consideration includes a very small region of the honeycomb cells. Consequently, for convenience it was decided to represent the honeycomb cells using the solid elements having isotropic material properties only. The seal area is located at least two rows of solid elements away from the honeycomb cells. Hence, the assumption of representing the honeycomb cells using isotropic solid elements will not have any significant effect on assessing the performance of the seal.

As shown in fig. 76, the cold face sheet and TPS and hot face sheet are represented with membrane elements attached to the solid elements on the outside and inside faces of the topwall, respectively. The TPS and hot face sheet were combined as one stiffness represented by a single isoparametric membrane element (0.08 in. thick). The cold face sheet is represented by an isoparametric membrane element (0.06 in. thick). The layout of such membrane elements is shown in fig. 77. Once again, the location and orientation of the coordinate axes used in defining the topwall model are identical to the ones used for the SPAR strut model.

The material used in the entire top panel is assumed to be Hastelloy X. The material properties were specified as isotropic and the Young's modulus was allowed to vary linearly with temperature. The material properties are similar to the ones used for the topwall analysis conducted earlier in the program and are as follows:

Young's modulus	$E = 28.73 \times 10^6 - (3152 \times \text{Temperature in } °F)$ psi
Poisson's ratio	$\mu = 0.32$

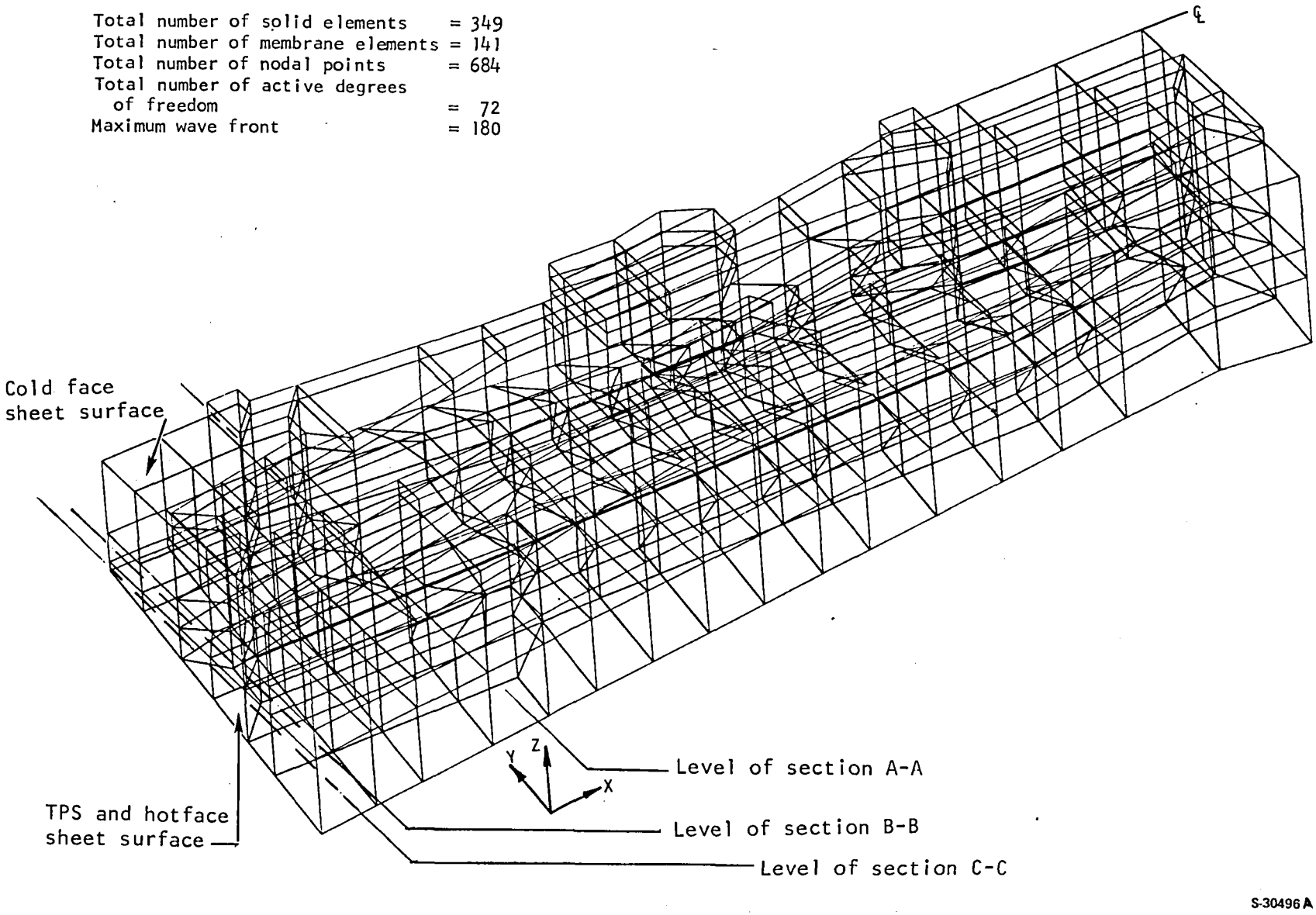

Figure 73.-NASA Scramjet, finite element model of the topwall (substructure No. 2). (Sections A-A, B-B and C-C are parallel to X-Y plane and are shown in figure 74).

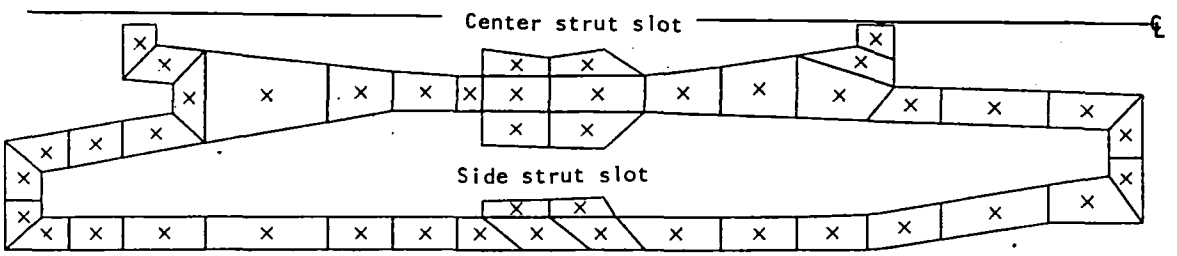

Section A-A (See fig. 73)

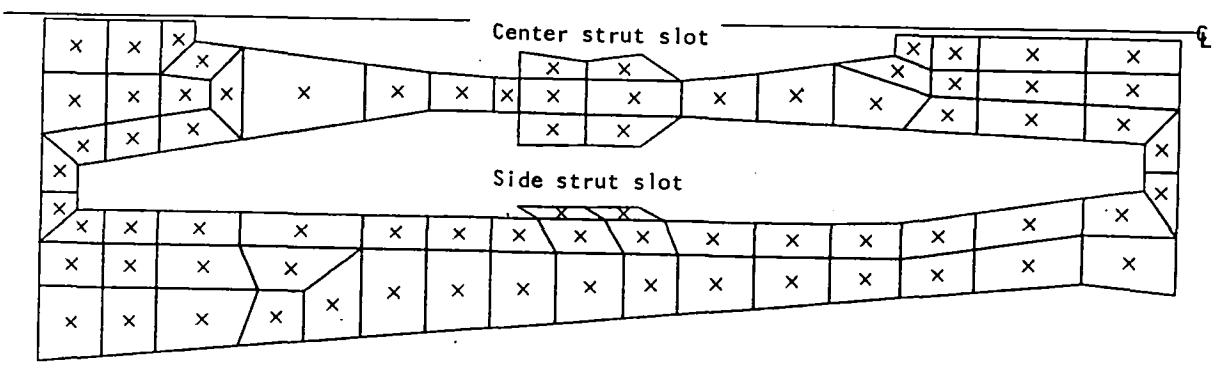

Section B-B (See fig. 73)

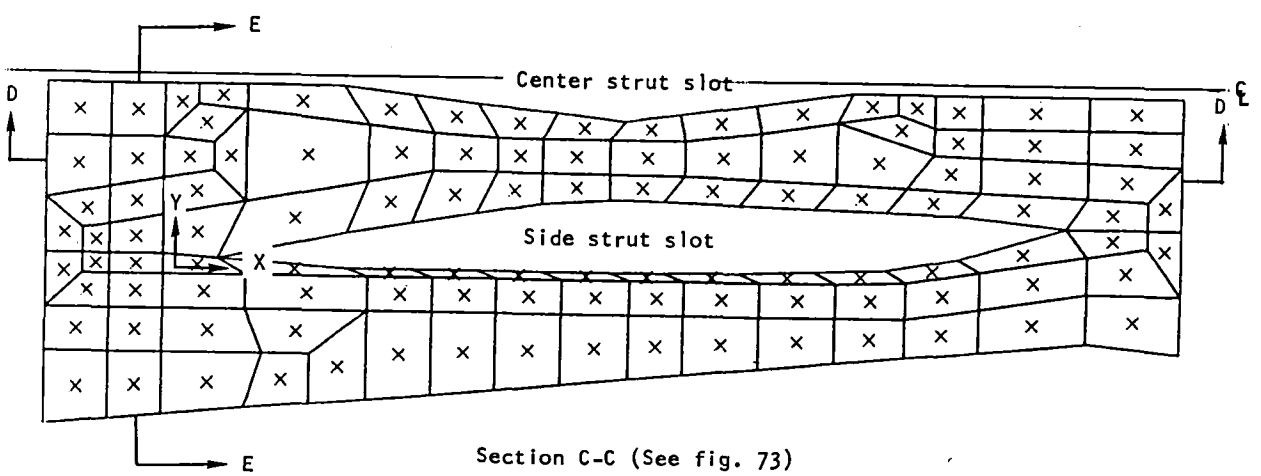

Section C-C (See fig. 73)

S-30492

Figure 74.-NASA Scramjet, typical horizontal sections (parallel to X-Y plane) through 3D solid finite elements of substructure No. 2 (topwall).

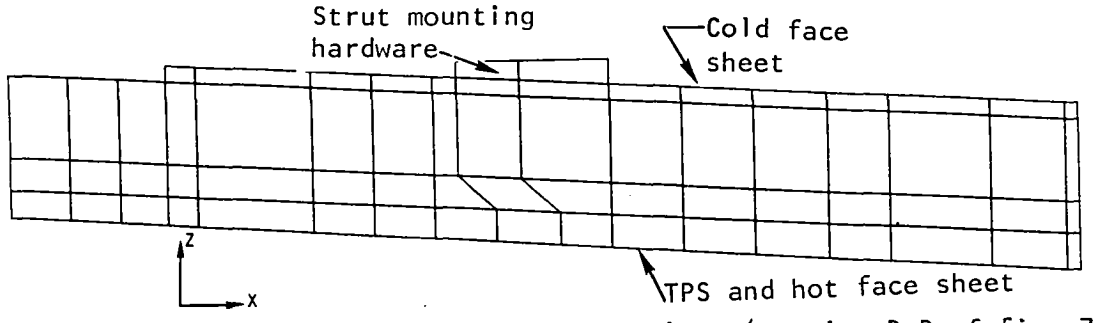

A. A section parallel to X-Z plane (section D-D of fig. 74)

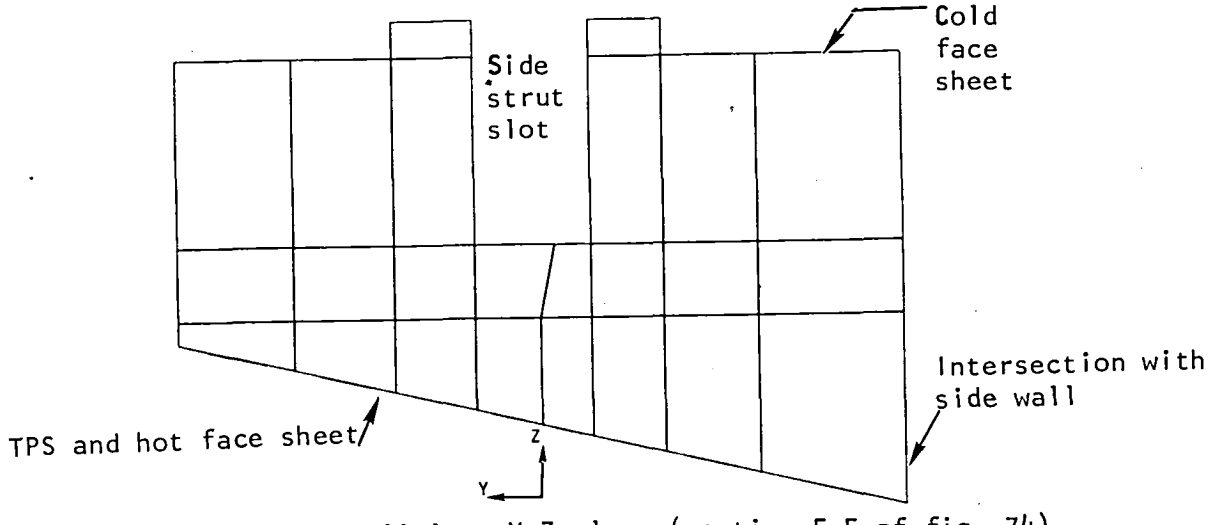

B. A section parallel to Y-Z plane (section E-E of fig. 74) S-30493A

Figure 75.-NASA Scramjet, vertical sections through 3D solid finite elements of substructure No. 2 (topwall).

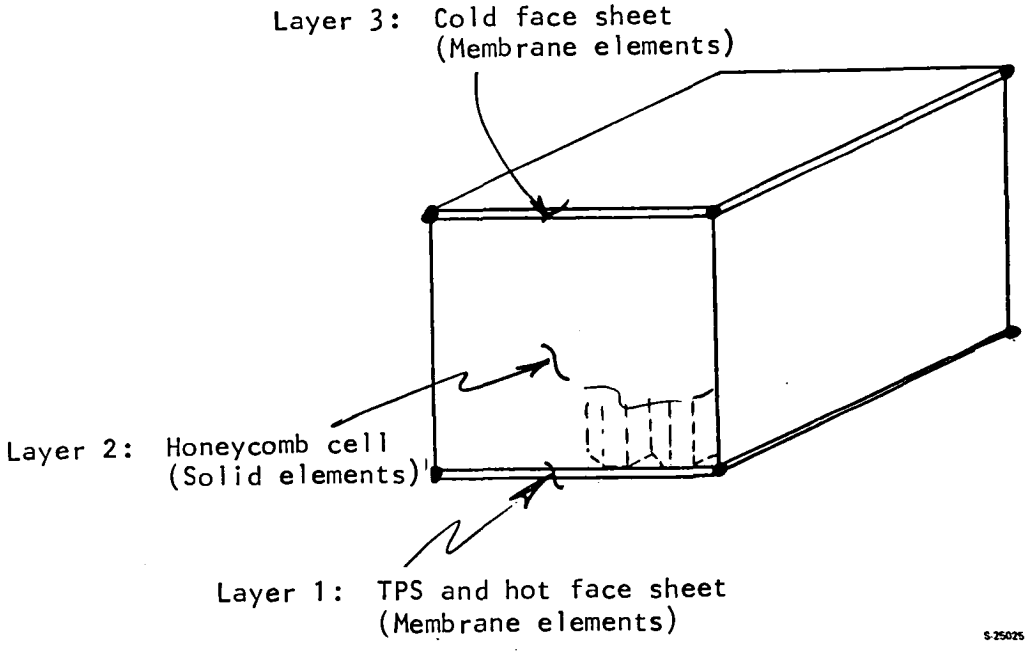

Figure 76.-Finite element representation of the layered honeycomb model.

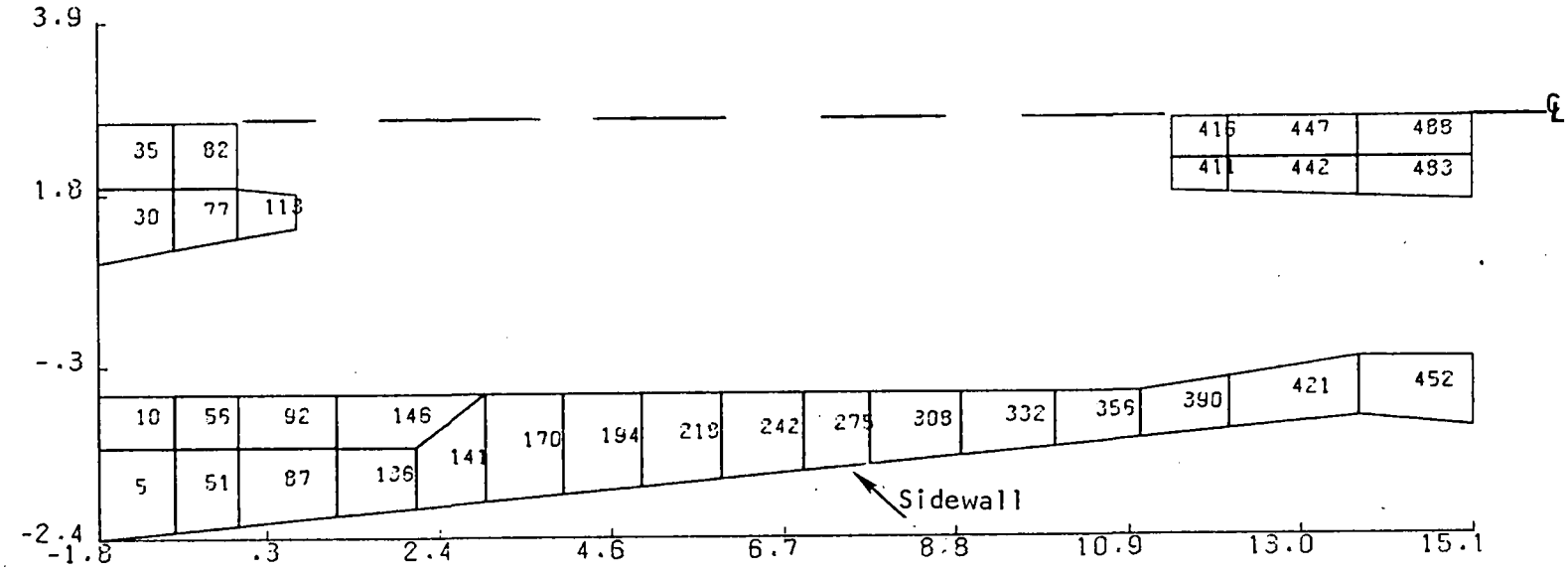

A. Cold face sheet (thickness = 0.060 in.)

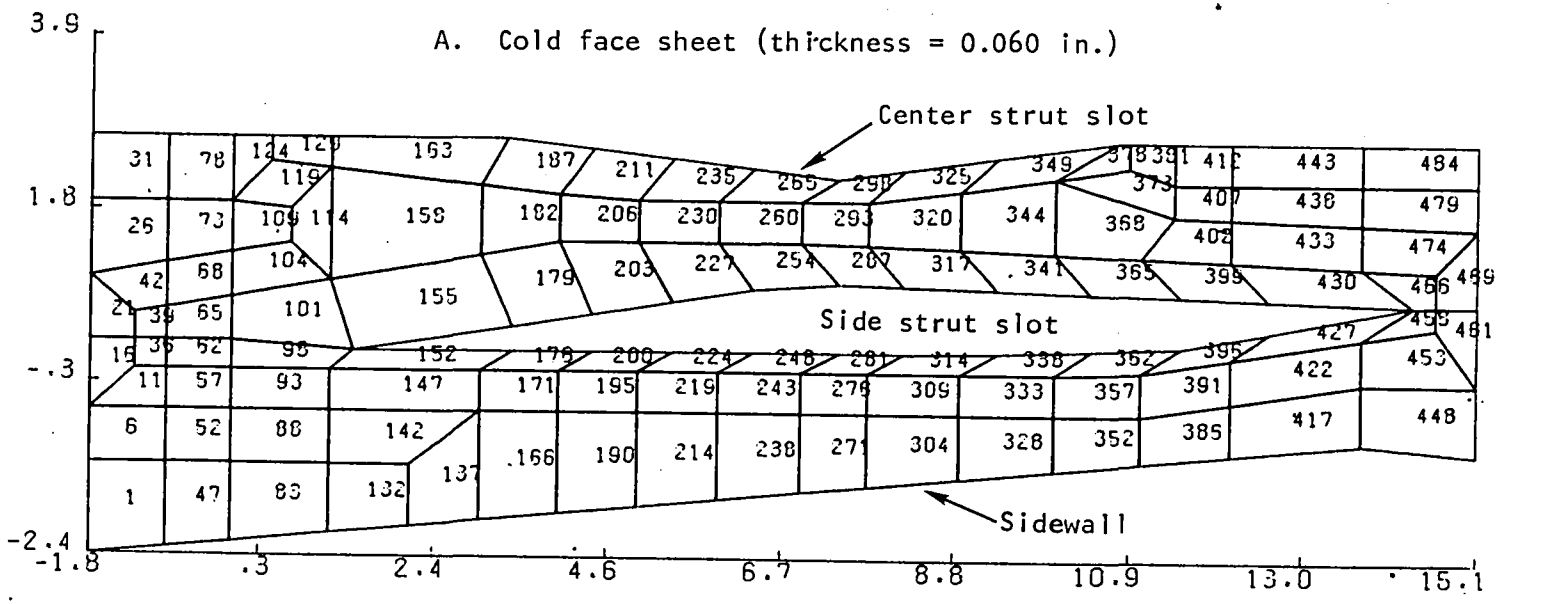

B. TPS/hot face sheet (thickness = 0.080 in.)

S-30494

Figure 77.-NASA Scramjet, layout of membrane finite elements to represent the cold and TPS/hot sheets in substructure No. 2 (topwall).

Coefficient of thermal expansion	$\alpha = 7.7 \times 10^{-6}$ in./in./°F
Density	$\rho = 0.300$ lb/cu in.
Stress-free temperature	T = 78°F

As mentioned earlier, the following two types of boundary conditions need to be specified in the substructure analysis:

- Constraints at specified nodes to reproduce the physical support conditions and imposed deflections, if any.
- Active degrees of freedom at selected nodes to retain the characteristics of the substructure for use in subsequent analyses.

For the substructure of the top panel, the following boundary conditions were specified:

(a) Nodes along the plane of symmetry: The translation degree of freedom along the Y axis was constrained.

(b) Nodes along the four isolating planes (edges of the model): The deflections from the previous all-honeycomb 3-D finite element analysis were imposed as boundary conditions for the translation degrees of freedom along X, Y, and Z axes. Note that in the 3-D model, the deflections and rotations are computed at the midplane of the topwall. In the present model there are at least three solid elements through the thickness of the topwall. Consequently, the computed deflections at the mid-plane had to be adjusted on the basis of the computed rotations at the mid-plane to determine the imposed translations through the thickness of the topwall (see fig. 78).

(c) Nodes 757, 766, 767, 774, 775, 782, 783, 790, 791, 798, 799, 806, 807, 814, 815, 822, 823, 832, 833, 841, 842, and 850: These nodes on the topwall are located at the intersection of the topwall and the side strut at the seal area. The translation degrees of freedom in the X, Y, and Z directions were retained as active degrees of freedom for use in the analysis of substructure No. 3 (see fig. 72).

(d) Nodes 998 and 999: These nodes represent the locations of the support for the top hinge of the side strut. The translation degrees of freedom in X, Y, and Z directions were retained as active degrees of freedom. These degrees of freedom are required during the analysis of substructure No. 3 for coupling with the appropriate degrees of freedom of the corresponding nodes on the side strut to reproduce the top hinge.

With these boundary conditions, the finite element model of the top panel with 2052 active degrees of freedom was reduced to a substructure with only 72 active degrees of freedom.

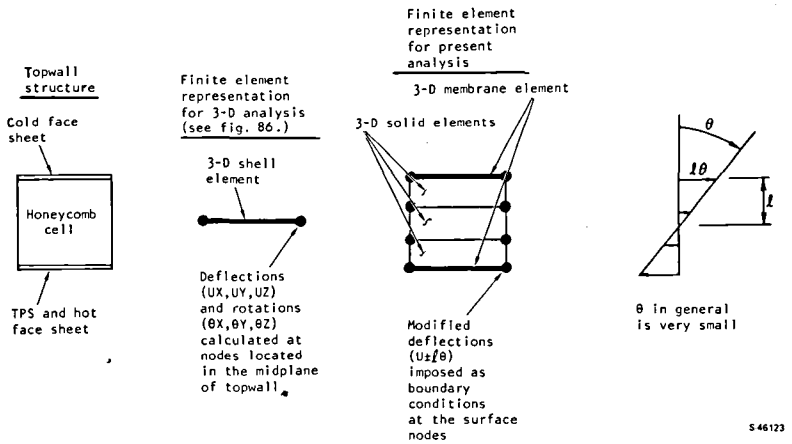

Figure 78. NASA Scramjet, derivation of boundary conditions for substructure No. 2

Once again, the inertia load input to the ANSYS computer program consists of specifying a "g" factor. For the substructure of the top panel, a 2-g downward load factor was used.

The engine unstart pressure distribution was defined by NASA-LaRC. Pressure distribution for the region under consideration here is shown in fig. 79.

An isotherm plot of the TPS hot face sheet temperature distribution was generated as part of the topwall thermal analysis, which is reported in another section of this document. The corresponding temperature distribution for the region under consideration here is shown in fig. 80a. The temperature distribution for the cold face sheet and through the thickness of the topwall shown in fig. 80b was also derived by interpolation from the ones used in the topwall analysis.

Substructure No. 3, Seal Between the Side strut and the Topwall: This substructure forms an interface between the side strut and the topwall and is located at the intersection of the two substructures, as shown in fig. 72. The finite element model consists of 22 three-dimensional interface elements representing the action of the seal. The geometry of the substructure model is already established by the previous two substructures.

The three-dimensional interface element represents two parallel surfaces in space which may maintain or break physical contact and may slide relative to each other in the directions parallel to the surfaces. The interface element is capable of supporting only compression in the directions normal to the surfaces. An initial clearance or gap between the two surfaces can be specified for the interface elements. The amount of specified initial clearance has a significant effect on the magnitude of the compressive force which develops between the two surfaces if they come into contact, or on the magnitude of the separation between the two surfaces if they don't come into contact. The clearance represents the deflection necessary for the seal prior to reacting the load between the topwall and strut. The amount of separation between the strut and topwall surfaces in excess of the initial clearance represents the

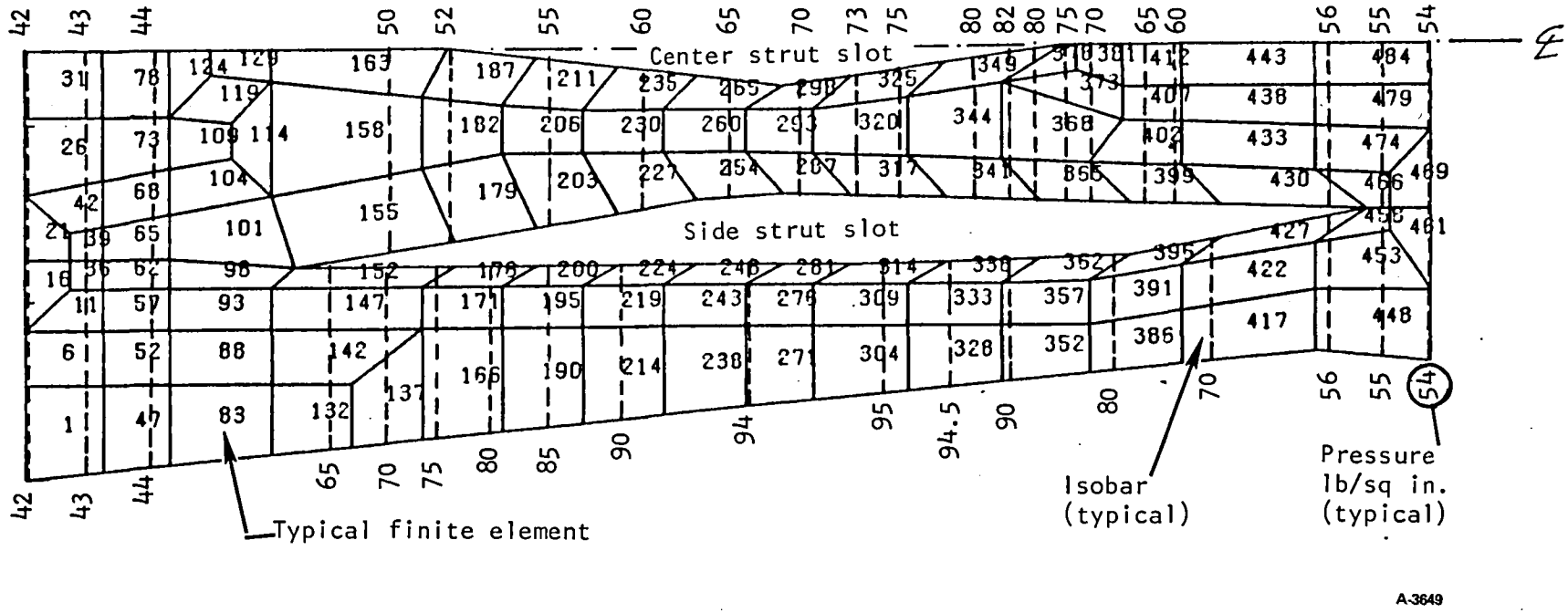

Figure 79.-NASA Scramjet, pressure distribution in substructure No. 2 (topwall) for symmetrical unstart condition, lb/sq in.

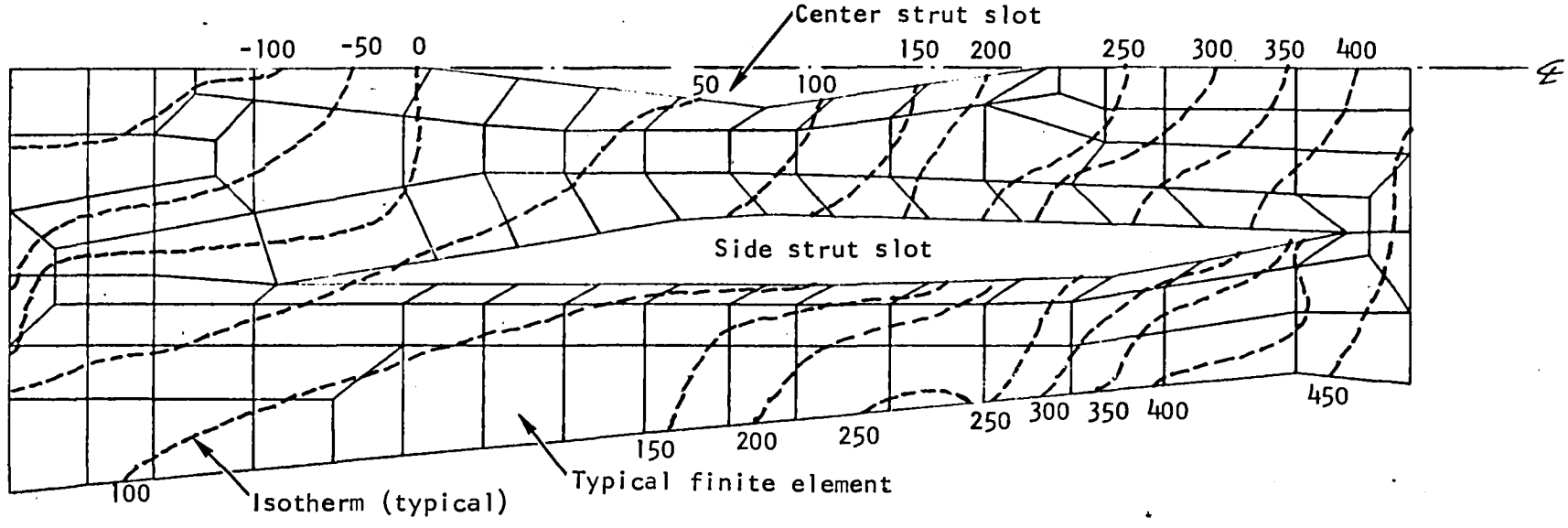

A. TPS/hot face sheet isotherms (°F)

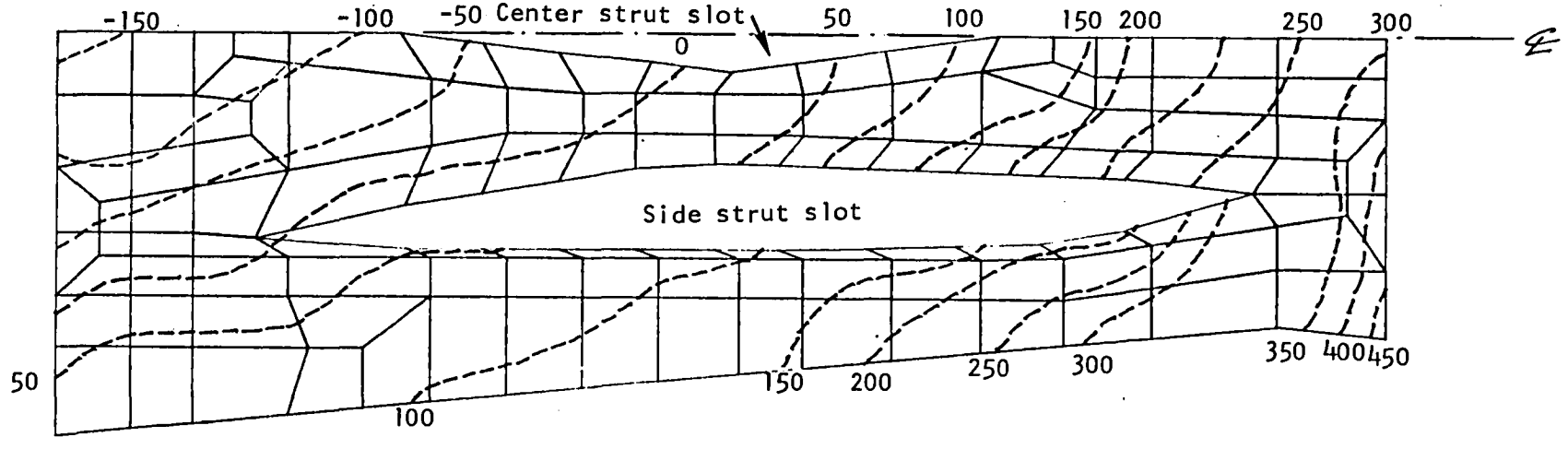

B. Cold face sheet and top wall isotherms (°F)

A-3652

Figure 80.-NASA Scramjet, temperature distribution in substructure No. 2 (topwall) for symmetrical unstart condition.

deflection the seal must accommodate to maintain sealing contact. To evaluate and to arrive at an acceptable performance of the seal, substructure No. 3 was analyzed for three different cases of initial clearance as follows:

- Case 1, initial clearance = 0.000 in.
- Case 2, initial clearance = 0.010 in.
- Case 3, initial clearance = 0.020 in.

With the use of interface elements, an iterative solution can be performed for each case to achieve equilibrium in all the interface elements. The performance of the seal can be observed from the status of the interface elements at equilibrium. The output for such elements includes the width of separation if the surfaces are not in contact, normal force if the surfaces are in contact, and the sliding movement.

This provides a definition of strut and topwall deflections in the seal area which must be accommodated by the seal and strut and seal reactions for different seal deflections.

The only material property required for an interface element is the coefficient of friction, which in the present analysis is assumed to be zero.

The following boundary conditions were specified:

(a) Node 287: As mentioned earlier, this node represents the location of the sliding ball joint at the bottom of the side strut and the cowl. The deflections from the previous all-honeycomb 3-D finite element analysis were imposed as boundary conditions for the translation degrees of freedom along X, Y, and Z directions.

(b) Nodes 293/998 and 305/999: These pairs of nodes correspond to the location of the top hinge between the strut and the topwall. The translation degrees of freedom along X, Y, and Z directions were coupled between each pair of nodes to simulate the hinge effect.

The initial clearance between the side strut and the topwall is included as a real constant specification for each element.

The inertia, pressure, and temperature loading on the side strut and the topwall are already included in the analysis of substructure Nos. 1 and 2, respectively, and no addiitonal loading needs to be specified for analyzing substructure No. 3.

Results and Conclusions: The analysis results for the three cases are summarized in Tables 14 through 16 and in fig. 81. The tables list a compression load or clearance in the directions normal to the surfaces and relative sliding displacements in the directions parallel to the surfaces for each pair.

TABLE 14.-NASA SCRAMJET, SUMMARY OF THE SEAL BEHAVIOR BETWEEN THE SIDE STRUT AND THE TOPWALL (CASE 1 - INITIAL CLEARANCE = 0.0 IN.)

Node Number On Side Strut Model	Node Number On Top Wall Model	Compression Force, lb 	Separation Distance, in. 	Relative Sliding Between Side Strut and Top Wall, in.	
				Horizontal X-Y Plane 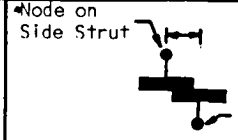	Vertical X-Z or Y-Z Plane 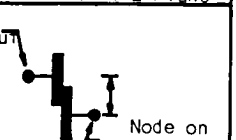
265	757	16990		0.02341	0.04461
266	766	1294		0.00918	0.03525
267	774		0.00074	0.00976	0.03082
268	782		0.00034	0.00999	0.02831
269	790	1890		0.01248	0.01581
270	798	5957		0.00870	0.02119
271	806	712		0.01295	0.02656
272	814	2647		0.01614	0.03173
273	822	682		0.01875	0.03498
274	832	76		0.02084	0.03704
275	841	496		0.02257	0.03768
276	850		0.02258	0.00811	0.03846
277	842		0.00021	0.02038	0.03659
278	833	359		0.01858	0.03400
279	823	95		0.01652	0.02949
280	815	2161		0.01406	0.02327
281	807	786		0.01105	0.01600
282	799	7070		0.00738	0.01025
283	791	2105		0.00991	0.00877
284	783		0.00020	0.01009	0.01769
285	775	720		0.01060	0.02353
286	767		0.00092	0.01057	0.03027

NOTE: 1 If compression is greater than zero, no separation exists.

2 If separation is greater than zero, no compression exists.

3 Where no value is listed, the value is zero.

TABLE 15.-NASA SCRAMJET, SUMMARY OF THE SEAL BEHAVIOR BETWEEN THE SIDE STRUT AND THE TOPWALL (CASE 2 - INITIAL CLEARANCE = 0.010 IN.)

Node Number On Side Stress-Model	Node Number On Top Wall	Compression Force, lb 	Separation Distance, in. 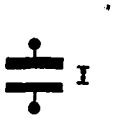	Relative Sliding Between Side Strut and Top Wall, in.	
				Horizontal X-Y Plane 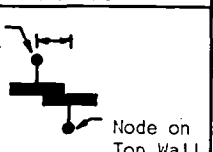	Vertical X-Z or Y-Z Plane 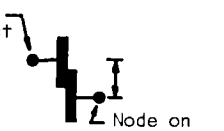
				Node on Side Strut / Node on Top Wall	Node on Side Strut / Node on Top Wall
265	757	5364		0.00285	0.04149
266	766		0.01506	0.01325	0.03396
267	774		0.01454	0.01359	0.02952
268	782		0.01354	0.01282	0.02740
269	790		0.01089	0.01415	0.01570
270	798		0.00764	0.01060	0.02050
271	806		0.00556	0.01490	0.02598
272	814		0.00159	0.01810	0.03116
273	822	150		0.02065	0.03437
274	832		0.00052	0.02276	0.03633
275	841	529		0.02438	0.03716
276	850		0.03361	0.02153	0.03879
277	842		0.02020	0.02136	0.03706
278	833		0.01889	0.01965	0.03445
279	823		0.01880	0.01780	0.02977
280	815		0.01588	0.01539	0.02327
281	807		0.01023	0.01205	0.01589
282	799		0.00608	0.00809	0.01005
283	791		0.00639	0.01055	0.00869
284	783		0.00589	0.01125	0.01739
285	775		0.00513	0.01241	0.02313
286	767		0.00480	0.01248	0.03008

NOTE: 1 If compression is greater than zero, no separation exists.

2 If separation is greater than zero, no compression exists.

3 Where no value is listed, the value is zero.

TABLE 16.-NASA SCRAMJET, SUMMARY OF THE SEAL BEHAVIOR BETWEEN THE SIDE STRUT AND THE TOPWALL (CASE 3 - INITIAL CLEARANCE = 0.020 IN.)

Node Number On Side Strut Model	Node Number on Top Wall	Compression, Force, lb 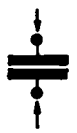	Separation Distance, in. 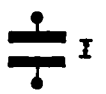	Relative Sliding Between Side Strut and Top Wall, in. Horizontal X-Y Plane 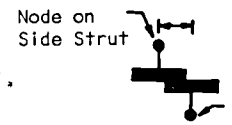	Vertical X-Z or Y-Z Plane 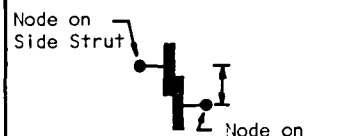
265	757		0.00465	0.02472	0.03922
266	766		0.03619	0.01572	0.03278
267	774		0.03139	0.01584	0.02857
268	782		0.02724	0.01451	0.02677
269	790		0.02229	0.01514	0.01561
270	798		0.01709	0.01175	0.02004
271	806		0.01327	0.01603	0.02555
272	814		0.00683	0.01924	0.03077
273	822		0.00294	0.02171	0.03404
274	832		0.00191	0.02375	0.03604
275	841	589		0.02511	0.03703
276	850		0.04385	0.03365	0.03905
277	842		0.04020	0.02153	0.03731
278	833		0.03749	0.01977	0.03468
279	823		0.03570	0.01786	0.02998
280	815		0.03064	0.01538	0.02345
281	807		0.02251	0.01195	0.01603
282	799		0.01659	0.00796	0.01013
283	791		0.01500	0.01060	0.00861
284	783		0.01219	0.01172	0.01708
285	775		0.00832	0.01351	0.02239
286	767		0.00363	0.01406	0.02906

NOTE: 1 If compression is greater than zero, no separation exists.

2 If separation is greater than zero, no compression exists.

3 Where no value is listed, the value is zero.

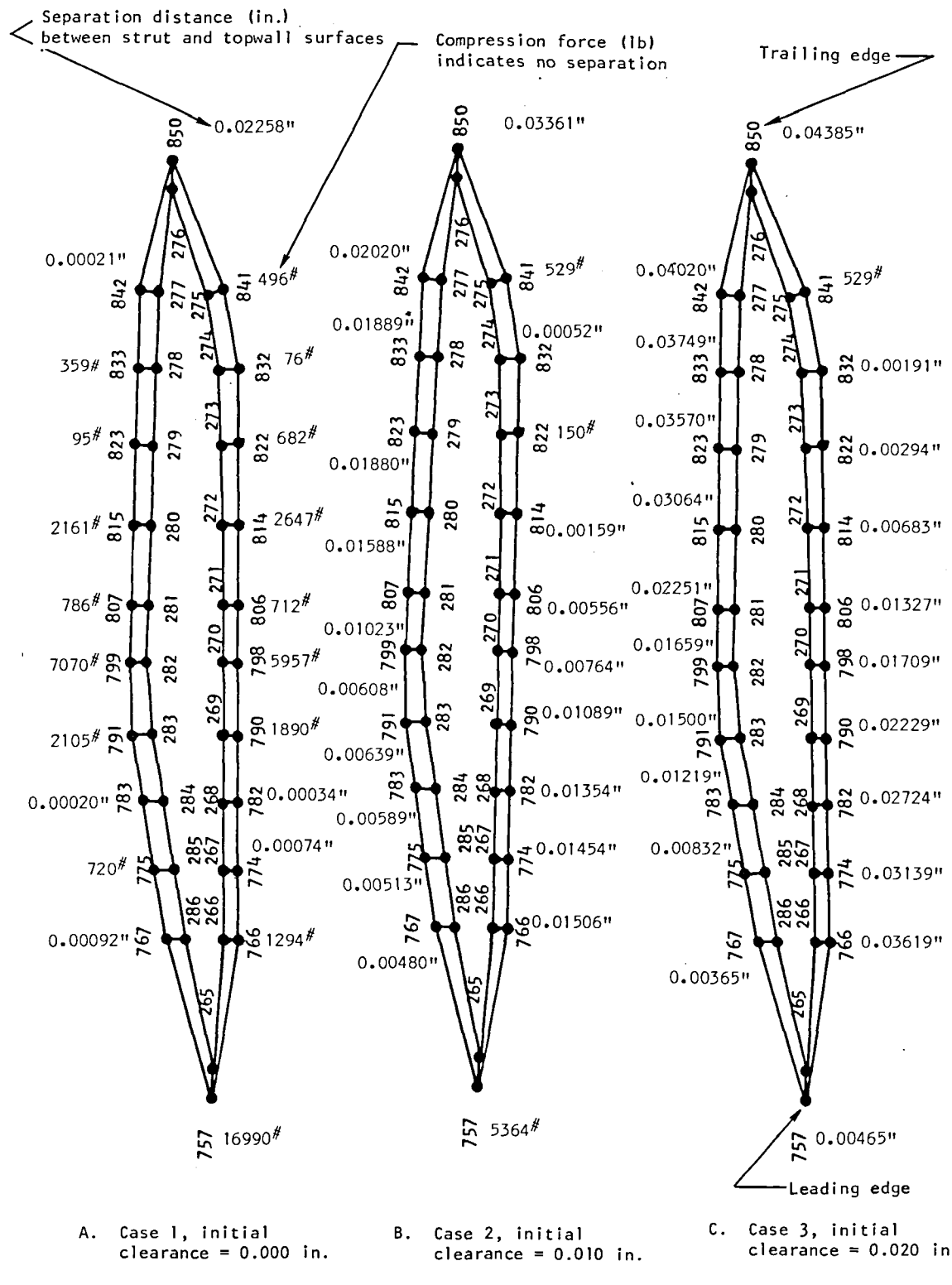

Figure 81.-Summary of seal performance for three different cases of initial clearance.

of nodes on the strut and topwall surfaces. The displacements parallel to the surfaces are more readily accommodated than those normal to the surfaces; as such, the latter are discussed in more detail. For the first two cases with initial clearance of 0.000 in. and 0.010 in., respectively, the side strut and the topwall come in contact at the leading edge and develop a high contact force. This situation could occur either due to an actual clearance of the value specified or by a rather rigid seal which would support the interface load with a deflection of the value specified. A force of this magnitude could cause surface damage over the small surface area of the leading edge. However, if the initial clearance is increased to 0.020 in., the side strut and the topwall remain separated by 0.0046 in., and no contact force is developed. This is a much more desireable situation. However, at the trailing edge, the side strut and the topwall are separated by 0.044 in., indicating that in addition to the initial specified clearance of 0.020 in., the two surfaces have moved further apart by 0.024 in. In this case, the seal must be capable of accommodating the extra separation of 0.024 in. in order to prevent leakage.

Any increase in initial clearance larger than 0.020 in. aggravates the situation by the resulting increase in the separation of the side strut and the topwall at the trailing edge. Thus, a seal design that represents an initial clearance of around 0.020 in. appears to offer an acceptable and near optimum solution. A seal that will provide sealing over a deflection range of 0.02 in. in compression to 0.024 in. in expansion while maintaining some resiliency will meet this requirement. Although details of the seal design have not been defined, the seal requirements identified in this analysis appear consistent with the seal design concept depicted in the layout drawings.

The deflections at the nodes equivalent to the top edge of the SPAR side strut model summarized in Table 17 are included from the Case 3 analysis, having an initial clearance of 0.020 in. These deflections can be specified as imposed deflections on the SPAR strut model for further analysis if desired.

Primary Structure

Three-dimensional finite element models.--The original reference design of the primary structure used a combination of beams and honeycomb to contain the high-pressure airflow. The concept, shown in fig. 82, included seven beams located parallel to the engine sweep line. Details shown in fig. 82 include the clip concept used to secure the beams to the honeycomb (the clip concept is discussed in ref. 3).

Two other structural concepts were considered in this study. The first is similar to the reference design except that the beams are oriented vertically (normal to the airflow). The second is an all-honeycomb design in which most of the beams were eliminated in favor of a thicker honeycomb structure.

TABLE 17.-NASA SCRAMJET, BOUNDARY CONDITIONS FOR THE SPAR SIDE STRUT MODEL (CASE 3 - INITIAL CLEARANCE = 0.020-IN.)

Node Number on Side Strut-Model	Deflections, in.		
	X	Y	Z
265	-.153838E-1	.247199E-1	.396306E-1
266	-.156787E-1	.161894E-1	.329433E-1
267	-.159497E-1	.114393E-1	.288263E-1
268	-.148768E-1	.702329E-2	.270170E-1
269	-.160220E-1	.276097E-2	.172734E-1
270	-.122562E-1	-.249988E-2	.208606E-1
271	-.163906E-1	-.667433E-2	.258358E-1
272	-.193956E-1	-.132132E-1	.308890E-1
273	-.218097E-1	-.170850E-1	.340582E-1
274	-.237872E-1	-.180936E-1	.360365E-1
275	-.251289E-1	-.200435E-1	.370201E-1
276	-.239257E-1	-.336449E-1	.390392E-1
277	-.218462E-1	-.202358E-1	.376660E-1
278	-.202252E-1	-.177311E-1	.360149E-1
279	-.183337E-1	-.164497E-1	.334283E-1
280	-.158212E-1	-.123910E-1	.299888E-1
281	-.126516E-1	-.525781E-2	.255728E-1
282	-.903118E-2	.453215E-3	.214637E-1
283	-.119595E-1	.319016E-2	.205799E-1
284	-.123087E-1	.720960E-2	.268857E-1
285	-.137028E-1	.114673E-1	.295479E-1
286	-.142313E-1	.162407E-1	.333468E-1
287	-.134733E-0	-.167059E-2	.804512E-1

NOTE: 1. Nodes 265 - 286 are at the top of the SPAR side strut-model.

2. Node 287 is at the bottom of the SPAR side strut model.

3. Location and orientation of the coordinate axes are identical to the ones used for the SPAR side strut model.

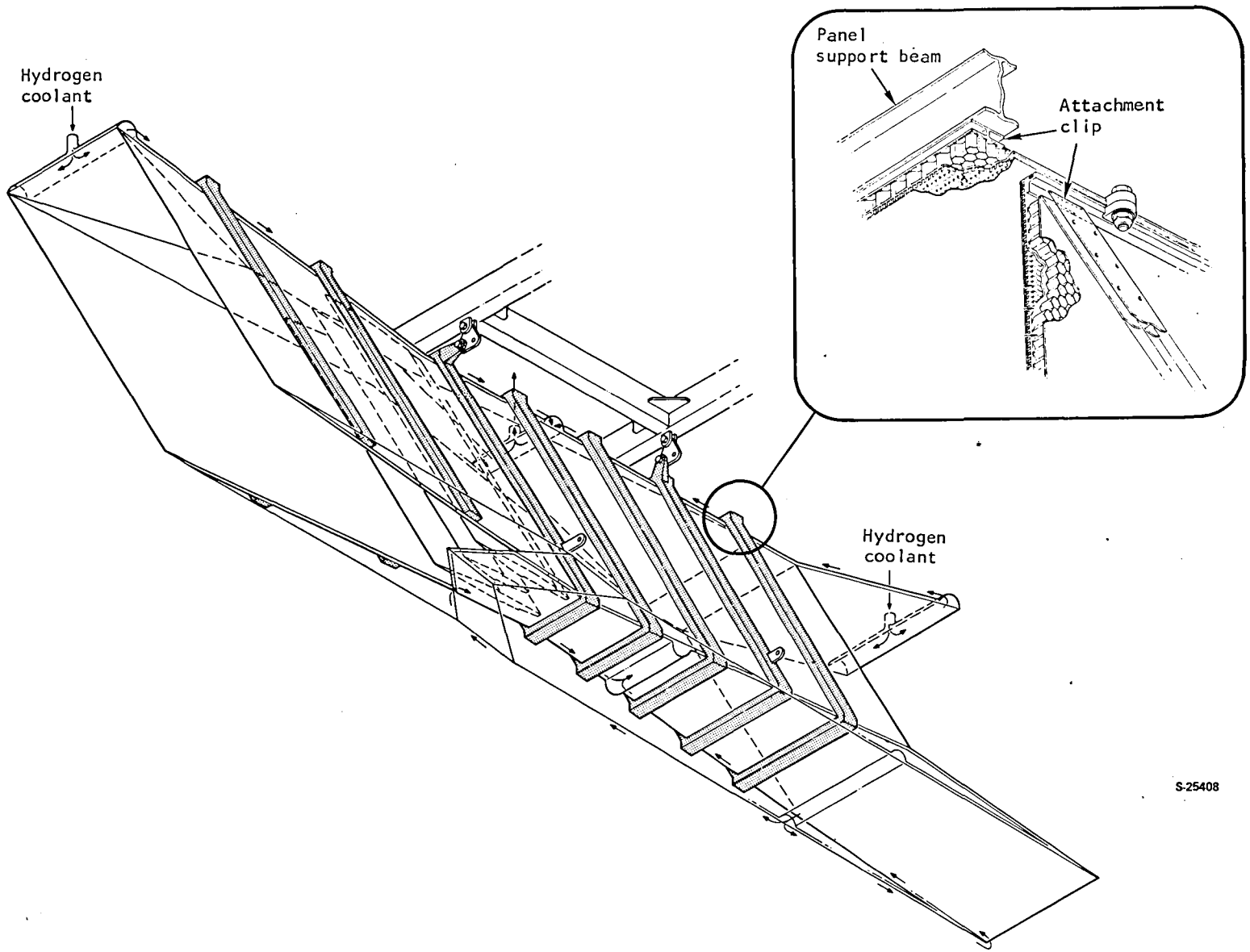

Figure 82.-Primary support structure for swept beam model.

Each of the three structures was analyzed using a large finite element model. Primary structure elements, which include the honeycomb, face sheets, clips, beams, and manifolds, are represented in the finite element models. The contribution of the TPS was neglected. The following elements are typical for all structures:

Honeycomb hot face sheet	1.5 mm (0.060 in.) thick
Honeycomb cold face sheet	1.3 mm (0.050 in.) thick
Honeycomb cell	6.4 mm (0.25 in.) hexagon, 0.08 mm (0.003 in.) gauge

Panel support beams are I-shaped and are mechanically joined to the attachment clips. Two vertical beams, located at the module mount locations, are retained in the all-honeycomb concept to help distribute the inertial loads. The beam-to-beam connections are rigidly joined and, in the combustor area, the beams form a continuous frame. In the swept and vertical beam models the panels are permitted to move with respect to the adjacent panel. Thus, gaps or interferences can occur at the sidewall-to-topwall or sidewall-to-cowl intersections. The panels may also deflect with respect to the adjacent panel in the axial direction.

In addition to the panel support beams, other structural elements that act as stiffening members are as follows:

(a) Coolant inlet and outlet manifolds

(b) Leading and trailing edge structures that also incorporate coolant manifolds

(c) Bottom surface of the cantilevered sidewalls (engine inlet)

(d) Sidewall panel edges--panel-to-panel seal support structure in the swept and vertical beam models

(e) Struts

Each of these elements was represented in the model as an equivalent cross-sectional area and moment of inertia.

The attachment clips are wide flanged beams brazed either to the TPS or to the sandwich panel that supports the TPS. Structural width of each particular clip is constant, but the depth varies from 2.5 to 9.5 mm (0.1 to 0.375 in.) depending on the location. The clips transmit pressure loads to the support beams and frames. Elongated bolt holes are provided in the clip flange to accommodate relative motion between the clip and beam to reduce thermal stresses. Clip geometry used in the analysis is shown in fig. 83.

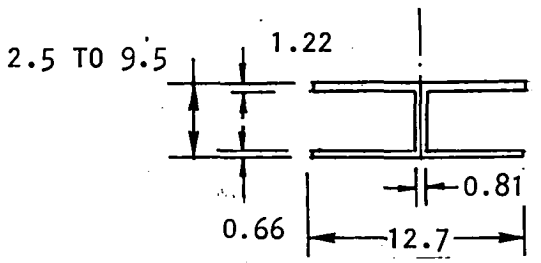

Figure 83.-Clip geometry used in analysis.

Slip between the beam and clip and the eccentricity between the beam and honeycomb structure centroids are represented by an interface element as shown in fig. 84. Slip is represented by stipulating a low coefficient of friction in the interface element along the longitudinal beam axis.

A constant 9.5-mm (3/8-in.)-thickness honeycomb is used for all panels in the swept and vertical beam model except for the external cowl and sidewall panel, which are 6.4-mm (1/4-in.) thick. Distribution of honeycomb thickness for the all-honeycomb model is defined in fig. 85. For the all-honeycomb model, it was assumed that the panel-to-panel intersections are rigidly connected.

Initial computer runs indicated an excessive deflection in the nozzle area, and hence, additional beams oriented along the main engine axis were placed along the topwall edges for reinforcement.

Each fuel injection strut was represented by a single sheet of elements of equivalent stiffness. A midspan tie was included.

Two materials were used throughout the structure: Inconel 718 for the panel support beams and Hastelloy X for all other engine structure. The honeycomb panel weight for inertial load calculations was approximated by using an equivalent density. The modulus of elasticity and thermal expansion coefficient were used as functions of temperature. Other mechanical properties such as Poisson's ratio and density were assumed constant because their influence is minor. The friction coefficient was held constant because reliable data describing this as a function of temperature are not available.

Model geometry: Finite element models for the three structural concepts are shown in fig. 86. One-half of an engine module is represented; the plane of symmetry is vertical and passes through the center strut and cowl apex. Model statistics are as follows:

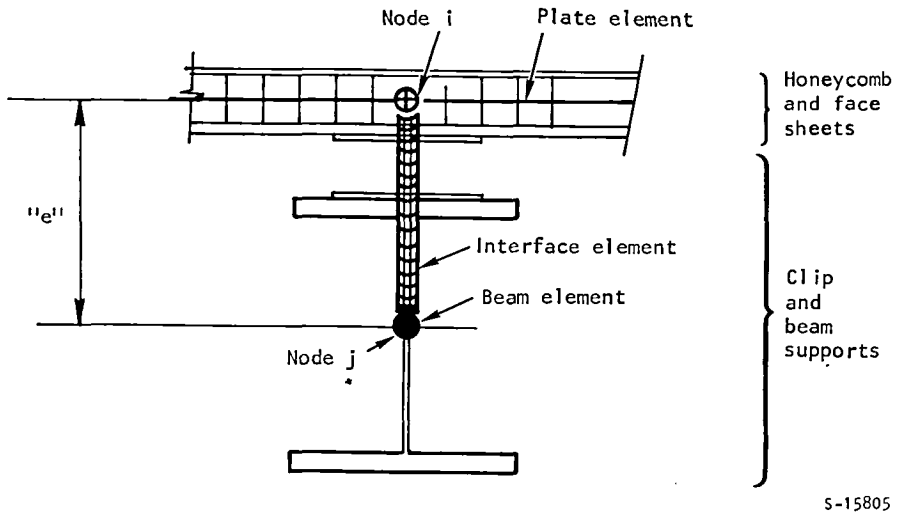

Figure 84.-Plate-beam element sliding connection simulation.

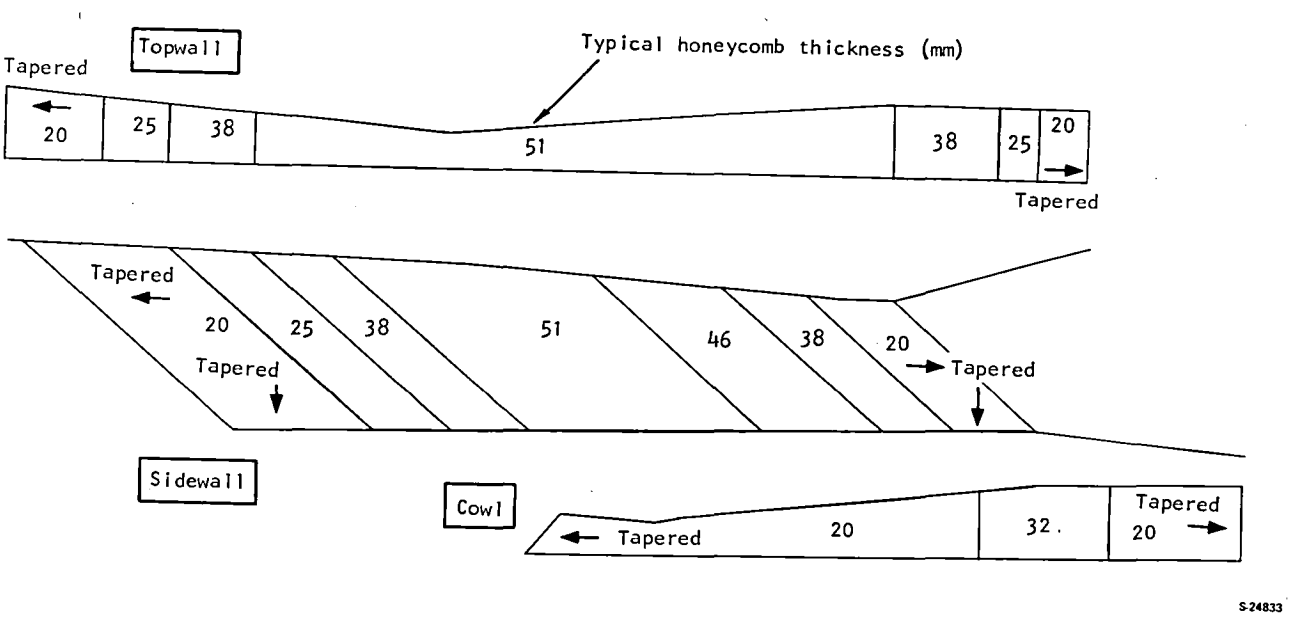

Figure 85.-Honeycomb thickness variation (all honeycomb model).

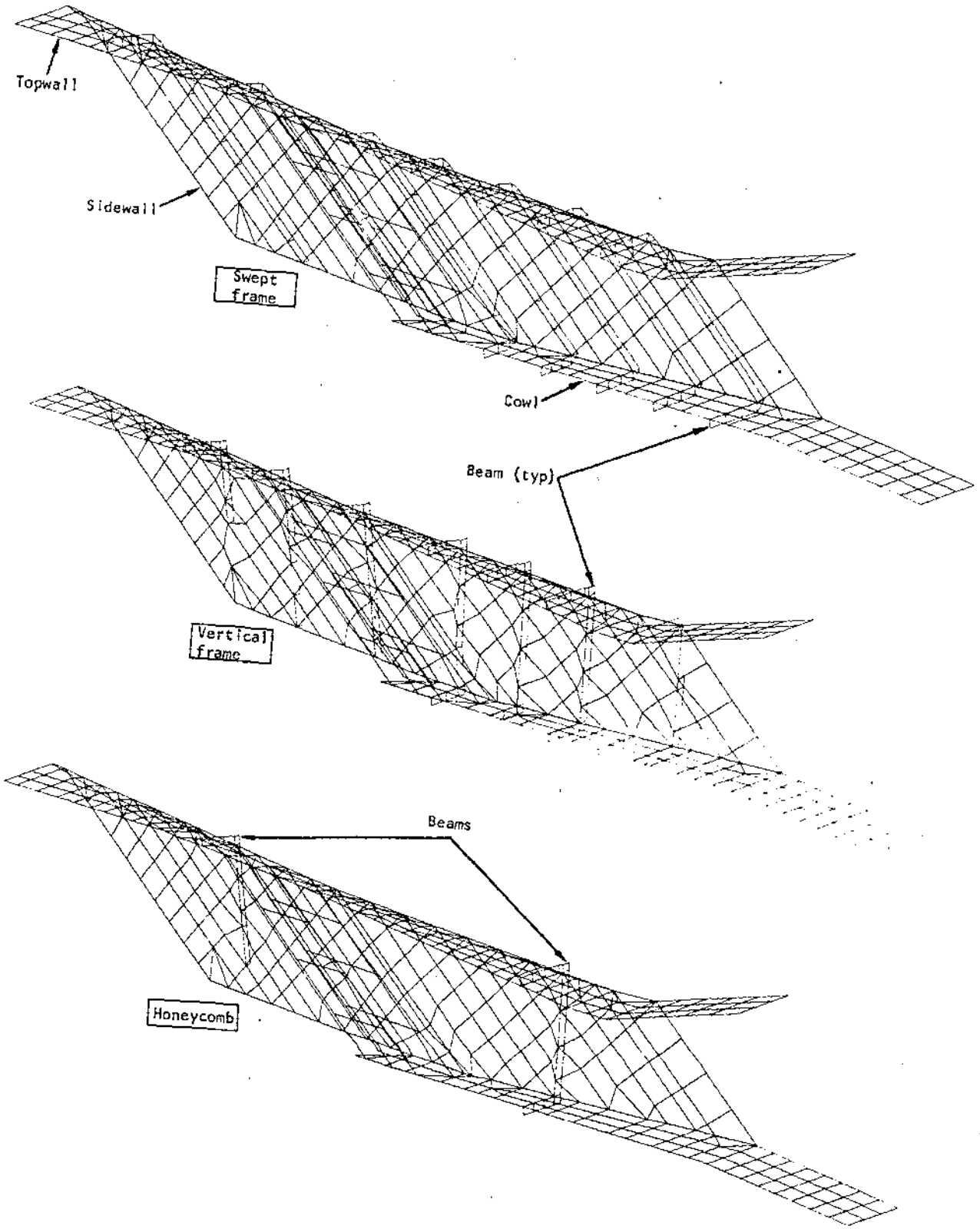

Figure 86.-Finite element models.

	Swept Beam	Vertical Beam	Honeycomb
Three-dimensional beam elements	416	398	155
Flat elastic shell elements	424	424	424
Total elements	840	822	579
Degrees of freedom	4146	4794	4710

The panel support beams are readily apparent because they are separate elements and an interface element exists between the clip and beam.

Loads: Maximum thermal (Condition H) and maximum pressure (unstart at Condition G) loads were applied to the structural models. The Condition H isotherms were used in both cases. The cumulative heat load does change between the G and H conditions, but the general heat flux distribution remains constant, as do the coolant inlet and outlet temperatures. Hence, the temperature gradients remain similar.

Panel performance: Computer results are summarized for the sidewall, topwall, and cowl in figs. 87, 88, and 89, respectively. Plots of displacements and isostress lines are shown for the honeycomb structure at the maximum pressure loading conditions. Generally, the honeycomb structure deflects less than the beam models under maximum pressure loading. The plots are similar for all structures.

The term "comparative" stress is used in the tabular data because the computer model uses a single element to represent the honeycomb primary structure. The element correctly represents the stiffness of the actual panel, and thus the computed deflections are valid while the computed stresses are somewhat fictitious. The maximum stress usually occurs in the outermost cold face-sheet. The computed stresses are representative of the structure, but a detailed analysis would be required to establish the actual values.

The distorted geometry for the sidewall is shown in fig. 90. Results are shown for the honeycomb structure, which is typical. The S-shape is a direct result of the applied temperature gradient--cold leading and trailing edges with a hot central portion. The major portion of the growth, about 0.1 in., is attributed to just the thermal growth. The topwall and cowl surfaces follow the sidewall S-shape.

It was found that the sidewall leading edge bends forward, changing the sweep angle, and in some cases in excess of the 0.4-deg angle change limit; however an angular deviation of the leading edge sweep is not critical. The deviation limit is mainly of concern with respect to the internal wedge angle.

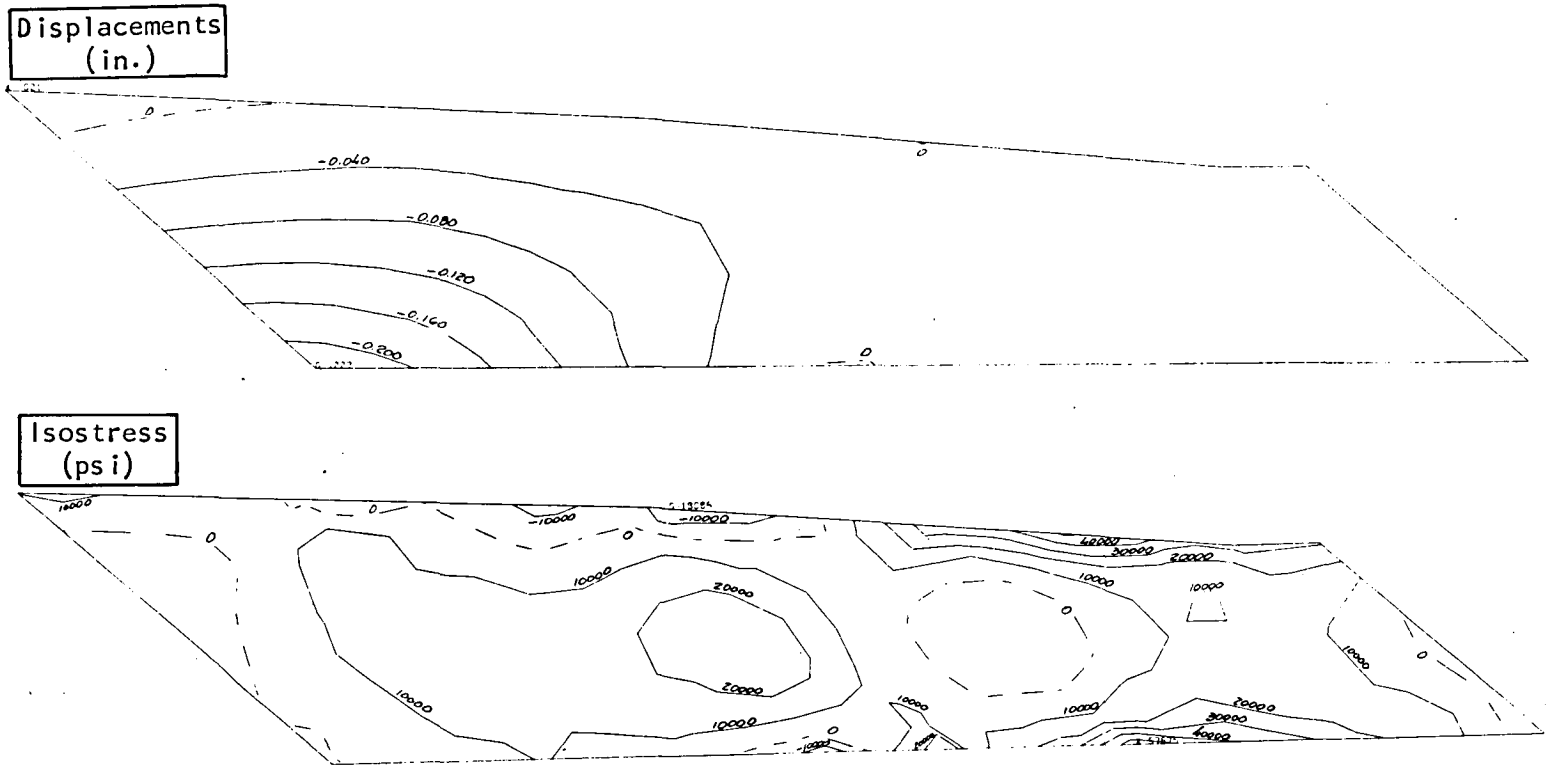

Structure	Maximum thermal load		Maximum pressure load	
	Displacement, mm (in.)	Comparative stress MPa, (ksi)	Displacement, mm (in.)	Comparative stress MPa, (ksi)
Swept beam	5.1 (.20)	496 (72)	55 (2.29)	469 (68)
Vertical beam	3.3 (.13)	414 (60)	27 (1.08)	593 (86)
Honeycomb (shown)	0.5 (.02)	248 (36)	5.8 (0.23)	400 (58)

S-25474

Figure 87.-Sidewall performance.

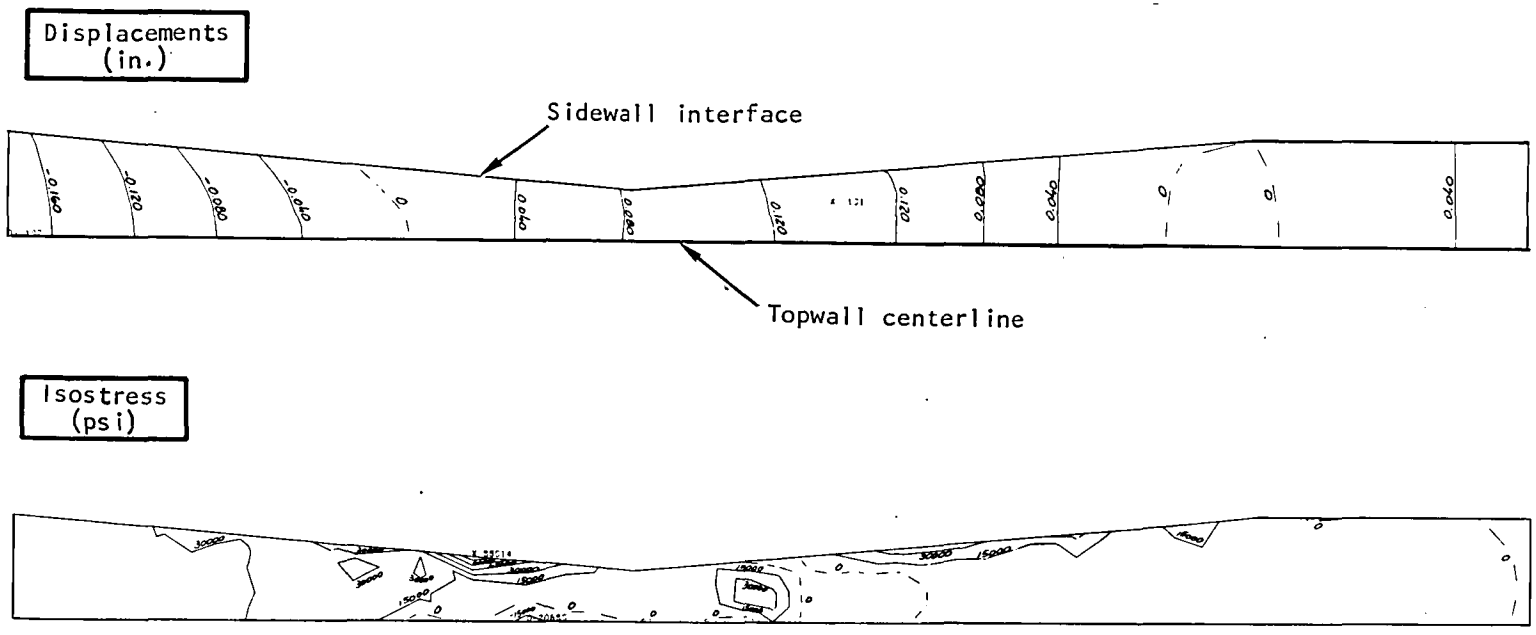

Structure	Maximum thermal load		Maximum pressure load	
	Displacement, mm (in.)	Comparative stress, MPa (ksi)	Displacement, mm (in.)	Comparative stress, MPa (ksi)
Swept beam	6.1 (.24)	207 (30)	24.4 (.96)	758 (110)
Vertical beam	2.5 (.10)	255 (37)	3.8 (.15)	979 (142).
Honeycomb (shown)	3.0 (.12)	441 (64)	4.6 (.18)	607 (88)

S-25395

Figure 88.-Topwall performance.

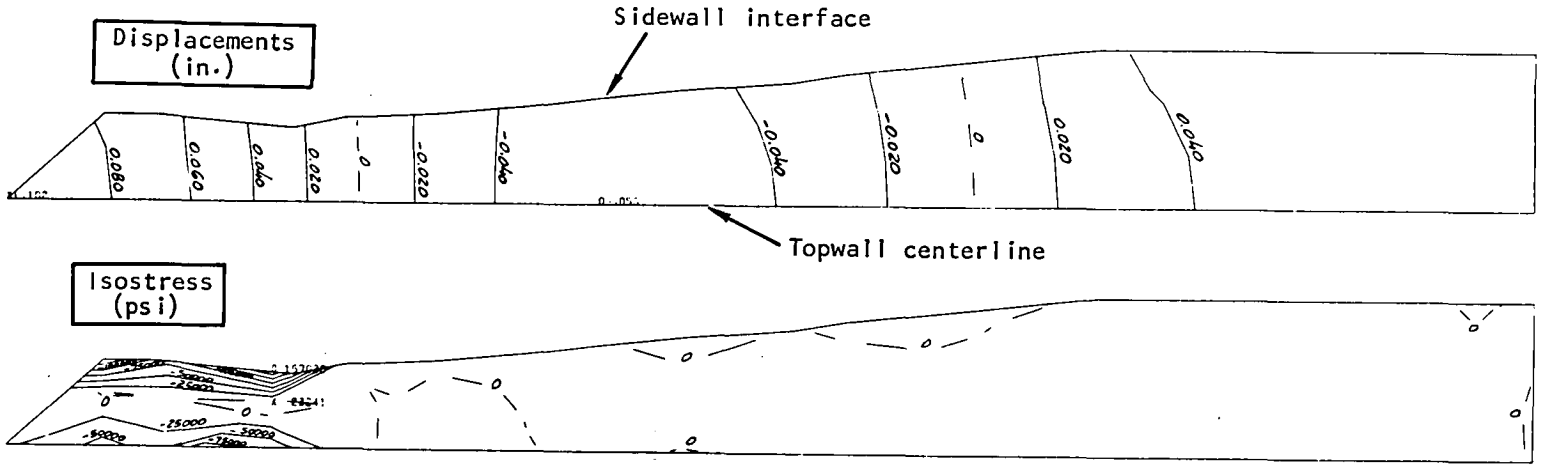

Structure	Maximum thermal load		Maximum pressure load	
	Displacement, mm (in.)	Comparative stress, MPa (ksi)	Displacement, mm (in.)	Comparative stress, MPa (ksi)
Swept beam	2.0 (.08)	724 (105)	2.5 (.10)	1090 (158)
Vertical beam	1.0 (.04)	634 (92)	1.0 (.04)	607 (88)
Honeycomb (shown)	1.0 (.04)	1160 (168)	1.0 (.04)	1150 (167)

IS-25475

Figure 89.-Cowl performance.

(a) Honeycomb results (dimensions in inches):

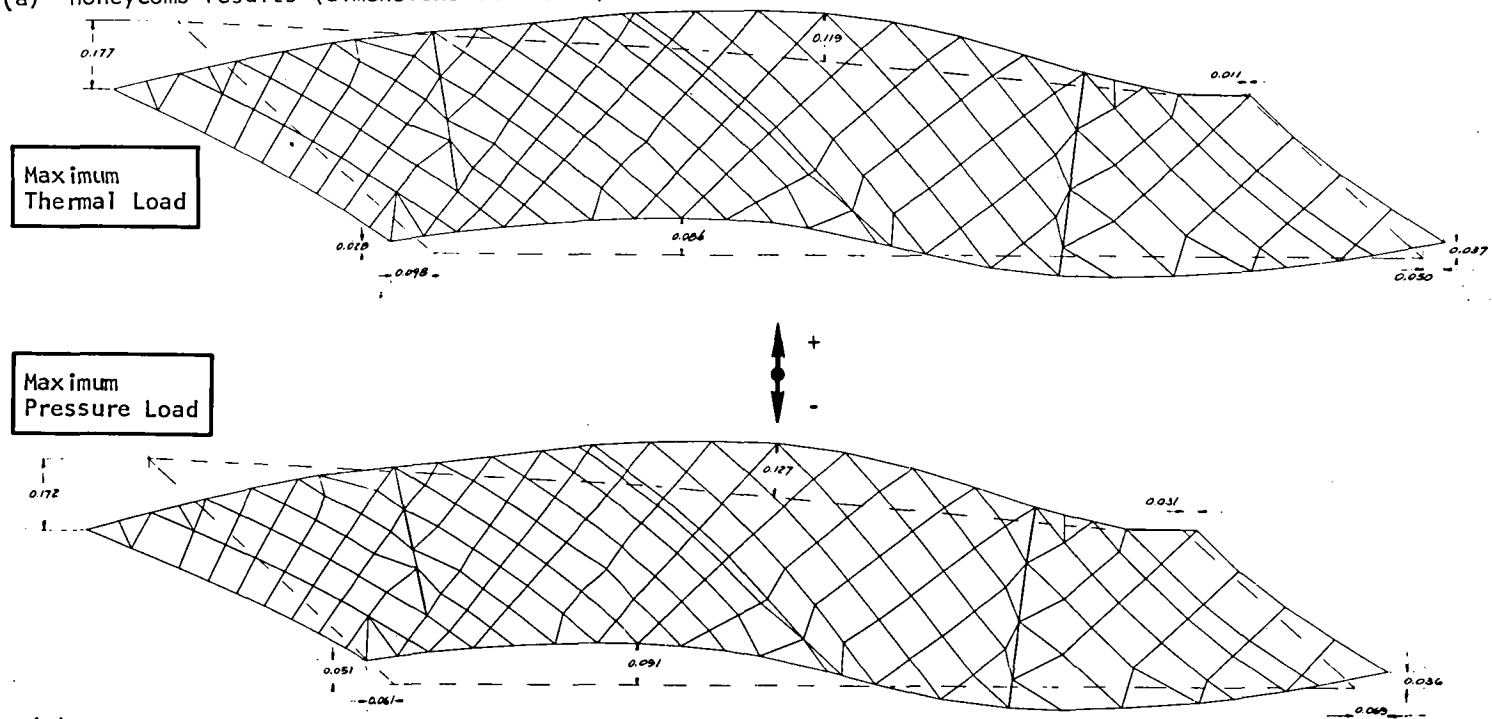

(b) Comparative results:

Structure	Vertical displacement, mm (in.) (maximum pressure load)						
	Leading edge top	Leading edge bottom	Mid-topwall	Mid-cowl	Trailing edge top	Trailing edge bottom	Leading edge angular change, degrees
Swept beam	+0.13 (+.005)	+7.62 (+.300)	+2.79 (+.110)	0 (0)	-2.34 (-.092)	-2.74 (-.108)	0.54
Vertical beam	-3.91 (-.154)	+3.71 (+.146)	+3.81 (+.150)	+4.17 (+.164)	0 (0)	+0.13 (+.005)	0.40
Honeycomb (shown)	-4.37 (-.172)	+1.30 (+.051)	+3.22 (+.127)	+2.31 (+.091)	0 (0)	+0.91 (+.036)	0.45

S-25414

Figure 90.-Sidewall distorted geometry.

Nozzle performance: Data are presented in fig. 91. The displacements are reasonable and the change in flow area is within specified limits for all configurations. The displacements are strongly influenced by the sidewall distortion. In an actual aircraft application, the topwall vertical displacement would be limited by the installation. Hence, the 1.1-deg topwall angle change for the vertical beam model would be less. The honeycomb configuration is best in terms of minimum flow area change.

Corner displacements: Relative motion between panels is summarized in Table 18. Displacements are similar for both swept and vertical beam models and are generally small except for a few areas. It appears that the panel corners could also be rigidly joined in the beam models, thus permitting the use of a simple static seal or even a welded corner design. There are no gaps in the honeycomb design because the corners are modeled as a continuous joint and no gaps are permitted.

Mass comparison: Estimated masses were determined for each structural design using layout drawings as a basis. The weights are consistent with the dimensions of the individual parts used in the finite element analysis. Results are listed in Table 19 for a six-module cluster. The honeycomb design is the least weight. The mass differences are not considered especially significant at the current level of detail design.

Design selection.--The honeycomb configuration was selected as the best design primarily because (1) it exhibits the least deflection in the sidewall and nozzle areas--an order of magnitude lower than the beam models; (2) it is the least complex structure--minimum beams and clips; and (3) it weighs less than the beam models. A reduced number of beams is desirable because the beams do act as a restraint to thermal growth and thereby increase stresses. Additional detailed layout design will be required to define means to carry loads around the corners (panel-to-panel) and across the manifolds, and to alleviate locally high stresses.

External cowl panel.--The bottom (external) surface of the engine cowl is a cooled structure supported by a honeycomb primary structure, which is tied to the engine sidewalls through flexures. A V-shaped coolant inlet manifold is incorporated in the structure.

The loads acting on this component consist of external aerodynamic pressure, inertia, and thermal loads due to a temperature gradient along the assembly. The net pressure acting on the cowl surface is approximated by assuming that the pressure in the cowl cavity is equal to the freestream static pressure. The following net pressure loads were determined.

	External pressure,		Internal pressure,		Net pressure load,	
	kPa	(psia)	kPa	(psia)	kPa	(psi)
Condition G	10.8	(1.57)	3.9	(0.57)	6.9	(1.00)
Condition H	7.1	(1.04)	1.0	(0.15)	6.1	(0.89)

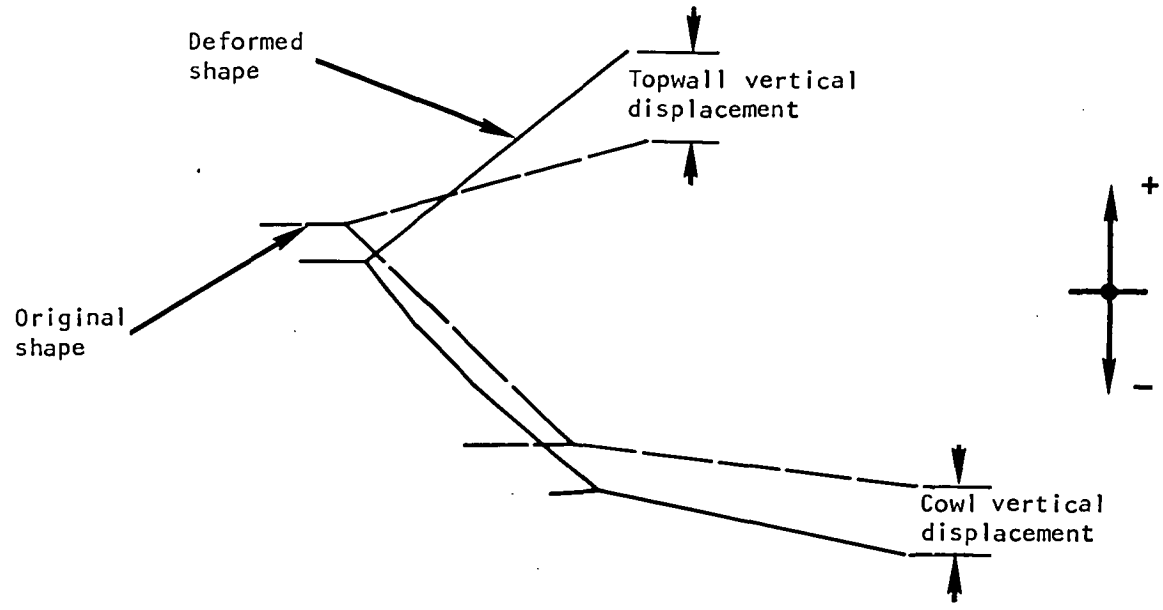

Structure	Maximum thermal load			Maximum pressure load		
	Topwall vertical disp, mm (in.)	Cowl vertical disp, mm (in.)	Δ flow area, %	Topwall vertical disp, mm (in.)	Cowl vertical disp, mm (in.)	Δ flow area, %
Swept beam	+7.6 (.30)	-5.8 (.23)	2.6	+1.3 (.05)	-5.1 (.20)	1.2
Vertical beam	+9.7 (.38)*	-3.6 (.14)	2.5	+4.6 (.18)	-2.5 (.10)	1.4
Honeycomb	+0.5 (.02)	-0.5 (.02)	0.2	+1.5 (.06)	+1.0 (.04)	0.1

*Angle change = 1.1^{o}

S-25476

Figure 91.-Nozzle deformation.

TABLE 18. -CORNER DISPLACEMENTS

Panel	Station	Corner Relative Displacement, mm (in.)	
		Maximum thermal load (Condition H)	Maximum pressure load (Unstart)
Topwall	11.0	.56 (.022)	1.30 (.051)
	17.3	.41 (.016)	.48 (.019)
	29.1	.28 (.011)	.69 (.027)
	37.0	.48 (.019)	2.74 (.108)
	40.9	.30 (.012)	2.34 (.092)
	49.1	1.04 (.041)	1.83 (.072)
	53.4	1.04 (.041)	1.45 (.057)
	61.7	.20 (.008)	.36 (.014)
	70.0	.08 (.003)	.18 (.007)
	80.8	.43 (.017)	.58 (.023)
Cowl	62.5	.58 (.023)	.18 (.007)
	70.0	.28 (.011)	.41 (.016)
	81.1	.20 (.008)	.58 (.023)
	92.3	.05 (.002)	.08 (.003)

TABLE 19. -MASS COMPARISON

6-Module Engine [36.6 by 45.7 cm (14.4 by 18 in.) Capture Area]			
Structure element	Mass, kg (lb)		
	Swept beam	Vertical beam	Honeycomb
TPS	408 (900)	408 (900)	408 (900)
Honeycomb core	42 (93)	42 (93)	114 (251)
Cold face sheet	209 (460)	209 (460)	209 (460)
Beams and clips	146 (322)	133 (294)	27 (59)
Manifolds	143 (315)	143 (315)	143 (315)
Leading and trailing edges	85 (188)	85 (188)	85 (188)
Struts (3)	166 (366)	166 (366)	166 (366)
Braze alloy	25 (56)	25 (56)	25 (56)
Weld and misc.	95 (209)	94 (207)	93 (205)
Total weight	1319 (2909)	1305 (2879)	1270 (2800)

Thermal analysis indicates that the temperature of the airflow-exposed surfaces will vary between 222 and 389 K (400° to 700°R) and the back side will be approximately 111 K (200°R) cooler.

The inplane temperature gradients are low and thermal stresses due to either the 111 K (200°R) ΔT between the hot and cold skin or the cowl in-plane temperature distribution will remain below the elastic limit of the material. Inertial loads were found to be negligible.

Topwall nonuniform heat flux analysis.--The heat flux on the inlet portion of the topwall is variable because the flow properties change between wave bays. The resulting nonuniform heating rate produces nonlinear temperature gradients and a corresponding thermal stress in the cooled structure. For the topwall, the problem is more complex because the surface is multiplanar. An analysis was conducted to predict the nonlinear, two-dimensional in-plane temperature profiles along the topwall surface. The corresponding thermal stresses were then computed and the critical stresses identified.

Two-dimensional aerodynamic heating analyses were performed on inlet and combustor sections of the topwall surface. Earlier analyses presented results based on a one-dimensional approach where the various inlet streamlines produced by the complex shock bay pattern were reduced to one streamline. This one streamline was a composite of those producing maximum heating along the engine axis. The purpose of this task was to determine the more realistic two-dimensional thermal loading by analyzing six distinct streamlines that best represent the shock bay pattern in the engine inlet (fig. 92). Heat fluxes were computed by the adiabatic wall reference enthalpy method (ref. 9). This method is consistent with the results of previous aerodynamic heating analysis, as was the engine operating condition, Condition H.

The basic features of the top surface flow field are presented in fig. 92. The complex structure of shock wave impingements and reflections on the sidewall and struts, as well as the intersection of two shock waves, result in 16 distinct bay areas with 16 different flow properties at the engine inlet upstream to the fuel injector struts. For a comprehensive 2-D thermal analysis, various flow paths were chosen to cover all of these bay areas. Six fluid streamlines shown in fig. 92 were chosen as representative flow paths to cover all of the 16 bays with the exception of Bay 7, which could be dispensed with since its flow properties are very close to those in Bay 6.

The shock (compression) or Mach (expansion) waves each of the streamlines encounters and the shock bays each passes through is indicated. Table 20 delineates the sequence of events for each of these streamlines. The direction of each streamline is controlled by the shock bay area and the adjacent wall surfaces. Bay 13 (fig. 92) is an exception to this because it results from the intersection of two shock waves. When the intersecting waves are of different strengths, a slip line will result in the bay with two different velocities. One velocity is defined for Bay 13, which implies the absence of a slip line. The flow direction in Bay 13 is therefore taken to be parallel to the axis of symmetry. The one-dimensional consideration in the combustor area is noted in fig. 92 for all stream lines.

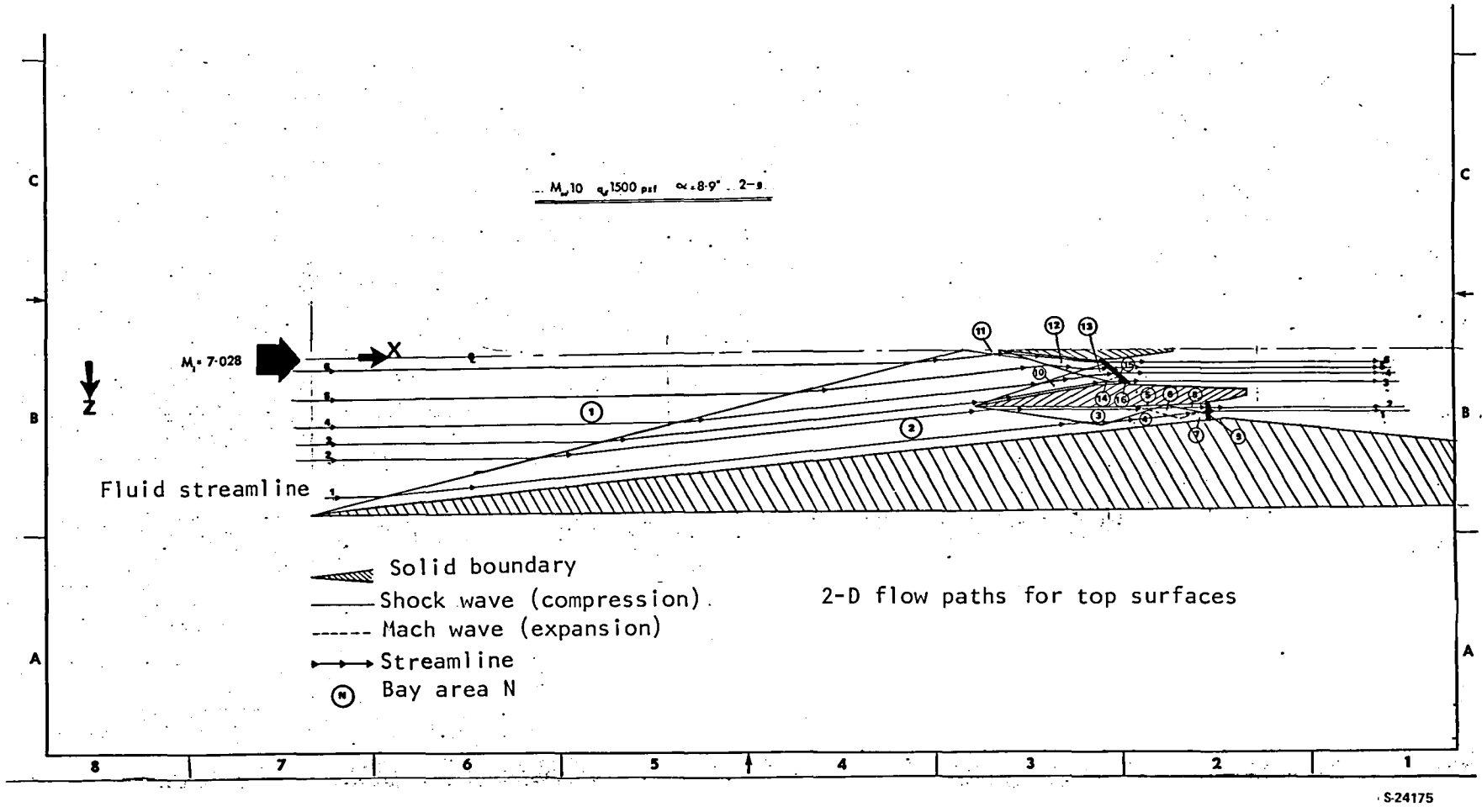

Figure 92.-Basic features of top surface flow field.

TABLE 20.–STREAMLINE SEQUENCE OF EVENTS

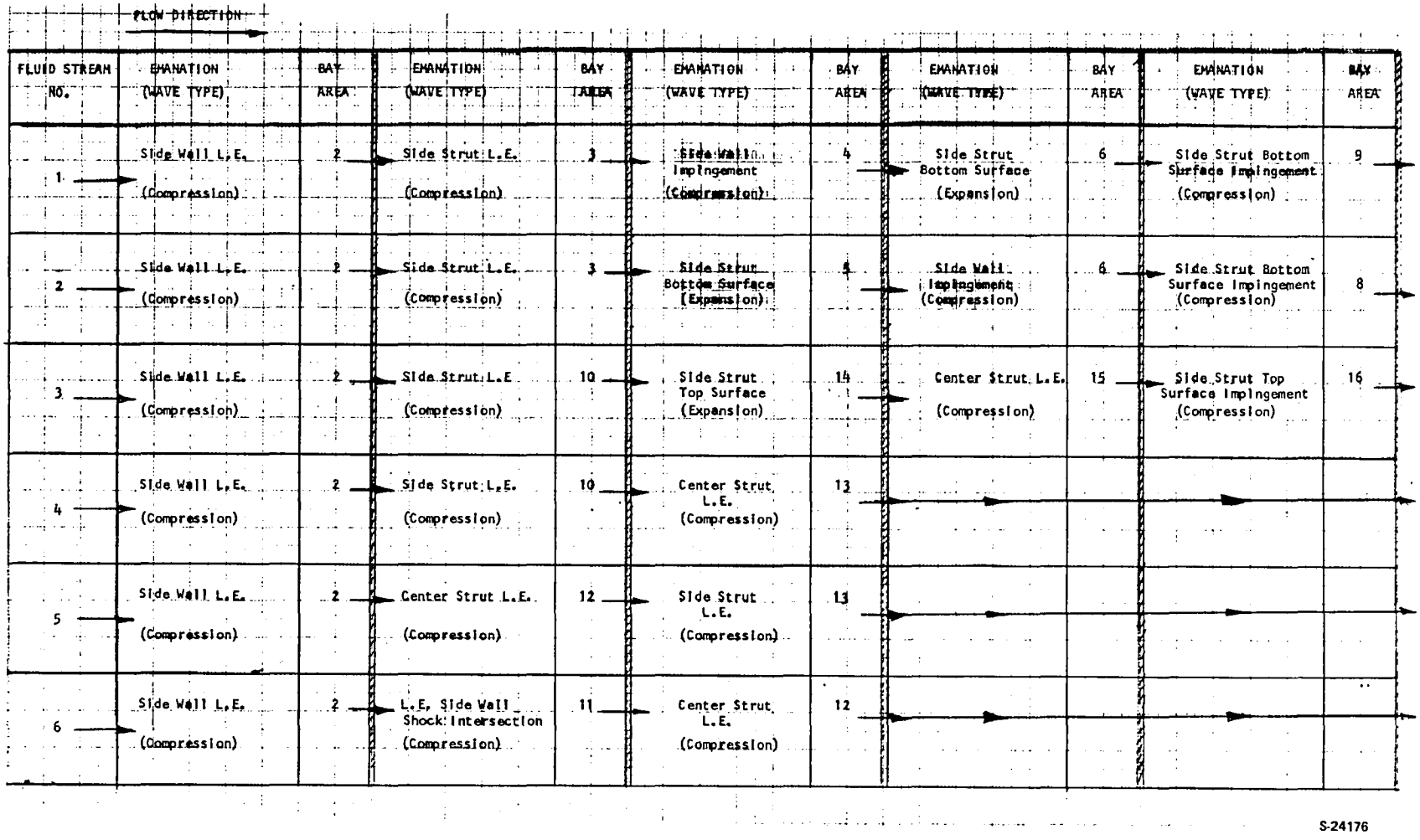

A last point to be observed in fig. 92 is the proximity of streamlines 2, 3, and 6 to the struts. This presentation is only symbolic, which serves the purpose of allowing the streamlines to pass through most of the bay areas, and should not be interpreted as interfering with the strut boundary layers.

Heat fluxes were computed along a certain flow path at specified increments along the x-axis. The adiabatic wall reference enthalpy method was used for both laminar and turbulent boundary layers. A value of 3.58×10^6 was used for transitional Reynold's number. Results are shown in figs. 93 and 94, where heat fluxes along various streamlines are plotted versus distances along the x-axis of the engine top surface. Fig. 93 illustrates the thermal loading of Streamline 5 for the entire engine length, including the nozzle. The successive rises in heat fluxes along Bays 1, 2, 12, and 13 are indicative of shock wave crossings. The peak thermal load is at about 41.0 in. from engine inlet and is located at a distance 4.1 in. downstream from the fuel injector strut. Fuel injection starts at 36.9 in. from engine inlet for Streamline 5. The combination of Streamlines 1, 3, 5, and 6 in fig. 94 provides a more meaningful picture for the two-dimensional effect. Streamlines 2 and 4 are not shown, but lie between the curves for Streamlines 1 and 5. This figure can best be interpreted with the help of fig. 92. For a particular streamline, a step change in heat flux is indicative of a change in shock bay. Crossing a shock wave causes an increase in flux; crossing an expansion wave causes a decrease in flux.

Of particular interest is Streamline 3 (solid line with circles), which is used to clarify the multiplicity of bay areas it passes through. In Bay 1, Streamline 3 starts with a heat flux of 18 Btu/sec-ft^2 sec, which remains constant until it reaches the point 13.4 in. from the engine inlet, where it passes to Bay 2 by crossing the side wall leading edge shock wave. The result is a heat flux increase to 38 Btu/sec-ft^2 and then a gradual decline to 32 Btu/sec-ft^2 at 31.0 in. from engine inlet.

It then enters Bay 10 through the shock wave emanating from the side strut leading edge. This causes a further step rise of heat flux to 49.0 Btu/ft^2 In Bay 10 there is a slight reduction as it flows downstream to the point 36.0 in. from the engine inlet, where it passes to Bay 14 through the Prandtl-Meyer expansion wave emanating from the side strut (fig. 92). The result is a drop in heat flux to a value of 25 Btu/sec-ft^2. Streamline 3 then passes through two successive compression zones in Bays 15 and 16 before entering the combustor. The point of interest here is the peak value of heat flux of 198 Btu/sec-ft^2 in Bay 16 resulting from the strong shock wave reflected from the side strut.

In fig. 94, the heat fluxes in the combustor zone for Streamlines 6, 5, and 3 are represented by a single curve for clarity. In reality there is a gradual delay in location along the x-axis due to the existing angle at the fuel injection region in the x-z plane. The delay is noted for Streamline 1, which exhibits a combustion zone response similar to Streamline 5, with a delay of a few inches in the x-direction. Streamlines 4, 5, and 6 have a peak heat flux of 191 Btu/sec-ft^2 at a point 4.1 in. downstream to the fuel injection strut. Streamlines 1 and 2 have a peak heat flux of 203.0 Btu/sec-ft^2 at about 2.0 in. downstream to the fuel injection strut.

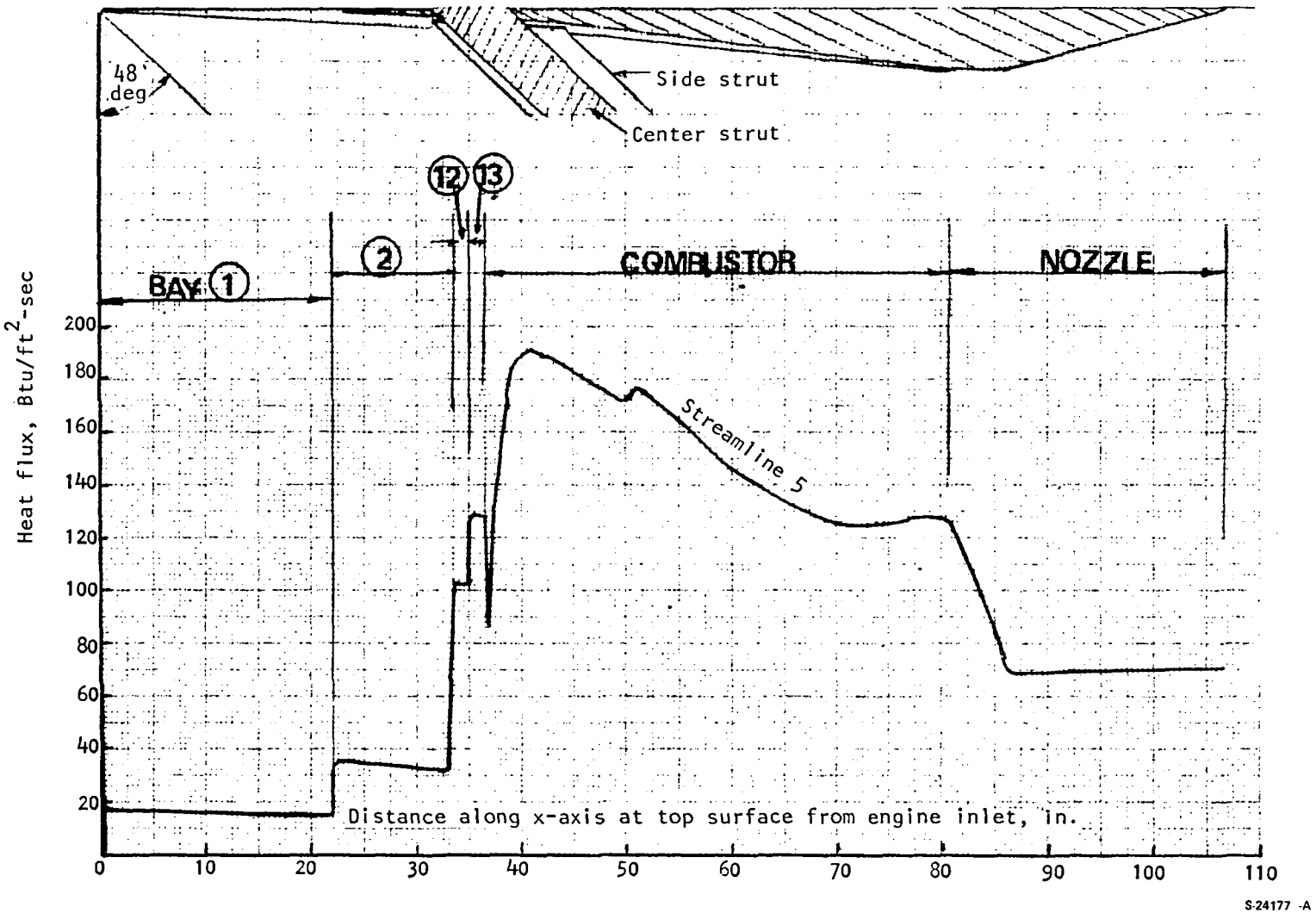

Figure 93.-Typical top surface heat flux distribution along a flow path (streamline 5).

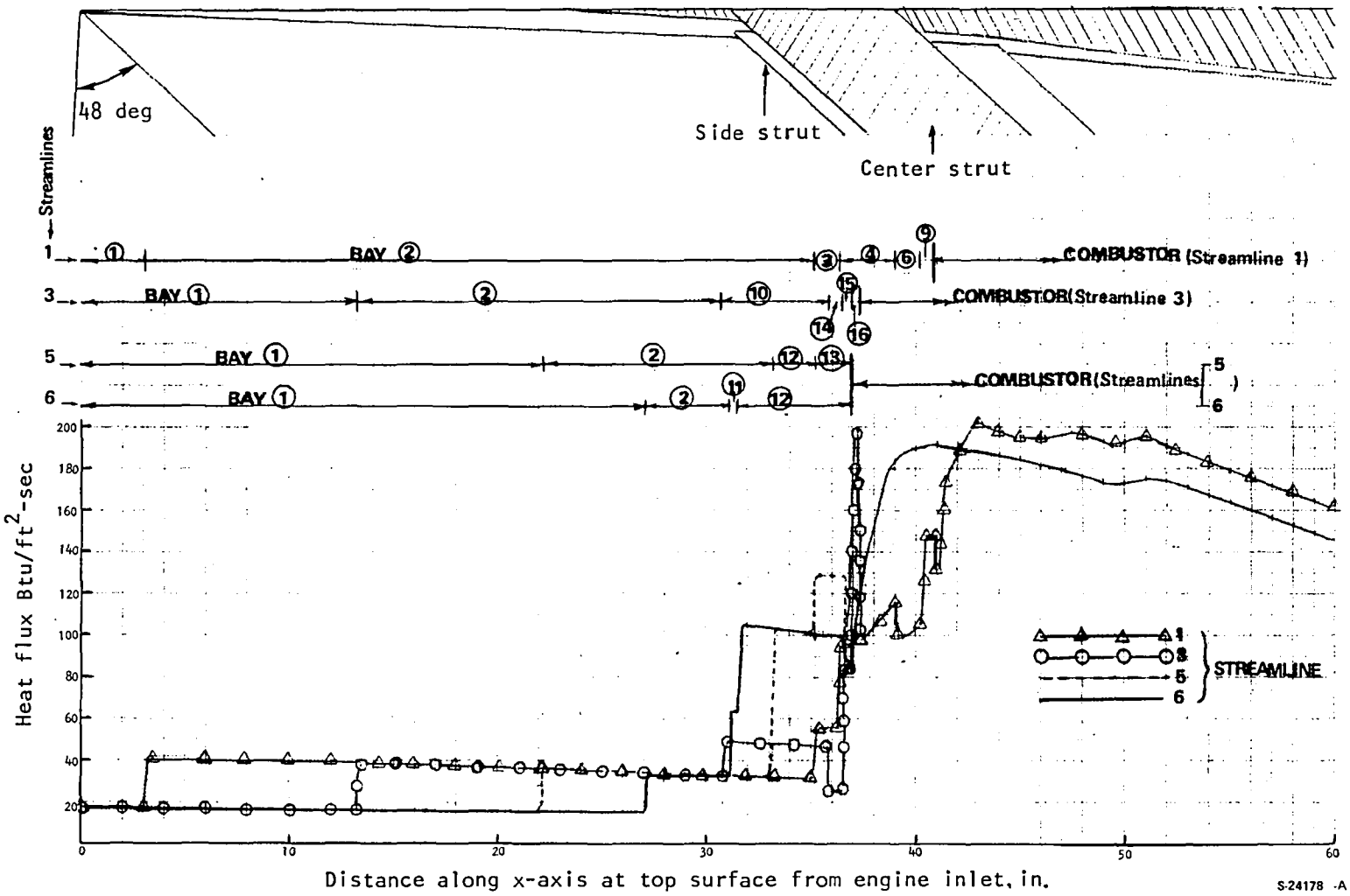

Figure 94.-Top surface heat flux distribution for a combination of flow paths.

The maximum topwall heat flux from the previous analysis was 200 Btu/sq ft-sec and occurred at 41 in. from start of inlet. This corresponds directly with the peak value of 191 Btu/sec-ft^2 in figs. 93 and 94. This slight difference of 5 percent is the result of procedural calculation differences between this and the previous analysis. This is considered to be in close agreement and is within acceptable tolerance for this type of analysis.

A three-dimensional steady-state thermal performance analysis was conducted on the forward topwall TPS panel using the new aerodynamic heating inputs. The geometry of the TPS panel surface is shown in fig. 95. Calculations were performed using an AiResearch computer program (PCM Channel Thermal Performance Program). Hastelloy X was used as the TPS material in this analysis.

The hydrogen coolant enters the engine inlet end of the top surface at 100°R and 1000 psia. It flows through the machined channel passages in a direction parallel to the main airstream for a distance of 58.83 in. from the engine inlet, where it is joined by the aft topwall coolant before entering the outlet manifold. The objective of the analysis was to calculate the temperature distribution along each of the six streamlines at prescribed axial increments (from 0.10 to 0.50 in.) One restriction was to limit the maximum TPS structural temperature to below 1600°R (1140°F). The condition was met following a parametric study using the computer program for the maximum heating path. Results of the study indicate that a value of about 0.0655 lb/sec produces a maximum TPS structural temperature of 1598°R at the outlet manifold location for the maximum heating path, Streamline 1. This flow compares closely with a value of 0.065 lb/sec from the previous analysis.

The metal temperatures at three locations within the TPS at axial stations along each of the fluid streams was calculated. These in-depth locations are defined in fig. 95 as TWO, TW1, and TS, and are used in the subsequent structural performance analysis.

The temperature distribution of the aerodynamically heated surface (TWO) is presented in fig. 96 for the maximum heating path, Streamline 1. Fig. 96 also shows the TPS ΔT (TWO-TS) distribution for this path. Results of the previous analysis are shown for comparative purposes. This previous thermal performance analysis was based on aerodynamic heating that was reduced to one streamline only. This streamline had constant flow properties across the top panel width and was a composite of those that produced maximum heating along the engine axis. The higher temperatures of this previous case are attributed to this composite maximum heating and to a higher coolant inlet temperature of 200°R as compared to 100°R. The present analysis is more realistic in this respect. The previous analysis used an offset plate-fin TPS passage geometry as compared to machined channels.

The combined temperature distributions of streamlines 1, 3, and 6 shown in fig. 97 provide a better perspective for the two-dimensional aerodynamic effect. Streamlines 2, 4, and 5 have been omitted for clarity of the streamlines shown. The omitted streamlines fall within the range of streamlines shown. The temperature steps are the result of crossing shock or Mach waves. The two-dimensional aerodynamic effect is particularly noticeable in the area upstream of the

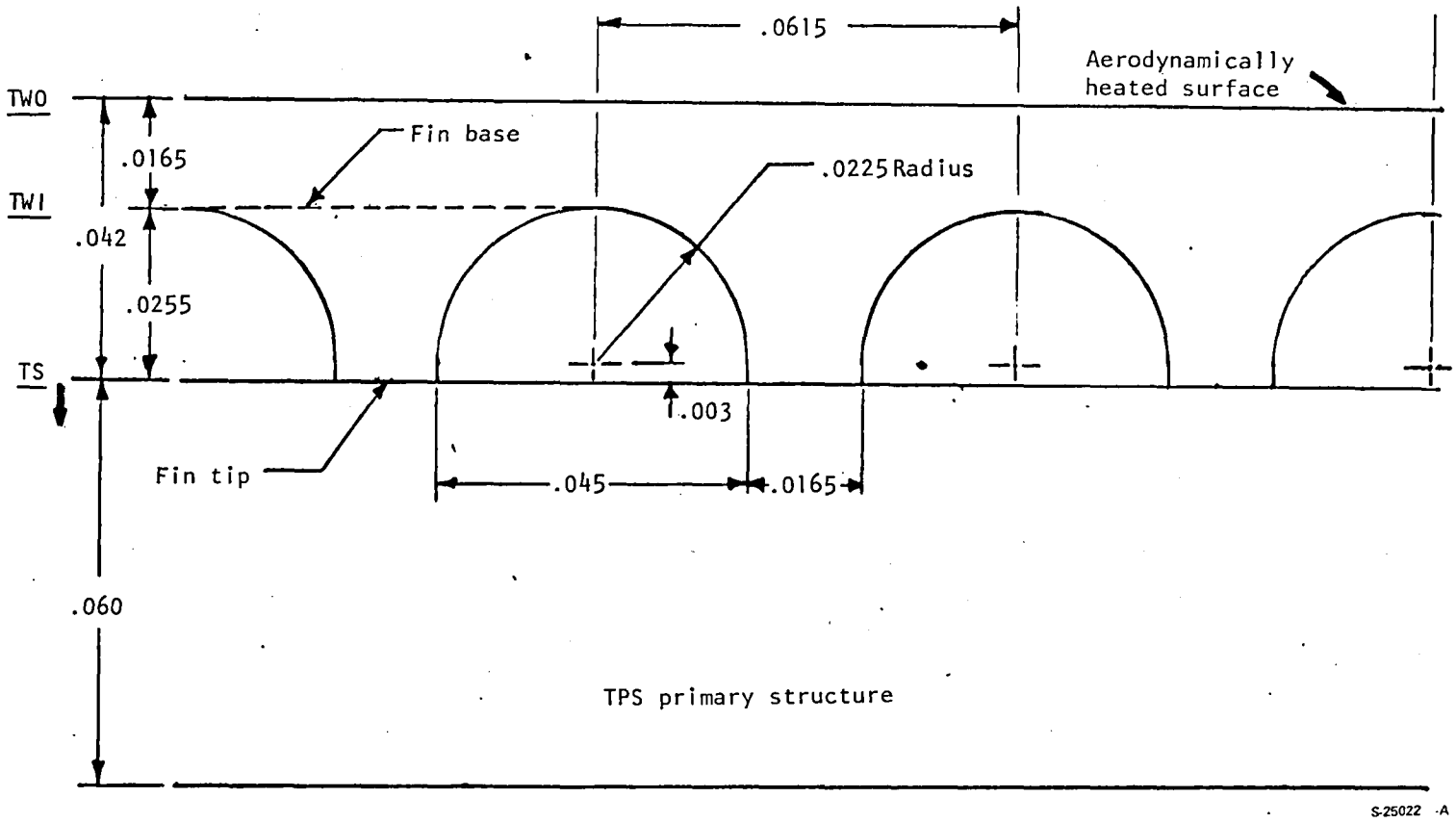

Figure 95.-Machined channel passage configuration.

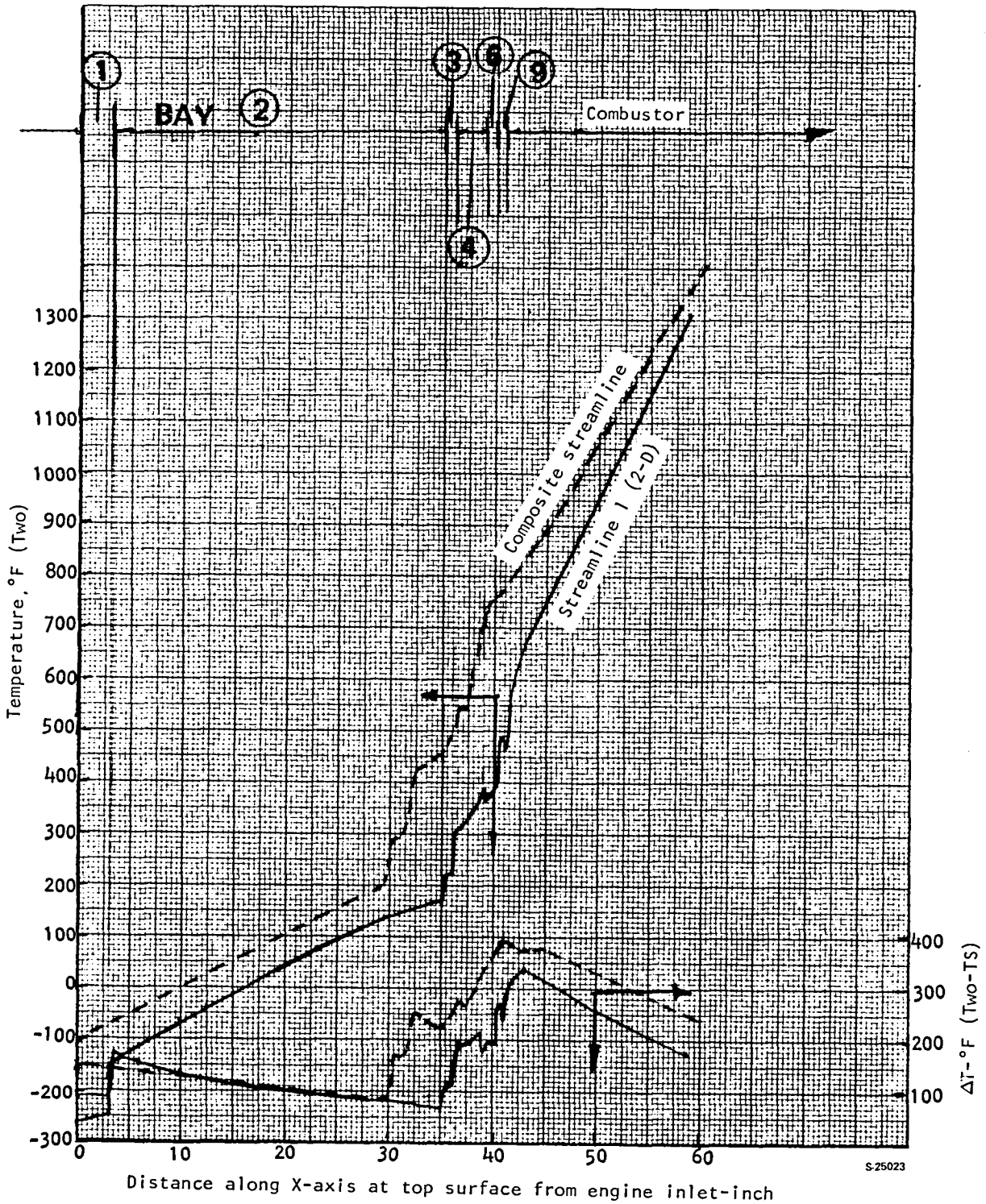

Figure 96.-Topwall temperature distribution for maximum heating path.

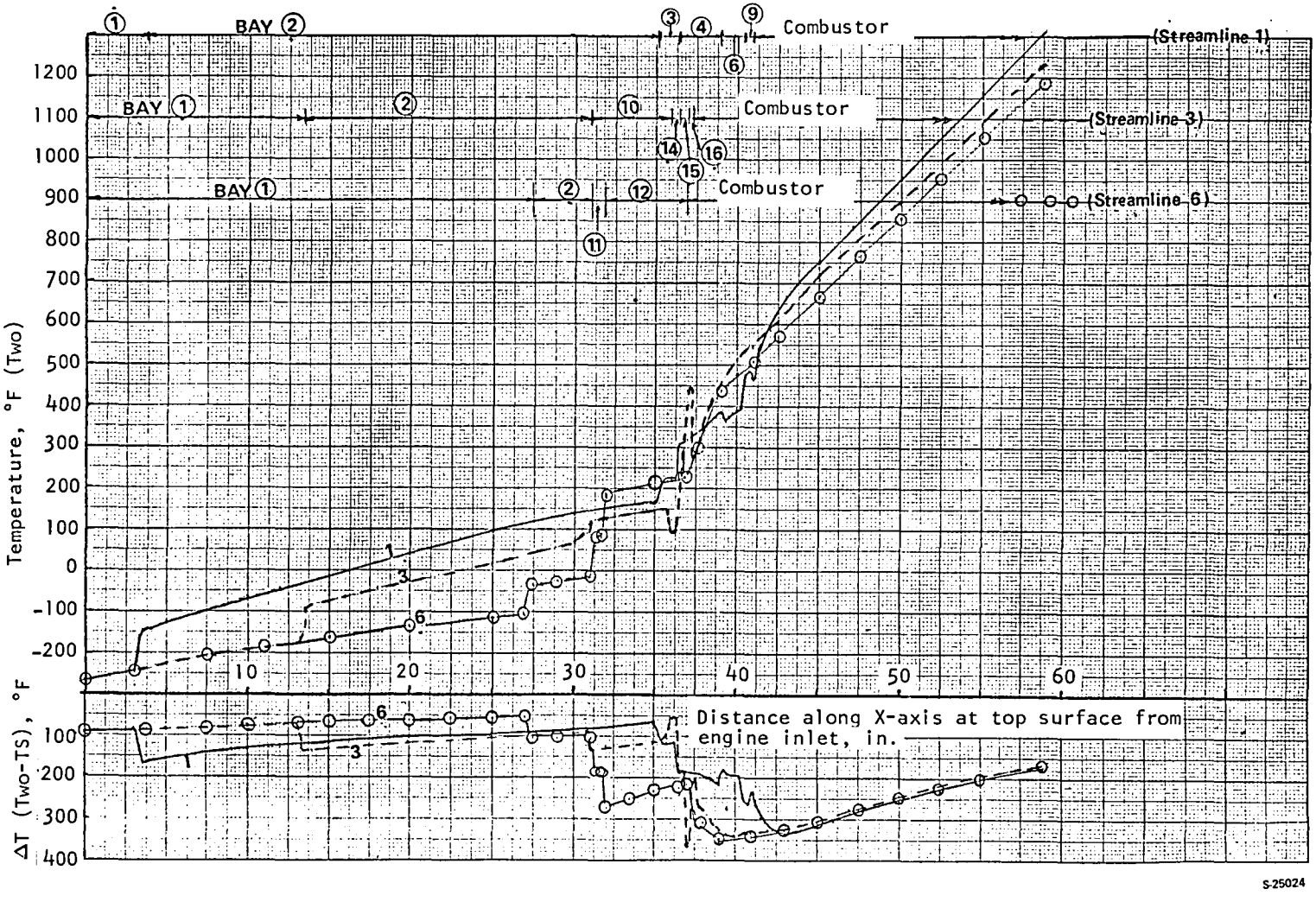

Figure 97.-Two-dimensional temperature distribution for topwall.

combustor zone, while downstream of the strut the one-dimensional effect is noted by the near parallel temperature lines for the streamlines. The results of the two-dimensional analysis are shown in fig. 98 as an isotherm plot on the topwall hot surface. Maximum temperature level and T's are summarized in Table 21 for the six streamlines. The temperature data presented here were used as a load condition for the stress analysis.

The all-honeycomb engine topwall stress analysis was performed using the ANSYS finite element computer program. A model was constructed to represent the significant stiffness and geometric features of the topwall. The model has 673 quadrilateral isoparametric membrane elements, 40 triangular membrane elements, 302 eight-noded isoparametric solids, and 2 six-noded solids. Fig. 99 shows an isometric view of the model. The model is basically three layers of elements as defined in fig. 76.

Solid elements were used to represent the properties of the honeycomb cells. Full orthotropic properties of the hexagonal honeycomb cells were calculated using the configuration in fig. 100.

A supplementary computer model shown in fig. 101 was used to determine constants where no formula was available. The model consists of 216 quadrilateral isoparametric shell elements. The basic definitions of the material properties were input as boundary conditions to the model to determine moduli and Poisson's ratio for the ribbon and non-ribbon directions.

In the topwall model, the stiffness of the TPS and hot face sheet of the honeycomb cell were combined and represented as a single, isoparametric membrane element (0.08-in.-thick). The cold face sheet of the honeycomb cell is represented by an isoparametric membrane element (0.06-in.-thick). The membrane elements are expected to reproduce the membrane stresses that would exist in the outermost fibers of the inside and outside surfaces of the engine topwall.

The model accurately reproduces overall bending stresses of the layered composite. Bending stresses due to temperature differentials across the TPS-hot face sheet are not reproduced by this modeling technique. Bending stresses were hand-calculated and linearly superimposed onto the stresses derived from the finite element model to obtain the effect of the temperature differential.

Each local cutout for the struts is modeled by a row of isoparametric solids which represent the stiffness of structure surrounding the strut cutouts. The stiffness of the leading edge manifold was not represented in the leading edge model. Since the leading edge area is relatively lightly loaded, the manifold has little effect on the stresses and would unduly complicate the model.

Young's moduli were input to the program as a function of temperature. Shear moduli and Poisson's ratio were held constant because less is known about the nature of these constants with respect to temperature. The entire engine topwall was assumed to be Hastelloy X.

Loads to the model are in the form of imposed boundary conditions and nodal temperatures. The Y-displacements (see fig. 99) from the all-honeycomb, three-dimensional model were used as boundary conditions at the sidewall/topwall interface. The interface edge was not permitted to rotate. A built-in (fixed) edge

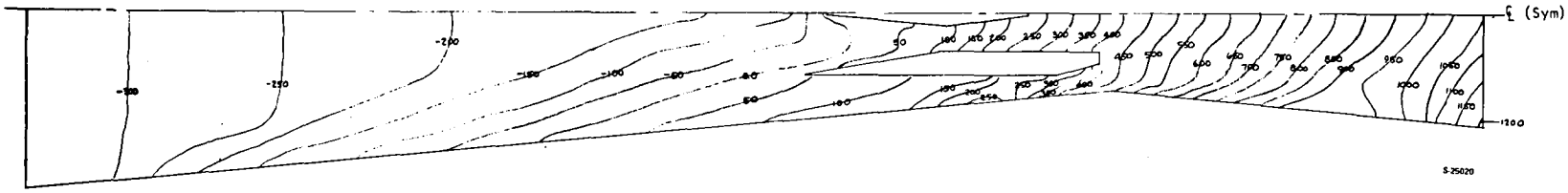

Figure 98.-NASA scramjet TPS/hot face sheet isotherms (°F).

TABLE 21.-NUMERICAL RESULTS, ENGINE TOPWALL

Streamline	Maximum ΔT (TWO-TS), °F	Location of maximum ΔT from engine inlet (from injector), in.	Outside wall temperature (TWO) at maximum ΔT, °F	Maximum wall temperature (TWO) at 58.83 in., °F
1	338	43.0 (2.1)	669.0	1310.0
2	346	43.0 (2.1)	642.0	1283.0
3	340	40.0 (2.8)	511.0	1230.0
4	344	39.5 (2.6)	476.0	1206.0
5	349	39.5 (2.6)	465.0	1194.0
6	351	39.5 (2.6)	459.0	1187.0

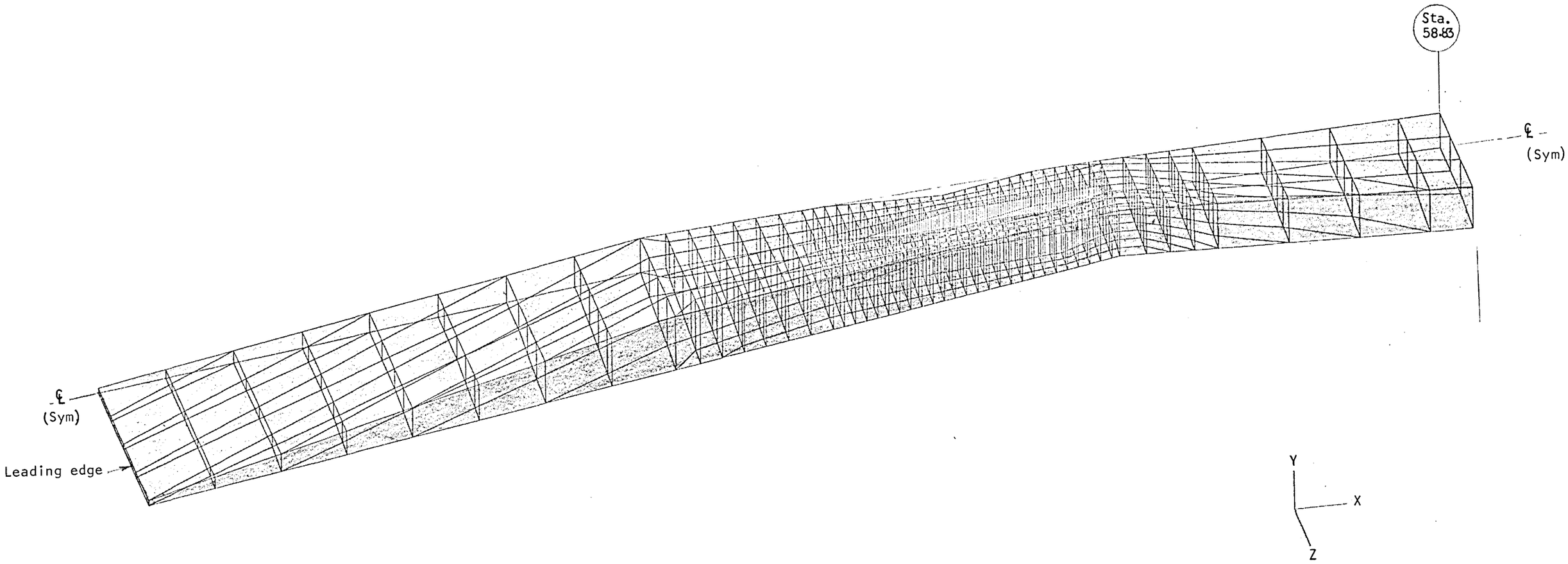

F-26935

Figure 99. -Topwall finite element model, isothermic view

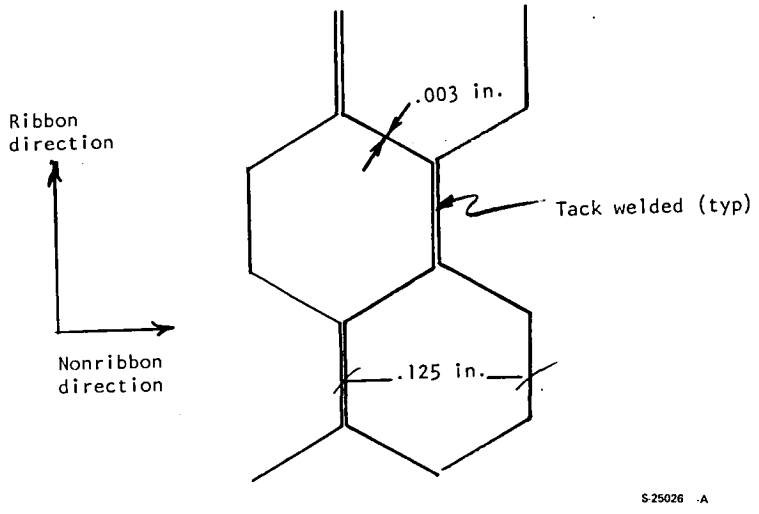

Figure 100.-Honeycomb cell configuration.

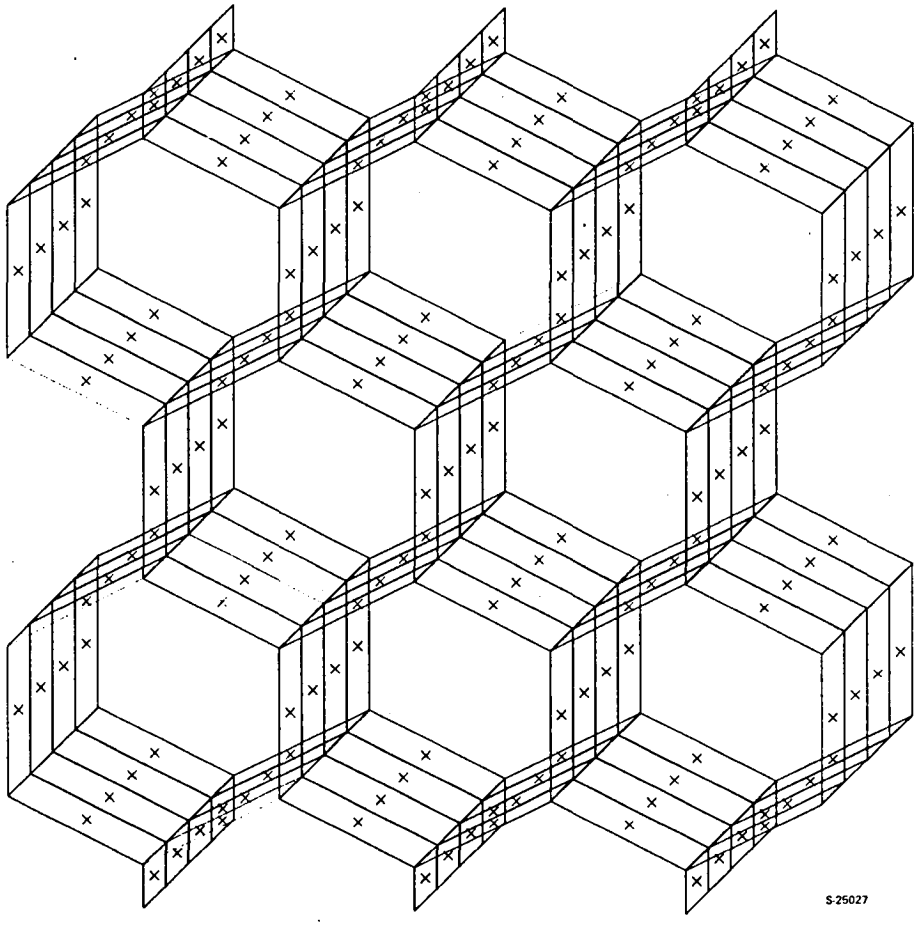

Figure 101.-Honeycomb cell finite element model.

is thus simulated. Rotations from the three-dimensional analysis were not used as boundary conditions because they were too heavily influenced by pressure loads and would unduly bias the thermal stress analysis. Conditions of symmetry were used as boundary conditions (along the centerline of symmetry). Three layers of temperature were input to the model. An average temperature of the TPS/hot face sheet was used for the inside layer. The honeycomb cells and the cold face sheet constituted the other four layers.

Computer plots of the stresses and configuration changes obtained from the analysis are shown in figs. 102 through 111. The von Mises stresses on the TPS hot face sheet and the cold face sheet are shown in fig. 112. The computer analysis calculated the nominal middle surface stresses of the TPS hot face sheet and the cold face sheet of the honeycomb cell. The critical nominal stresses for the topwall are shown in Table 22.

Some yielding occurs at the middle surfaces, but these levels of stress are tolerable for 1000 cycles of operation. The stresses in the table will add to those produced by the temperature differential across the TPS. This temperature differential is 360°F at Station 38-40. The resulting combined stresses at Sections 41 and 25 will be less than two times yield strength. As a result, LCF life will remain above 1000 cycles. Since there is no combustion in this area, transient stresses are not of concern. The stresses at Stations 55 and 58 were assessed as part of the 2-D transient analysis.

Thermal transient analysis.--During an off-design transient condition, e.g., at engine ignition, the temperature gradients developed in the structure can become controlling with regard to structural design. Analyses were therefore performed to assess the magnitude of the transient temperature gradients and their effect on the selected design concepts. An initial analysis was conducted on the original reference primary structure designs (combination beam and honeycomb). A second analysis was conducted on the selected primary structure design (all-honeycomb).

Reference structure transient analysis: A typical structure, shown in fig. 113, was subjected to a two-dimensional nodal point thermal transient analysis. The beam material was Inconel 718. The honeycomb and TPS were either Hastelloy X or Nickel-200. The network forcing function was a time-varying coolant convective heat transfer coefficient and TPS metal temperature. Conditions near the coolant outlet manifold were specified because the metal temperatures reach a maximum here.

The primary source of heating is aerodynamic heating, which will almost entirely be absorbed by the TPS coolant, which in turn will dissipate to the structure during transients. The time constant of the TPS and the adjacent 1.5 mm (0.060-in.)-thick plate is a few seconds so that these parts will essentially track the coolant temperature.

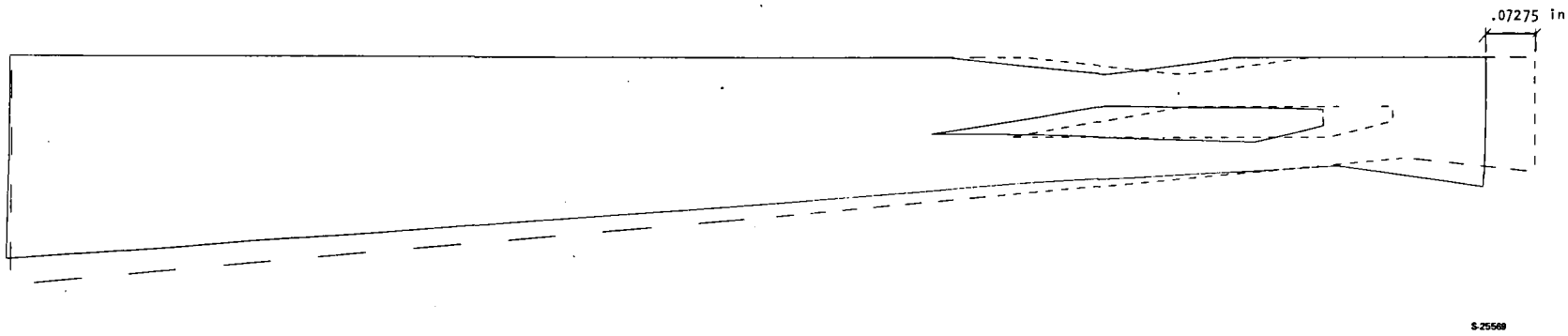

Figure 102.-Distorted geometry of the cold face sheet.

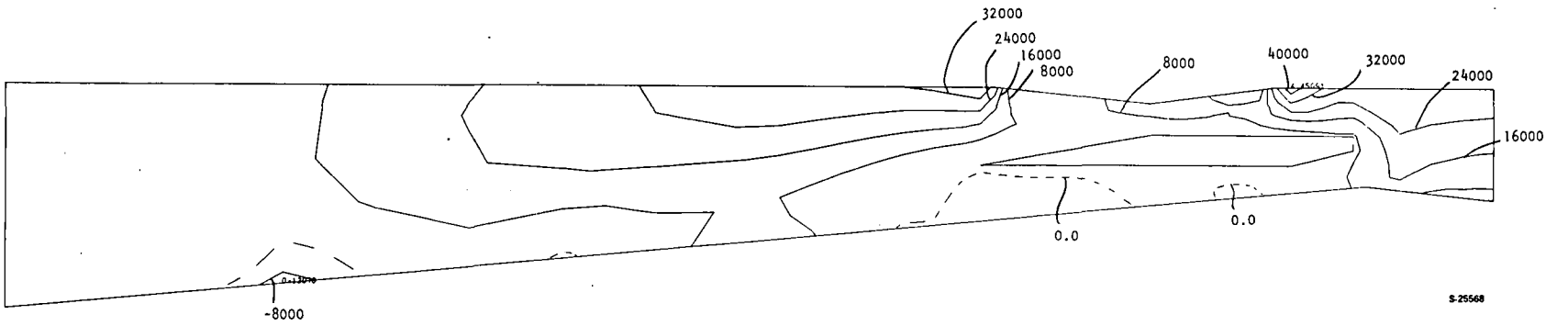

Figure 103.-Maximum principal stresses of the cold face sheet.

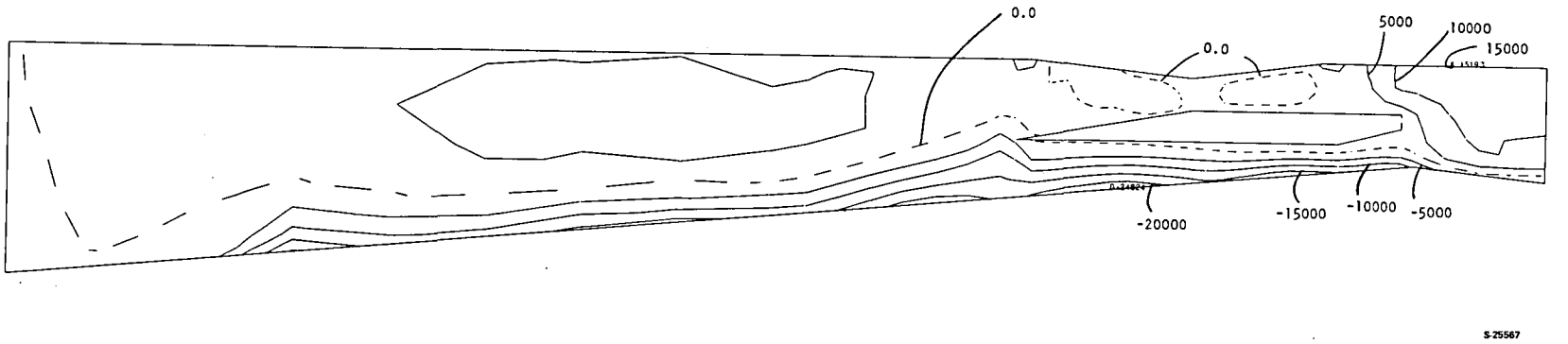

Figure 104.-Minimum principal stresses of the cold face sheet.

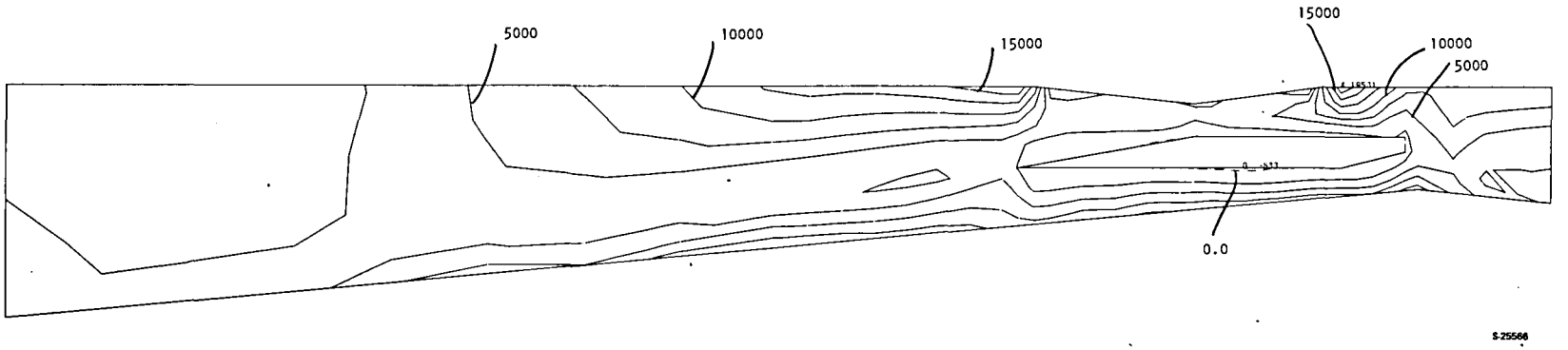

Figure 105.-Maximum shear stresses for the cold face sheet.

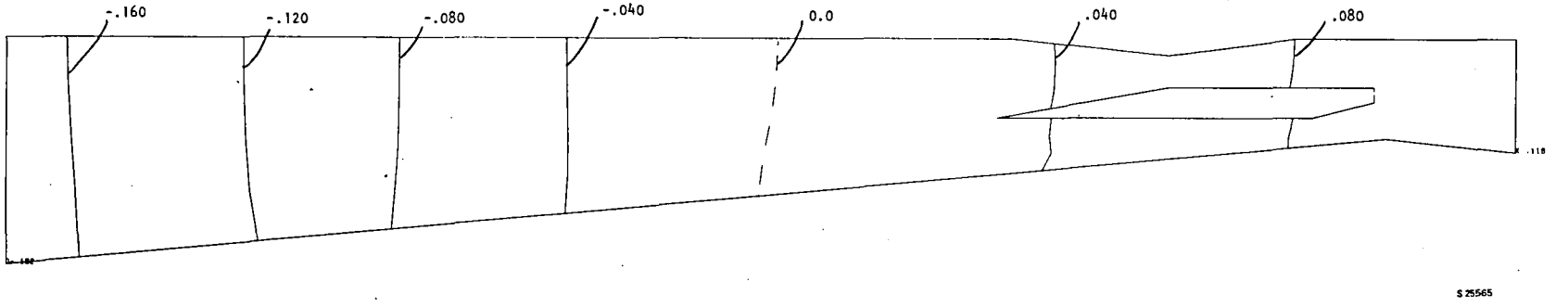

Figure 106.-Perpendicular displacement contours for the cold face sheet.

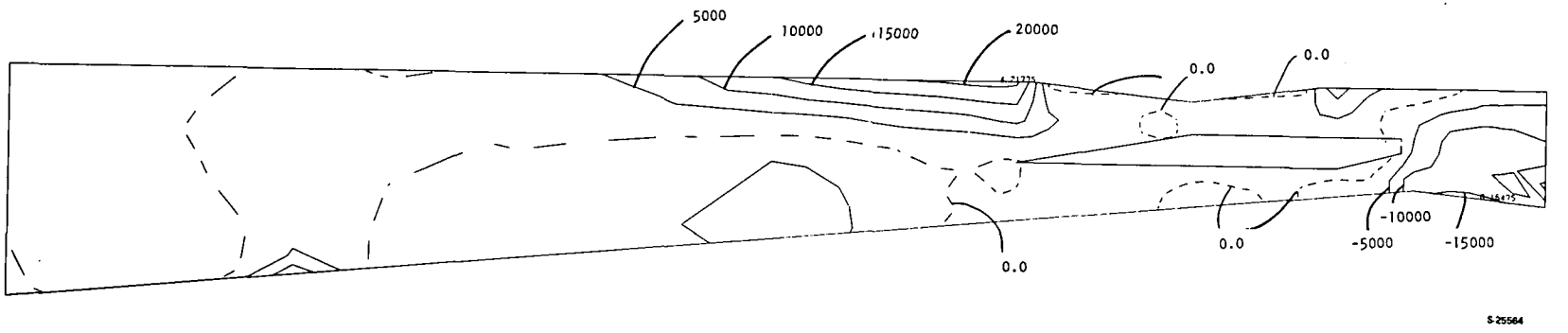

Figure 107.-Maximum principal stresses for the TPS hot face sheet.

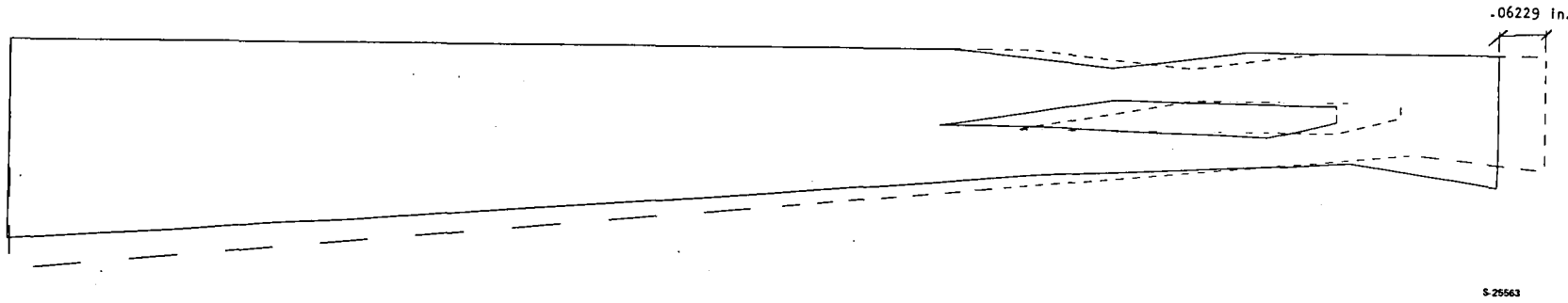

Figure 108.-Distorted geometry for the TPS hot face sheet.

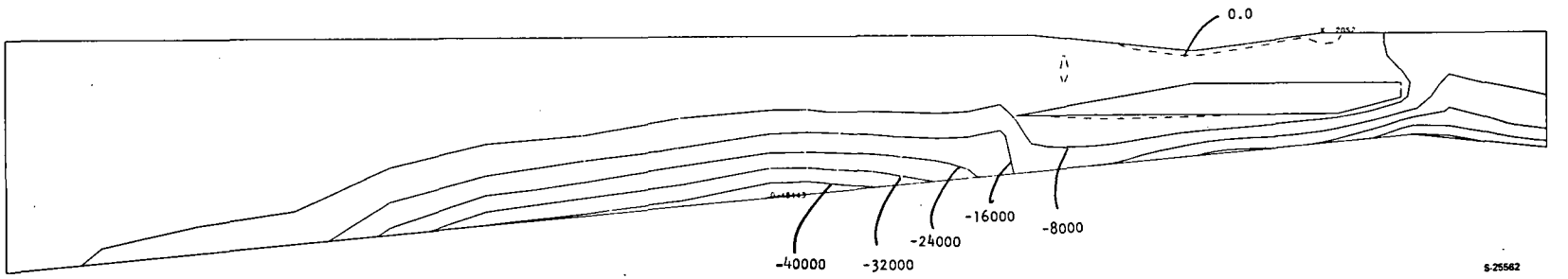

Figure 109.-Minimum principal stresses for the TPS hot face sheet.

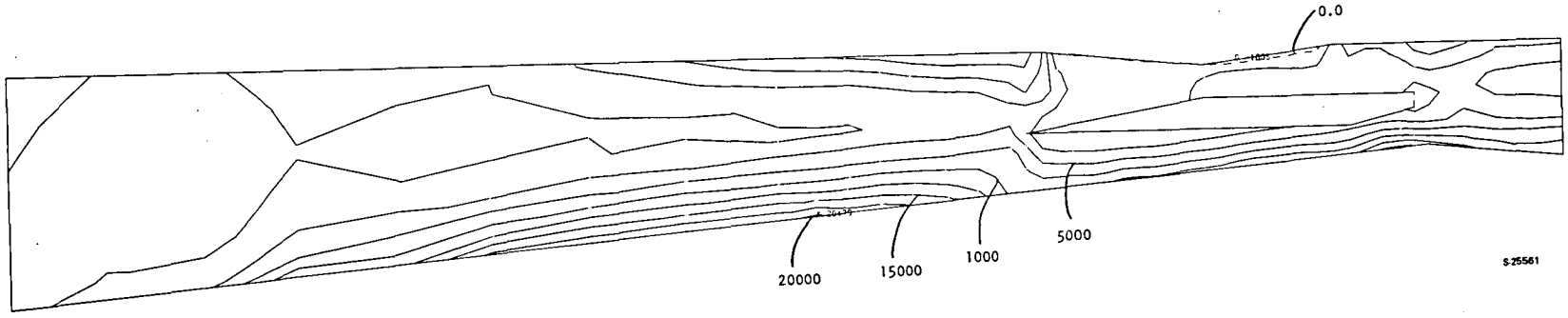

Figure 110.-Maximum shear stress for the TPS hot face sheet.

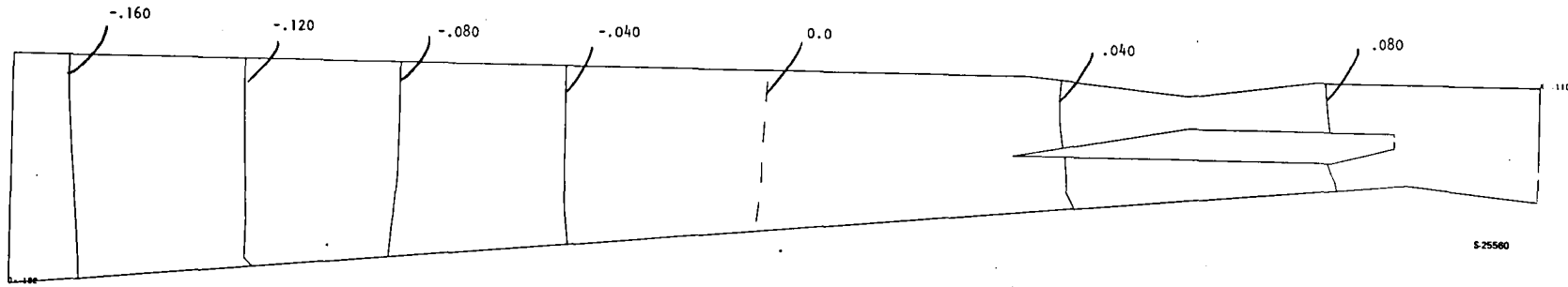

Figure 111.-Perpendicular displacement contours for the TPS hot face sheet.

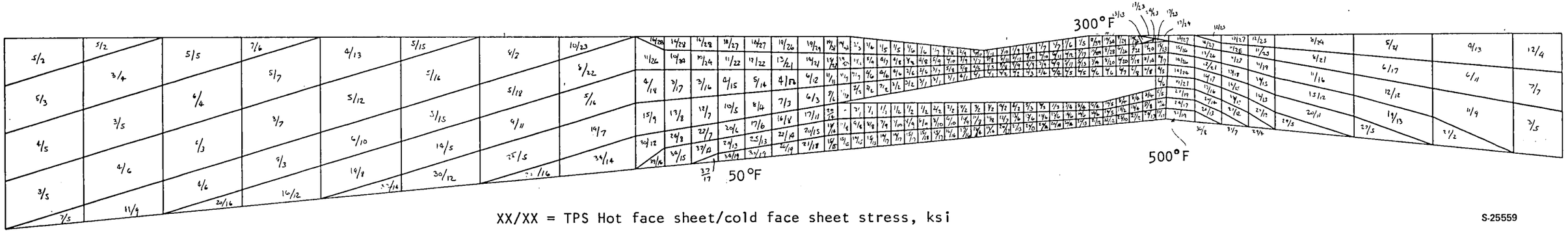

XX/XX = TPS Hot face sheet/cold face sheet stress, ksi

S-25559

Figure 112.-Effective Stresses of TPS hot face sheet and cold face sheet.

TABLE 22.-CRITICAL TOPWALL STRESSES

Station	Location	Middle surface stress, ksi	Temperature, °F	Minimum yield, ksi	1-percent creep in 1000 hr, ksi
41	Cold face sheet	45	169	43	-
25	TPS hot face sheet	-49	31	45	-
55	TPS hot face sheet	21	1000	34	-
58	TPS hot face sheet	7	1100	32	35

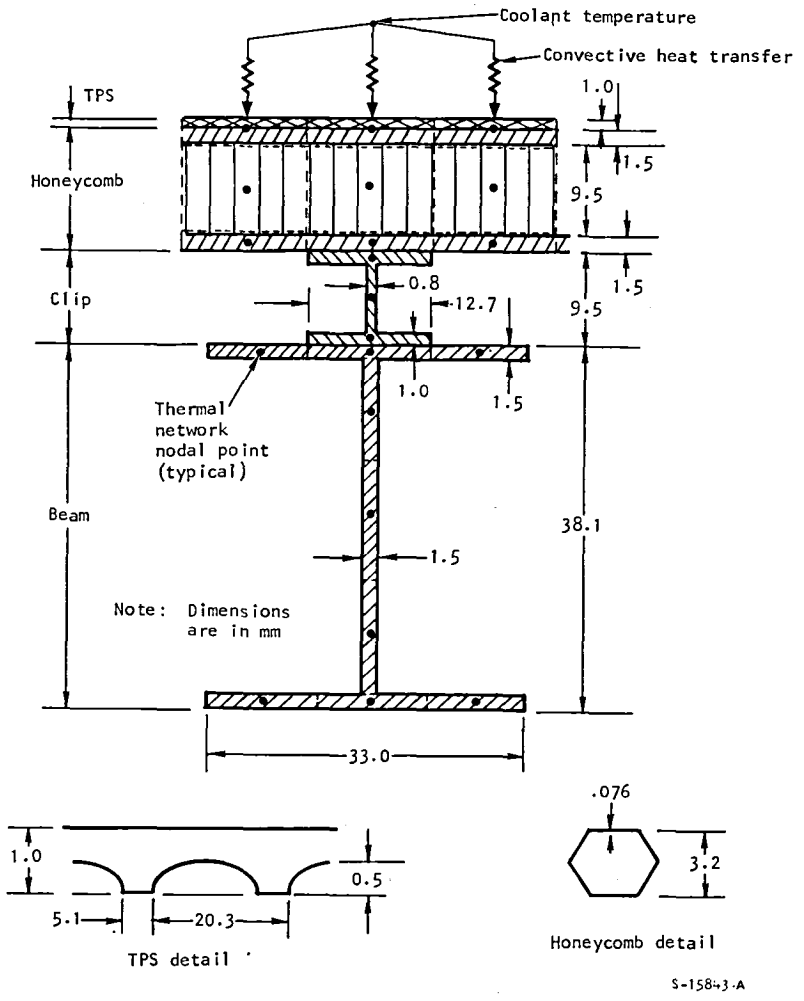

Figure 113.-Model for transient temperature analysis

A mission profile typical for a research airplane was used and is shown in fig. 114. An estimate of the coolant temperature is shown in fig. 115. The engine is uncooled below Mach 3 and the effective temperature is equal to the freestream recovery temperature. At 75 sec, the coolant flow begins and the engine is initially over-cooled. The coolant flow and temperature gradually increases as the airplane accelerates. Combustion occurs at 120 sec, at which point the coolant has reached a maximum design condition of 889 K (1600°R). At this same instant, the coolant flow is doubled because the heat load with combustion is about twice the unlit value. The inverse of these operations occurs during deceleration.

Structural temperature response is shown in fig. 116 for a Hastelloy X structure. The TPS temperature essentially tracks the local coolant temperature. At the midbeam position, the response is slow compared with the TPS; the maximum temperature rise for the 300-sec mission is 88°C (190°F). The maximum honeycomb ΔT is 500 K (900°R) for Hastelloy X and 378 K (680°R) for nickel. Both of these high temperature gradients occur just at the onset of combustion when the TPS prime structure is at 889 K (1600°R) and the honeycomb cold side is just beginning to respond.

As indicated, the midbeam temperature is unresponsive to the several operations of this mission. When accelerating to Mach 6 and maintaining a long cruise at this speed, the midbeam will take approximately 0.5 to 1 hr to reach steady state at a value near the local coolant temperature. Conversely, the opposite effect will occur on a deceleration from a long-duration Mach 6 cruise. The midbeam temperature will take approximately 0.5 to 1 hr to cool to ambient conditions.

Because the midbeam response is slow, the temperature difference from top surface midbeam to sidewall midbeam and from sidewall midbeam to cowl midbeam at a particular cross-section should be small (less than 111 K (200°R)). It is concluded, therefore, that sliding beam-to-beam connections are not required because the differential thermal growth between beams will not be excessive. A rigid joint can be made between beams and the resultant stresses can be held within the elastic limit.

As noted above, a high temperature gradient can be developed across the honeycomb primary structure during a thermal transient and this will produce a high stress. Estimated temperature gradients in the honeycomb panel are shown in fig. 117. Maximum temperature differential across the panel is 514 K (925°R) and occurs at 125 sec. Panel temperatures across the width are assumed constant.

All-honeycomb structure transient analysis: A more detailed transient thermal and stress analysis was conducted on the selected primary structure design, the all-honeycomb configuration. An engine cross-section where the highest temperature gradients occur was analyzed. The transient performance was assessed by considering the thermal response for a mission representative of a research airplane. Two cruise durations were investigated: 1 minute and 1 hr. The 1-hr cruise duration is representative of a commercial application; however, the times to reach cruise altitude and for descent would be greater. The mission profile and coolant schedules, shown in figs. 114 and 115, are the same as were used in the previous thermal-structural transient

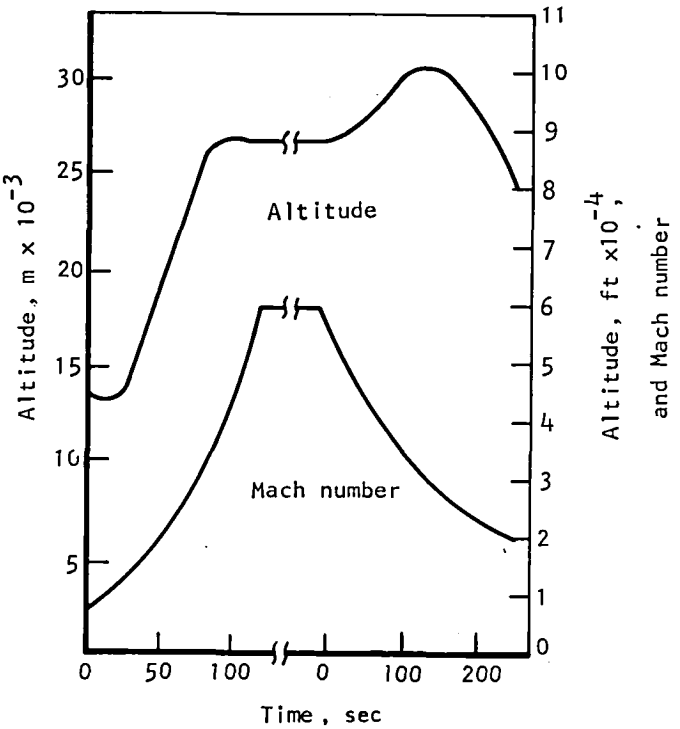

Figure 114.-Mission profile.

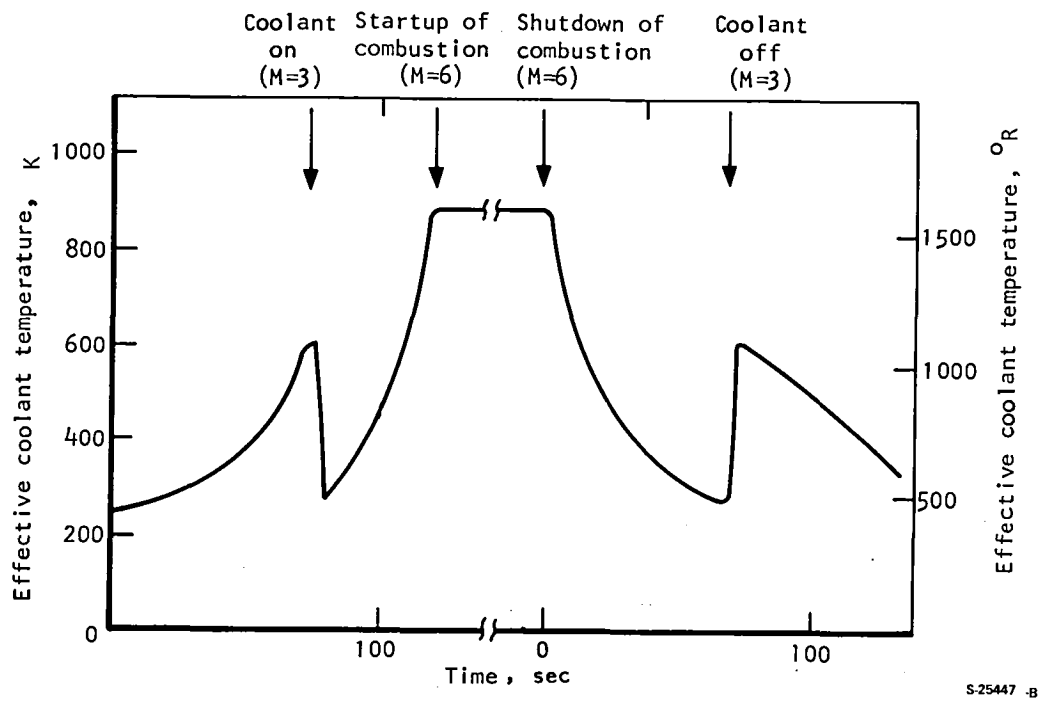

Figure 115.-Coolant outlet temperature.

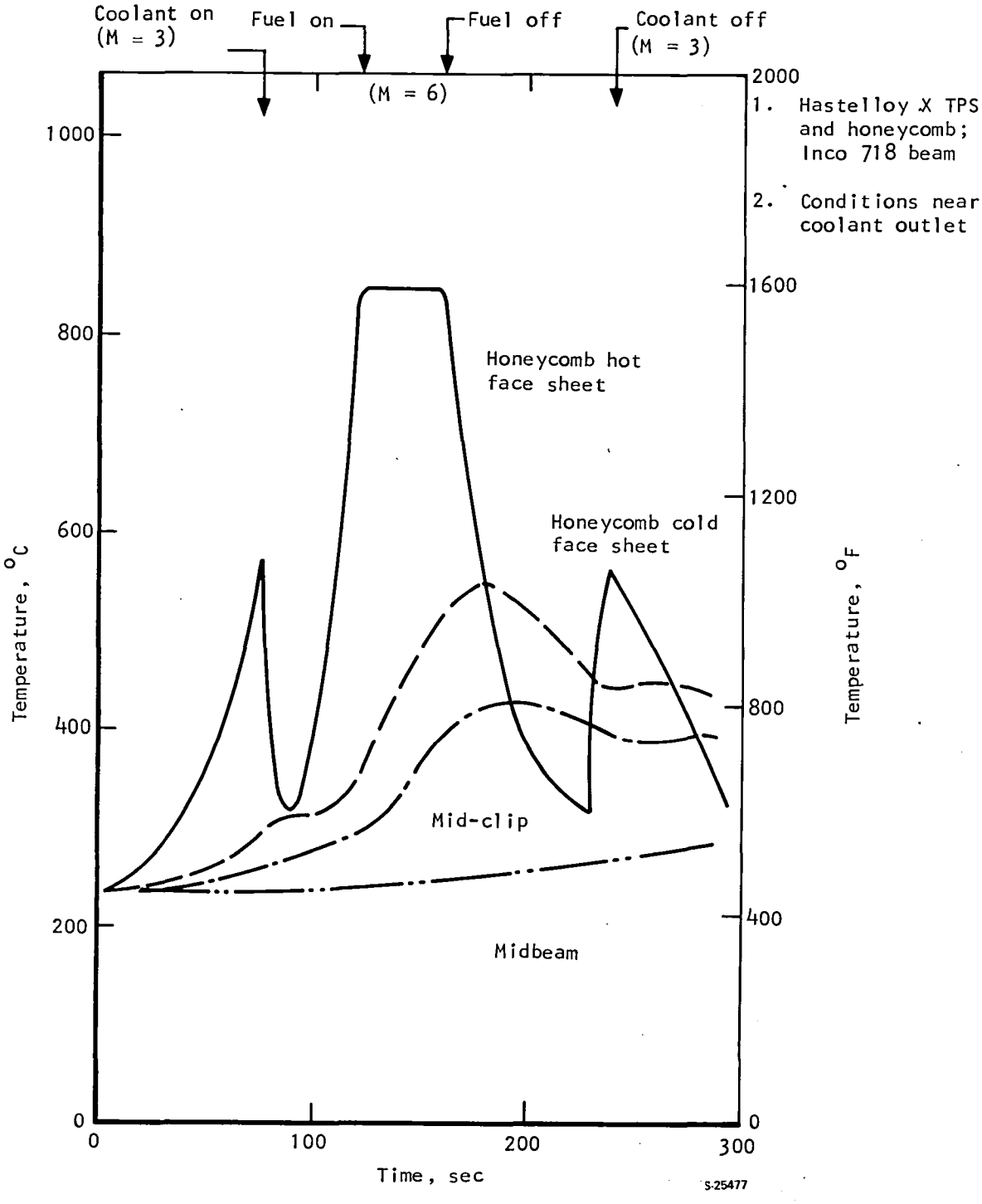

Figure 116.-Structural temperature response.

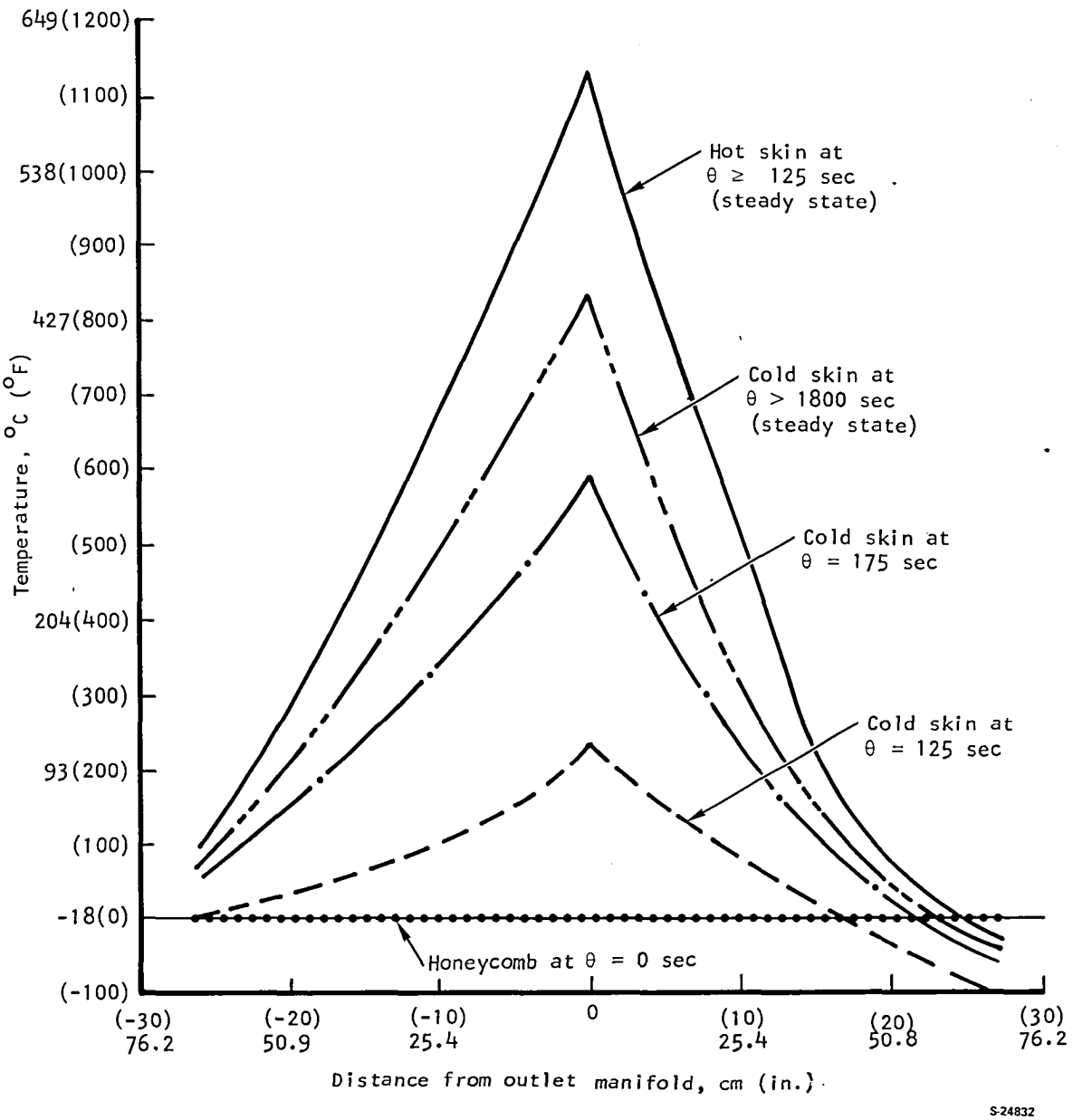

Figure 117.-Sidewall honeycomb panel temperature profiles.

The transient study was conducted at the axial station 58.83 (coolant outlet manifold location). This area will undergo the largest temperature gradients, as well as being subjected to maximum temperatures. The engine thermal response in this region will be one-dimensional, except at the corners that join the topwall to the sidewall and the sidewall to the cowl. The thermal nodal network is illustrated in fig. 118 for the topwall-sidewall corner. The nodal arrangement indicated was governed primarily by the extent that the corner 2-D effect was felt.

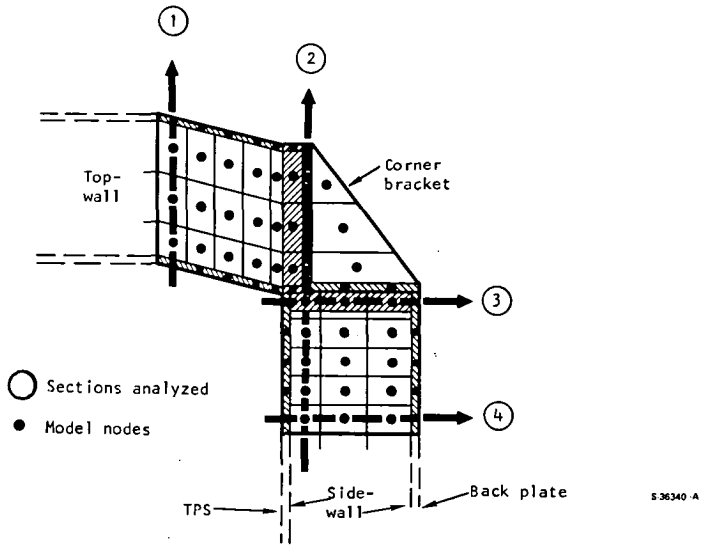

Figure 118.-Honeycomb transient analysis thermal model, topwall-sidewall corner.

The material for the TPS and back plates was Hastelloy X. For the honeycomb and corner structure, two types of materials were considered: Hastelloy X (0.003-in. cell thickness) and Nickel-200 (0.006-in. cell thickness). Nickel-200 has a thermal conductivity about three times that of Hastelloy X.

The results presented in the following paragraphs and figures are for the second or cruise mission only. The engine structure is allowed to reach thermal steady-state conditions prior to shutdown. This mission produces equal or higher temperature differences than temperature differences of the research mission. Temperature differences during startup are equal for both missions since the flight profile and the coolant and combustion scheduling are identical. During cruise, the slow-responding back side of the structure reaches the temperature of the TPS. At shutdown the TPS quickly cools off, creating a temperature difference reversal with the structure relative to that at startup.

The principal concern in this study was the assessment of the honeycomb thermal lag behind the TPS. Figs. 119 through 121 demonstrate this lag. In fig. 119, the relative responses of nodes 12 (TPS), 17, 22 and 27 (honeycomb), and 33 (back plate) for the sidewall are delineated. The maximum ΔT between nodes 12 and 33 is about 1200°R for Hastelloy X and occurs at 140 sec (2-1/3 min) after start. During shutdown, the maximum ΔT between these nodes is 1018°R at 70 sec after shutdown. These temperature differences are reduced by a small amount using Nickel-200 for the honeycomb material. The maximum ΔT during start

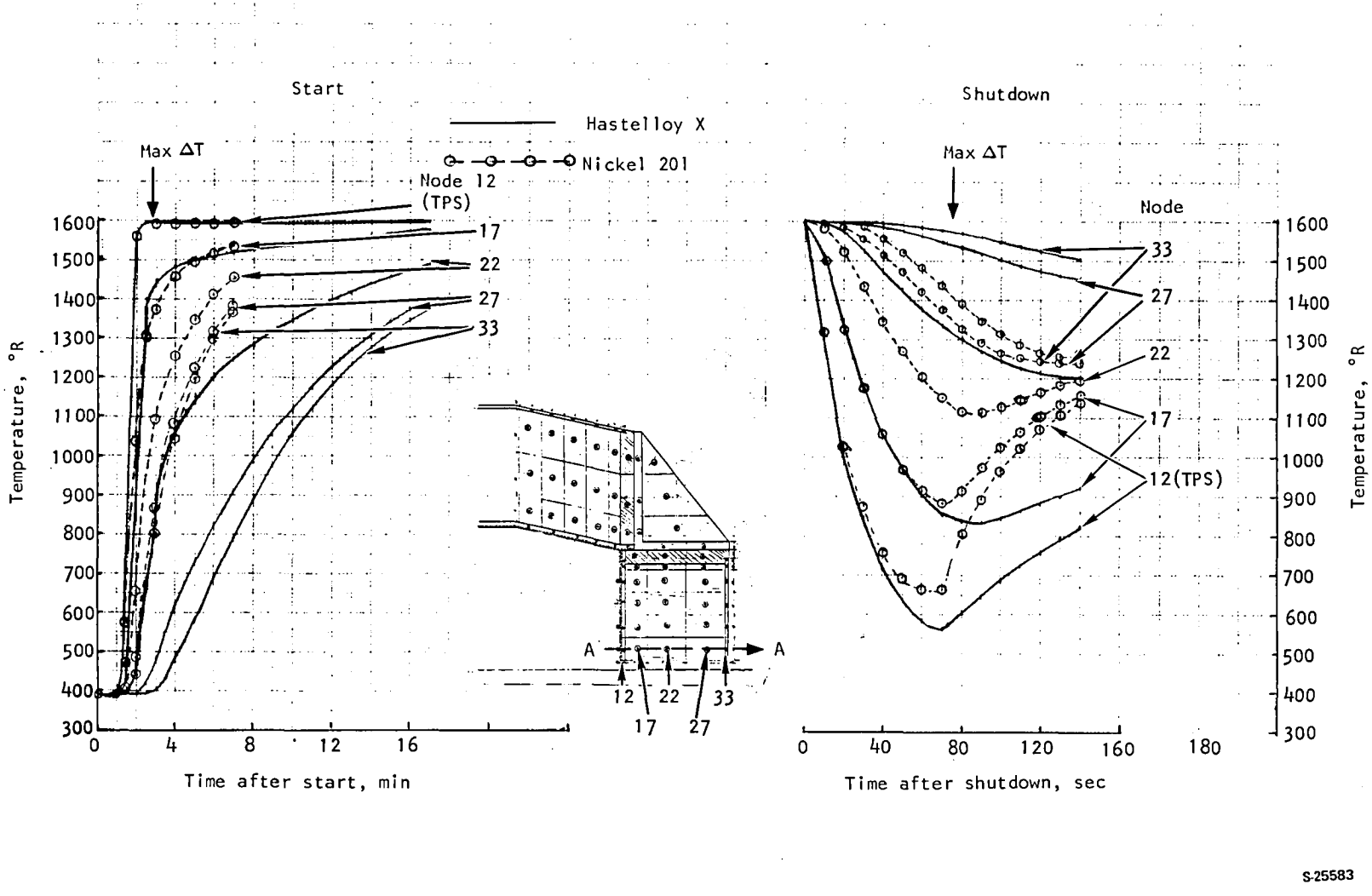

Figure 119.-Sidewall temperature histories, cruise mission.

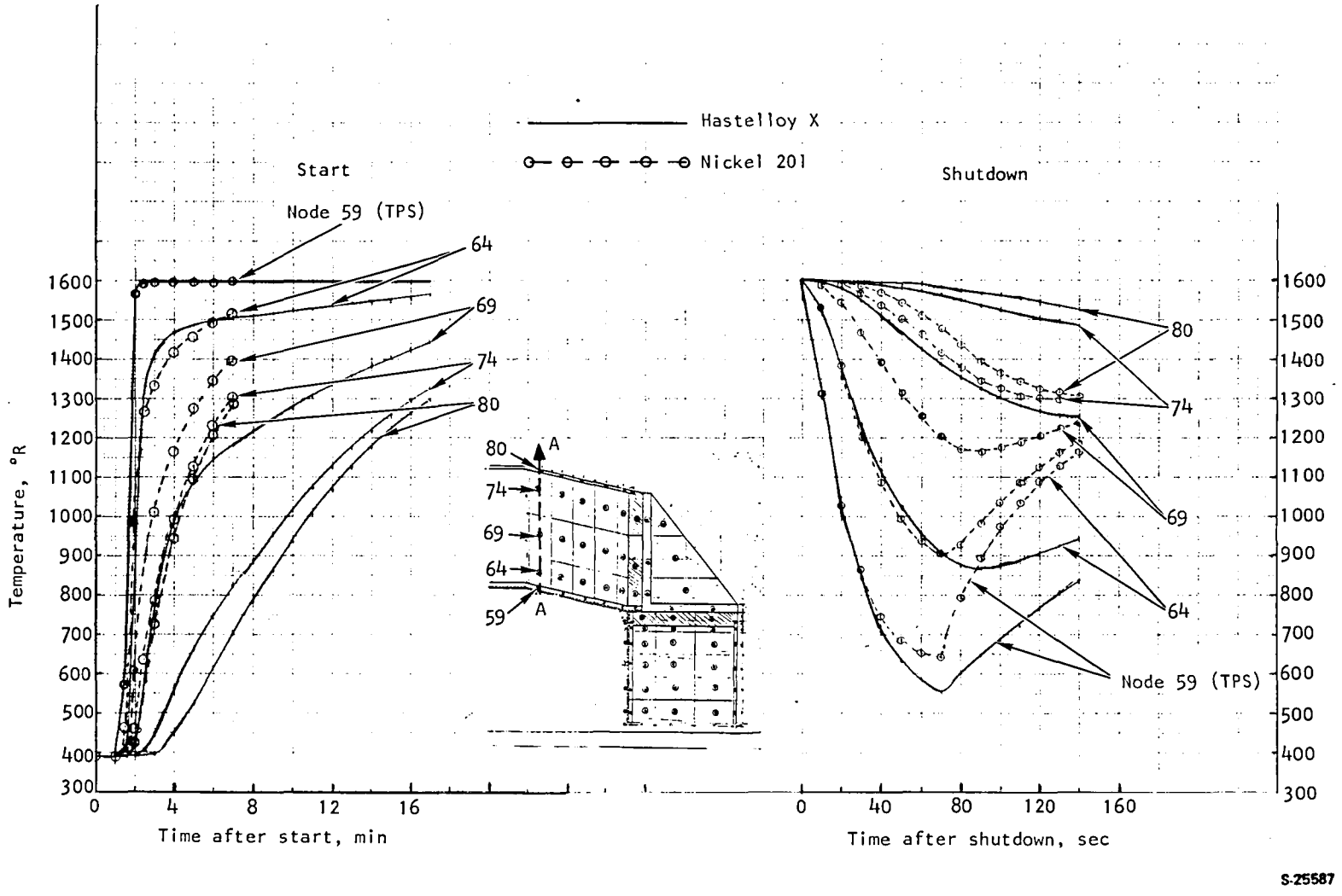

Figure 120.-Topwall temperature histories, cruise mission.

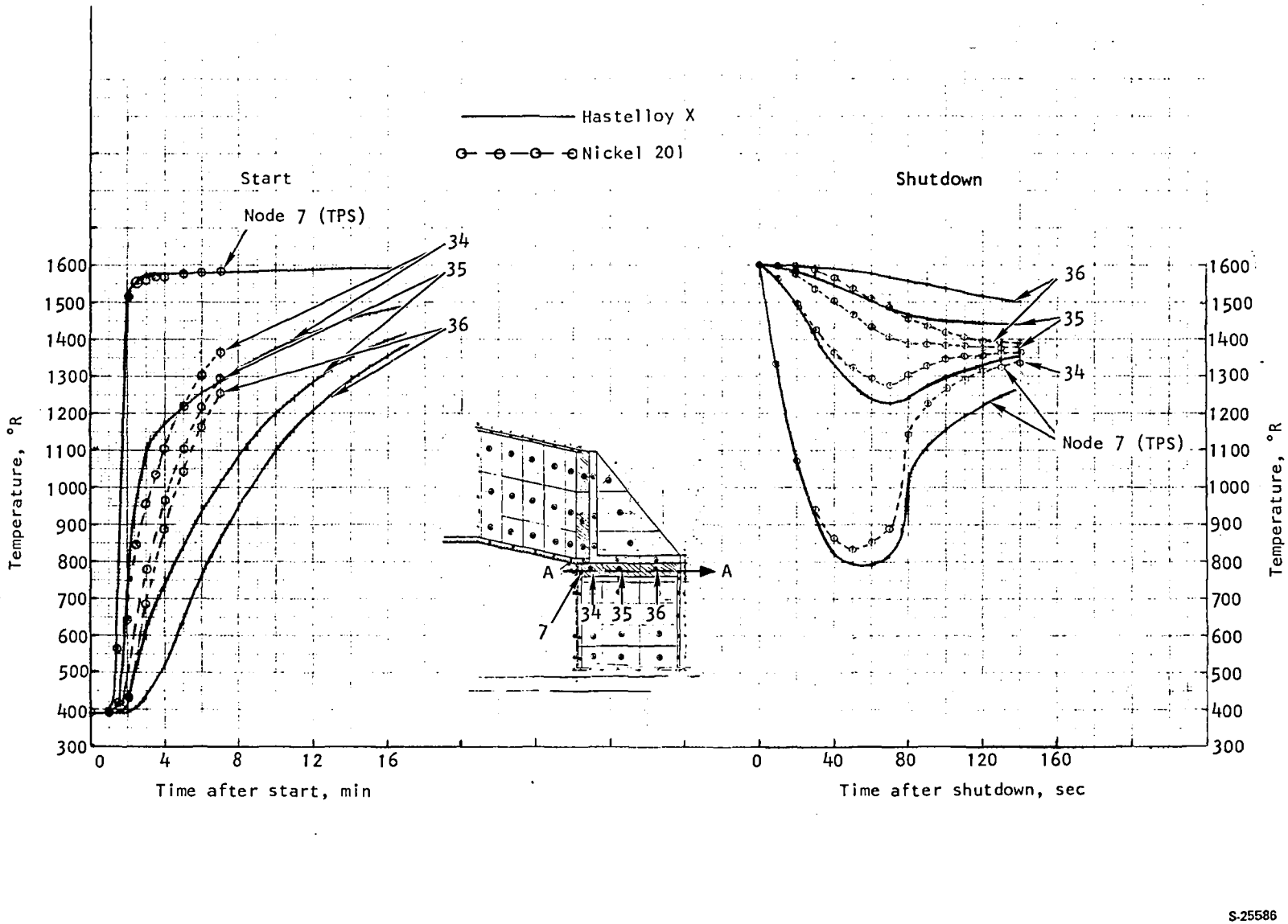

Figure 121.-Sidewall temperature histories, cruise mission.

for Nickel-200 is now 1119°R at 120 sec after start and 826°R at 50 sec after shutdown. In figs. 120 and 121, the responses for the topwall and sidewall corner plate are shown. While there is only a minor reduction in ΔT with Nickel 200 (0.006-in. cell thickness), the response is faster (ΔT's diminish more quickly) than with Hastelloy X (0.003-in. cell thickness).

In fig. 122, the temperature distribution is depicted for the topwall at specific times. A slight improvement in ΔT results from using Nickel-200 instead of Hastelloy X. The 2-D effect of the corner structure is shown in fig. 123 for the sidewall.

The results given above indicate that there are large temperature gradients during mission startup. The honeycomb lags behind the TPS by as much as 1200°R with Hastelloy X and 1119°R using Nickel 200. The implications of these temperature differences for structural performance are evaluated in the stress analysis.

A finite element model of a slice of the all-honeycomb engine at station 58.83 was constructed on the ANSYS computer program. The model consists of 205 elements and is shown in fig. 124. There are five elements through the thickness of the cowl, sidewall, and topwall. Both the TPS/hot-face sheet and the cold-face sheet are isoparametric shell elements (6 deg of freedom/node). The honeycomb was modeled as three isoparametric solid elements (2 deg of freedom/node) through the thickness to obtain a good aspect ratio. The attachment bracket of the topwall and sidewall honeycomb cells have isoparametric shell elements to close out the edge for bolting purposes.

The engine was assumed to be all Hastelloy X. Material properties for all of the shell elements were input as a function of temperature. The honeycomb cells are orthotropic in nature and material properties were input as constants with exception of the modulus and coefficient of thermal expansion, which were input as functions of temperature. Boundary conditions were as nearly as possible plane stress in the engine axial direction. The elements were free to deform on the plane taken through station 58.83. Three conditions were analayzed: 140 sec into the startup, steady-state, and 80 sec into the shutdown. These conditions yield the highest stress amplitude and are sufficient to perform a cyclic life analysis. Distortions as a result of the analysis are shown in figs. 125 through 127.

The peak stresses are shown in fig. 128 for each of the major surfaces. These stresses are such that a reduction in ΔT across the honeycomb is in order. To reduce these stresses, a reduction in ΔT can be accomplished by the following.

(a) Use less severe start and shutdown transient conditions. This would occur with a less severe mission.

(b) Control the coolant flow during startup and shutdown to damp out the transients.

(c) Incorporate a heat exchanger on the back side of the honeycomb in the critical area to reduce the ΔT across the honeycomb (see fig. 129).

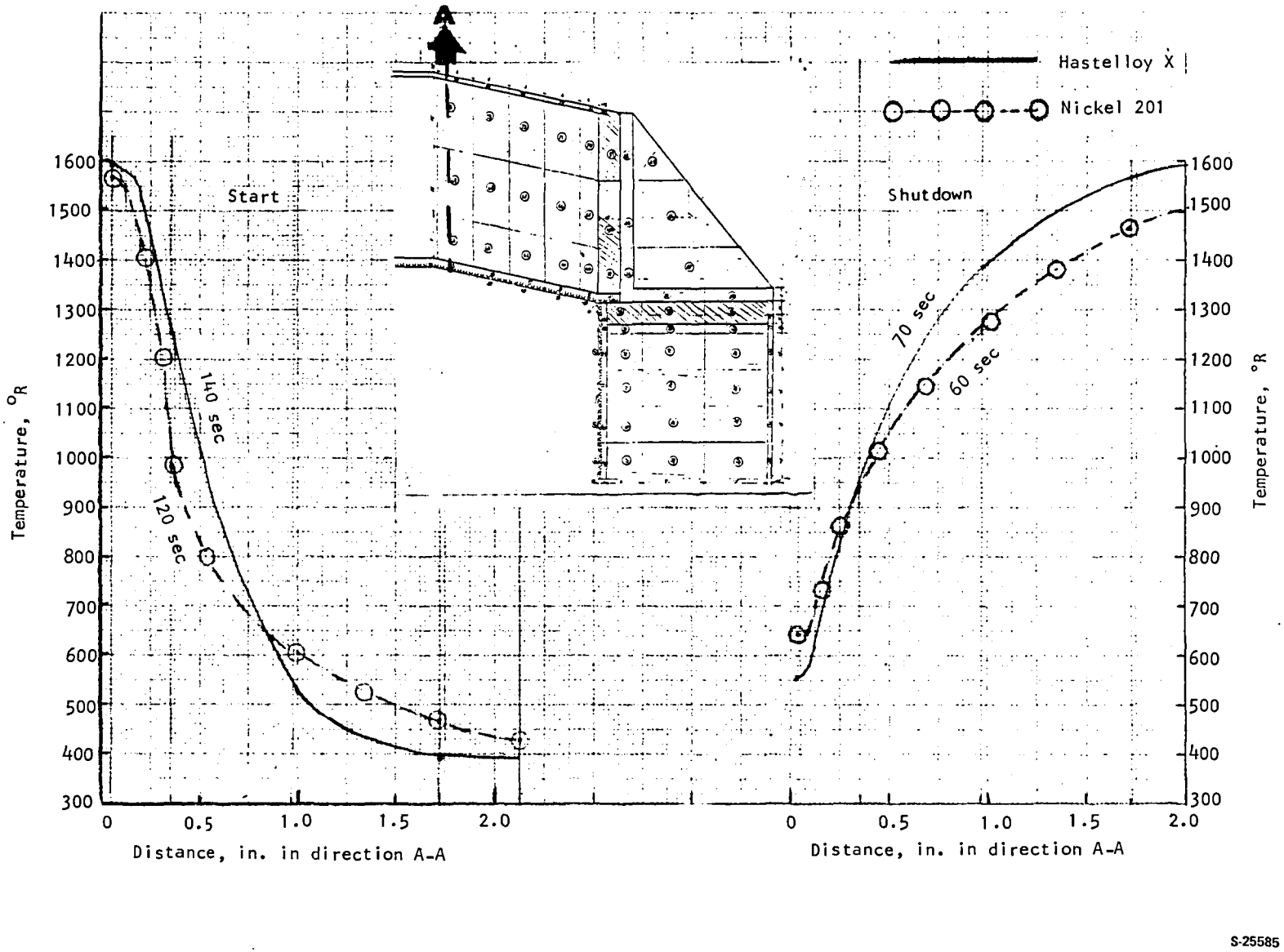

Figure 122.-Topwall temperature distribution, cruise mission.

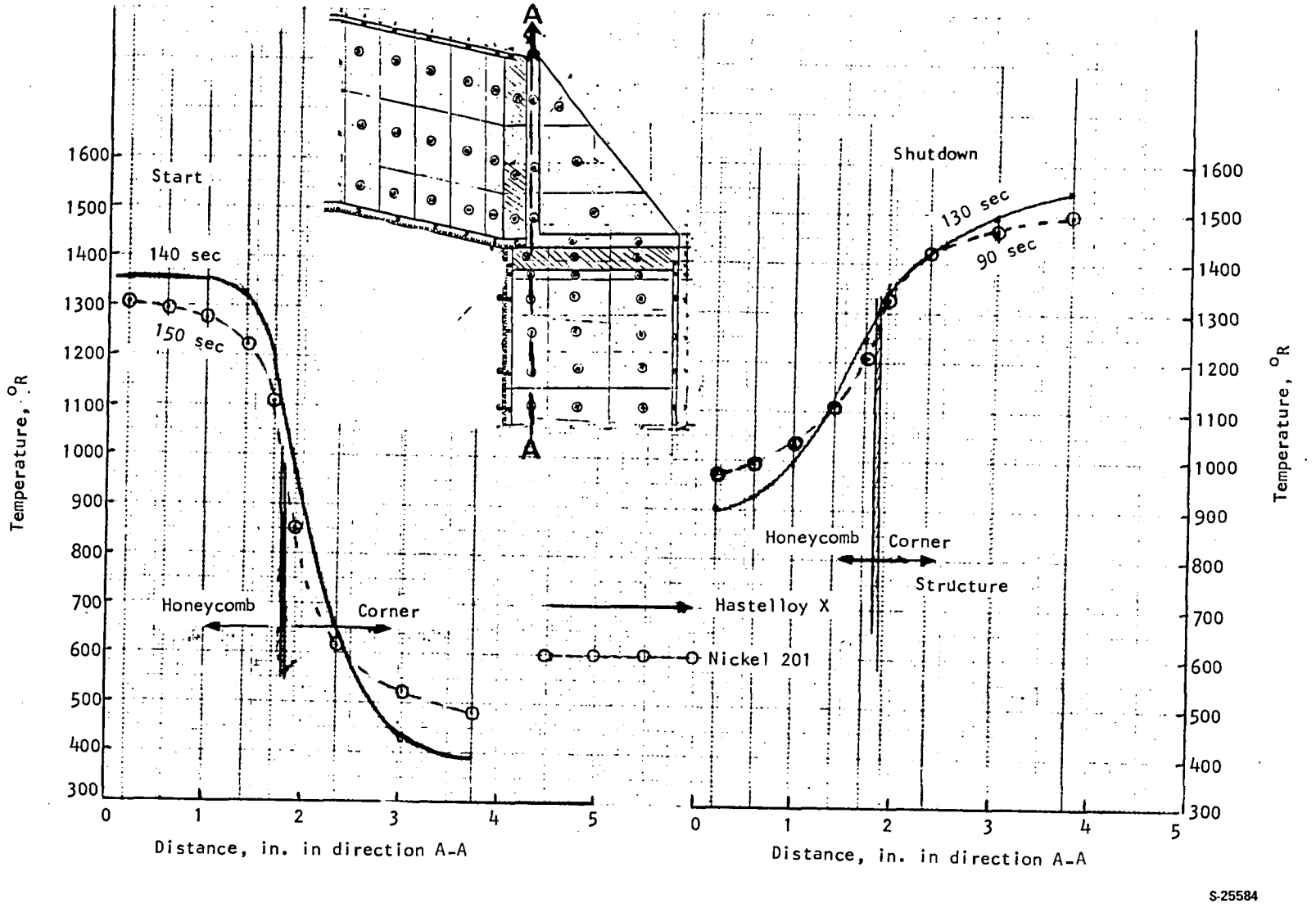

Figure 123.-Topwall/sidewall temperature distribution, cruise mission.

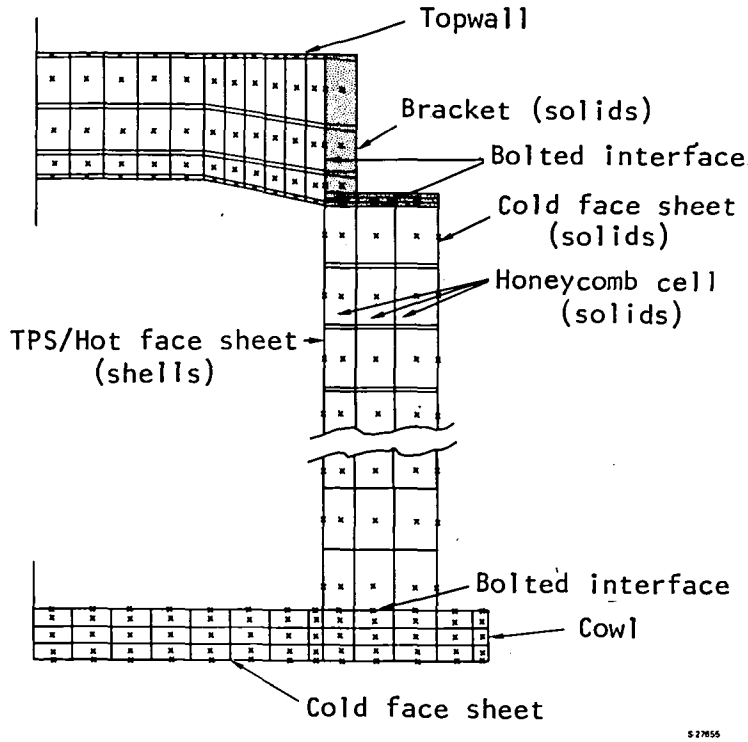

Figure 124.-Transient stress analysis model.

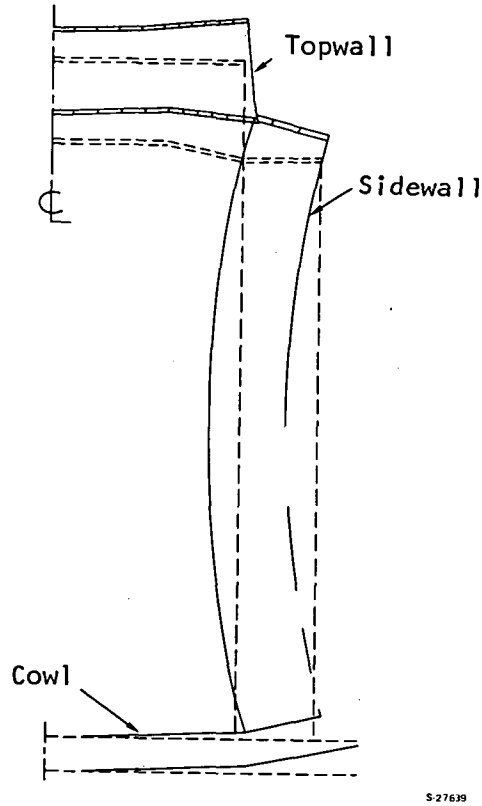

Figure 125.-Startup transient distortions.

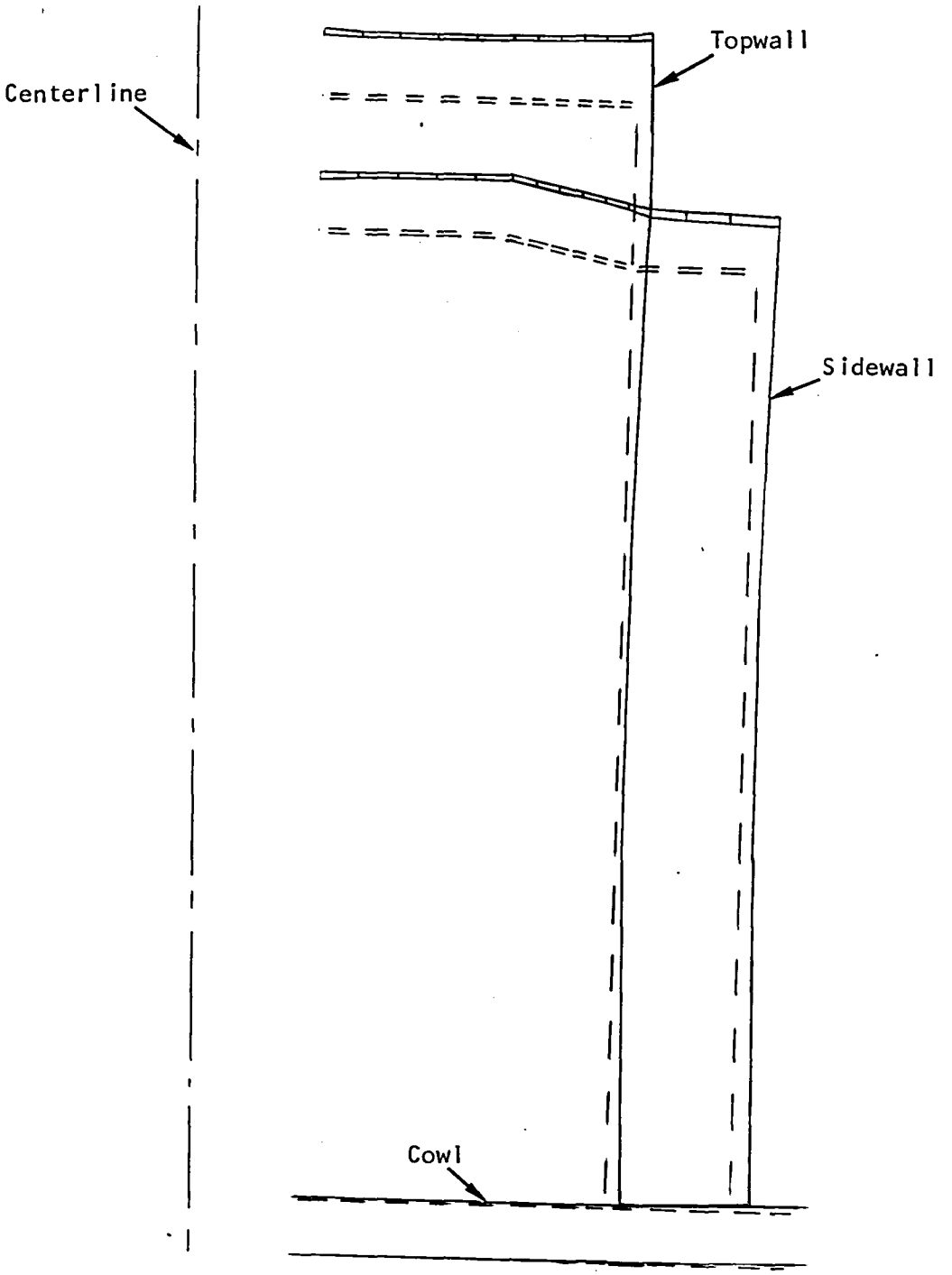

Figure 126.-Steady-state distortions of the Scramjet honeycomb model (Stn. 58.83).

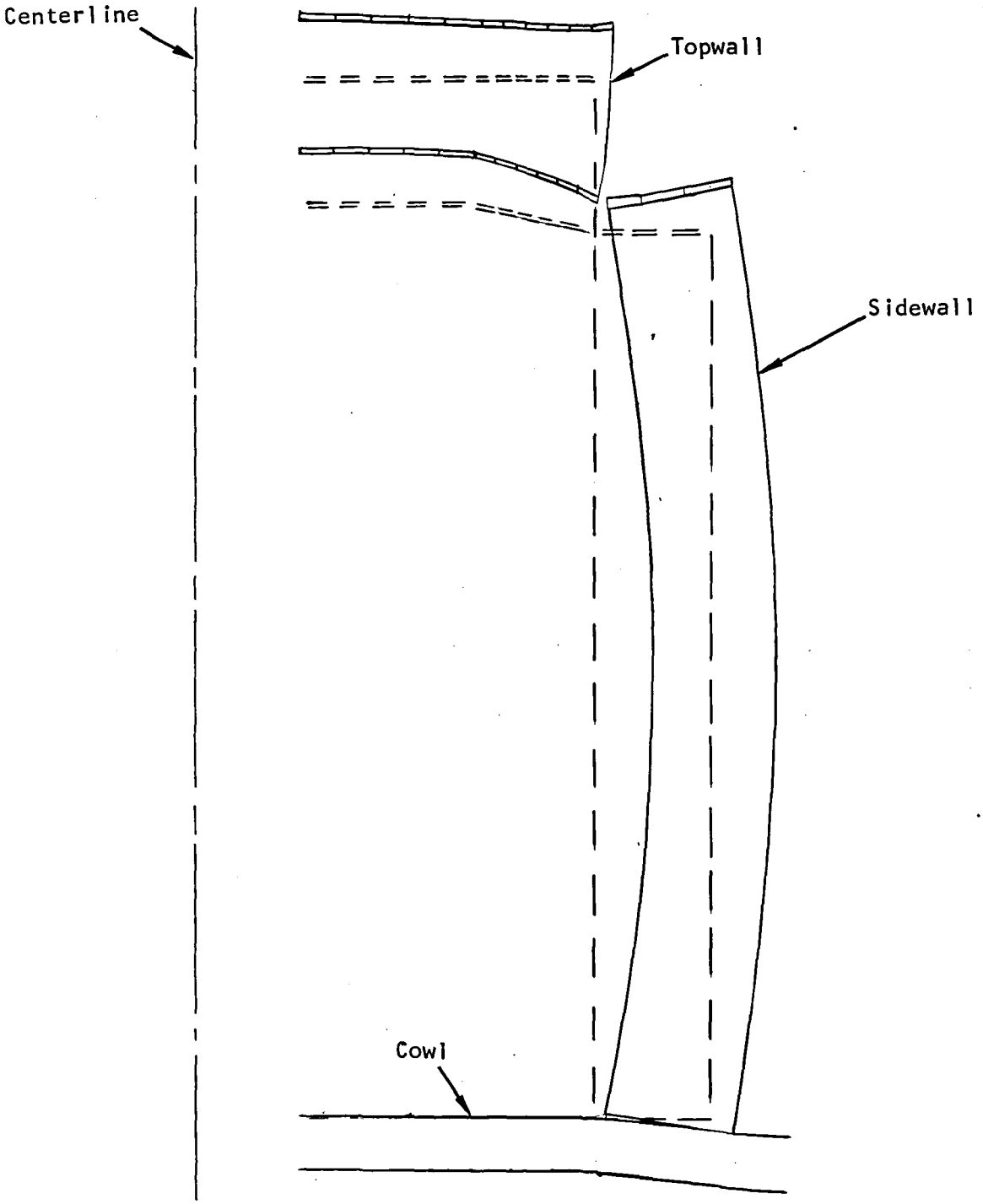

Figure 127.-Shutdown distortions of the Scramjet honeycomb model (Stn. 58.83).

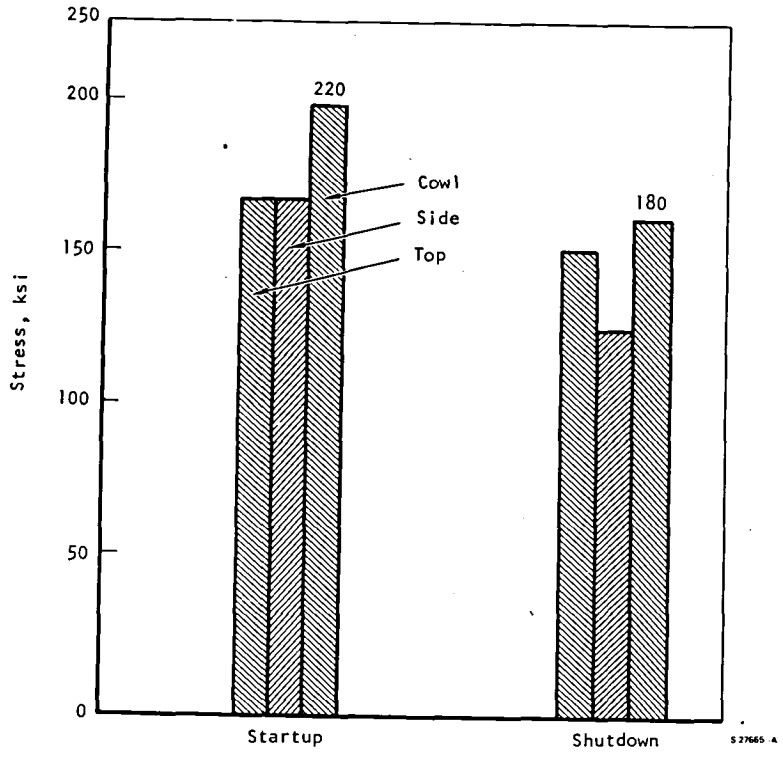

Figure 128.-Peak thermal stresses (elastic).

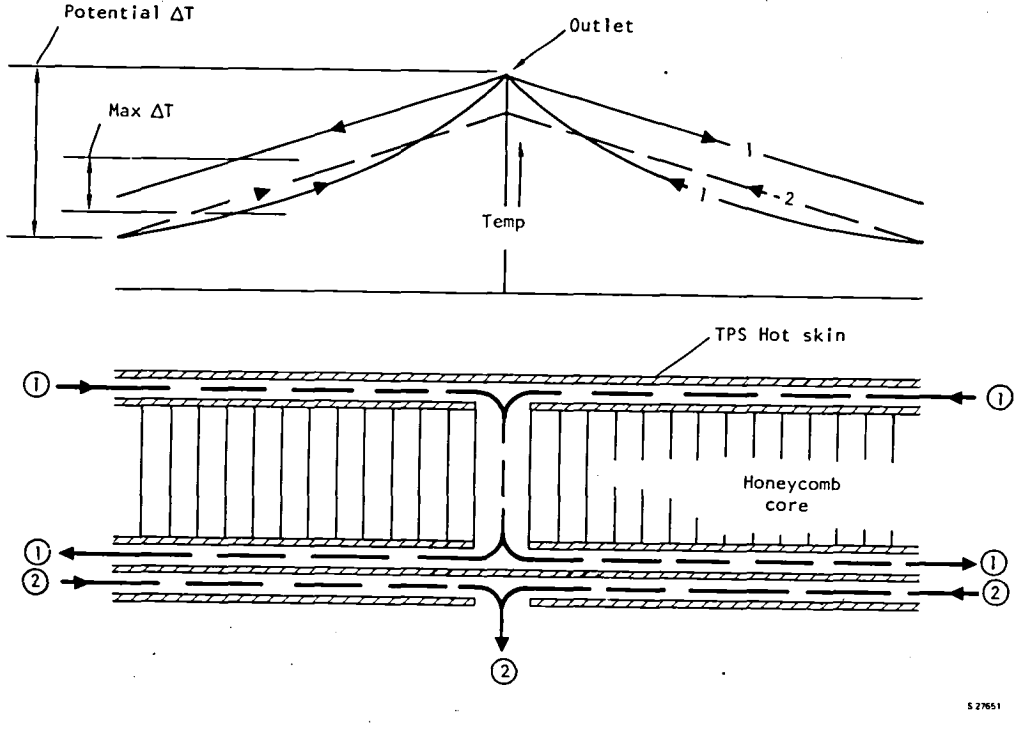

Figure 129.-Backside heat exchanger, 2-pass TPS/structure.

Concepts (a) and (b) listed above are operational changes, while (c) involves design changes and unwanted complexity. Studies indicate that the required reduction in ΔT can be accomplished entirely by the operational changes. The high transient ΔT's that occur because of rapid starting and stopping of coolant and fuel flows can be controlled by ramping of temperature and flow.

In performing the transient stress analysis, the shear modulus of the hexagonal honeycomb configuration appeared to be too small by at least an order of magnitude for the thickness honeycomb being used. The shear modulus was increased to a higher value (840 ksi) and the analysis completed. This increase in modulus can be accomplished physically by changing the honeycomb cell configuration to rectangular instead of hexagonal, as shown in fig. 130.

Engine layout design--Layout drawings of the selected primary structure engine design were prepared both as a result of, and in support of, the study analysis. The drawings reflect the current engine design and show details of primary structure, TPS, struts, coolant flow routing, and engine-aircraft interface. No backside heat exchanger for limiting ΔT's across the primary panel structure has been incorporated in the drawings. The need for this has not yet been established because the ΔT's may be sufficiently reduced by operational considerations.

The drawings for the all-honeycomb engine design are listed below and presented on the following pages.

Drawing 194112	Engine installation, airframe-integrated Scramjet
Drawing 194113	Engine assembly airframe-integrated Scramjet (6 module)
Drawing 194223	Strut assembly, airframe integrated Scramjet
Drawing 192224	Top panel assembly, airframe-integrated Scramjet

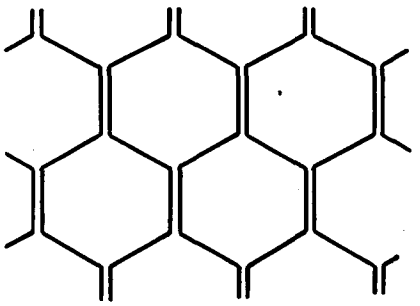

Hexagonal-brazed
G = 80 ksi

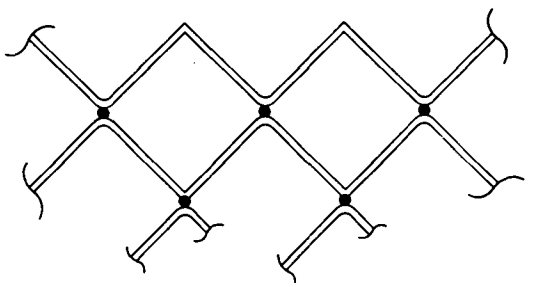

Square-welded
G < 800 ksi

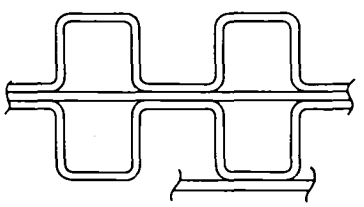

Square-brazed
G ~ 800 ksi

S-27647

Figure 130.-Honeycomb core design, large ΔT.

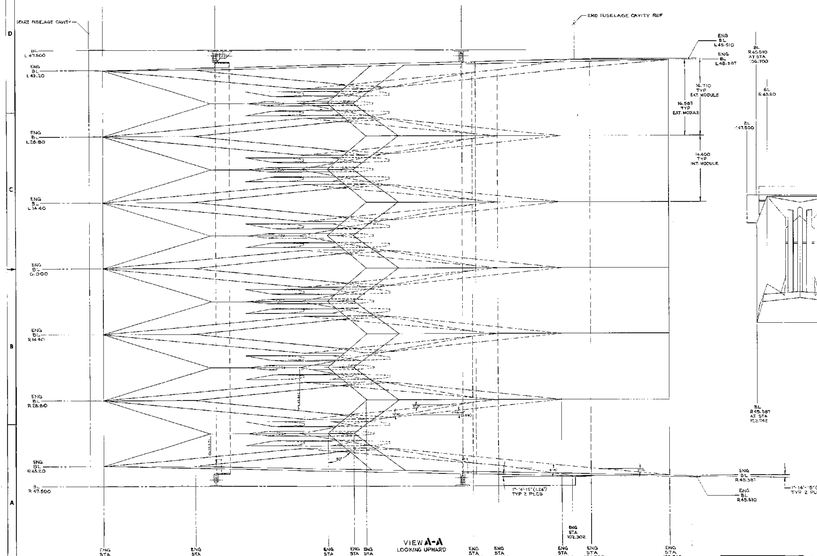

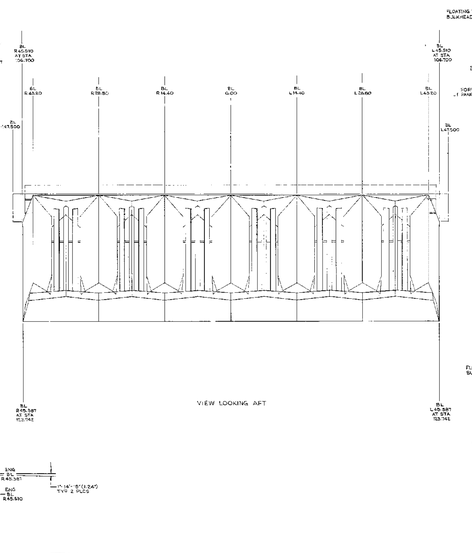

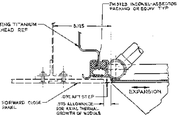

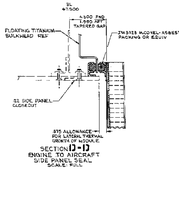

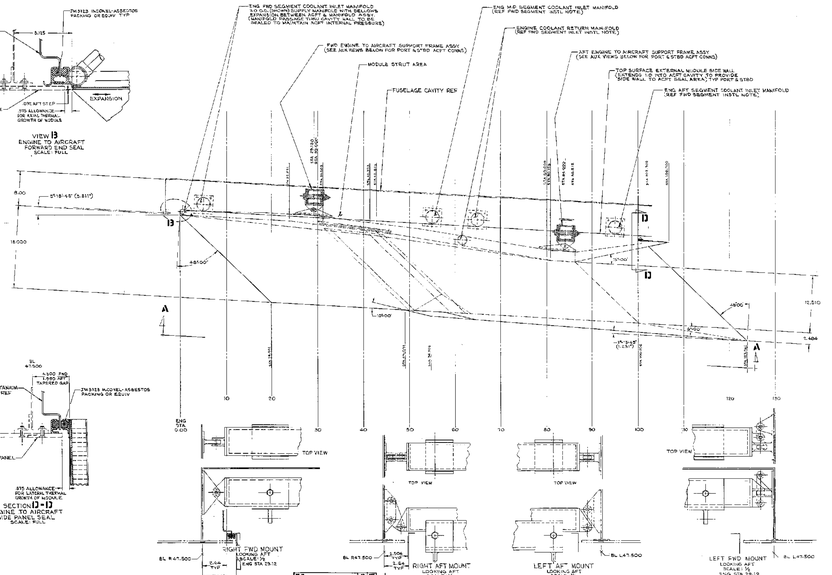

REVISIONS			
LTR	DESCRIPTION	DATE	APPROVED

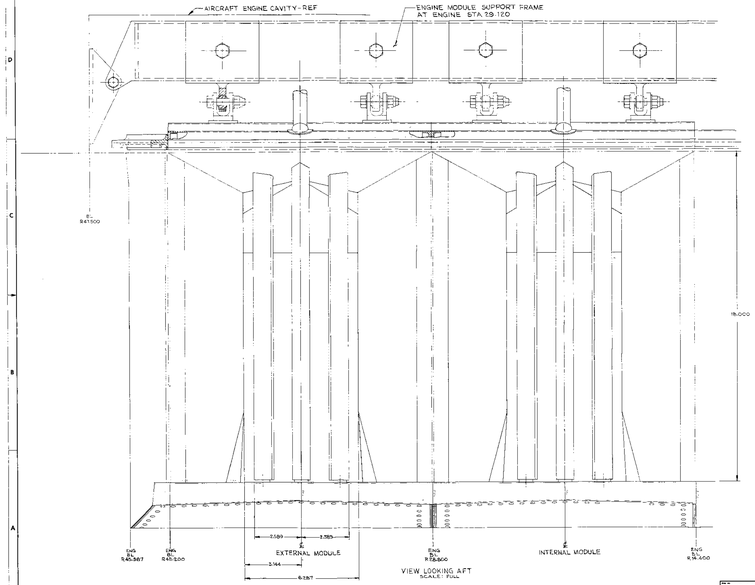

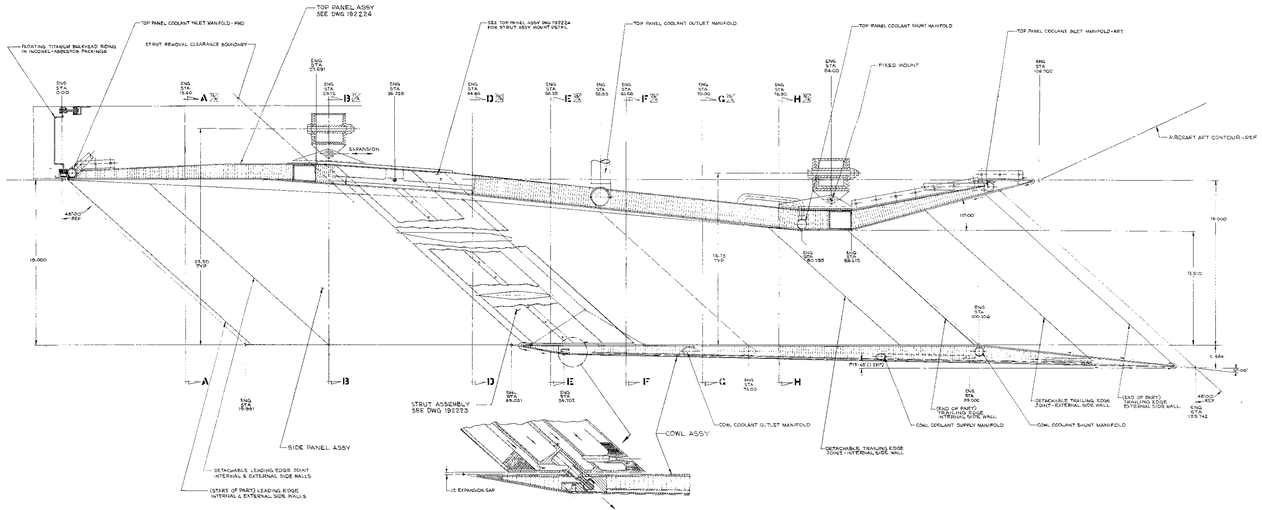

ASSEMBLY SEQUENCE

1. ASSEMBLE L.H. & R.H. SIDE WALL PANELS TO DETACHABLE LEADING / TRAILING EDGE, INSTALL BOTTOM PANELS TO FORWARD END OF SIDE WALL PANELS.
2. ASSEMBLE TOP PANEL, DWG NO. 192224, TO SIDE PANEL ASSEMBLY - SECURE BY BOLTING AT CORNER POINTS.
3. ASSEMBLE STRUTS, DWG NO. 192223, TO TOP PANEL ASSEMBLY, DWG NO. 192224, FROM TOP SIDE AND SECURE BY BOLTING TO SUPPORT BRACKETS.
4. ASSEMBLE COWL ASSEMBLY BY REGISTERING
   A. COWL TO TOP PANEL (STRUT & FIXED MOUNT PANEL REMOVED - INSTALL BOLTS AND WASHERS AS REQ'D TO SECURE)
   B. COWL TO SIDE WALL BOTTOM SEAL STRIP
   C. STRUT END TO THERMAL EXPANSION MOUNT
   D. MODULE TO MODULE TIE BOLTS
5. ASSEMBLE PLUMBING CONNECTIONS TO TOP PANEL, SIDE PANELS, STRUTS AND COWL.
6. ASSEMBLE FLEX PLUMBING CONNECTIONS TO COWL BOTTOM PANEL - INSTALL HOSES BOLTING TO COWL SEAL MOUNTS.
7. ASSEMBLE COMPLETED ENGINE CLUSTER TO ENGINE SUPPORT FRAME, DWG. NO. 194113.
8. INSTALL ENGINE CLUSTER INTO AIRCRAFT CAVITY AND BOLT TO ENGINE SUPPORT BRACKETS, DWG NO. 194113.
9. ASSEMBLE ALL AIRCRAFT/ENGINE INTERCONNECTS TO PLUMBING AND INSTRUMENTATION.
10. INSTALL ALL AIRCRAFT LAYN CLOSE-OUT PANELS AGAINST AIRCRAFT CAVITY/ENGINE SEAL MOUNTS.

REVISIONS			
ZONE	REVISION	DATE	APPROVED

DRAWING SIZE	CODE IDENT NO.	DRAWING NO.	
SCALE	WEIGHT	SHEET	

ENGINE ASSEMBLY, AIRFRAME-INTEGRATED NACELLE TO MODULE

7170210	194113	
NEXT ASSY	USED ON	

194113 S.H. 1

NOTES UNLESS OTHERWISE SPECIFIED

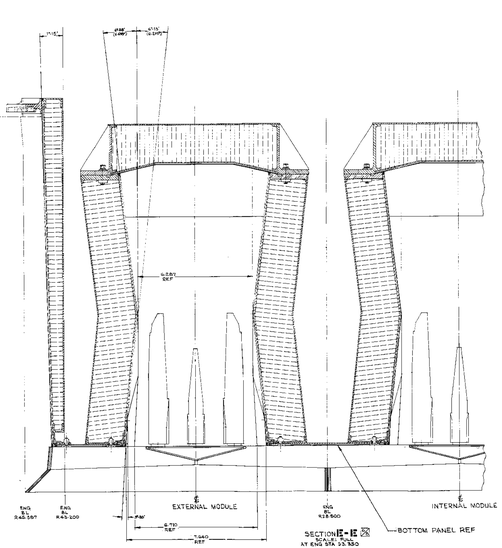

SECTION E-E
SCALE: 1"=1"
AT ENG STA 33.330

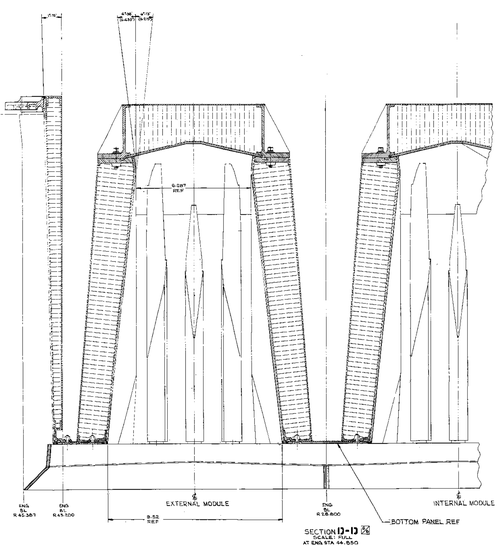

SECTION D-D
SCALE: 1"=1"
AT ENG STA 44.550

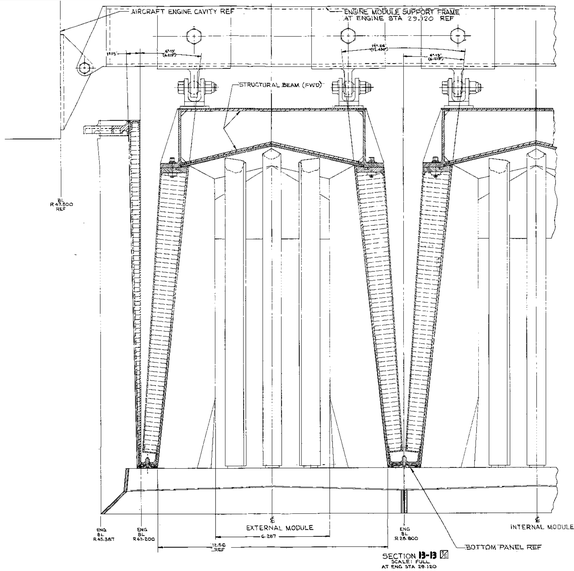

SECTION B-B
SCALE: 1"=1"
AT ENG STA 29.150

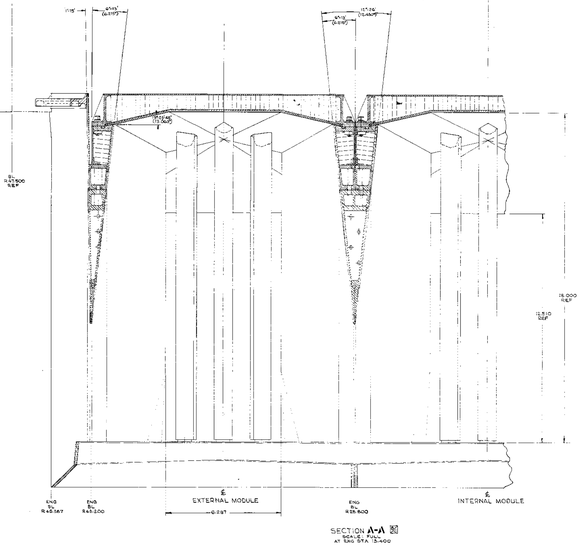

SECTION A-A
SCALE: 1"=1"
AT ENG STA 21.400

194113 Z

194113 Z

J 70210 194113

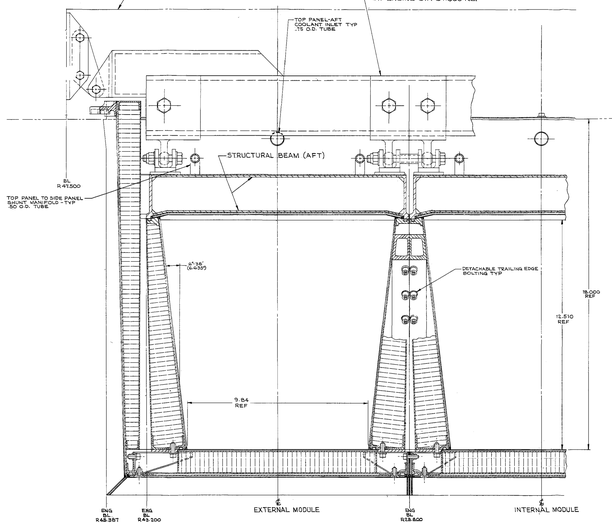

SECTION H-H
SCALE 1.5/1
AT ENG STA 78.900

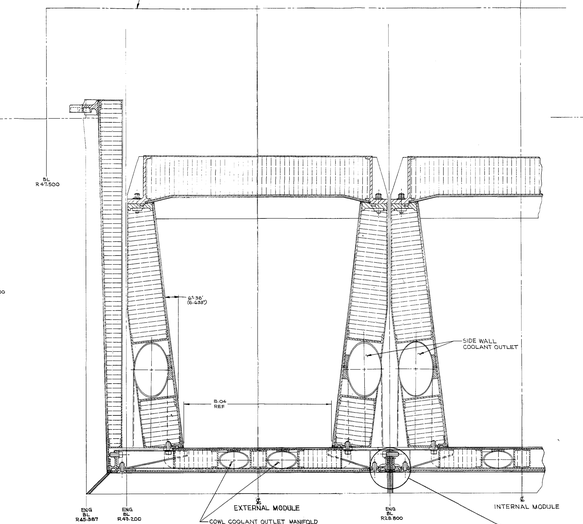

SECTION G-G
SCALE 1.5/1
AT ENG STA 70.000

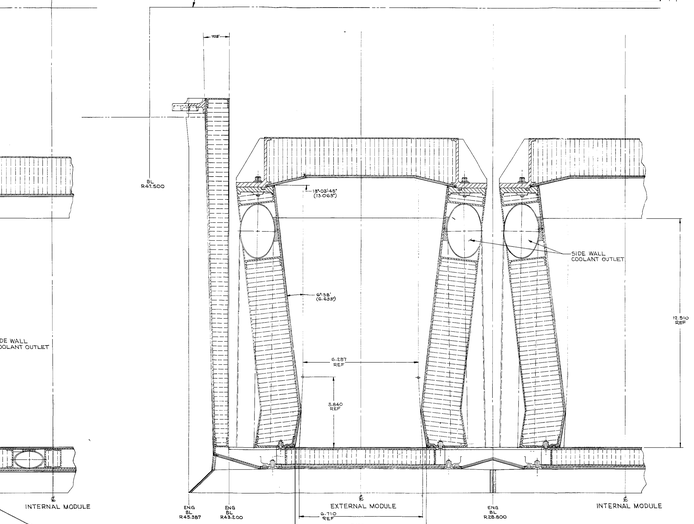

SECTION F-F
SCALE 1.5/1
AT ENG STA 61.460

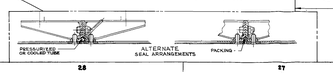

DWG. NO.	REV.
194113	J

DWG. NO.	REV.
194113	J

DWG. NO.	REV.
J 70210	194113

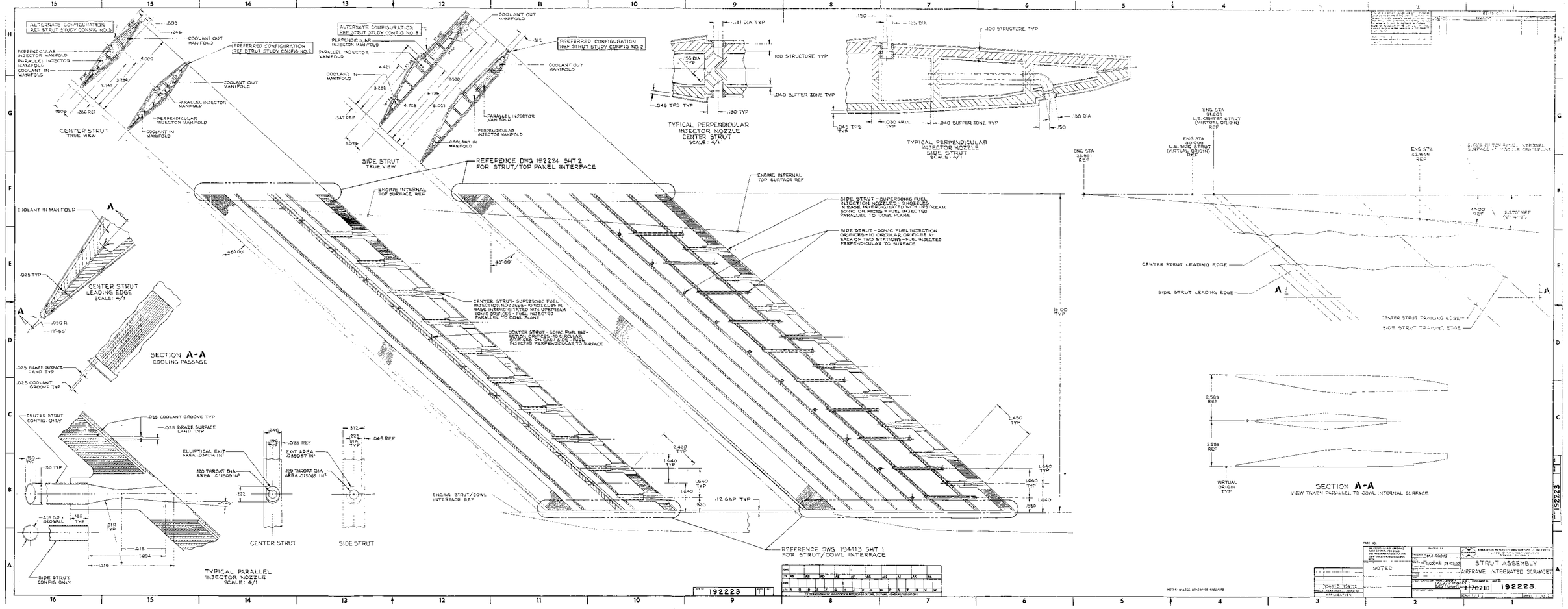

NOTES

STRUT ASSEMBLY AIRFRAME INTEGRATED SCRAMJET

SIZE	CAGE CODE	DWG NO.	REV
A	80091	192223	

SCALE 1:1 SHEET 1 OF 1

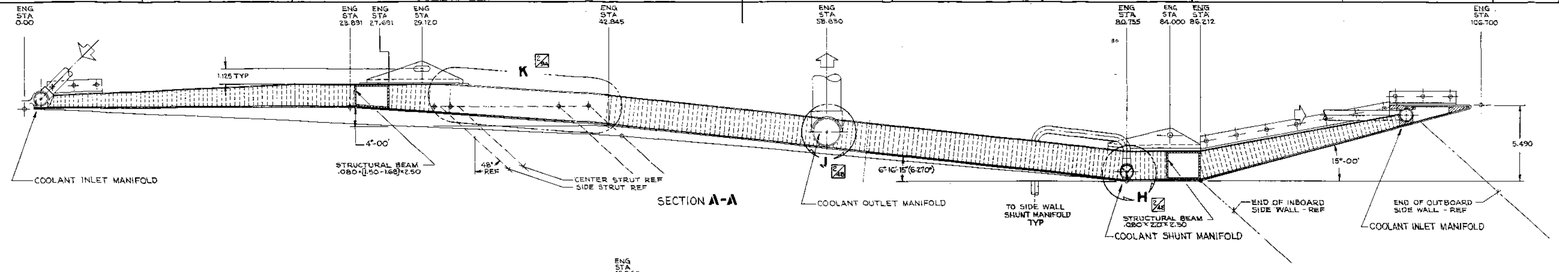

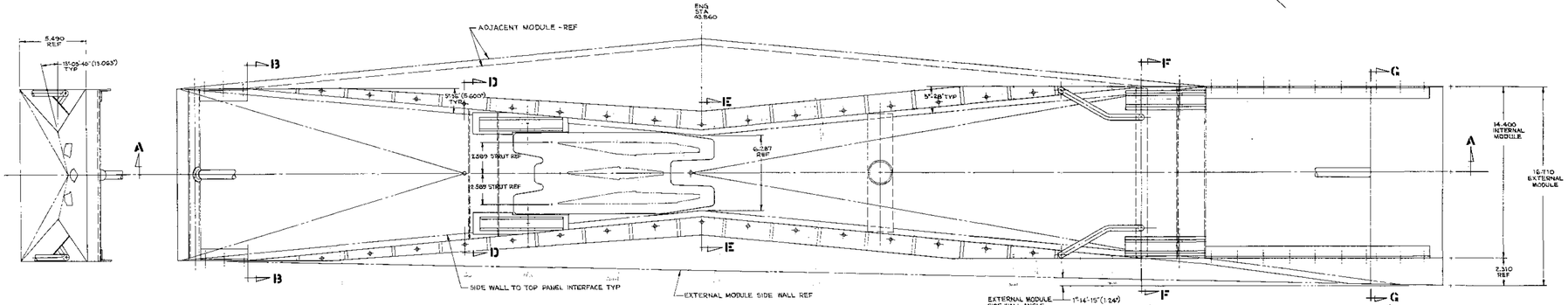

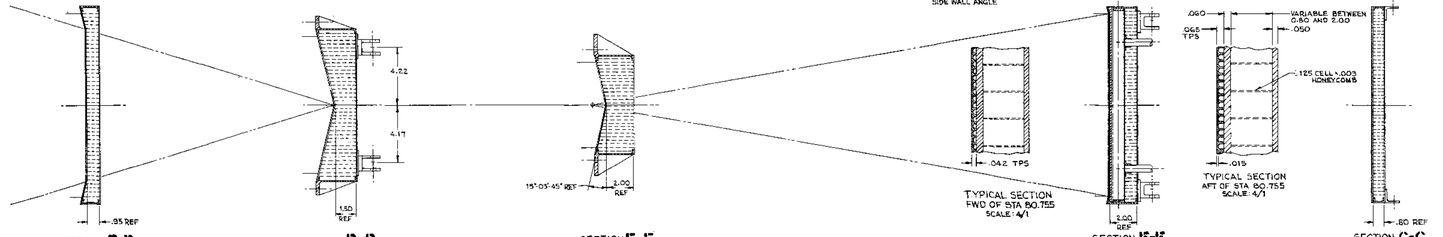

NOTES: UNLESS OTHERWISE SPECIFIED

REVISIONS			
ZONE	LTR	DESCRIPTION	DATE	APPROVED

| | | | |

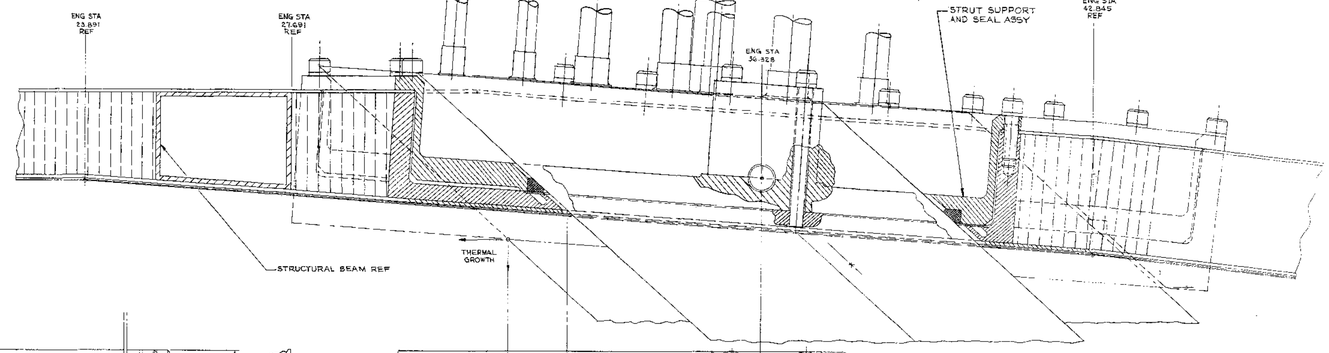

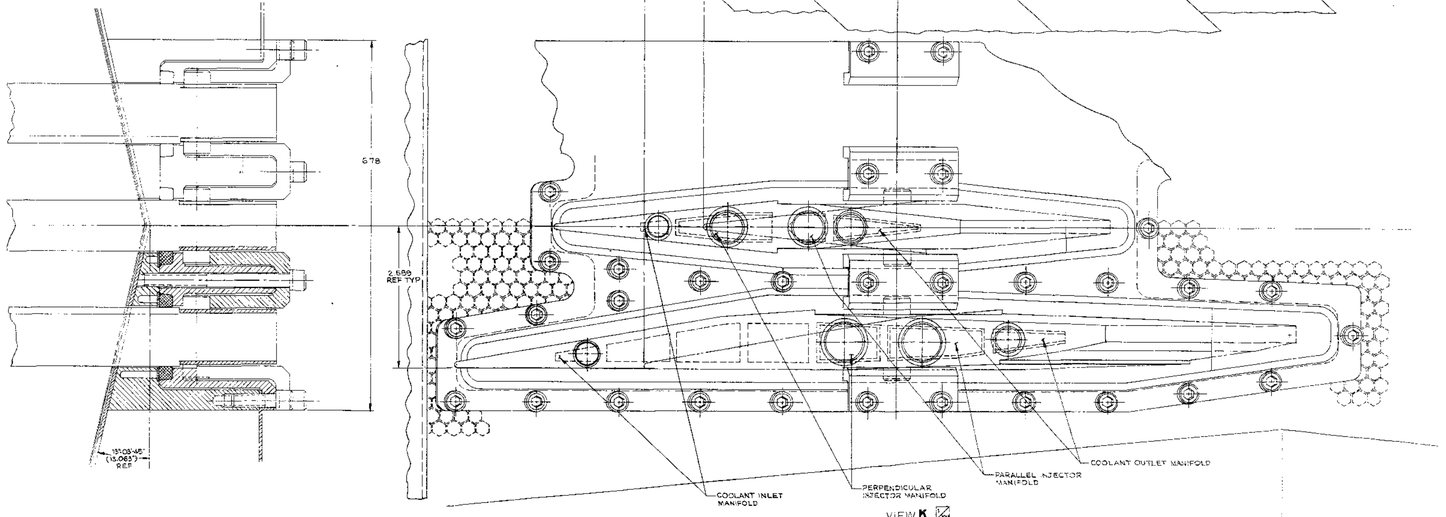

VIEW K
STRUT MOUNTING
SCALE: 2/1

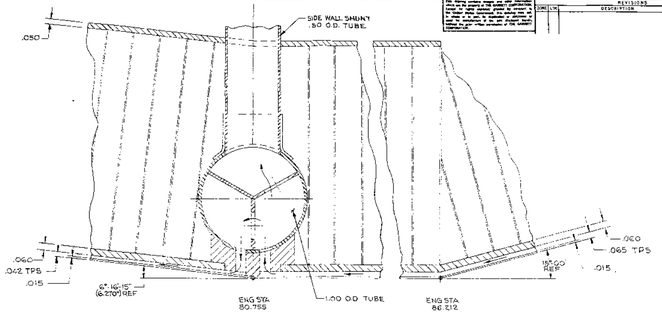

COOLANT SHUNT MANIFOLD
SCALE: 4/1
VIEW H

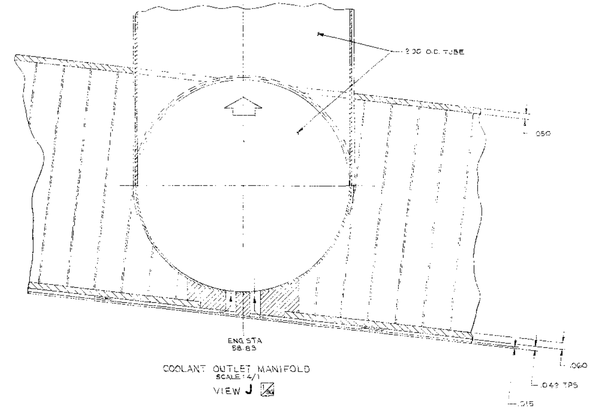

COOLANT OUTLET MANIFOLD
SCALE: 4/1
VIEW J

192224 2

J 70210 192224

ENGINE-AIRCRAFT INTERFACE

A separate mounting frame is used to join the engine modules to the aircraft. Module loads are transmitted through the topwall honeycomb structure to the mounting frame. The frame transmits engine thrust, drag, and inertial loads to the aircraft and should prevent excessive deflections. The airframe attachment links should be greater than three to satisfy fail-safe criteria. Truss arrangements are effective in meeting the stiffness/weight goals, but the cross members interfere with the hydrogen ducting. The frame must accommodate module thermal growth and must not impose excessive thermal deflections on the airframe.

The selected concept is shown in fig. 131. In this case, a total of six modules comprise the engine assembly. The frame is rectangular with cross members at the module split line. It was assumed that the maximum temperature of the mounting frame will not exceed 316°C (600°F). This temperature is based on calculations made for the HRE environment and assumes the use of flow baffles to limit convective heating by leakage flow in the engine compartment. Inconel 718 was selected as the preferred material.

Six mounts join the engine frame to the airframe. All mounts carry vertical loads; thrust loads are through the three forward mounts; the two center mounts carry lateral loads (see fig. 131b). Swing and sliding links are used to accommodate thermal growth. An alternative is to use only the four outboard mounts. This may be necessary because of limited accessibility to the center mounts.

The spacing between the fore and aft mounting frame beams ("wheelbase") should be maximized to reduce deflections between leading and trailing edges and aircraft outer skin. The corresponding fore and aft module attachment points should be located where the primary structure temperatures are equal. This locating scheme will minimize differential thermal growth between fore and aft mount points, thereby keeping the module axial centerlines parallel during operation. These criteria can be met by locating the frame beams shown in fig. 131a at stations 29 and 85, where the topwall primary structure is about 24°C (75°F) during normal operation.

As shown in fig. 131c, the aft module mount is fixed axially while the forward mount is free to slide axially. The central modules are fixed laterally along the inboard sidewall at both fore and aft mounts. Lateral growth of an individual module is outward from the engine centerline, and is cumulative.

The engine compartment must be sealed to prevent ingress of hot gas. Required sliding seals are indicated in fig. 131d. The fore and aft seals must also accommodate vertical deflection due to fuselage bending. As previously noted, the effect of this deflection is minimized by increasing the mounting frame wheelbase.

(a) Mounting Frame Spacing

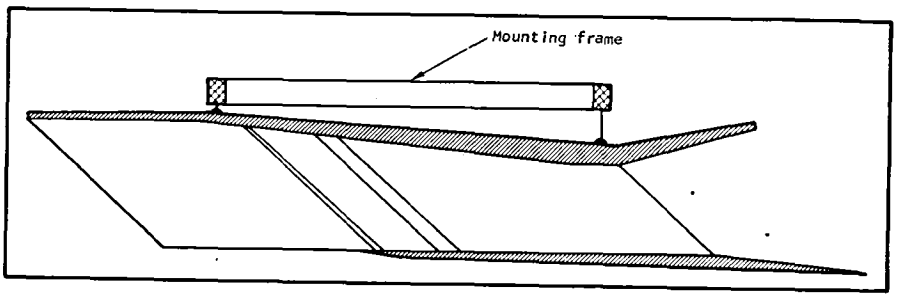

(b) Provisions for Mounting Frame Thermal Growth

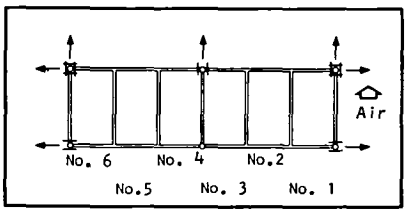

Thermal growth indicated by →

(c) Provisions for Module Thermal Growth

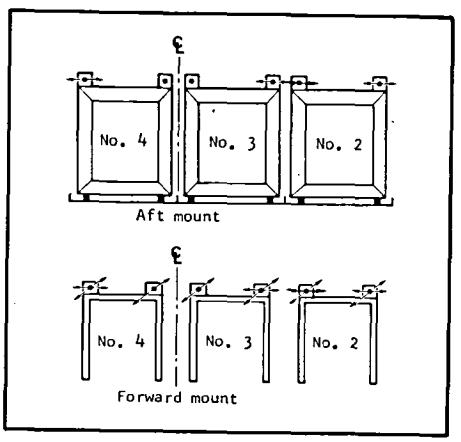

(d) Sealing Requirements

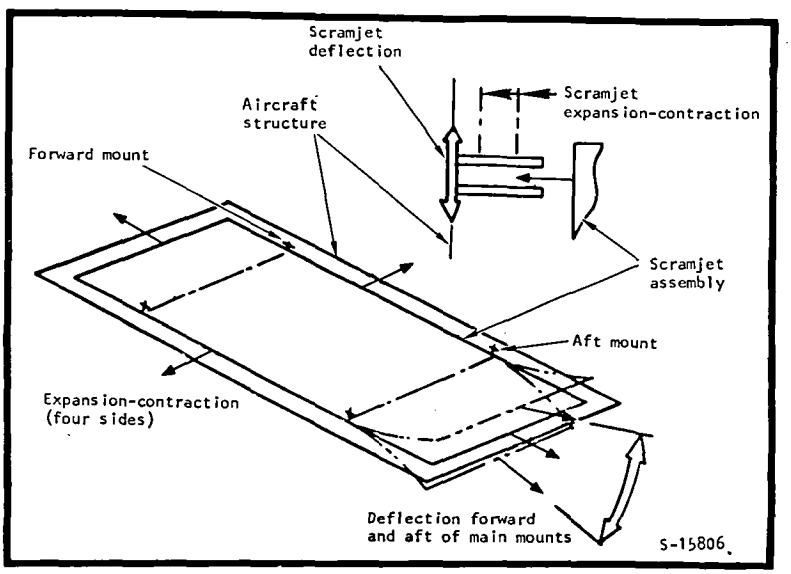

Figure 131.-Engine mounting considerations.

The space surrounding the mounting frame must be kept clear for hydrogen manifolding. An additional area above the mounting frame, about 15 to 30 cm (6 to 12 in.) in height, is desirable for installation of the hydrogen fuel and coolant valves. These valves should be installed close to the engine modules to obtain optimum control response and to minimize the plumbing and the number of firewall penetrations. The entire engine compartment cavity should be purged for safety. Overboard vents will be required for dumping hydrogen during engine shutdown, i.e., whenever coolant flow rates exceed combustion fuel flow rates.

The engine is modularized; however, because common sidewall leading and trailing edges are used and because of limited access in general, a complete single module assembly cannot be separated from the engine cluster. Repair of an individual panel, except for the external cowl, will also require removal of the engine assembly from the aircraft. Strut removal is through the topwall only. Access to the cowl interior and the space between sidewalls with the engine installed on the aircraft is possible by removing a panel on the external cowl.

HYDROGEN FLOW CONTROL

Coolant Flow Routing

As previously discussed, the proportion of the total heat load absorbed by any individual flow circuit is not constant throughout the flight envelope. To achieve maximum coolant utilization, active controls will be required to maintain the coolant outlet temperature close to the 890 K (1600°R) limit. The number of controls (coolant flow regulating valves) is dependent on how closely the 890 K (1600°R) limit must be met. A minimum number of valves will be required to ensure that the desired interpanel temperature differentials are not exceeded and that the matching is close to that shown in fig. 14.

Maximum coolant utilization can be achieved by using a valve to control coolant flow to each individual module flow route--at least seven valves per module; a total of 42 valves for a six-module engine. Mission analyses are necessary to assess the resulting savings in coolant utilization as compared with control concepts using fewer valves.

The least complex approach is to valve all forward-flow routes in parallel and all aft-flow routes in parallel among the six modules. A third valve controls all strut flow routes. This concept divides the engine into three sections: (1) the inlet section, (2) the combustor/nozzle section, and (3) the struts. It is assumed that there is no large difference in heating rate between modules.

Calibrated orificing is used to establish the basic flow split between the topwall, sidewalls, and cowl within the forward and aft circuits. This approach presumes that the heat load split between panels will remain in a reasonably fixed proportion for all flight conditions. Temperature sensors

are imbedded in the thermal protection system panels near the outlet of the flow circuit and adjacent to the outlet manifold. During operation, it is expected that the coolant temperatures at the exits of the parallel flow routes will not necessarily be equal. A computer (microprocessor) will monitor all temperature sensors and will drive the coolant regulating valve (CRV) to maintain the sensor with the maximum temperature reading at 890 K (1600°R). Thus, one of the panel flow circuits within the forward or aft sections can be slightly overcooled.

As noted, the entire cooling capacity in the fuel is not utilized ($\emptyset_c$ is less than 1.0) over most of the operating envelope (see figs. 4 and 17). If the remaining capacity is not used for airframe cooling, then it would be possible to operate the engine structure at a lower temperature level by using the entire flow rather than just the portion based on an 890 K (1600°R) outlet temperature. Control valves would still be required to regulate the flow split. This scheme does offer potential improvements. It was not considered except for the struts because one of the goals of the study is to conserve coolant.

No provision has been made to shut down a single module in the event of an unstart or other abnormal condition. Since the transient conditions in the engine are severe for even normal operation, operation without combustion in one of the modules may prove feasible as is. Control system response, in turn, may be too slow to prevent the imposition of the large ΔT's associated with combustion shutdown in one module. Additional valving might be of no benefit in such a case. Further detailed study will be required to evaluate the effects of these conditions on both the engine structure and control system configuration.

Fuel System

A preliminary study was conducted to define the Scramjet fuel system. Estimates of the component sizes and weights were made. To permit selection and sizing of the turbopump system, it was assumed that the equipment would be used in a research airplane in which the flight duration is 40 sec of cruise at Mach 6.

All hydrogen lines have been sized on the basis of a total fuel flow of 3.85 kg/sec (8.5 lb/sec) and 0.644 kg/sec (1.42 lb/sec). This is the fuel flow for a total of six modules and one module, respectively.

Fuel system schematic.--A schematic diagram of the installation is shown in fig. 132. The modules are grouped in two sets of three. A separate turbopump, coolant regulating valves, and fuel valves are used for each set of three modules. This arrangement permits testing either a three- or six-module cluster on the research airplane.

For maximum response rate, the coolant regulating and fuel control valves should be located adjacent to the engine modules. It is possible, however, to locate the turbopumps in a remote location, closer to the hydrogen supply tank. The computer should be installed in a controlled environment.

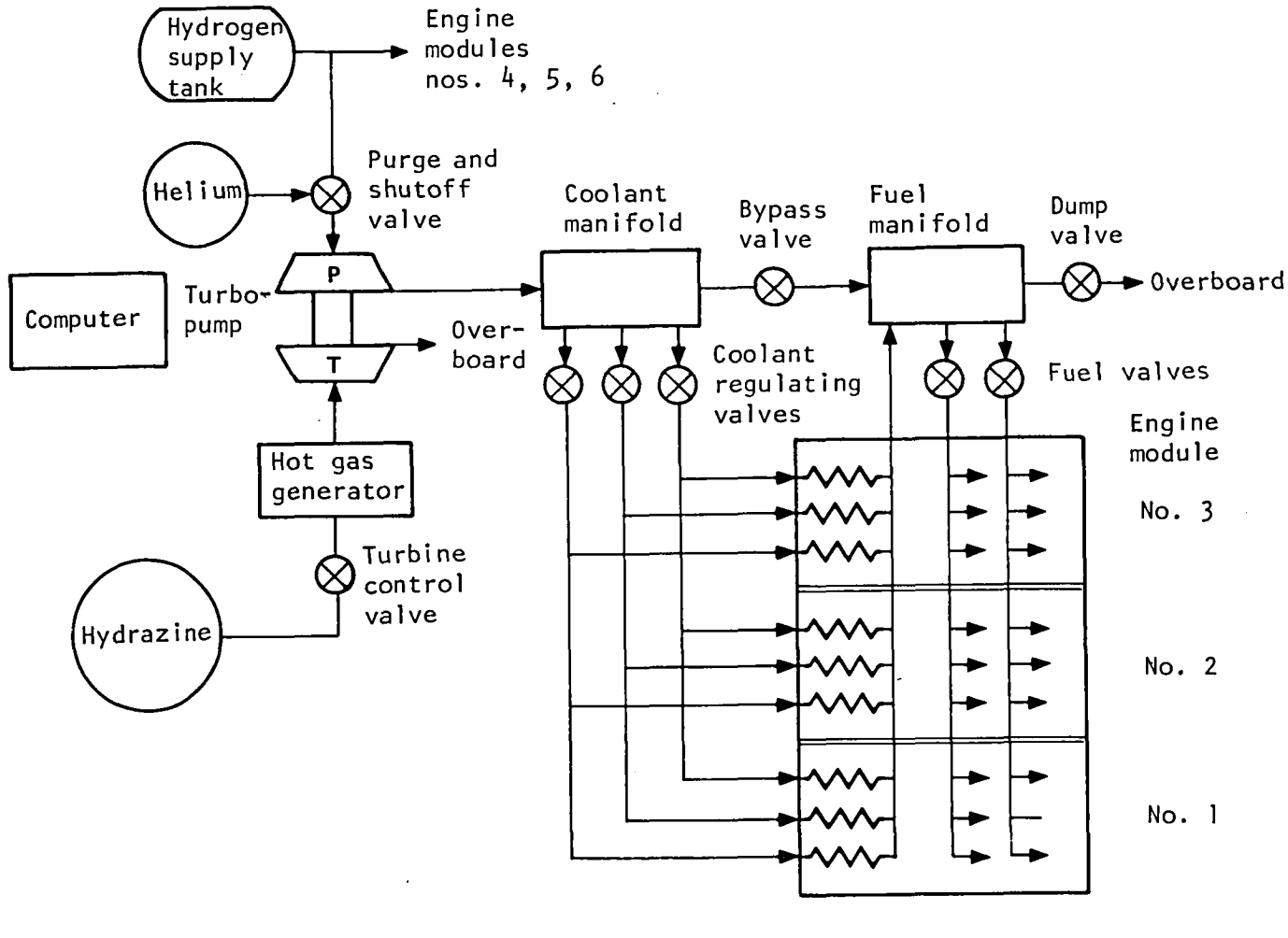

Figure 132.-Engine fuel system.

Overall dimensions and weights of the system components are summarized in Table 23. Each valve will consume 2.7 watts except for the purge and shutoff valve that will consume 35 watts when energized. Component descriptions are presented below.

Hydrogen supply.--The hydrogen supply in the tank is very close to saturation. It has been assumed that the turbopump can be designed to operate at this condition by using a specially designed inducer. A separate boost pump may be required. Alternatively, the hydrogen supply tank could be maintained at 0.34 MPa (50 psig).

Helium supply.--A separate helium supply tank is utilized to purge the hydrogen system after use and to provide a flow of purge gas in the payload bay after the research airplane drops from the B-52. A helium supply line is also routed to the engine compartment to supply helium to the fuel control valve actuators.

The tank is assumed to be spherical with an operating pressure of 34.5 MPa (5000 psia). The volume is 42.5 liters (1.5 cu ft) and the tank mass is 72.5 kg (160 lb), including 4.5 kg (10 lb) of helium.

Computer.--The basic control system approach is to utilize a central programmable digital computer that will handle upwards of 300 input parameters and control some 30 output control variables. All valves in the various hydrogen circuits will be under the command of the digital computer. The computer provides all logic and control signals necessary for (1) operating the combustor fuel feed and distribution as required by speed and altitude for desired equivalence ratios, (2) regulating coolant flows to the engine module panels to maintain the desired skin temperatures, and (3) performing numerous safety and self-checking functions.

Estimated size is that of a 1/2-ATR (short) standard size case, 12.4 cm (4.88 in.) wide by 31.8 cm (12.52 in.) long by 19.4 cm (7.62 in.) high. Total volume is equal to 8500 cc (0.3 cu ft). Estimated power requirement is 40 watts, 28 vdc. The estimated mass is 13.6 kg (30 lb).

Turbopump subsystem.--A hot-gas-driven turbopump is recommended rather than a bootstrap-type design as used on the HRE. The reasons are:

(a) The coolant ϕ is less than 1.0 compared to about 3.0 on the HRE. Hence, additional hydrogen would be required to drive the turbopump. A bootstrap design may be feasible if the coolant ϕ is maintained at unity at all conditions.

(b) The plumbing required to supply hot hydrogen from the modules to the turbopump is eliminated. This is especially important if the turbopump is in a remote location.

(c) A separate hot gas supply may still be required to start the turbopump in addition to the bootstrap arrangement.

(d) Greater flexibility for research testing.

TABLE 23.- FUEL SYSTEM COMPONENTS (TWO GROUPS OF THREE MODULES; SIX MODULES TOTAL)

Component	Envelope		Unit mass		Total mass	
	cm	in.	kg	lb	kg	lb
Valve						
Coolant regulating (6)	17.8 dia by 22.9 lg	7.0 dia by 9.0 lg	5.1	11.3	30.8	67.8
Fuel control - parallel injector (2)	17.8 dia by 22.9 lg	7.0 dia by 9.0 lg	5.1	11.3	10.3	22.6
Fuel control - perpendicular injector (2)	20.3 dia by 22.9 lg	8.0 dia by 9.0 lg	5.8	12.8	11.6	25.6
Bypass (2)	15.2 dia by 23.9 lg	6.0 dia by 9.4 lg	3.6	8.0	7.3	16.0
Dump (1)	15.2 dia by 22.9 lg	6.0 dia by 9.0 lg	8.2	18.0	8.2	18.0
Purge and shutoff (1)	15.7 by 22.9 by 31.5	6.2 by 9.0 by 12.4	6.4	14.0	6.4	14.0
Turbine control (2)	5.8 by 13.5 by 13.7	2.3 by 5.3 by 5.4	2.7	6.0	5.4	12.0
Computer (1)	12.7 by 20.3 by 34.8	5.0 by 8.0 by 12.5	13.6	30.0	13.6	30.0
He supply tank (1)	45.7 dia	18.0 dia	72.6	160.0	72.6	160.0
Turbopump (2)	23.4 dia by 25.9	9.2 dia by 10.2	29.5	65.0	59.0	130.0
Gas generator (2)	13.0 dia by 10.2 lg	5.1 dia by 4.0 lg	3.4	7.5	6.8	15.0
Total mass					232	511

The characteristics of the hydrogen turbopump and hot gas generator are summarized in Table 24. This particular design is for a fuel flow of 2.56 kg/sec (5.65 lb/sec), which occurs with four modules at a Mach 6 condition. Thus, the turbopump has growth capability and would be suitable for an 8-module engine cluster.

Two different hot gases were considered--hydrazine* (H_2N_2) and hydrogen peroxide (H_2O_2). The resultant turbine and gas generator sizes are about equal. For a given mission duration, less hydrazine is required, and considering that oxygen is a decomposition product of hydrogen peroxide, it is believed that hydrazine is safer to use with hydrogen.

It was determined that by using two turbopumps in parallel rather than a single unit for all six modules, a mass savings of 10.4 kg (23 lb) could be achieved.

Valves.--The designs are electropneumatic poppet valves and were scaled from existing designs originally developed for the HRE program.

Coolant regulating valves: Three CRV's are shown in fig. 118, with one valve controlling the same flow circuit in each module (a parallel-flow arrangement).

Fuel control valves: For minimum complexity, only one valve is used for each set of parallel and perpendicular injectors. With a single set of fuel valves, however, it will be necessary to shut down the entire set of three modules in the event of an off-limit condition (e.g., unstart). The cost of a research flight as well as flight safety considerations in any ultimate application will probably dictate the ability to shut down an individual module. Hence, two fuel control valves will be required for each module.

Bypass valve: A bypass valve is utilized because the fuel flow required by the Scramjet exceeds the coolant flow requirement ($\phi_c < 1.0$). The coolant regulating valves will be controlled to maintain the hydrogen outlet temperature (at the fuel manifold) at 889 K (1600°R). The bypass valve will be controlled to maintain the fuel manifold pressure at 5.2 MPa (750 psia).

Fuel dump valve: The fuel dump valve has been sized to handle the total coolant flow requirement. It has been assumed that at the end of the Scramjet cruise, the fuel flow will be turned off, but the engine will still require full cooling for a short period of time.

Line size: Line size and hydrogen conditions for each location are summarized in Table 25. The helium supply line to the engine compartment is 9.5 mm (3/8 in.) diameter.

*Hydrazine is currently used by the Concorde and F-16 emergency power units and the Space Shuttle APU.

TABLE 24.-TURBOPUMP SUBSYSTEM, THREE MODULES

Turbopump	Hydrogen pump	Hot gas turbine	
		H_2O_2	N_2H_2
Inlet temperature, K (°R)	20.6 (37)	1006 (1810)	1200 (2160)
Inlet pressure, MPa (psia)	.21 (30)	2.76 (400)	2.76 (400)
Discharge pressure, MPa (psia)	7.58 (1100)	.14 (20)	.14 (20)
Flow, kg/sec (lb/sec)	2.56 (5.65)	.62 (1.37)	.40 (.88)
Efficiency, percent	79	71	58
Power, MW (hp)	.350 (470)	.373 (500)	.373 (500)
Impeller dia, cm (in.)	104 (4.1)	11.9 (4.7)	11.7 (4.6)
Housing dia, cm (in.)	23.4 (9.2)	19.1 (7.5)	18.0 (7.1)
Total mass, kg (lb)	29.5 (65)		
Gas generator	H_2O_2	N_2H_2	
Diameter, cm (in.)	14.0 (5.5)	13.0 (5.1)	
Length, cm (in.)	10.2 (4.0)	10.2 (4.0)	
Mass (each), kg (lb)	3.9 (8.6)	3.4 (7.5)	

TABLE 25.- FUEL SYSTEM PLUMBING LINE SIZE

Location	Flow		Pressure		Temperature		Outside diameter	
	kg/sec	lb/sec	MPa	psia	K	°R	cm	in.
Pump inlet	4.15	9.15	.14	20	21	37	8.9	3.5
Pump discharge	4.15	9.15	7.58	1100	56	100	5.1	2.0
Coolant regulating valve outlet	.17	.38	6.55	950	56	100	1.9	.75
Bypass valve outlet	1.54	3.40	5.52	800	111	200	6.4	2.5
Turbine inlet	.29	.65	4.14	600	889	1600	5.1	2.0
Turbine discharge	.29	.65	.14	20	556	1000	11.4	4.5
Dump valve discharge	2.31	5.10	.69	100	889	1600	10.2	4.0

CONCLUDING REMARKS

Overall objectives for the Scramjet engine design can be met. It is possible to attain a life of 100 hr and 1000 cycles, which is the goal for the intended research application. The coolant equivalence ratio is less than 1.0 throughout the engine operating envelope; however, at the maximum altitude and Mach number conditions a fuel equivalence ratio of 1.5 was used. Estimated coolant equivalence ratios for stoichiometric combustion at these conditions indicated a coolant equivalence ratio increase to 1.239. Thus, stoichiometric combustion requires the use of additional fuel for cooling at the Mach 10 condition with a 2-g turn. The mechanical design is feasible for manufacture using conventional materials. For the cooled structures in a six-module engine, the mass per unit capture area is 1328 kg/m^2 (259 lb/ft^2). The total mass of a six-module engine assembly including the fuel system is 1502 kg (3311 lb).

Cooled Structure

An all-honeycomb primary structure is better than beam and honeycomb combinations in terms of minimum deflection and complexity for equal mass. The required honeycomb material, cell dimensions, overall size, and contour are feasible for manufacture. The engine panels (i.e., the topwall, sidewall, and cowl) may be rigidly joined at the corners and no dynamic hot gas seals are required. Selected materials are Hastelloy X for the honeycomb primary structure, Inconel 718 for the strut primary structure, Hastelloy X or Nickel-200 for the TPS, and Nickel-200 for the leading edges.

The transient performance of the TPS/structure during engine startup and shutdown governs the design. For the most severe assumptions concerning mission trajectory and engine operating procedures, ΔT's can range to 670 K (1200°R). Reduction of ΔT's to acceptable levels is possible by changes in operating procedures and, if required, in design of the TPS.

Specific structural design solutions have been identified for the engine. These have been incorporated in layout drawings of the engine. Analyses have verified that there are no basic structural problems once the transient operation is accommodated.

The design objectives for the engine, given control of the temperatures during transients, are feasible: 1000 cycles and 100 hr of engine operation. TPS temperatures are being limited to 1140 K (1600°F) on the surface and 890 K (1600°R) at the prime structure. Deflections during normal engine operation can be limited to the specified values and remain acceptable during the severe loadings assumed for engine unstart.

Coolant Flow Routing

It is best to introduce coolant at the leading and trailing edges and let it flow toward the engine throat, where it is withdrawn. This basic flow scheme

must be adjusted, however, to achieve temperature matching between panels. Uniformity in temperature gradients between panels is crucial in meeting thermal stress limitations. Active controls will be required to obtain maximum coolant utilization. The minimum number of flow routes to be controlled is three--forward and aft portions of the panels and a separate control for the struts.

Thermal Protection System

In the HRE program, low-cycle fatigue of the offset-fin plate fin TPS was identified as the primary limitation on structural life. For the Scramjet, two heat exchanger geometries were determined to yield significantly better fatigue life. For the panels, topwall, sidewalls, and cowl, a machined channel design is specified. For the struts, a pin-fin surface is recommended. Experimental data are required to substantiate the predicted low-cycle fatigue life and creep-rupture behavior of the selected TPS structures. A NASA-sponsored fabrication and material technology development program presently in progress is expected to provide such data. Test data are also required to confirm that the corner heat flux is not significantly higher than that at the engine centerline.

Leading Edges

Low-cycle fatigue is the controlling design parameter. High performance is achieved by impinging the entire panel flow at the minimum supply temperature, 100°R, on the respective leading edges. Nickel-200 was specified because of its high thermal conductivity and ductility, two factors that contribute to increased fatigue life. The one-dimensional analysis (on which results in this report are based) should be extended to two dimensions to more precisely define the problem. Experimental data are required because of the intensity of the heat flux, complexity of the flow path, and the impact of brazing and other manufacturing operations on fatigue life.

Fuel Injection Struts

External pressure loads, such as occur during an unsymmetrical unstart, combined with thermal stresses, impose major design problems for the slender struts. Design feasibility was proven, however. A midspan tie between struts is necessary to withstand unstart loads using minimal coolant flow. A preferable alternate that eliminates the tie is to overcool the struts.

The limited space within the struts dictates the fuel and coolant flow routing. Integral manifolding with flow from one end of the strut remains as the most feasible approach.

The dynamic response of the struts to the unstart transient should be evaluated. Significant load amplification could occur because the pressure pulse period is close to the strut natural frequency.

Engine-Aircraft Interface

Hydrogen flow control valves and manifolding should be located on the module mounting frame to provide an integral assembly, especially for a research application, and to achieve optimum control response. Behavior of the overall module cluster and the assembly response to an individual module shutdown deserve further attention to define the sealing problem and interface thermal stresses.

Hydrogen Flow Control

The minimum number of valves has been specified. Additional valves may be required to provide for shutdown of an individual module or closer regulation of coolant temperatures.

REFERENCES

1. Staff of Langley Research Center and AiResearch Manufacturing Company, The Garrett Corporation: Hypersonic Research Engine Project Status 1971. NASA TM X-2572, 1972.

2. Flieder, W. G., Richard, C. E., Buchmann, O. A., and Walters, F. M.: An Analytical Study of Hydrogen Cooled Panels for Application to Hypersonic Aircraft. NASA CR-1650, April 1971.

3. Richard, C. E., Duncan, J. D., Gellersen, E. W., and Demogenes, C.: Thermal and Structural Tests of a Hydrogen Cooled Panel. NASA-CR-2105, May 1972.

4. Wieting, Allan R., and Guy, Robert W: Thermal-Structural Design/Analysis of an Airframe-Integrated Hydrogen-Cooled Scramjet. J. of Aircraft, Vol. 13, No. 3, March 1976, pp. 192 to 197.

5. Buchmann, O.A.: Summary Report, Thermal-Structural Design Study of an Airframe-Integrated Scramjet. NASA CR-3141, December 1978.

6. Hearth, Donald P., and Preyss, Col. Albert E., USAF: Hypersonic Technology--Approach to an Expanded Program, Astronautics and Aeronautics Vol. 14, No. 12, Dec 1976, pp. 20 to 37.

7. Kelly, H. Neale, Wieting, Allan R., Shore, Charles P., and Nowak, Robert J.: Recent Advances in Convectively Cooled Engine and Airframe Structures for Hypersonic Flight. 11th Congress of the International of the Aeronautical Sciences, Lisbon, Portugal, Sept. 10 to 16, 1978.

8. Wieting, Allan R.: Exploratory Study of Transient Unstart Phenomena in a Three-Dimensional Fixed Geometry Scramjet Engine. NASA Technical Note TN D-8156, March 1976.

9. Engineering Staff, Hypersonic Research Engine Project - Phase IIA: Structures and Cooling Development, Second Interim Technical Data Report. Data Item 55-7.02, AiResearch Report No. AP-67-2537, August 23, 1967, NASA CR 11770.

10. Fay, J. A., and Riddell, F. R.: Theory of Stagnation Point Heat Transfer in Dissociated Air. J. of the Aeronautical Science, Feb. 1959, p. 17.

11. Stainback, P., and Weinsten, L.: Aerodynamic Heating in the Vicinity of Corners at Hypersonic Speeds. NASA TN D-4130, Nov. 1967.

12. Kays, William, and London, A. L.: Compact Heat Exchangers. 2nd ed., McGraw-Hill Book Co., New York, 1964.

13. Sines, G., and Waisman J.L., editors: Metal Fatigue. McGraw Hill Co., 1959.

14. Halford, G. R., Hirschberg, H. M., and Manson, S. S.: Temperature Effects on the Strainrange Partitioning Approach for Creep Fatigue Analysis. Fatigue at Elevated Temperatures, American Society for Testing and Materials (ASTM) STP 520, 1973, pp. 658 to 669.

15. Whetstone, W.D.: SPAR Structural Analysis System. NASA CR 145098-1, February 1977.

16. De Salvo, G. J., and Swanson, J. A.: ANSYS Engineering Analysis System User's Manual. Swanson Analysis Systems, Elizabeth, Pa. 15037, March 1, 1975.

17. Spera, D. A.: Calculation of Thermal-Fatigue Life Based on Accumulated Creep Damage. NASA TN-D-5489, Oct. 1969.

18. Spera, D. A.: The Calculation of Elevated-Temperature Cyclic Life Considering Low-Cycle Fatigue and Creep. NASA TN-D-5317, July 1969.

19. Manson, S. S.: The Challenge to Unify Treatment of High Temperature Fatigue--A Partisan Proposal Based on Strainrange Partitioning. Fatigue at Elevated Temperatures, American Society for Testing and Materials (ASTM) STP 520, 1973, pp. 744 to 782.

20. Spera, D. A.: Comparison of Experimental and Theoretical Thermal Fatigue Lives for Five Nickel-Base Alloys. Fatigue at Elevated temperatures, American Society for Testing and Materials (ASTM) STP 520, 1972, pp. 648 to 657.

21. Perlmutter, M.: inlet and Exit-Header Shapes for Uniform Flow Through a Resistance Parallel to the Main Stream. Trans. ASME, J. of Basic Engineering, Vol. 83, September 1961, pp. 361 to 370.

22. Heyda, J.F.: An Analytical Study of a Balanced Reverse-Folded Flow. XDC 60-1-158, General Electric Company Report, reprinted by Dept. of Commerce, January 1960.

23. Wolf, S.: Flow Losses for Heat Exchangers with Oblique Flow Headers. TR No. 60, Department of Mechanical Engineering, Stanford University, June 1964.

24. London, A.L.: Flow Losses for Heat Exchangers with Oblique Flow Headers. Supplement to TR No. 60, Department of Mechanical Engineering, Stanford University, September 1964.

25. London, A.L., Klopfer, G., and Wolf, S.: Oblique Flow Headers for Heat Exchangers--The Ideal Geometries and the Evaluation of Losses. TR No. 63, Department of Mechanical Engineering, Stanford University, August 1966.

26. Liepmann, H. W., and Roshko, A.: Elements of Gasdynamics. John Wiley and Sons, Inc., New York, New York, 1957.

27. Klopfer, G.: Oblique Flow Headers for Heat Exchangers--The Influence of Inlet Velocity Profiles. TR No. 65, Department of Mechanical Engineering, Stanford University, July 1967.

28. National Bureau of Standards: Thermodynamic Properties of Para Hydrogen From the Freezing Liquid Line to 5000°R for Pressures to 10,000 psia. NBS Technical Note 617.

APPENDIX

CONVERSION FACTORS

(Taken from NASA SP-7012, The International System of Units, Physical Constants and Conversion Factors, 2nd revision, 1973, Mechtly, pp. 11 to 20)

The following table expresses the definitions of miscellaneous units of measure as exact numerical multiples of coherent SI units, and provide multiplying factors for converting numbers and miscellaneous units to corresponding new numbers and SI units.

The first two digits of each numerical entry represent a power of 10. An asterisk follows each number which expresses an exact definition. For example, the entry "-02 2.54*" expresses the fact that 1 inch = 2.54×10^{-2} meter, exactly, by definition. Most of the definitions are extracted from National Bureau of Standards documents. Numbers not followed by an asterisk are only approximate representations of definition, or are the results of physical measurements. The conversion factors are listed alphabetically.

To convert from	To	Multiply by
British thermal unit	joule	+03 1.055 056
British thermal unit (thermochemical)/second	watt	+0.3 1.054 350 264 488
Celsius (temperature)	kelvin	$t_K = t_C$ +273.15
Degree (angle)	radian	-02 1.745 329 251 994 3
Fahrenheit (temperature)	kelvin	$t_K = (5/9)\ (t_F$ +459.67)
Fahrenheit (temperature)	celsius	$t_C = (5/9)\ (t_F$ -32)
Foot	meter	-01 3.048*
Horsepower (550 foot lbf/second)	watt	+02 7.456 998 7
Inch	meter	-02 2.54*
lbf (pound force, avoirdupois)	newton	+00 4.448 221 615 260 5*
lbm (pound mass, avoirdupois)	kilogram	-01 4.535 923 7*
Rankine (temperature)	kelvin	$t_K = (5/9) t_R$
Second (angle)	radian	-06 4.848 136 811

1. Report No.	2. Government Accession No.	3. Recipient's Catalog No.
NASA CR-159039		

4. Title and Subtitle	5. Report Date
THERMAL-STRUCTURAL DESIGN STUDY OF AN AIRFRAME-INTEGRATED SCRAMJET-FINAL REPORT	May 1980
	6. Performing Organization Code

7. Author(s)	8. Performing Organization Report No.
J.J. Killackey, E.A. Katinszky, S. Tepper, A.A. Vuigner, C.C. Wright, and G.G. Stockwell	78-15442-2
	10. Work Unit No.

9. Performing Organization Name and Address	11. Contract or Grant No.
AiResearch Manufacturing Company of California, A Division of The Garrett Corporation, Torrance, California 90509	NAS1-13984
	13. Type of Report and Period Covered Contractor Report June 1975-December 1979

12. Sponsoring Agency Name and Address	14. Sponsoring Agency Code
National Aeronautics and Space Administration Washington, D.C. 20546	

15. Supplementary Notes

Langley Technical Monitor: Allan R. Wieting

16. Abstract

The overall objectives of this study are to: (1) develop and evaluate a design concept for the cooled structures assembly for the Langley Scramjet engine; (2) develop concepts for engine subsystems in sufficient detail to show feasibility and estimate mass, volume, and operating requirements; and (3) establish design concepts for the aircraft/engine interface. These overall objectives for the Scramjet engine can be met. A thermal protection system has been defined that makes it possible to attain a life of 100 hr and 1000 cycles, which is the specified goal. The coolant equivalence ratio at the Mach 10 maximum thermal loading condition is 0.6, indicating a capacity for airframe cooling. The mechanical design is feasible for manufacture using conventional materials. For the cooled structures in a six-module engine, the mass per unit capture area is 1256 kg/m^2 (259 lb/ft^2). The total mass of a six-module engine assembly including the fuel system is 1502 kg (3311 lb). This report presents the results of the study.

17. Key Words (Suggested by Author(s))	18. Distribution Statement
Regeneratively cooled structure Scramjet Thermal protection systems Hypersonic engine	Unclassified-unlimited

19. Security Classif. (of this report)	20. Security Classif. (of this page)	21. No. of Pages	22. Price*
Unclassified	Unclassified	226	

* For sale by the National Technical Information Service, Springfield, Virginia 22161

NASA Contractor Report 159039

Distribution List
NAS1-13984

	No. Copies
NASA Langley Research Center Hampton, VA 23665 Attn: Report and Manuscript Control Office, Mail Stop 180A Allan R. Wieting, Mail Stop 395	1 25
NASA Ames Research Center Moffett Field, CA 94035 Attn: Library, Mail Stop 202-3	1
NASA Dryden Flight Research Center P. O. Box 273 Edwards, CA 93523 Attn: Library	1
NASA Goddard Space Flight Center Greenbelt, MD 20771 Attn: Library	1
NASA Lyndon B. Johnson Space Center 2101 Webster Seabrook Road Houston, TX 77058 Attn: JM6/Library	1
NASA Marshall Space Flight Center Marshall Space Flight Center, AL 35812 Attn: Library, AS61L	1
Jet Propulsion Laboratory 4800 Oak Grove Drive Pasadena, CA 91103 Attn: Library, Mail Code 111-113	1
NASA Lewis Research Center 21000 Brookpark Road Cleveland, OH 44135 Attn: Library, Mail Stop 60-3	1
NASA John F. Kennedy Space Center Kennedy Space Center, FL 32899 Attn: Library, NWSI-D	1
National Aeronautics and Space Administration Washington, DC 20546 Attn: RTM-6	1
NASA Scientific and Technical Information Facility 6571 Elkridge Landing Road Linthicum Heights, MD 21090	30 plus original